The Strain Dependent Dielectric Behaviour of Carbon Black Filled Natural Rubber

Menglong Huang

A thesis submitted for the degree of Doctor of Philosophy

School of Engineering and Materials Science

Queen Mary University of London

September 2015

Abstract

The behaviour of filled elastomer materials is of practical importance in many fields of engineering science. The exact mechanisms that result in increases in the physical behaviour such as the modulus, strength, damping or toughness of the resulting composite materials is still being widely debated in the academic literature. In this work, a new and novel approach has been developed to study the reinforcing mechanisms of such composite systems using dielectric spectroscopic measurements of the filled elastomer materials. The materials used are mostly Natural Rubber (NR) filled with either carbon black (CB) or silica.

Initially broadband dielectric spectroscopy (ranging from around 0.1 Hz to 0.3 THz) on NR/CB composites was developed using a wide range of different technologies that included impedance measurements, microwave testing and quasi-optical free space measurements. The carbon black makes a large contribution to the permittivity measured using the impedance method as a consequence of filler percolation effects. At higher frequencies, tested using either of the other two technologies, the measured permittivity shows an increase almost proportional to the filler volume fraction. By examining different types of carbon black, this behaviour was found to be independent of the filler surface area.

The polymer dynamics of NR filled with either CB or silica has also been studied in detail using temperature-domain impedance spectroscopy. A technique has been developed to measure the bulk glass transition temperature, Tg from the alpha relaxations. The bulk Tg of the filled NR compounds is, to within the accuracy of the experiment, almost totally unchanged by the incorporation of the filler materials. This suggests that the polymer dynamics of the NR chains around the filler surface are either very similar in behaviour to the bulk matrix polymer or at least they have too small a volume to be measured as a change in the bulk properties.

An entirely new technique was developed to measure the permittivity of natural rubber filled with either CB or silica under strain. This required the building of a simultaneous

dielectric and mechanical spectroscopy facility. Both the real and imaginary part of the permittivity decrease when the strain is larger than 1% for all the filled samples. This decrease comes from the deactivation of the dipoles around the filler-polymer interface with strain. The electrical permittivity versus strain behaviour follows a very similar softening effect to the mechanical Payne and Mullins effects albeit to a much greater extent and at a different level of strain. This allows an independent measure to be made of changes in the filler network structure with strain and this facilitates a better understanding of the actual network structures that might exist.

The dielectric behaviour versus strain relationship presents an opportunity to develop novel strain sensors. The prototype capacitance strain sensors made using a carbon black filled NR exhibited a much larger sensitivity when compared to other recently reported sensors.

Declaration

I hereby declare that all the works presenting in this thesis are originally done by myself during my graduate study. And all the referenced and collaborating works have been illustrated as they are.

Menglong Huang

Signature:

Date

Acknowledgements

I would like to thank Professor James Busfield for his supervision of my study. His tremendous help and encouragement enabled me to finish my work during my PhD. I would like to thank all the members from the Soft Matter Group in Queen Mary University of London. They are my families in London and make me feel like studying in my home country. Especially I would like to thank Dr. Lewis Tunnicliffe for all the discussions and experiments. I would like to thank Dr. Haixue Yan and Professor Xiaoyong Wei for discussing dielectric physics and Professor Alan Thomas for discussing rubber physics. I would also like to thank Professor Guang Li in Donghua University, who initiated my research in polymer science.

I would like to thank the CSC scholarship provided by the government of P.R.China to support my graduate study in London. I am proud of my country.

Most of the experiments of chapter three and four were done in Professor Wei Ren's lab in Xi'an Jiaotong University. I would like to thank his support in Xi'an. I would like to thank Dr. Jian Zhuang and Zenghui Liu for their kind hosting when I was visiting Xi'an. The microwave tests were done in Xi'dian University with the help of Professor Jiaming Tang and Dr. Gang Zhao. The quasi-optical tests were done with the help of Dr. Bin Yang of the University of Bolton. Part of chapter four and the corresponding paper were collaborations with Dr. Lewis Tunnicliffe from the Soft Matter Group in Queen Mary University of London. I would like to thank their kind help.

I would like to thank all of my friends in London, in particularly my colleagues Dr. Chen Chen, Dr. Xiao Liu, Guangchang Wu, Jian Wang, Dr. Xiaocong Wang, Dr. Jian Yao and Yi Zhang in Queen Mary University. I would like to thank Lily De La Cruz for hosting me in her home in London.

At last, I would like to express my deepest thanks to my mother Yunhua Ouyang and my fiancée Wei Zhu. They support and encourage me under any circumstance, continuously and selflessly.

Table of Contents

Abstract I
Declaration III
Acknowledgements IV
Table of Contents V
List of Abbreviations VIII
List of Symbols XI
List of Equations XVI
List of Tables XXI
List of Figures XXII
1 Chapter One: Introduction 1
2 Chapter Two: Literature Review 4
2.1 Basic knowledge of Rubber Materials 4
2.1.1 What is Rubber 4
2.1.2 Vulcanisation of Rubber 7
2.1.3 Mechanical Properties of a Rubber 10
2.1.4 Rubber Material Reinforcement using Nanoparticles 14
2.2 Fundamental Concepts of Dielectric Behaviour 22
2.2.1 Dielectric Matter in Static Electrical Field 22
2.2.2 Dielectric Matter in a Dynamic Electrical Field 24
2.2.3 Testing Technologies for Characterising Dielectric Properties of Solids: 29
2.3 Nanodielectric Elastomers 35
2.3.1 Twenty Years of Nanodielectrics: Opportunities and Challenges 35
2.3.2 Dielectric Relaxation of Cis-polyisoprene (PI) 41
2.3.3 Dielectric Properties of Carbon Black 47
2.3.4 The Interface of Nanodielectrics 49
2.3.5 The Mixing Laws of Inhomogeneous Systems 55
2.3.6 Percolation Theory 56
2.3.7 The Strain Dependent Dielectric Behaviour of Elastomers 62
2.4 Summary 66
3 Chapter Three: Broadband Dielectric Spectroscopy of Natural Rubber and Carbon Black Composites 68
3.1 Introduction 68

3.2 Experiments 69
3.2.1 Materials 69
3.2.2 Impedance test: 0.1 Hz - 1 MHz 70
3.2.3 RF Impedance test: 100 MHz-1 GHz 71
3.2.4 Microwave test: 7-40 GHz 71
3.3 Theory 72
3.3.1 Dielectric Relaxation Process 72
3.3.2 Classifying the Dipoles of Nanodielectrics 73
3.3.3 Percolation Theory 74
3.4 Results and Discussion 75
3.4.1 The Broadband Dielectric Spectrum 75
3.4.2 Explanation of the Dielectric Behaviour using the Percolation Theory 79
3.5 Summary 82
4 Chapter Four: Segmental Dynamics at the Filler-Rubber Interface 84
4.1 Introduction 84
4.2 Experiments 85
4.2.1 Materials 85
4.2.2 Impedance spectroscopy 86
4.2.3 Dynamical Mechanical Analysis 86
4.3 Results and Discussion 86
4.3.1 The Dielectric Relaxation Presented by 3D Dielectric Plots 86
4.3.2 The Segmental Relaxation of Unfilled NR 90
4.3.3 The Segmental Relaxation of Filled NR 92
4.4 Summary 98
5 Chapter Five: Measuring Dielectric Properties under Strain using Stretchable Electrodes 99
5.1 Introduction 99
5.2 Experiments 101
5.2.1 Materials 101
5.2.2 Standard Impedance Test (under no Strain) 101
5.2.3 Impedance Test under Strain: AgNW as Stretchable Electrodes 102
5.2.4 Impedance Test under Strain: Carbon Grease (CG) as Electrodes 106
5.2.5 Impedance Test under Strain: Rigid Copper as Electrodes 108
5.3 Results and Discussion 110
5.3.1 Dielectric Property of NR under No Strain: via Standard Impedance Test 110
5.3.2 Capacitance-Strain Relationship in SMDS & DDMS 111
5.3.3 Error Analysis of the SDMS and DDMS test 117

5.3.4 Disadvantages of Rigid Copper as Electrodes 120
5.4 Conclusion 121
6 Chapter Six: The Dielectric Behaviour of Strained Nanodielectric Elastomers 122
6.1 Introduction 122
6.2 Experiments 124
6.2.1 Materials 124
6.2.2 Tensile Mechanical Tests: 124
6.2.3 Electrical Test (dc) 125
6.2.4 Dielectric Test without Strain 125
6.2.5 Simultaneous Dielectric-Mechanical Spectroscopy (SDMS) test 125
6.2.6 Dielectric Compression Tests 126
6.3 Result and Discussion 126
6.3.1 Carbon Black Networks in NR 126
6.3.2 Effects of Filler Dispersion Quality on Dielectric Properties of Unstrained NR/CB 128
6.3.3 SDMS of Unfilled NR 129
6.3.4 SDMS of Carbon Black Reinforced NR 131
6.3.5 Dielectric vs Mechanical Spectroscopy 136
6.3.6 SDMS at Different Strain Rates 140
6.3.7 The Dielectric Behaviour of NR/CB Composites under Compression 142
6.3.8 SDMS of NR filled by Carbon Black with Different Morphologies. 143
6.4 Conclusion 144
7 Chapter Seven: Conclusion, Ongoing Work and Future Work 145
7.1 Conclusion 145
7.2 Ongoing Investigations 147
7.2.1 Smart Strain Sensors Using SDMS Technology 147
7.2.2 Quasi-optical Test of Nanodielectric Elastomers under Strain 148
7.3 Future work 150
References 152
Appendix 1： LabVIEW Remote Controlling Program 164
Appendix 2： The MATLAB Code for Data Analysis 167
Appendix 3： Refereed Journal and Conference Papers Published by The Author as Part of This Thesis 174

List of Abbreviations

6PPD	N-(1,3-Dimethylbutyl)-N´-phenyl-1,4-benzenediamine
AC	Alternative current
AFM	Atomic Force Microscopy
BDS	Broadband Dielectric Spectroscopy
BET	Brunauer Emmett and Teller
BR	Polybutadiene
CB	Carbon black
CG	Carbon grease
CNT	Carbon nanotube
COAN	The oil absorption number of a compressed sample
CR	Polychloroprene
CVS	Conventional silica
CS_TEVS	Tri-ethoxyvinyl silane modified conventional silica
CSC	China Scholarship Council
CTAB	Cetyltrimethylammonium bromide
CV	Conventional vulcanisation
DBP	Dibutylphthalate oil absorption
DCP	Dicumyl peroxide
DDMS	Discrete Dielectric Mechanical Spectroscopy
DMA	Dynamic Mechanical Analyser
EV	Efficient vulcanisation
HAF	High abrasion furnace
HDS	Highly dispersible silica
HDS_TEVS	Tri-thoxyvinyl silane modified highly dispersible silica
HTV	High temperature vulcanisation
HN	Havriliak-Negami
HOMO	The highest occupied molecular orbital
IEEE	Institute of Electrical and Electronics Engineers
IIR	Polyisobutylene
IS	Impedance Spectroscopy

LCR	Resistor-Capacitor-Inductor
LUMO	The lowest unoccupied molecular orbital
MBTS	Benzothiazyl disulfide
MUT	Material under test
MWCNT	Multi-wall carbon nanotube
MWS	Maxwell-Wagner-Sillars
NMR	Nuclear Magnetic Resonance
NR	Natural Rubber
NRW	Nicolson, Ross and Weir
OLED	Organic Light-emitting diodes
OPV	Organic photovoltaics
PC	Polycarbonate
PDMS	Polydimethyl siloxane
PET	Polyethylene terephthalate
PI	Cis-polyisoprene
PTFE	Polytetrafluoroethylene
PVDF	Polyvinylidene fluoride
RC	Resistor-Capacitor
RF	Radio frequency
RTV	Room temperature vulcanisation
RTV-A	Room temperature vulcanisation by addition reaction
RTV-C	Room temperature vulcanisation by condensation reaction
SBR	Styrene butadiene rubber
SDMS	Simultaneous Dielectric Mechanical Spectroscopy
SEV	Semi-efficient vulcanisation
SMR	Standard Malaysian Rubber
SSBR	Solution styrene butadiene rubber
TARRC	Tun Abdul Razak Research Centre
TEM	Transmission Electron Microscopy
TEVS	Tri-ethoxyvinyl silane
TPU	Thermoplastic polyurethane
TR	Transmission and reflection

UK	United Kingdom
USA	United State of America
VDF-TrFE	Poly(vinylidene fluoride-co-trifluoroethylene)
VFT	Vogel-Fulcher-Tamman
VL	Vacuum level
VNA	Vector Network Analyser
WLF	Williams-Landel-Ferry

List of Symbols

A	The fitting parameter of multi-HN process
A_i	The fitting parameter of the jth HN process
B_j	The fitting parameter of the jth HN process
C	Capacitance
C_0	The capacitance of the material at initial state
C_{corr}	The fringing and parasitic capacitance
C_i	The capacitance of the material at any time
C_S	The capacitance based on RC series model
C_P	The capacitance based on RC parallel model
D	Dielectric loss
$\boldsymbol{D}$	Electrical displacement
$\boldsymbol{D}_0$	Amplitude of the dynamic electrical displacement
$\boldsymbol{E}$	Electrical field
$\boldsymbol{E}_0$	Amplitude of the dynamic electrical field
E_1	The electrical field in phase one
E_2	The electrical field in phase two
$\boldsymbol{E}_L$	Local electrical field
F	Force
G	Elastic constant or shear moduli
G^*	Complex shearing moduli
G'	Storage moduli (shear)
G''	Loss moduli (shear)
I	The applied current in an impedance test
I^*	Complex current in an impedance test
I_0	Amplitude of applied current in an impedance test
M^*	Complex electrical moduli

M'	The real part of electrical moduli
M''	The imaginary part of electrical moduli
M_c	The average chain molecular weight between crosslinks
M_w	Molecular weight
N	The number of chains
$\boldsymbol{P}$	Electrical polarisation
$\boldsymbol{P}_A$	Dipole moment vector of an A-type chain
$\boldsymbol{P}_B$	Dipole moment vector of a B-type chain
$\boldsymbol{P}_C$	Dipole moment vector of a C-type chain
P_M	Molar polarisation
Q	Absorbed heat
R	The real part of impedance
R_{gas}	Gas constant
S	Entropy
T	Temperature
T_0	Ideal glass transition or Vogel temperature
U	Internal energy
U_0	Amplitude of applied voltage in an impedance test
U^*	Complex voltage in an impedance test
W	Work done to the system
X	The imaginary part of impedance
Z^*	Complex impedance
d_0	Initial thickness of the sample
d_1	The thickness of phase two
d_2	The thickness of phase one
d_i	Thickness of the sample at any time
e	Mechanical tensile strain
f	Electrical frequency

f_0	Fitting parameter of VFT function
f_{max}	The frequency of the loss peak
i	$\sqrt{-1}$
$j_{current}$	Current density
$j_{current1}$	Current density phase one
$j_{current2}$	Current density phase two
k_B	Boltzmann constant
l	Length
l_i	Length of the sample at any time
$\boldsymbol{r}$	End-to-end vector
t	Time
w_0	Initial width of the sample
w_i	Width of the sample at any time
$\Delta\kappa_j$	The dielectric strength of the jth HN process
ϕ	Filler volume fraction
ϕ_c^{ac}	ac Percolation threshold
ϕ_c^{dc}	dc Percolation threshold
ϕ_q	The volume fraction of the qth phase
α	Segmental relaxation
α_j	The shape parameter of the jth HN process
β	Relaxation normal mode
β_j	The shape parameter of the jth HN process
γ	Shear strain
γ_0	The amplitude of shear strain
δ	Phase angle
η	Gauge factor
κ	Dielectric constant (static)
κ^*	Complex permittivity (dielectric constant)

κ'	The real part of permittivity
κ''	The imaginary part of permittivity
κ_{∞}	Instantaneous relative permittivity ($f \rightarrow \infty$)
$\kappa_{\infty j}$	The instantaneous relative permittivity of the jth HN process
κ_1'	The real part of permittivity of phase one
κ_2'	The real part of permittivity of phase two
κ'_i	The real part of permittivity measured at any time under strain
κ'_m	The real part of permittivity of the polymer matrix phase
κ'_q	The real part of permittivity of the qth phase
κ_s	Static relative permittivity ($f \rightarrow \infty$)
κ_{sj}	Static relative permittivity of the jth HN process
κ_{vac}	Dielectric constant of vacuum
λ	Extension ratio
λ_1	Extension ratio along the length
λ_2	Extension ratio along the width
λ_3	Extension ratio along the thickness
μ	Dipole moment of per unit contour length
ν_p	Poison's ratio
ρ	The density of the material
σ'_{ac}	The real part of the ac electrical conductivity
σ''_{ac}	The imaginary part of the ac electrical conductivity
σ_{dc}	dc conductivity
σ_{dc1}	The dc conductivity of phase one
σ_{dc2}	The dc conductivity of phase two
σ_{dcq}	dc conductivity of the qth phase
σ_{eng}	Engineering stress
τ	Relaxation time

τ_j	The relaxation time the jth HN process
τ_{shear}	Shear stress
τ_{shear0}	The amplitude of shear stress
φ	Phase angle of the electrical field
ω	Angular frequency

List of Equations

$F = \left(\frac{\partial U}{\partial l}\right)_{v,T} - T\left(\frac{\partial S}{\partial l}\right)_{v,T}$ Equation 2-1 10

$\left(\frac{\partial S}{\partial l}\right)_{v,T} = -\left(\frac{\partial F}{\partial T}\right)_{v,l}$ Equation 2-2 10

$\left(\frac{\partial U}{\partial l}\right)_{v,T} = F - T\left(\frac{\partial F}{\partial T}\right)_{v,l}$ Equation 2-3 10

$U = Q + W$ Equation 2-4 11

$W = -Q = -T\Delta S$ Equation 2-5 11

$\Delta S = -\frac{1}{2} N k_B (\lambda_1^2 + \lambda_2^2 + \lambda_3^2 - 3)$ Equation 2-6 12

$W = \frac{1}{2} G(\lambda_1^2 + \lambda_2^2 + \lambda_3^2 - 3)$ Equation 2-7 12

$G = N k_B T = \rho R_{gas} T / M_c$ Equation 2-8 12

$\lambda_1 = \frac{1}{\lambda_2^2} = \frac{1}{\lambda_3^2}$ Equation 2-9 12

$W = \frac{1}{2} G\left(\lambda_1^2 + \frac{2}{\lambda_1} - 3\right)$ Equation 2-10 12

$\sigma_{eng} = \frac{dW}{d\lambda_1} = G\left(2\lambda_1 + \frac{1}{\lambda_1^2}\right)$ Equation 2-11 12

$\gamma(t) = \gamma_0 \sin(\omega t)$ Equation 2-12 13

$\tau_{shear} = \tau_{shear0} \sin(\omega t + \delta)$ Equation 2-13 13

$\gamma(t) = \gamma_0 \exp(i\omega t)$ Equation 2-14 13

$\tau_{shear}(t) = \tau_{shear0} \exp[i(\omega t + \delta)]$ Equation 2-15 13

$G^* = \frac{\tau_{shear}(t)}{\gamma(t)} = \frac{\tau_{shear0}}{\gamma_0} \exp(i\delta)$ Equation 2-16 13

$G^* = \frac{\tau_{shear0}}{\gamma_0} \cos(\delta) + i\frac{\tau_{shear0}}{\gamma_0} \sin(\delta) = G' + iG''$ Equation 2-17 13

$\boldsymbol{P} = (\kappa - 1)\kappa_{vac}\boldsymbol{E}$ Equation 2-18 22

$\boldsymbol{D} = \kappa_{vac}\kappa\boldsymbol{E} = \kappa_{vac}\boldsymbol{E} + \boldsymbol{P}$ Equation 2-19 22

$\boldsymbol{P} = N\left(\alpha \boldsymbol{E}_L\right)$ Equation 2-20 22

$\boldsymbol{P} = \frac{\kappa+2}{3} N\alpha \boldsymbol{E}$ Equation 2-21 23

$\frac{\kappa-1}{\kappa+2} = \frac{N\alpha}{3\kappa_{vac}}$ Equation 2-22 23

$\frac{\kappa-1}{\kappa+2} \times \frac{M_w}{\rho} = \frac{N_A \alpha}{3\kappa_{vac}} = P_M$ Equation 2-23 23

$\boldsymbol{E}\left(\omega t\right) = \boldsymbol{E}_0 \exp\left(i\omega t\right)$ Equation 2-24 24

$\boldsymbol{D}\left(\omega t\right) = \boldsymbol{D}_0 \exp\left[i\left(\omega t - \varphi\right)\right]$ Equation 2-25 24

$\kappa^* = \kappa' - \boldsymbol{i}\kappa'' = \frac{\boldsymbol{D}_0}{\kappa_{vac}\boldsymbol{E}_0} \exp\left(-i\varphi\right)$ Equation 2-26 25

$\kappa^* = \kappa_\infty + \frac{\kappa_s - \kappa_\infty}{1 + i\omega\tau}$ Equation 2-27 25

$\kappa' = \kappa_\infty + \frac{\kappa_s - \kappa_\infty}{1 + (\omega\tau)^2}$ Equation 2-28 25

$\kappa'' = \frac{\kappa_s - \kappa_\infty}{1 + (\omega\tau)^2} \omega\tau$ Equation 2-29 25

$\left(\kappa' - \frac{\kappa_s + \kappa_\infty}{2}\right)^2 + \left(\kappa''\right)^2 = \left(\frac{\kappa_s - \kappa_\infty}{2}\right)^2$ Equation 2-30 25

$U\left(t\right) = U_0 \sin\left(\omega t\right)$ Equation 2-31 30

$I\left(t\right) = I_0 \sin\left(\omega t - \varphi\right)$ Equation 2-32 30

$U^* = U_0 \exp\left(i\omega t\right)$ Equation 2-33 30

$I^* = I_0 \exp\left[i\left(\omega t - \varphi\right)\right]$ Equation 2-34 31

$Z^* = \frac{U^*}{I^*} = R + iX = \frac{U_0}{I_0}\cos\left(\varphi\right) + i\frac{U_0}{I_0}\sin\left(\varphi\right)$ Equation 2-35 31

$D = \frac{R}{X} = \frac{\kappa''}{\kappa'}$ Equation 2-36 31

$C_S = C_P\left(1 + D^2\right)$ Equation 2-37 31

$C = -\frac{1}{2\pi fX}$ Equation 2-38 33

$C = \kappa_{vac}\kappa' \frac{Area}{Thickness}$ Equation 2-39 33

$M^* = M' + iM'' = \frac{1}{\kappa^*}$ Equation 2-40 33

$\sigma^*_{ac} = \sigma'_{ac} - i\sigma''_{ac} = i2\pi\kappa_0\left(\kappa^* - 1\right)$ Equation 2-41 33

$\boldsymbol{P}_A = \mu \boldsymbol{r}$ Equation 2-42 42

$\kappa_1' \cdot E_1 = \kappa_2' \cdot E_2$ Equation 2-43 54

$j_{current} = \sigma_1 \cdot E_1 = \sigma_2 \cdot E_2$ Equation 2-44 54

$\int_0^\infty \left(j_{current1} - j_{current2}\right) dt = \frac{\kappa_0\left(\sigma_1\kappa'_2 - \sigma_2\kappa'_1\right)}{d_2\sigma_1 - d_1\sigma_2} U$ Equation 2-45 54

$\left(\kappa'\right)^n = \sum_q \phi_q \left(\kappa'_q\right)^n$ Equation 2-46 55

$\frac{1}{\sum_q \varphi_q \left(\kappa'_q\right)^{-1}} \le \kappa' \le \sum_q \varphi_q \kappa'_q$ Equation 2-47 55

$\sigma_{dc} \propto \sigma_0 \left|\phi - \phi_c^{dc}\right|^{\pm t_{dc}}$ Equation 2-48 57

$\kappa' \propto \kappa'_m \left|\phi - \phi_c^{ac}\right|^{-s}$ Equation 2-49 58

$\kappa' \propto \omega^{s'-1}$ Equation 2-50 58

$\sigma_{ac} = \sigma_{dc} + A\omega^r$ Equation 2-51 59

$\kappa^* = \sum_{j=1}^{n} \left\{ \kappa_{\infty j} + \frac{\Delta\kappa_j}{\left[1 + \left(i\omega\tau_j\right)^{\alpha_j}\right]^{\beta_j}} \right\}$ Equation 3-1 72

$\kappa' = \sum_{j=1}^{n} \left[\kappa_{\infty j} + \Delta\kappa_j \cdot A_j^{-\beta_j/2} \cdot \cos\left(\beta_j B_j\right) \right]$ Equation 3-2 72

$\kappa'' = \sum_{j=1}^{n} \left[\Delta\kappa_j \cdot A_j^{-\beta_j/2} \cdot \sin\left(\beta_j B_j\right) \right]$ Equation 3-3 72

$A_j = 1 + \left(\omega\tau_j\right)^{2\alpha_j} + 2\left(\omega\tau_j\right)^{\alpha_j} \cdot \cos\left(\frac{\pi\alpha_j}{2}\right)$ Equation 3-4 72

$B_j = \arctan\left[\frac{(\omega\tau_j)^{\alpha_j}\cdot\sin\left(\frac{\pi\alpha_j}{2}\right)}{1+(\omega\tau_j)^{\alpha_j}\cdot\cos\left(\frac{\pi\alpha_j}{2}\right)}\right]$ Equation 3-5 73

$\kappa'' = \sum_{j=1}^{n}\left[\Delta\kappa_j\cdot A_j^{-\beta_j/2}\cdot\sin(\beta_j B_j)\right] + \frac{\sigma_{dc}}{\kappa_{vac}\omega^t}$ Equation 3-6 73

$\kappa' = \kappa'_m\left|\frac{\phi_c^{ac}}{\phi_c^{ac}-\phi}\right|^s$ Equation 3-7 74

$\kappa'' = \kappa''_{MWS} + \kappa''_{rest-dipoles} + \kappa''_{dc}$ Equation 3-8 77

$\log f_{max} = \log f_0 - \frac{A_0}{T-T_0}$ Equation 4-1 89

$C = \kappa_{vac}\kappa'\frac{wl}{d}$ Equation 5-1 111

$\Delta w / w_0 = \Delta d / d_0 = \nu_p \times \Delta l / l_0$ Equation 5-2 111

$l_i = (1+\Delta l / l_0)\, l_0$ Equation 5-3 111

$w_i = (1-\Delta w / w_0)\, w_0$ Equation 5-4 111

$d_i = (1-\Delta d / d_0)\, d_0$ Equation 5-5 111

$C_i = \kappa_{vac}\kappa'_i\frac{l_0 w_0}{d_0}\lambda$ Equation 5-6 111

$C_0 = \kappa_{vac}\kappa'_0\frac{l_0 w_0}{d_0}$ Equation 5-7 112

$C_i = C_0\lambda$ Equation 5-8 112

$\frac{\Delta C}{C_0} = (C_i - C_0)/C_0 = e$ Equation 5-9 112

$\frac{\Delta C}{C_0} = \eta\times e$ Equation 5-10 112

$C_i = \kappa_{vac}\kappa'_i\frac{l_0 w_0}{d_0}\lambda + C_{corr}$ Equation 5-11 114

$C_0 = \kappa_{vac}\kappa'_0\left(\frac{w_0 l_0}{d_0}\right) + C_{corr}$ Equation 5-12 114

$\Delta C = \left(\kappa_{vac} \frac{l_0 w_0}{d_0} \right) \kappa' e$ Equation 5-13 115

$\frac{\Delta C}{C_0} = \left(1 - \frac{C_{corr}}{C_0} \right) e$ Equation 5-14 115

$\eta = 1 - \frac{C_{corr}}{C_0}$ Equation 5-15 115

List of Tables

Table 2-1. Commonly encountered rubber materials and their chemical structure and features. 6

Table 2-2 Classification of carbon black grades and their typical properties taken from ASTM D 1765[24]. 17

Table 2-3. Various functions to describe the dielectric relaxation. Taken from the book by Kremer and Schönhals[39]. 27

Table 2-4. The dielectric properties of different rubber products treated by different methods. Taken from the literature[101] 44

Table 3-1. List of the different materials samples used in this chapter. (phr: per hundred grams of rubber) 70

Table 4-1. Samples used in this study and their curing conditions. 85

Table 5-1. Summary of the capacitance strain sensor reported in recent literatures.* 113

Table 6-1. Samples codes and corresponding volume fractions used in this study 124

List of Figures

Figure 2-1. A short history of rubber: from a tropical plant to the heart of modern industry. 5

Figure 2-2 Typical vulcanisation cure traces measured by the oscillating disc type rheometer. Taken from the literature[8]. 8

Figure 2-3. The peroxide curing reactions (abstraction type). 9

Figure 2-4. The stress-elongation graph deconvoluted using Equation 2-2 and Equation 2-3. Samples were natural rubbers cured by 8 phr sulphur at 147 degree for 180 min[10]. 11

Figure 2-5. Carbon black production processed using the oil furnace method. Taken from the website of Asahi Carbon Co., LTD[14]..... 15

Figure 2-6. The structure of carbon black (CB) [15] at different length scales (a) 2D carbon platelet. (b) primary CB particle. The inset graph is a high resolution electron micrograph of a carbon black N285 primary particle[16]. (c) CB aggregate. The inset picture is a TEM image of carbon black N134 aggregates[17]. 16

Figure 2-7. (a) High resolution image of carbon-rubber gel network for carbon black N326 in SBR at 50 phr. (b) TEM pictures of carbon-rubber gel network for MT in SBR at 150 phr[28]. The carbon black-rubber gel refers to uncured rubber-filler compounds that have been extracted in benzene. 19

Figure 2-8. A qualitative explanation of the nonlinearity of the dynamic modulus-strain curve. 21

Figure 2-9. Strain dependent behaviour of the shearing storage (a) and loss (b) moduli of SSBR filled by carbon black N234 with different concentrations. Taken from the literature[36]. 21

Figure 2-10. A schematic relationship between the time dependence of the applied electrical field and the permittivity..... 24

Figure 2-11. (a) Debye type relaxation presented as $\omega \sim \kappa^*$. (b) The Cole-Cole plot.... 25

Figure 2-12. Some important equivalent circuit models. Z is the impedance. Y is admittance, C is capacitance, $\chi = \kappa - 1$ is the susceptibility. In Z, Y and C columns, all graphs use the real part as the x-axis while use the imaginary part as the y-axis. The arrows in each plot means the increase of angular frequency. In $\chi(\omega)$ column, x-axis is

the angular frequency while the y-axis is the amplitude of either the real (solid line) or the imaginary part (dashed line) of susceptibility. Taken from the literature[43]. 28
Figure 2-13. (a) A dielectric relaxation sketch; (b) different dielectric techniques and their working frequency range; (c) the sample arrangements for different techniques.[39] .. 29
Figure 2-14. A general schematic of the impedance test. 32
Figure 2-15. The frequency dependence of RC series capacitance C_S , RC parallel capacitance C_P and dielectric loss D of: (a) natural rubber filled by 15 phr carbon black N330; (b) natural rubber filled by 20 phr carbon black N330. 32
Figure 2-16. The transmission/reflection coefficients in a transmission/reflection test. 34
Figure 2-17. (a) Free space reflection test. Red line: incident wave. Green line: reflected wave. (b) Sample holder of the reflection test. Taken from the literature[61]. 35
Figure 2-18. Enhancing the dielectric permittivity of PVDF using different fillers. Data taken from literatures [84, 90]. 39
Figure 2-19. TEM pictures of different core-shell particles made by Ag (core) and a carbonaceous (shell). Taken from the literature[97]. 40
Figure 2-20. Illustrations of (a) Type-A chain and (b) Type-B chain. The red arrows stands for the dipole moments of each unit of the polymer chain. The black dashed arrow stands for the end-to-end chain vector. 43
Figure 2-21. The 3D plot of the frequency and temperature dependence of the imaginary part of permittivity of cis-polyisoprene with a molecular weight of 11700 $g \cdot mol^{-1}$, taken from Schönhals[120]. 44
Figure 2-22. Decomposition of the imaginary part of permittivity of cis-polyisoprene at 216 K. Molecular weight is 1400 $g \cdot mol^{-1}$. Taken from the literature[125]. 45
Figure 2-23. The dielectric (a) and mechanical (b) spectrum of linear polyisoprene melt with a molecular weight of 50,000 $g \cdot mol^{-1}$ at a temperature of 295 K. The mechanical spectrum is built by the time-temperature superposition technique using a DMA. Taken from the literature[126]. 45
Figure 2-24. The relaxation time of the normal mode process for cis-polyisoprene measured at a temperature of 320 K as a function of the molecular weight. Taken from the literature[39]. 46

Figure 2-25. The (a) real and (b) imaginary part of the permittivity against the specific surface area. The filled circle and the triangle are graphite. The unfilled diamonds show pure carbon and the unfilled triangle is carbon black. Other symbols are different coal powders. Taken from the literature[130]. 48
Figure 2-26. The electrical structure of the metal-organic interface. Taken from the literature[93]. (a) Interfacial energy diagram with a shift of vacuum level (VL) of Δ at the interface due to dipole layer formation. E_F is the Fermi level. LUMO is the lowest unoccupied molecular orbital while HOMO is the highest occupied molecular orbital. Φ_B^n and Φ_B^p are the injection barriers for electron and hole respectively. (b) Compared to (a), it shows an interfacial energy diagram with band bending. The energy levels are bent by the charge redistribution in the organic layer to achieve the electrical equilibrium with the alignment of the Fermi levels of the two sides. This leads to the formation of built-in potential V_{bi} within a diffusion layer of thickness W 50
Figure 2-27. The possible factors that form and affect the dipoles around the interface, summarised by Ishii[93]. (a1) & (a2) Charge transfer of the metal surface. (b) The surface charge formed by the process of (a1) or (a2) induces the image charge in the vacuum phase. (c) Rearrangement of the electron cloud on the metal surface. (d) Chemical reactions rearrange the existing bond or form new bonds. (e) The interface may serve as a charge buffer. (f) The orientation effect of permanent dipoles in the organic phase surface. 51
Figure 2-28. The multi-core model of the nanodielectrics and the interface electrical double layer[67, 137]. 52
Figure 2-29. The capacitor model of the charge accumulation on the interface. Figure is redrawn from the literature[43]. 55
Figure 2-30. The percolation behaviour of dc conductivity as well as ac conductivity measured at different frequencies of PET filled by MWCNT with different volume fractions. Taken from the literature[163]. 59
Figure 2-31. The frequency dependent behaviour of (a) the real and imaginary part of permittivity and (b) the real part of the ac conductivity of polycarbonate filled by multiwall carbon nanotubes with different volume fractions. Taken from the literature[164]. 60

Figure 2-32. The strain dependent of dielectric loss of vulcanised unfilled natural rubber at different mechanical strain. (a), (b) and (c) were measured at 1 kHz, 10 kHz and 100 kHz respectively. Taken from the literature[100]. 63
Figure 2-33. The segmental relaxation times of (a) unfilled natural rubber and (b) layered silicate filled natural rubber that measured at different temperature and at different strain. Taken from the literatures[70, 169]. 64
Figure 2-34. The strain induced crystallisation of natural rubber characterised by both X-ray and dielectric technologies. X_c is the crystallinity index and $\Delta\varepsilon$ is the dielectric strength. Taken from the literature[169]. 64
Figure 2-35. (a) The experimental set-ups to measure the dielectric properties of rubber materials under strain that designed by M. Hernández et al.[169] and C. Brosseau et al.[172] 65
Figure 3-1. (a) The temperature controlling system and (b) the sample stage of Novocontrol Concept 40 Dielectric Spectrometer. The symbols refer to: 1. The sample stage; 2. Nitrogen out; 3. The temperature controller chamber; 4. Nitrogen in; 5. Temperature controller; 6. Upper electrode; 7. Bottom electrode. 71
Figure 3-2. The frequency dependent dielectric behaviour of carbon black N134 (a, b & c) and N330 (d, e & f) filled natural rubber presented by the real and imaginary part of permittivity as well as the real part of the ac conductivity. Symbols shown in (c) and (f) are the same for the rest of the graphs. 76
Figure 3-3. Fitting the real part of the permittivity of N134/0.13 (red dots) and N134/0.17 (blue dots) using Equation 3-2 where $j=1$ (adopting a single relaxation process). 78
Figure 3-4. Comparison of the real part of permittivity between NR/N134 and NR/N330 at three different frequencies. 79
Figure 3-5. The filler concentration dependent dielectric behaviour of carbon black N134 (a, b & c) and N330 (d, e & f) filled natural rubber presented by the real and imaginary part of permittivity as well as the real part of the ac conductivity. Symbols shown in (c) and (f) are the same for the rest of the figures. 80
Figure 3-6. The percolation fitting of carbon black N134 and N330 filled natural rubber at different frequencies. (a) & (c) are at 1 Hz while (b) & (d) are at 10 kHz. All the solid and dashed lines are from data fitting of the results. There may be several fitting

approaches shown in the same graph where the numbers show the value of the percolation threshold from the fitting. The inset graphs in (a) & (c) are shown to highlight the fit quality. 82
Figure 4-1. The frequency and temperature dependence of the complex permittivity of (a) & (b) unfilled natural rubber NR/0 and (c) & (d) HD filled natural rubber ($\varphi = 0.2$). (a) & (c) both show the data for the real part of the permittivity while (b) & (d) are the imaginary parts of the permittivity. 88
Figure 4-2. Frequency domain dielectric relaxation of unfilled NR/0 at specific temperatures. 90
Figure 4-3. (a) The α relaxation fitting results of unfilled NR/0 with a comparison with data digitized from the works by D. Fragiadakis[95] and M. Hernández[185]. (b) The α relaxation fitting results of NR/0 that are cured for different times and with various different concentrations of the curatives (DCP). The Tg was obtained from the VFT fitting of the temperature dependence of the α relaxation. 91
Figure 4-4. Frequency domain dielectric relaxation of HDS/0.2 measured at different temperatures. 92
Figure 4-5. Comparison of the α relaxation peak for unfilled NR/0 and those filled using different fillers at 223.15 K. 94
Figure 4-6. The normalised α relaxation peaks of natural rubber, unfilled or filled with different silicas. 95
Figure 4-7. Example of the de-convolution of the low frequency relaxation process of the polymer using an HN function and a conductivity contribution. The green dots are the original data while the blue and the red dots are fitted by the dc conductivity term and the HN term respectively. The black solid line is the overall fitting. 95
Figure 4-8. (a) The α relaxation peak of CB/0.093 at 223.15 K. (b) The normalised α relaxation peak of NR/0 (red dots) and N330/0.093 (blue dots). 96
Figure 4-9. The temperature dependence of the relaxation time for different samples. 97
Figure 4-10. Storage and loss modulus of unfilled and filled natural rubber. 97
Figure 5-1. The side view of the impedance test with different types of contact: (a) Materials under test (MUT) is coated by a thin layer of conductive materials such as gold or silver and then clamped using rigid electrodes. Numbers are defined as follows: 1.

Rigid electrode; 2. Coating layer; 3. MUT. (b) MUT is directly clamped by two rigid electrodes. (c) A schematic to show a capacitance gap of a finite size between the electrode and the sample. d_1 and d_2 are the distances between each electrode and the sample. t is the thickness of the sample. The air layer between the electrode and the sample can be treated as capacitors which are marked as C_{a1} and C_{a2}. The specimen itself is also a capacitor: C_{MUT} 99
Figure 5-2. Typical setup to measure the impedance of the materials using stretchable electrodes. 100
Figure 5-3. (a) AgNW electrodes before removing from a PTFE filter membrane. (b) Several Silver AgNW on top of a PTFE filter membrane. (c) AgNW electrodes, the highlighted area is showing the entangled AgNWs. (d) AgNW electrodes bonded to the top of a NR sample at approximately 50% strain. The arrows indicate the cracks generated by strain. 103
Figure 5-4. (a) Manufacturing processes of silver nanowire electrodes and the transfer method to locate them onto a rubber sample (side view). (b) Connections that link the test sample to the LCR meter. A top view and a cross sectional view of the sample gives details of each. Each number is defined as: 1. Top fixture; 2. AgNW electrode; 3. Rubber sample; 4. Adhesive; 5. Bottom fixture (only this type is glued to the sample). (c) Filtering set up. (d) Sample coated by two layers of AgNW one each on either side. (e) Sample fixed to the bottom fixture (top fixture has still to be glued). (f) Sample positioned using the DMA tension clamp. 104
Figure 5-5. The four-terminal pair configuration (4TP) for the LCR meter[189]. 106
Figure 5-6. Preparation of the specimen for dielectric test under strain using carbon grease as stretchable electrodes. (a) Mould. (b) Place a specimen on the mould. (c) Close the mould with sample trapped inside. (d) Pour PDMS into the moulds. (e) Close the cover. (f) Sample with the moulded PDMS layers on both sides. (f) Cover the carbon grease onto the PDMS layer on one side and then coat the carbon grease with another layer of PDMS as protection. A thin aluminium plate was used to create an effective electrical connection. (h) A finished sample and its side view. 108
Figure 5-7. Experiment set up for measuring the dielectric property under strain using rigid metal electrodes. Each number is defined as: 1. Sample holder; 2. Materials under

test (MUT); 3. Drop gauge for measuring the thickness of MUT; 4. Upper electrode: The inner ring is the testing electrode while the outer ring is for shielding. 5. Bottom electrode. 109
Figure 5-8. The permittivity and dielectric loss of unfilled NR under no strain at room temperature. Data was obtained using a Novocontrol Concept 40 Impedance Spectrometer. 110
Figure 5-9. (a) The capacitance of unfilled NR tested by SDMS at an electrical frequency of 1 kHz. Tests 1 to 3 refer to three repeat tests for three different specimens. (b) The permittivity of NR calculated from SDMS tests and DDMS tests. 115
Figure 5-10. The relationship between the gauge factor and the shape factor of capacitance strain sensors reported in the literature. 116
Figure 5-11. (a)-(c) the real (*R*) and imaginary (*X*) part of impedance as well as the dielectric loss (*D*) of unfilled NR tested at different strains and different frequencies using the SDMS test. (d) The dielectric loss data obtained by DDMS test of unfilled NR at different frequencies. 119
Figure 5-12. Typical data obtained from SDMS test of NR. The impedance data was measured at 1 kHz. Data was based one SDMS test without been averaged. 120
Figure 5-13. The permittivity of NR under strain tested with the rigid copper electrodes. Black squares are the data before calibration and red diamonds are the data after calibration. 121
Figure 6-1. Schematic of the multi-hysteresis loading cycle use in the SDMS technique. 126
Figure 6-2. DC percolation trend for carbon black N330 filled NR. The inset graph is a SEM cryo-fracture surface image of the state of aggregate distribution throughout the NR matrix for sample N330/0.071. 127
Figure 6-3. (a) Influence of mixing time on the measured dielectric properties. Samples were N330/0.13 mixed 50 times/100 times/300 times by two roll mill, named as 50 mix, 100 mix and 300 mix respectively. (b) Uniaxial stress-strain behaviour of the same samples. 129
Figure 6-4. The (a) real part and (b) imaginary part of permittivity of unfilled NR as a function of strain and frequency. (c) is the top view of (b). 131

Figure 6-5. (a) Sensitivity limits of the SDMS method. The data is based on a single SDMS test of unfilled NR. All the dielectric data was measured at 1 kHz electrical frequency. (b) Measured capacitance under strain for different samples. The inset graph shows a magnification of data for NR/0, N330/0.049 and N330/0.071. 132

Figure 6-6. (a) The relationship between permittivity κ' and filler volume fraction, ϕ under different frequencies and strain conditions. (b) Dielectric loss against ϕ under different conditions. The filler is carbon black N330. 133

Figure 6-7. The strain dependent dielectric behaviour of Silica/0.2 and NR/0 measured at 1 kHz. 134

Figure 6-8. (a) & (b) Strain (e) and electrical frequency (f) dependent behaviour of the permittivity and the dielectric loss of N330/0.071. (c) & (d) Projections of data from (a) and (b) respectively with selected data. Solid lines connect the data measured at the same strain (Frequency-Permittivity plane) or frequency (Strain-Permittivity plane) as guides for the eye. 136

Figure 6-9. κ' and stress vs strain for N330/0.071. (a) Multi-hysteresis data from 0 to 50% strain. (b) & (c) Sub-data taken from the multi-hysteresis sweeps showing the 0-5 % cycle data more clearly. All SDMS data was measured at an electrical frequency of 1 kHz. Data was collected from one test and all data collected during the test is presented. 137

Figure 6-10. (a) Static modulus (stress/strain) vs strain collected simultaneously with the dielectric data. (b) & (c) Strain-dependence of permittivity and loss factor of all samples (measured at 1 kHz electrical frequency). 139

Figure 6-11. The strain dependent behaviour of standardised modulus and the permittivity of unfilled and filled (N330) materials. 140

Figure 6-12. (a) Strain steps and the (b) corresponding dielectric data (measured at 1 kHz) of a various strain rate test. The sample under test is N330/0.071. 141

Figure 6-13. The strain dependent behaviour of the real part permittivity of N330/0.093 that measured at 1 kHz under different strain rate. (c) is the overall data represented from Figure 6-12 while (a) & (b) are shown step by step. Arrows indicate the tension or retraction steps. 142

Figure 6-14. The dielectric behaviour of N330/0.071 under compression. 143

Figure 6-15. Comparison of the strain dependent dielectric behaviour of samples filled by different kinds of carbon blacks. 144
Figure 7-1. The sensing behaviour of IR filled by carbon black N220 with a volume fraction of 0.093. Data measured at 1 kHz. Carbon grease is used as the electrode... 148
Figure 7-2. (a) The setup of a quasi-optical dielectric testing system (transmission). (b) A close up of the sample holder shown in (a). 149
Figure 7-3. The THz range dielectric properties of (a) unfilled NR cured by different amount of DCP (b) NR filled by carbon black N330 with a volume fraction of 0.049. The 150

1 Chapter One: Introduction

Filled elastomers are involved in a huge number of different daily activities from the tyres on our vehicles to the washers in our taps. These elastomers are made from polymer materials with a glass transition level that is lower than the operating conditions and which also exhibit little or no crystallisation. They are soft and surprisingly tough materials whose behaviour can be modified by the incorporation of fillers to create elastomer composites. Historically the most important properties for elastomers have been related to their mechanical performance or their environmental resistance to exposure to chemicals or extremes of temperature. There has always been an interest though in the dielectric behaviour of these materials, as often rubber materials have been used as electrical insulators, or when filled with a conductive filler above the percolation threshold, as electrical conductors.

In recent times, these various different filled polymer materials have become known as nanodielectric composites. Their study has become of greater importance as these composites are increasingly being used not only for their good mechanical performance but also as functional dielectric materials as a consequence of their outstanding dielectric properties. They can be easily designed and manufactured for a relatively low cost. Among all the different types of nanodielectric composites, nanodielectric elastomers stand out because of their large elasticity. Compared to traditional dielectrics which are essentially rigid, this type of dielectrics can be used in a wide range of smart applications such as artificial skin, strain sensors and foldable energy harvesters. Although the dielectric properties are very important in these applications, there are very few reported investigations into their mechanical dielectric behaviour in the literature. When they are discussed, the dielectric properties are only measured and then typically discussed in an unstrained state. In most cases, the values reported are assumed to be constant that do not alter throughout the devices' working life. This is particularly surprising as in most cases these devices would operate under a dynamic mechanical loading environment. The dielectric performance of such materials in the dynamically deformed state has only very rarely been discussed.

As it has already been noted, though elastomers filled with reinforcing nanoscale fillers have been used for a long time. This is because the nanometric fillers can impart a significant change to the structural properties such as the modulus, toughness, strength, chemical resistance, damping or thermal conductivity when compared to the polymer alone. The enhancement of many of these properties is referred to as the reinforcement of the elastomer. However, the detailed mechanisms of this reinforcement are not yet clearly established in the literature despite more than a century of investigations. It is very clear though that the dielectric spectrum of nanodielectrics is highly dependent upon the detailed nature of the interface between the polymer molecules and the filler as well as the detailed nature of the filler's structure[1]. By studying this behaviour, it might be possible to understand how these enhanced properties might be developed by modifying the filler in the composite. Another benefit is that the dielectric relaxation method can be used to directly measure the changes in the polymer dynamics[2]. Therefore, the dielectric technique becomes a powerful tool to help understand the mechanical properties of nanodielectrics.

This thesis aspires to tackle three tasks: Firstly, to apply broadband dielectric spectroscopy to evaluate the filler network of carbon black filled elastomers and then additionally using the dielectric results, to answer the question: are the molecular dynamic of the polymer chains around the filler surface have been slowed down compared to the bulk polymer chains. Secondly, design and build a reliable testing system to measure the dielectric spectroscopy of rubber composites simultaneously under mechanical strain. Thirdly, by using the newly developed system, to answer the question: if the dielectric permittivity of filled elastomers has a strain dependent behaviour and how it is linked to the filler reinforcement? The structure of the thesis is as follows:

Chapter 2 presents a detailed literature review of both the mechanical properties and the dielectric properties of the nanodielectrics. It especially focuses on the electrical structures at the interface between fillers and the polymer matrix. These ideas are further developed throughout the rest of the thesis.

Chapter 3 examines a very broadband of dielectric spectroscopy (0.1 Hz to 40GHz) for a conventional carbon black filled natural rubber. Such broadband data has rarely if ever been presented previously in the literature as a consequence of the complexity of undertaking the test. It gives a general view of the dielectric properties of the materials under investigation. A percolation theory is used to characterise the resulting data.

Chapter 4 studies the changes to the polymer dynamics, using a dielectric technique, as a consequence of using different curing processes, filler systems and the filler-polymer interactions. The segmental relaxation processes are checked in detail for each of these different systems.

Chapter 5 explains how different approaches were developed to determine the strained dielectric spectrum. These include how to effectively prepare flexible electrodes for such a test from materials such as carbon grease, silver nanowires as well as rigid copper.

Chapter 6 examines how the methodology developed in Chapter 5 can be used to examine the dielectric spectrum in strained nanodielectric elastomers to understand how the filler network changes under the application of a strain. A new method to classify the different dipoles in this system is introduced. The strained dielectric spectrum is also contrasted carefully with the simultaneously measured dynamic mechanical spectrum.

Chapter 7 summarises the key findings developed throughout this thesis and presents some of the ongoing and future work that this thesis leads into.

2 Chapter Two: Literature Review

2.1 Basic knowledge of Rubber Materials

2.1.1 What is Rubber

The word "rubber" is defined according to ASTM D 1566-14[3] as a material *'that is capable of recovering from large deformations quickly and forcibly…'*. It therefore represents a wide range of elastic and rubbery materials rather than a single specific type of material. Its elasticity is derived from its unusual molecular structure: including a non-crystalline macromolecular network with a low glass transition temperature, which ensures that it is rubbery at room temperature. Another constraint for a rubber material is that it is not soluble in a suitable boiling solvent. The word "elastomer" has broadly a very similar meaning without the requirement for the insolubility in a solvent. In many cases in the literature elastomer is used interchangeably with rubber. ASTM D 1566-14[3] defines elastomers as a group of materials that '*have similar properties to those of rubber'*.

Before the development of synthetic polymers, the word "rubber" referred only to materials that were naturally available. In the main this class of materials is now more specifically known as natural rubber (NR), which exists in the latex of some types of plants (more than 2500 types) such as Hevea Brasiliensis, Guayule and Russian dandelion. Among all these various plant varieties found to contain natural rubber, Hevea rubber is by far the most significant agricultural crop. In Amerindian, NR was known as *cachuchu* which means: "tears of tree" and it is the original etymological source for the name of rubber in many different modern European languages such as *caoutchouc* (French), *caucho* (Spanish), *kautschuk* (German) and *borracha* (Portuguese). The name in English is alternatively derived from an observation by the famous scientist Joseph Priestly[4] (1770) that the material was "excellently adapted to the purpose of wiping from paper the mark of black-lead-pencil". As shown in Figure 2-1, Hevea has been used for hundreds of years in Tropical America before it had been introduced to European by Christopher Columbus as an evidence of the interesting new American continent in 1490s. Hevea seeds were eventually "smuggled" to Europe for crop creation almost 400

years later in 1876. Next the seedlings were transported to former British colonies in Asia such as Sri Lanka, Indonesia, Malaysia and Singapore where their use as an agricultural crop expanded rapidly and where the natural rubber industry for the whole world was developed.[5] In 2014, more than 92% of NR was still produced in the Asia-Pacific area.

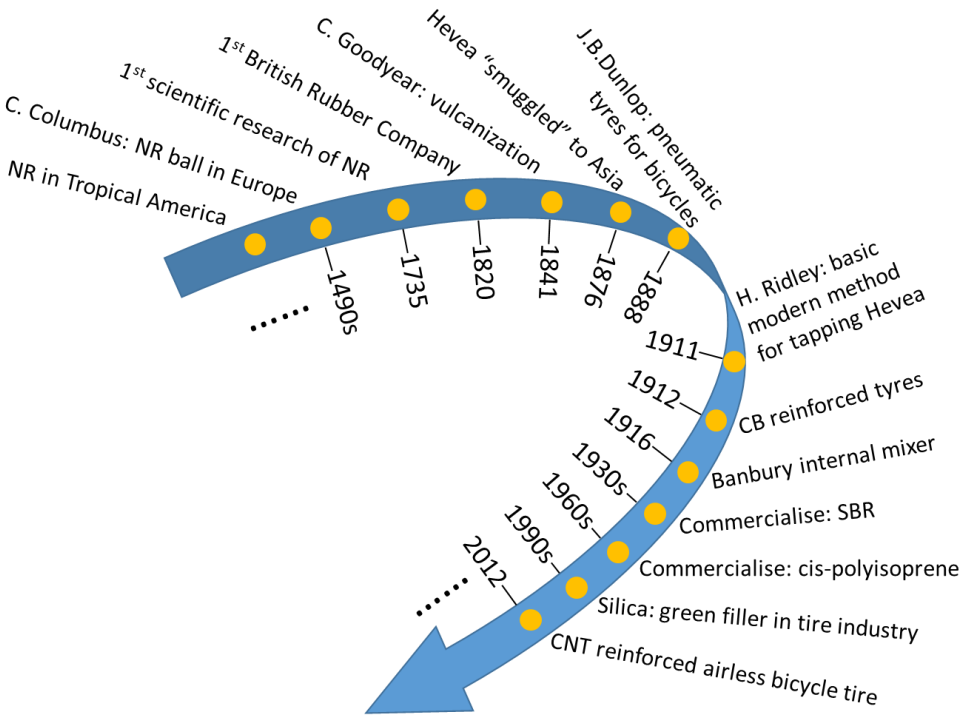

Figure 2-1. A short history of rubber: from a tropical plant to the heart of modern industry.

In 1909, the first synthetic rubber was produced in the Bayer laboratory. It was rapidly exploited during the world wars because of the shortage of NR. The synthesised natural rubber (cis-polyisoprene), IR was developed and commercialised in 1960s. At around this time, the global production of synthetic rubbers surpassed the amount of NR produced. A short list of the most typical different rubber families is presented in Table 2-1. A significantly greater amount of detail can be found in the fourth chapter of the book by C.M. Blow[6].

In this thesis the focus is on two families of elastomer: cis-polyisoprene (both NR & IR) and polydimethyl siloxane (PDMS).

Table 2-1. Commonly encountered rubber materials and their chemical structure and features.

Name	Chemical structure
Cis-polyisoprene (NR, IR)	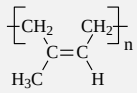
Styrene Butadiene Rubber (SBR)	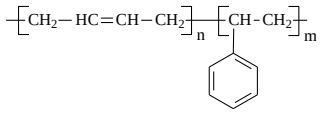
Polybutadiene (BR)	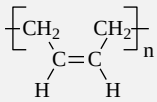
Polyisobutylene (IIR)	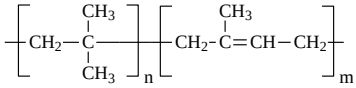
Polychloroprene (CR)	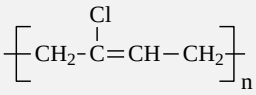
Polydimethyl Siloxane (PDMS)	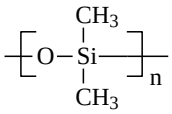
Acrylic Elastomer	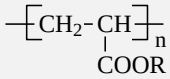
Thermoplastic Polyurethane (TPU)	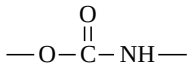

Natural Rubber (NR)

The commercial NR bales are concentrated from Hevea latex. The grade is specified by either its light colour (SMR L) or viscosity (SMR CV), where SMR stands for Standard Malaysian Rubber. For example, “SMR CV 60” grade stands for NR having a Mooney viscosity of around 60 Mooney units at 100 ^{o}C.

NR contains around 95% cis-polyisoprene and a few percent of non-rubber components such as proteins, fatty acid and resin. These non-rubber parts are very important for NR. They modify the properties of NR when compared to the synthetic cis-polyisoprene (known as synthetic natural rubber or IR). They impart a higher mechanical strength and a greater extent of strain induced crystallisation behaviour. That is why even today, NR

still accounts for around 42% of the global rubber consumption. The "cis" structure brings NR a low glass transition temperature (Tg) of around -66 $^{\circ}C$ while the Tg of Gutta Percha rubber (trans-polyisoprene) is around 20 degrees higher. NR also has a broad molecular weight distribution (MWD) typically of around $10^4 \sim 10^7$ while the MWD is much narrower for IR.

Polydimethyl Siloxane (PDMS)

PDMS is the most widely used silicone rubber. It has two methyl groups attached to a silicon atom while these silicon atoms are also connected by oxygen atoms. The silicon-oxygen chain is very flexible so that it has a very low Tg of around $-120^{\circ}C$. Moreover, the silicon-oxygen bond is more stable at high temperatures when compared to the carbon-carbon bond. Therefore, PDMS can keep its elasticity at both extremely low and high temperatures ($-60 \sim +250^{\circ}C$) when compared to NR. It also has a very good biocompatibility so it has been widely used in dental and biomedical applications. However, pure PDMS has a low mechanical strength and so it is normally reinforced by fumed silica to improve its properties.

2.1.2 Vulcanisation of Rubber

Sulphur Curing System

The curing process can be well detected using an oscillating disc type rheometer where the measured torque is proportional to the intensity of the crosslink density. A typical curing curve is shown in Figure 2-2. Most of the rubber products are vulcanised using a sulphur curing system. The concept is very simple: using sulphur bonds to connect the hydrocarbon chains. However, to create these bonds requires a complex chemical system that normally contains sulphur (which provides the connection between chains), accelerators such as benzothiazyl disulfide (MBTS, which are there to shorten the curing time), activators such as zinc oxide and stearic acid (which decreases the chemical processes activation energy and which also therefore increases the crosslink density) as well as antioxidants such as 6PPD. By changing the amounts and the ratios between the sulphur and the accelerators, the cure behaviour can change. Typically three different

systems are possible and these are known as conventional, semi-efficient and efficient vulcanisation systems (CV, SEV and EV respectively). They can bring completely different properties to the vulcanised rubber[7]. Considering the chemical complexity of this system, this thesis uses a much simpler peroxide curing system.

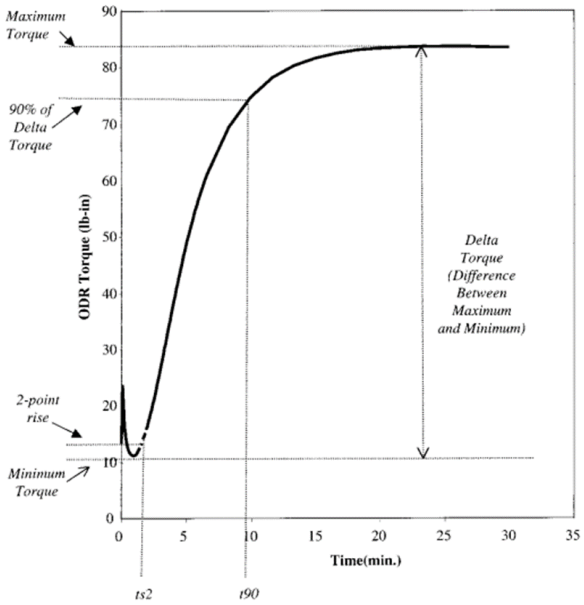

Figure 2-2 Typical vulcanisation cure traces measured by the oscillating disc type rheometer. Taken from the literature[8].

Peroxide Curing System

Dluzneski[8] gave a review in 2001 of peroxide curing systems. The peroxide cure system is a free radical type reaction. As shown in Figure 2-3, there are three steps: firstly, the peroxide breaks into two alkyl free radicals as shown in the first equation. Secondly, both kinds of the alkyl free radicals can attack the side methyl carbon which abstracts one hydrogen atom and generates a carbon free radical. It can also attack the tertiary carbon in the main chain which decreases the amount of unsaturated double bonds (addition type). Thirdly, two chains that contain a carbon free radical can react to create a crosslink (Figure 2-3 only shows the hydrogen abstraction type reaction). Therefore, the peroxide cure can provide a direct carbon-carbon connection between the rubber chains. Carbon-carbon bonds are more stable at elevated temperatures compared to sulphur bonds. These free radical reactions are highly sensitive to temperature. The

curing time decreases rapidly with an increase of the temperature when compared to sulphur system. There may be other types of reaction that take place at higher temperatures which also might complicate the curing mechanism and which might also change the mechanical properties of the final products. Finally, there is no over-curing process compared to the sulphur curing system. Therefore, with peroxide curing, one can achieve almost 100% cure once all the curatives in the material have been consumed by the crosslinking reaction.

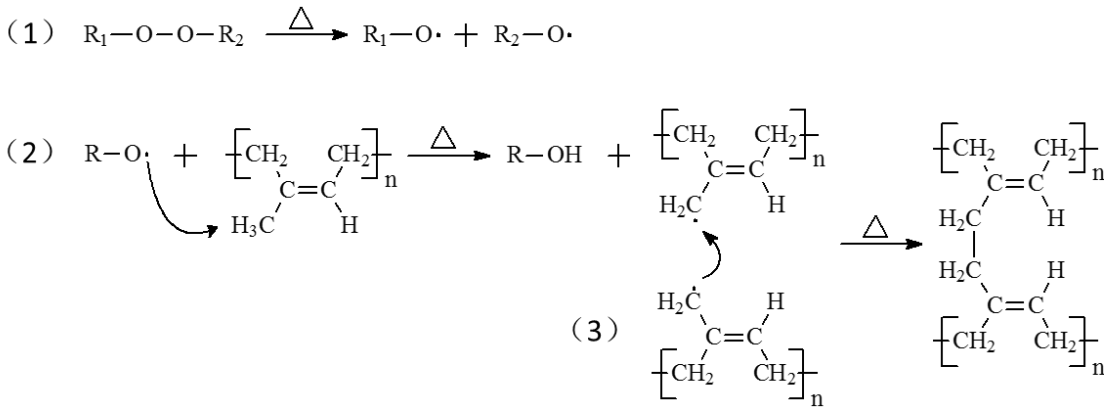

Figure 2-3. The peroxide curing reactions (abstraction type).

Curing Strategies of PDMS

Uncured PDMS is oily and is normally a transparent liquid. It can be cured by either: room temperature vulcanisation (RTV) or high temperature vulcanisation (HTV) where RTV can be achieved by addition (RTV-A) or condensation reaction (RTV-C)[9]. HTV types of PDMS normally use peroxide as the curative so that the methyl group of the two chains can be crosslinked using a free radical reaction. RTV type PDMS can be made as a single-part or two-part system. The former is sealed with all the additives together with PDMS and the vulcanisation is triggered when it meets moisture in the air. Two-part system normally use PDMS, fillers and curative as part-A while using PDMS and a catalyst as part-B. The cure process initiates when the two parts are mixed together. The two-part RTV PDMS has a longer shelf life and it has been widely adopted for use in electronic devices as an adhesive or as a sealing medium.

2.1.3 Mechanical Properties of a Rubber

Elasticity

From the classical thermodynamic analysis, the elasticity of rubber is driven by changes in entropy. Based on the assumption that the volume change of rubber under an applied strain is a constant $dV = 0$, then the applied tensile force *F* can be expressed as:

$$F = \left(\frac{\partial U}{\partial l}\right)_{v,T} - T\left(\frac{\partial S}{\partial l}\right)_{v,T} \qquad \text{Equation 2-1}$$

where *S* is entropy; *U* is internal energy; *T* is temperature; *l* is length; *V* is the volume. This means that the applied force has two contributions potentially derived from either a change in the internal energy or a change in the entropy. The equation was first developed by Antony in 1942[10], as discussed in Treloar's famous book on rubber physics.[11] Entropy is difficult to determine through normal experimental approaches, but it can be worked out by measuring the force at fixed strain over different temperatures according to the following relationship:

$$\left(\frac{\partial S}{\partial l}\right)_{v,T} = -\left(\frac{\partial F}{\partial T}\right)_{v,l} \qquad \text{Equation 2-2}$$

Note that, the real tests are normally carried out at a constant pressure $\partial p = 0$ and there is always a very tiny change of the volume. However, the volume change is too small to make a considerable contribution to the internal energy. Therefore, volume change can be ignored and the data measured under constant pressure conditions can be used as an approximation of a constant volume. Substitution of Equation 2-2 into Equation 2-1, allows the change in the internal energy to be derived as:

$$\left(\frac{\partial U}{\partial l}\right)_{v,T} = F - T\left(\frac{\partial F}{\partial T}\right)_{v,l} \qquad \text{Equation 2-3}$$

Figure 2-4 shows the experimental data for each of the three terms of Equation 2-3 against strain[10]. The figure shows that the internal energy change is almost negligible at different strains whilst the measured force is dominated by the entropy term. Any small changes arising from changes to the volume are ignored. That is $dU \cong 0$. Therefore,

the applied force causes a decrease of the entropy while the retraction force is driven by an increase of the entropy. From the first law of thermodynamics:

$$U = Q + W \qquad \text{Equation 2-4}$$

where *Q* is the absorbed heat and *W* is the work done to the system. As $dU \cong 0$, all the work done to the system is released as heat to the environment for an isothermal process:

$$W = -Q = -T\Delta S \qquad \text{Equation 2-5}$$

For an adiabatic process, this work causes an increase of the temperature of the material.

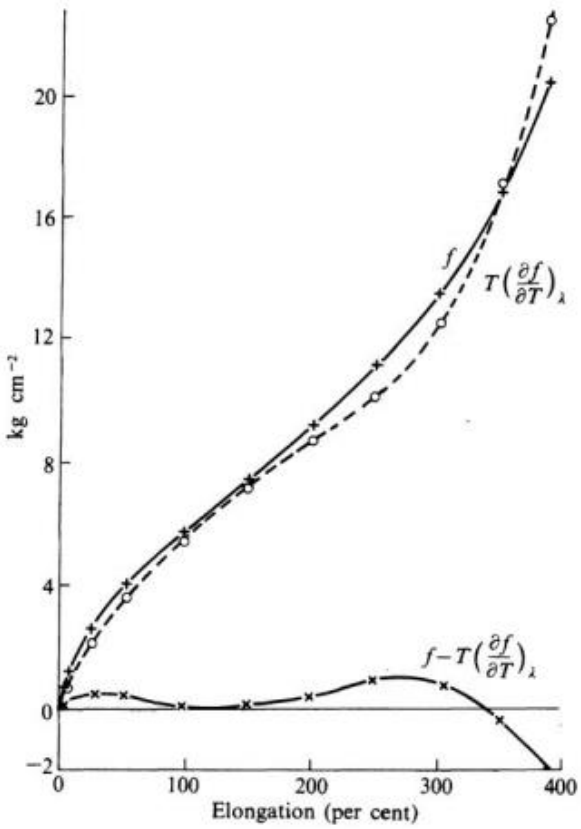

Figure 2-4. The stress-elongation graph deconvoluted using Equation 2-2 and Equation 2-3. Samples were natural rubbers cured by 8 phr sulphur at 147 degree for 180 min[10].

Beside the thermodynamic approach, the change of entropy can also be calculated from a statistical analysis. Considering a rubber network consisting of Gaussian chains which undergo an affine deformation with respect to the crosslink junctions upon deformation, the change of the entropy under a 3-D deformation can be written as:

$$\Delta S = -\frac{1}{2} N k_B (\lambda_1^2 + \lambda_2^2 + \lambda_3^2 - 3) \qquad \text{Equation 2-6}$$

where *N* is the number of chains per unit volume. Here the chain is defined as the segments between the two nearest crosslink joints. k_B is the Boltzmann constant. λ_1, λ_2 and λ_3 are the extension ratios along the length, width and the thickness of the materials. Substituting Equation 2-6 into Equation 2-5 gives:

$$W = \frac{1}{2} G (\lambda_1^2 + \lambda_2^2 + \lambda_3^2 - 3) \qquad \text{Equation 2-7}$$

$$G = N k_B T = \rho R_{gas} T / M_c \qquad \text{Equation 2-8}$$

where G is an elastic constant known as the shear modulus, ρ is the density of the material, R_{gas} is the gas constant, M_c is the average chain molecular weight between crosslinks. Equation 2-6 to Equation 2-8 can be used to describe any type of homogeneous isotropic deformation. For example, using the uniaxial tensile test:

$$\lambda_1 = \frac{1}{\lambda_2^2} = \frac{1}{\lambda_3^2} \qquad \text{Equation 2-9}$$

Substitute Equation 2-9 into Equation 2-7:

$$W = \frac{1}{2} G \left(\lambda_1^2 + \frac{2}{\lambda_1} - 3 \right) \qquad \text{Equation 2-10}$$

and the engineering stress can be calculated as:

$$\sigma_{eng} = \frac{dW}{d\lambda_1} = G \left(2\lambda_1 + \frac{1}{\lambda_1^2} \right) \qquad \text{Equation 2-11}$$

This statistical distribution approach is based on the assumption that there is no volume change and that the mean square end-to-end distance is much smaller when compared to the actual chain length. This is only applicable for relatively modest strains as the deformation at larger strains contain contributions to the deformation arising from non-Gaussian, finite network extensibility effects and potentially strain-induced crystallisation which introduce an additional complexity to the model.

Viscoelasticity

The previous section discussed the origins of the elasticity in rubber materials. In reality, any polymeric material should be treated as viscoelastic which indicates that it behaves with a combination of both elastic solid and viscous liquid types of behaviour. Unlike a pure elastic material that simply obeys Hooke's elasticity law, a viscoelastic material creeps over time under a constant load and the stress relaxes when held under a constant strain. Viscoelasticity can also describe the behaviour when the material is subjected to dynamic loading. For example, when applying a sinusoidal shearing strain to the material:

$$\gamma(t) = \gamma_0 \sin(\omega t) \qquad \text{Equation 2-12}$$

where γ_0 is the maximum amplitude of shear strain, ω is the angular frequency and *t* is time, the shear stress τ_{shear} is also approximately sinusoidal but it has a different phase angle:

$$\tau_{shear} = \tau_{shear0} \sin(\omega t + \delta) \qquad \text{Equation 2-13}$$

where τ_{shear0} is the stress amplitude and δ is the phase angle. δ is equal to 0° and 90° for ideal elastic or viscous materials respectively. For all other viscoelastic materials the phase angle falls between these two extreme limits, $0^o < \delta < 90^o$. Equation 2-12 and Equation 2-13 can be rewritten using complex number notation:

$$\gamma(t) = \gamma_0 \exp(i\omega t) \qquad \text{Equation 2-14}$$

$$\tau_{shear}(t) = \tau_{shear0} \exp\left[i(\omega t + \delta)\right] \qquad \text{Equation 2-15}$$

The complex moduli can thus be defined as:

$$G^* = \frac{\tau_{shear}(t)}{\gamma(t)} = \frac{\tau_{shear0}}{\gamma_0} \exp(i\delta) \qquad \text{Equation 2-16}$$

The storage moduli G' and loss moduli G'' can be obtained using:

$$G^* = \frac{\tau_{shear0}}{\gamma_0} \cos(\delta) + i \frac{\tau_{shear0}}{\gamma_0} \sin(\delta) = G' + iG'' \qquad \text{Equation 2-17}$$

The complex moduli can be characterised under different test conditions using a dynamic mechanical analyser (DMA). The measured results depend upon the mechanical frequency (time) and the temperature. Interestingly, for some simpler unfilled materials the time and the temperature effects have been proven to be equivalent when examining the viscoelasticity of the materials. For example, rubber materials become glassy (rigid) when the temperature is decreased below the Tg. The same behaviour can also be observed at room temperature by increasing the test frequency. Moreover, the mechanical spectrum measured at low temperatures and at a low frequency can be considered equivalent to being tested at a higher frequency condition and at a higher temperature. This is very important to map the behaviour of rubber over a very wide range of frequencies using say a $G^* \sim \omega$ graph as the mechanical frequency is limited by the DMA (normally $\omega / 2\pi < 100$). This technique is known as time-temperature superposition and it can be described using the Williams-Landel-Ferry (WLF) function[12].

2.1.4 Rubber Material Reinforcement using Nanoparticles

Carbon Black (CB)

Some rubber materials such as PDMS have a weak mechanical strength even after vulcanisation. Fortunately, the mechanical properties can be effectively reinforced by nanometric fillers such carbon black (CB) and silica. Most carbon blacks are produced by incomplete combustion (thermal-oxidative decomposition) of hydrocarbons (oils or gases)[13]. Figure 2-5 shows a typical method to produce carbon black using the oil furnace method. The left side is the first combustion zone where the fuel is burning with the help of air and generating continuous hot gases at around 1300 $^{\circ}C$. These gases will blow the feedstocks to the reaction zone where most of the feedstock is pyrolyzed and decomposed into carbon black. The products are then cooled down to around 1000 $^{\circ}C$ by quenching with water which ceases the reaction. The size and morphology of the carbon black produced can be controlled by modifying the processing conditions such as the reaction temperature and time.

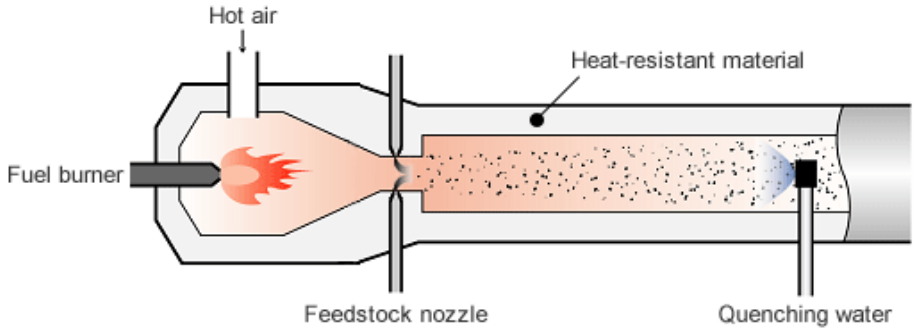

Figure 2-5. Carbon black production processed using the oil furnace method. Taken from the website of Asahi Carbon Co., LTD[14].

Figure 2-6[15] shows different levels of CB structure. The dimensions shown in this figure were calculated by Rivin[16] and are based on the medium grade range of CBs. Figure 2-6(a) shows the 2D crystallite of carbon black basal plane which has the same morphology as a graphite layer. Note that, the chemical structure of the CB surface is rather complex. It has considerable amounts of oxygen and hydrogen groups (such as carboxyl, carbonyl, hydroxyl, xanthene, quinone, lactone, lactol and ether) which can affect the physico-chemical properties of the final product[13]. Several layers of such 2D structures bundle together as a unit to form the primary CB particles as shown in Figure 2-6(b). The industrial CB for reinforcement applications normally has a dimension between 10-100 nm. Because of the high aspect ratio and the high surface energy, these primary particles connect to each other and form CB aggregates connected together by both van der Waals forces and chemical bonding. Completely separated primary particles are rarely encountered unless they are relatively large in size. Therefore, CB aggregates can be treated as the basic inseparable units in typical CB reinforced composites. The dimensions of the aggregates depend on the filler size. Normally finer CB particles form larger and more complex aggregates. This geometric complexity is described as the filler structure, with smaller particles having a greater structure and larger CB particles forming lower structure aggregates. As the size of the aggregates is still very small, they further associate by van der Waals forces to form a more complex and undispersed structure, which is known as a CB agglomerate.

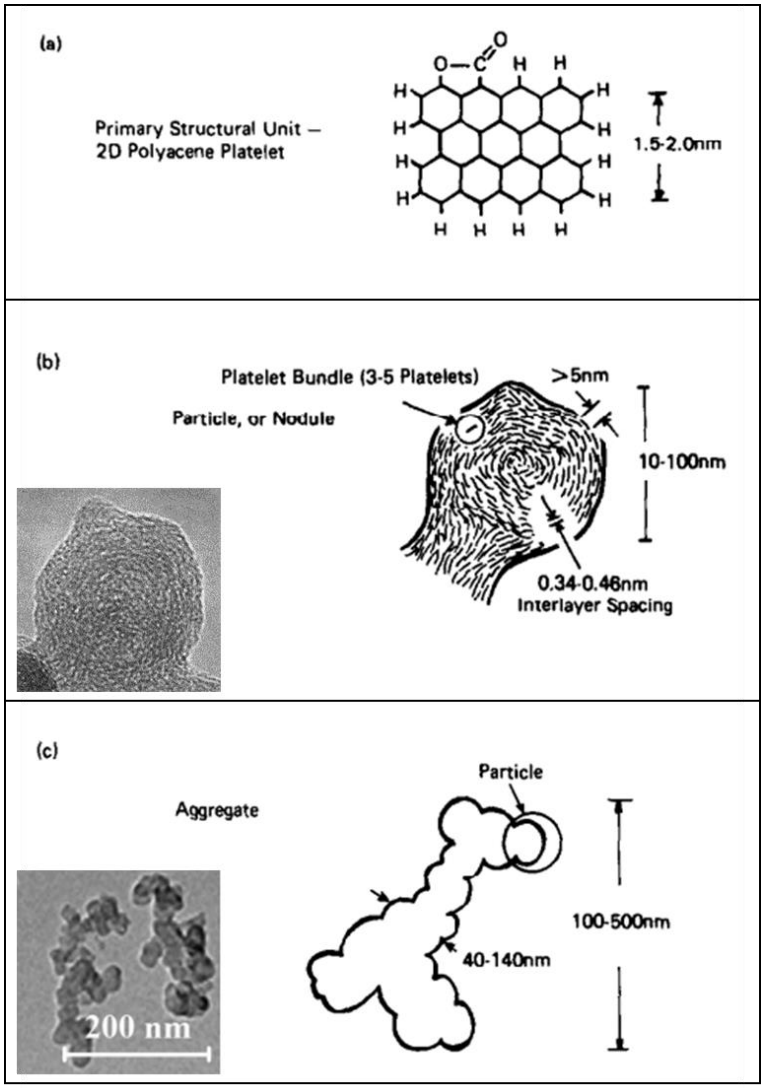

Figure 2-6. The structure of carbon black (CB) [15] at different length scales (a) 2D carbon platelet. (b) primary CB particle. The inset graph is a high resolution electron micrograph of a carbon black N285 primary particle[16]. (c) CB aggregate. The inset picture is a TEM image of carbon black N134 aggregates[17].

The specific surface area of CB can be used to describe the size of the primary particles and their distribution. It can be obtained by a statistical method using TEM or using fluid/gas adsorption measurements. The latter is more accurate where the surface area can be defined by the volume of the gas or liquid that is adsorbed by a certain amount of CB. Brunauer, Emmett and Teller[18] (BET) derived the most famous theory to determine gas absorption by solids, and nitrogen is often used in a real test (ASTM D6556-14[19]). Liquids such as iodine (I_2No , ASTM D 1510-13[20]) or

cetyltrimethylammonium bromide (CTAB, ASTM D 3765-03[21]) can also be used to determine the surface area. Beside the primary particle size, the structure of the aggregates is also important which can be characterised by dibutyl-phthalate oil absorption number (DBP, ASTM D 2414-14[22]) or the oil absorption number of a compressed sample (COAN, ASTM D3493-14[23]). The idea of these tests is to quantify the extent of the porosity of the carbon blacks. Table 2-2 gives the whole range of the carbon blacks classified using the ASTM D1765 standard where the carbon black grades used in this study have been highlighted.

Table 2-2 Classification of carbon black grades and their typical properties taken from ASTM D 1765[24].

	Iodine No. mg/g	DBP No. mg/g	CDBP No. mg/g	NSA m^2/g	STSA m^2/g	Tint strength %	Pour density kg/m^3
N110	145	133	97	127	115	123	345
N115	160	133	97	137	124	123	345
N120	122	134	99	126	113	129	345
N121	121	132	111	122	114	119	320
N125	117	104	89	122	121	125	370
N134	142	127	103	143	137	131	320
N135	151	135	117	141	/	119	320
S212	/	85	82	120	107	115	415
N219	118	78	75	/	/	123	440
N220	121	114	98	114	106	116	355
N231	121	92	86	111	107	120	400
N234	120	125	102	119	112	123	320
N293	145	100	88	122	111	120	380
N299	108	124	104	104	97	113	335
S315	/	79	77	89	86	117	425
N326	82	72	68	78	76	111	455
N330	82	102	88	78	75	104	380
N335	92	110	94	85	85	110	345
N339	90	120	99	91	88	111	345
N343	92	130	104	96	92	112	320
N347	90	124	99	85	83	105	335
N351	68	120	95	71	70	100	345
N356	92	154	112	91	87	106	/
N358	84	150	108	80	78	98	305
N375	90	114	96	93	91	114	345
N539	43	111	81	39	38	/	385
N550	43	121	85	40	39	/	360

N582	100	180	114	80	/	67	/
N630	36	78	62	32	32	/	500
N642	36	64	62	39	/	/	/
N650	36	122	84	36	35	/	370
N660	36	90	74	35	34	/	440
N683	35	133	85	36	34	/	355
N754	24	58	57	25	24	/	/
N762	27	65	59	29	28	/	515
N765	31	115	81	34	32	/	370
N772	30	65	59	32	30	/	520
N774	29	72	63	30	29	/	490
N787	30	80	70	32	32	/	440
N907	/	34	/	9	9	/	640
N908	/	34	/	9	9	/	355
N990	/	43	37	8	8	/	640
N991	/	35	37	8	8	/	355

Bound Rubber and Occluded Rubber

Unvulcanised rubbers swell and dissolve in suitable solvents such as toluene. It was discovered in 1920s[25] that once an unvulcanised rubber has been filled using nanometric fillers such as carbon black or silica, a large proportion of the rubber network becomes bound to the filler particles and as a consequence a considerable proportion of the rubber remains insoluble. This part of the rubber is gel-like and sticks on the filler surfaces. Although the insoluble part can be decreased by increasing the extraction temperature or by using a better solvent, it is never fully removed. This part of insoluble rubber is later defined as bound rubber[26, 27], which is caused by a strong interaction between the filler and the polymer. Figure 2-7(a) shows the bound rubber in SBR/carbon black N326 gel[28].

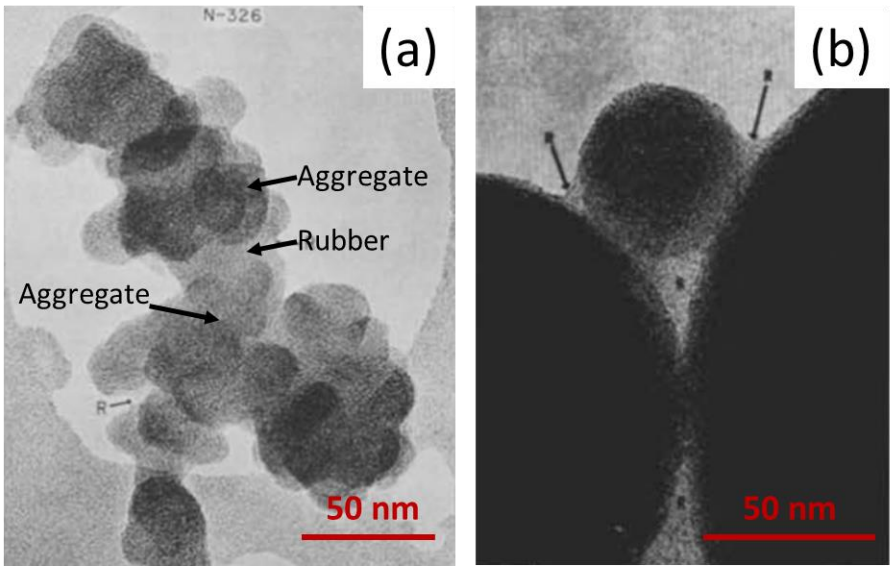

Figure 2-7. (a) High resolution image of carbon-rubber gel network for carbon black N326 in SBR at 50 phr. (b) TEM pictures of carbon-rubber gel network for MT in SBR at 150 phr[28]. The carbon black-rubber gel refers to uncured rubber-filler compounds that have been extracted in benzene.

Bound rubber is formed during mixing, with most of the bound rubber being formed during the first few minutes of compounding[27]. However, the amount can be further increased with an increase of the storage time which has also been confirmed by NMR (Nuclear Magnetic Resonance) studies[29]. The thickness of the bound rubber layer has been studied and has been found to be around several nanometres also by using NMR[30]. The amount of bound rubber is highly dependent upon the filler type and its specific values of particle size, surface area, structure and surface activity, the polymer type and the specific values for molecular weight, polarity and chain flexibility, the mixing condition and even the measuring method[31]. It has therefore been regarded as a global measurement of the filler-polymer interaction for specific systems. Moreover, bound rubber has also been regarded as one of the key contributions to filler reinforcement. This is because the adsorbed bound rubber has a lower molecular mobility when compared to the soluble parts of the polymer. It can form a second polymer network which is used to bond the separate filler aggregates together[32].

The volume between filler particles can be filled completely by rubber chains. For some parts of the network, they can completely be surrounded by rigid filler particles. As a

consequence, the trapped rubber behaves rather like the surrounding rigid filler particles. Therefore, the effective filler volume fraction is increased if include this trapped rubber as being rigid. This component of trapped rubber is known as occluded rubber. The occluded rubber component may, however, be released when the composite material is under strain and the net movement of the surrounding fillers liberates the occluded rubber. This is one of the sources of the nonlinear elasticity of filled rubber with strain. Figure 2-7(b) is a TEM picture of the occluded rubber.

Payne Effect

It was first observed by Fletcher and Gent in 1954[33] that a filled elastomer has nonlinear dynamic mechanical behaviour. That is, the storage modulus decreases with an increase in the strain. In 1960s, Payne[34, 35] performed a series of investigations on this phenomenon and related it to the filler-filler network. As shown in Figure 2-8, Payne attributed the decrease of the storage modulus $\Delta G = G_0 - G_\infty$ to changes in the filler structure behaviour. That is, before a certain strain (normally of around 0.1%), the filler structure remains unaltered while it breaks and releases the occluded rubber as the strain increases. Therefore, the apparent filler volume fraction decreases to the real fraction and the measured storage modulus decreases. Most of the structure is broken down by around 100% strain. In the rubber industry, this phenomenon has been used to evaluate the dispersion state as better dispersion typically has a smaller Payne effect (smaller ΔG). In addition, the loss modulus also shows a strain dependent behaviour. It has a peak while the storage modulus decreases as shown in Figure 2-9. As the loss modulus represents the energy dissipation, this peak relates to the dissipated energy during the breakage and reformation of the filler network during a dynamic cyclical test. The Payne effect is mainly attributed to the filler structure and concentration, the viscoelasticity of the polymer (which becomes more obvious as the test temperature approaches the glass transition temperature for the polymer), strain amplitude and strain rate[36, 37].

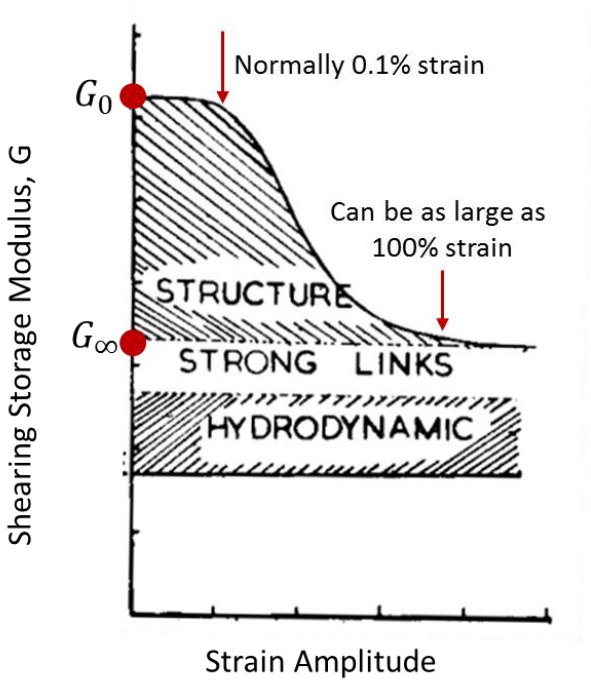

Figure 2-8. A qualitative explanation of the nonlinearity of the dynamic modulus-strain curve.

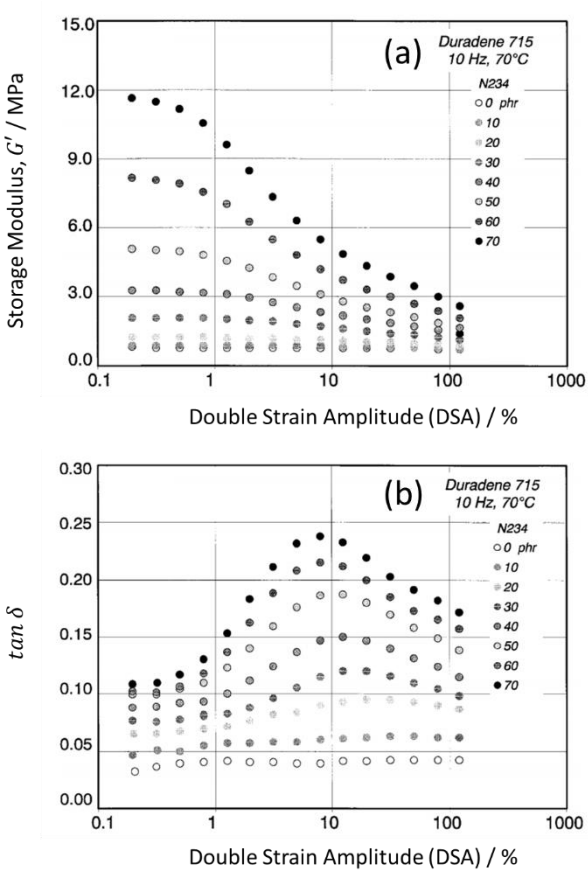

Figure 2-9. Strain dependent behaviour of the shearing storage (a) and loss (b) moduli of SSBR filled by carbon black N234 with different concentrations. Taken from the literature[36].

2.2 Fundamental Concepts of Dielectric Behaviour

2.2.1 Dielectric Matter in Static Electrical Field

When considering a dielectric material held in a static electrical field, in contrast to a conductive material where the charge carriers (such as the free electrons or holes) flow throughout the material, the electrical charges can only be shifted or vibrated to neighbouring positions until the overall system reaches an equilibrium state. The positive charges try to follow the direction of the electric field, whilst the negative charges are driven in the opposite direction. This process is known as the polarisation of the material. It produces additional dipole moments inside the material which can be expressed by the amount of the charge dispersed on the material's surface. Those surfaces charges generate an additional electrical field that opposes the direction of the applied electrical field. Therefore, the polarisation $\boldsymbol{P}$ is defined as '*a vector quantity expressing the magnitude and direction of the electric moment per unit volume induced in the material by the applied field*'[38]:

$$\boldsymbol{P} = (\kappa - 1)\kappa_{vac}\boldsymbol{E} \qquad \text{Equation 2-18}$$

where κ is the relative dielectric constant or the relative permittivity of the material and κ_{vac} is the permittivity of the vacuum. Note that, such linear relationship in Equation 2-18 between $\boldsymbol{P}$ and $\boldsymbol{E}$ is only accurate when the external electrical field is small. Another parameter called dielectric displacement $\boldsymbol{D}$ is defined as:

$$\boldsymbol{D} = \kappa_{vac}\kappa\boldsymbol{E} = \kappa_{vac}\boldsymbol{E} + \boldsymbol{P} \qquad \text{Equation 2-19}$$

Unlike $\boldsymbol{P}$, this dielectric displacement is only mathematically, not physically, defined by Equation 2-19. To understand the polarisation in detail, one has to focus on the behaviour at the molecular scale for the materials as it arises from the dipole moments in each polarized molecule:

$$\boldsymbol{P} = N(\alpha\boldsymbol{E}_L) \qquad \text{Equation 2-20}$$

where N is the average number of molecules per unit volume of the materials, α is the average polarizability of molecules and $\boldsymbol{E}_L$ is the local electrical field. Generally speaking, there are three types of molecular polarisations, each having different

relaxation times: electron polarisation ($\tau \approx 10^{-15}$s), atomic polarisation ($\tau \approx 10^{-13}$s) and orientation polarisation ($\tau \approx 10^{-9}$s). The polarizability α can be regarded as a linear summation of these three polarisations. Moreover, the first two polarisations are also known as induced polarisation as the dipole moments are generated by the external electrical field. The latter one arises from the orientation of the permanent dipoles of polar molecules. It already existed prior to the application of the external field. Therefore, there is no orientation polarisation for non-polar molecules because of the lack of permanent dipoles in the systems.

As each molecule is not only affected by applied electrical field but also affected by the electrical field generated by its neighbours, the actual overall local electrical field is defined as $\boldsymbol{E}_L = \boldsymbol{E} + \sum \boldsymbol{E}_d$ where $\boldsymbol{E}$ is the applied electrical field (the external field), $\sum \boldsymbol{E}_d$ is the sum of the electrical fields generated by all the dipoles inside of the material. It is very hard to derive a mathematical solution for this summation term. Lorentz[38] used a simplified model to give an approximate value of $\sum \boldsymbol{E}_d = \boldsymbol{E}(\kappa - 1)/3$ for non-polar molecular matter. Therefore, Equation 2-20 can be rewritten as:

$$\boldsymbol{P} = \frac{\kappa + 2}{3} N\alpha \boldsymbol{E} \qquad \text{Equation 2-21}$$

Substituting Equation 2-21 into Equation 2-18, creates the famous Clausius-Mossotti[38] equation:

$$\frac{\kappa - 1}{\kappa + 2} = \frac{N\alpha}{3\kappa_{vac}} \qquad \text{Equation 2-22}$$

or

$$\frac{\kappa - 1}{\kappa + 2} \times \frac{M_w}{\rho} = \frac{N_A \alpha}{3\kappa_{vac}} = P_M \qquad \text{Equation 2-23}$$

where N_A is Avogadro's number, ρ is the density of the materials and $P_M = \frac{N_A \alpha}{3\kappa_{vac}}$ is defined as the molar polarisation.

2.2.2 Dielectric Matter in a Dynamic Electrical Field

When there is a change of the applied electrical field $\Delta \boldsymbol{E}$, the dipoles orientate to reach an equilibrium state. At the moment when the electrical field is changed (giving no time for dipoles to respond), the polarisation measured is $\boldsymbol{P} = \boldsymbol{P}_\infty$. The permittivity is known as the instantaneous permittivity: $\kappa = \kappa_\infty$. Conversely, all the dipoles reach the equilibrium state when sufficient time is allowed. Therefore, the polarisation measured is maximised: $\boldsymbol{P} = \boldsymbol{P}_s$ and so as the permittivity: $\kappa = \kappa_s$ (static permittivity). The development of the polarisation is shown schematically in Figure 2-10. In practice, it is of no interest to characterise step changes in the field but more typically experiments utilise a sinusoidal fluctuating electrical field:

$$\boldsymbol{E}(\omega t) = \boldsymbol{E}_0 \exp(i\omega t) \qquad \text{Equation 2-24}$$

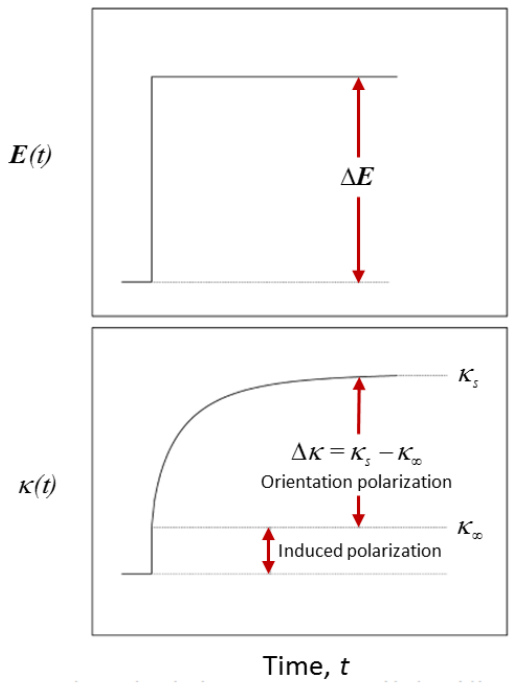

Figure 2-10. A schematic relationship between the time dependence of the applied electrical field and the permittivity.

The electrical displacement can be written as:

$$\boldsymbol{D}(\omega t) = \boldsymbol{D}_0 \exp\left[i(\omega t - \varphi)\right] \qquad \text{Equation 2-25}$$

In this case, the permittivity should also be expressed in a complex format:

$$\kappa^* = \kappa' - i\kappa'' = \frac{\boldsymbol{D}_0}{\kappa_{vac}\boldsymbol{E}_0}\exp(-i\varphi) \qquad \text{Equation 2-26}$$

According to Debye's[38, 39] derivation, Equation 2-26 can be expressed as:

$$\kappa^* = \kappa_\infty + \frac{\kappa_s - \kappa_\infty}{1 + i\omega\tau} \qquad \text{Equation 2-27}$$

where

$$\kappa' = \kappa_\infty + \frac{\kappa_s - \kappa_\infty}{1 + (\omega\tau)^2} \qquad \text{Equation 2-28}$$

and

$$\kappa'' = \frac{\kappa_s - \kappa_\infty}{1 + (\omega\tau)^2}\omega\tau \qquad \text{Equation 2-29}$$

Figure 2-11 (a) shows a typical plot of a Debye type relaxation. From Equation 2-28 and Equation 2-29, the well-known Cole-Cole plot (κ' *vs* κ''), as shown in Figure 2-11 (b), can be obtained whereby:

$$\left(\kappa' - \frac{\kappa_s + \kappa_\infty}{2}\right)^2 + (\kappa'')^2 = \left(\frac{\kappa_s - \kappa_\infty}{2}\right)^2 \qquad \text{Equation 2-30}$$

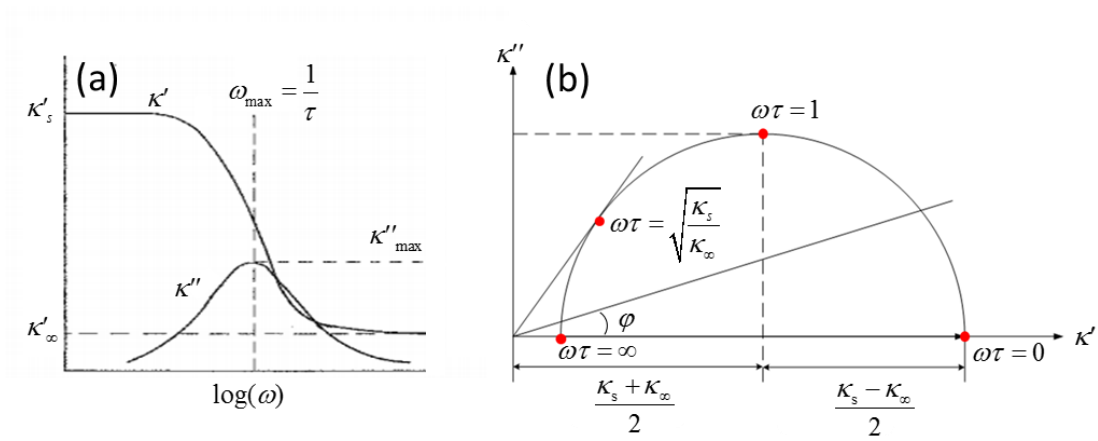

Figure 2-11. (a) Debye type relaxation presented as $\omega \sim \kappa^*$. (b) The Cole-Cole plot.

However, in the real tests, most of the experimental data cannot be directly fitted using Equation 2-27 because of the distribution of the relaxation times. Therefore, alternative

relationships such as the Cole and Cole[40] equation and the Havriliak-Negami (HN)[41] equation have been developed to describe the behaviour of real materials. The details of some of these equations are summarised in Table 2-3. The relationships mentioned in Table 2-3 (except Debye's original equation) are only empirical formulas. The physical meanings behind some of the parameters (such as the shape factors in HN function) are still unknown.

Moreover, for most of the cases, the material under test can hardly be treated as a single dielectric matter, especially for those filled inhomogeneous systems. This can be mathematically solved using different equivalent circuit models using the frequency dependent permittivity / impedance / admittance / susceptibility plots. It is very useful as it sometimes can help separate the error caused by the electrode-material interface[42] (this is discussed in more details in the following section). Some of the most important models are summarised in Figure 2-12[43]. Those models can be made even more complex for better fitting. For example, D.P. Almond et al.[44, 45] and R.K.H. Galvao et al.[46] used random distributed resistor-capacitor networks to model the dielectric behaviour of filler materials. And their simulations corresponded very well to Debye's physical model and Jonscher's universal dielectric power law[47]. Moreover, these models can also be used to explain the ac percolation behaviour which are discussed in Section 2.3.6.

Table 2-3. Various functions to describe the dielectric relaxation. Taken from the book by Kremer and Schönhals[39].

	Dielectric function	Real part	Imaginary part	Relaxation Time Distribution
Model function	$\frac{\varepsilon^*(\omega)-\varepsilon_\infty}{\Delta\varepsilon}$	$\frac{\varepsilon'(\omega)-\varepsilon_\infty}{\Delta\varepsilon}$	$\frac{\varepsilon''(\omega)}{\Delta\varepsilon}$	$L(\tau)$
Debye	$\frac{1}{1+i\omega\tau_D}$	$\frac{1}{1+(\omega\tau_D)^2}$	$\frac{\omega\tau_D}{1+(\omega\tau_D)^2}$	$\delta(\tau_D)$
Cole/Cole	$\frac{1}{1+(i\omega\tau_{CC})^\beta}$ $0<\beta\leq 1$	$(1+\omega\tau_{CC})^\beta\cos(\beta\pi/2))\, r^{-1}(\omega)$ $r(\omega)=1+2(\omega\tau_{CC})^\beta\cos(\beta\pi/2)+(\omega\tau_{CC})^{2\beta}$	$(\omega\tau_{CC})^\beta\sin(\beta\pi/2))\, r^{-1}(\omega)$	$\frac{1}{2\pi}\frac{\sin\beta\pi}{\cosh(\ln\tau/\tau_{CC})+\sin\beta\pi}$
Cole/Davidson	$\frac{1}{(1+i\omega\tau_{CD})^\gamma}$ $0<\gamma\leq 1$	$\cos(\Phi)^\gamma\ \cos\gamma\Phi$ $\tan\Phi=\omega\tau_{CD}$	$\cos(\Phi)^\gamma\ \sin\gamma\Phi$ $\tan\Phi=\omega\tau_{CD}$	$\frac{\sin\gamma\pi}{\pi}\left[\frac{\tau}{\tau_{CD}-\tau}\right]^\gamma$ for $\tau\leq\tau_{CD}$ 0 for $\tau>\tau_{CD}$
Havriliak/Negami	$\frac{1}{(1+(i\omega\tau_{HN})^\beta)^\gamma}$ $0<\beta\leq 1$ $0<\beta\gamma\leq 1$	$r(\omega)\cos[\gamma\psi(\omega)]$ $r(\omega)=\left[1+2(\omega\tau_{HN})^\beta\cos\left(\frac{\beta\pi}{2}\right)+(\omega\tau_{HN})^{2\beta}\right]^{-\gamma/2}$ $\psi(\omega)=\arctan\left[\frac{\sin(\beta\pi/2)}{(\omega\tau_{HN})^{-\beta}+\cos(\beta\pi/2)}\right]$	$r(\omega)\sin[\gamma\psi(\omega)]$	$\frac{1}{\pi}y^{\beta\gamma}(\sin(\gamma\Theta(y))\Omega(y)$ $y=\tau/\tau_{HN}$ $\Omega(y)=[1+2y^\beta\cos(\pi\beta)+y^{2\beta}]^{-\gamma/2}$ $\Theta(y)=\arctan\left[\frac{\sin(\pi\beta)}{y^\beta+\cos(\pi\beta)}\right]$

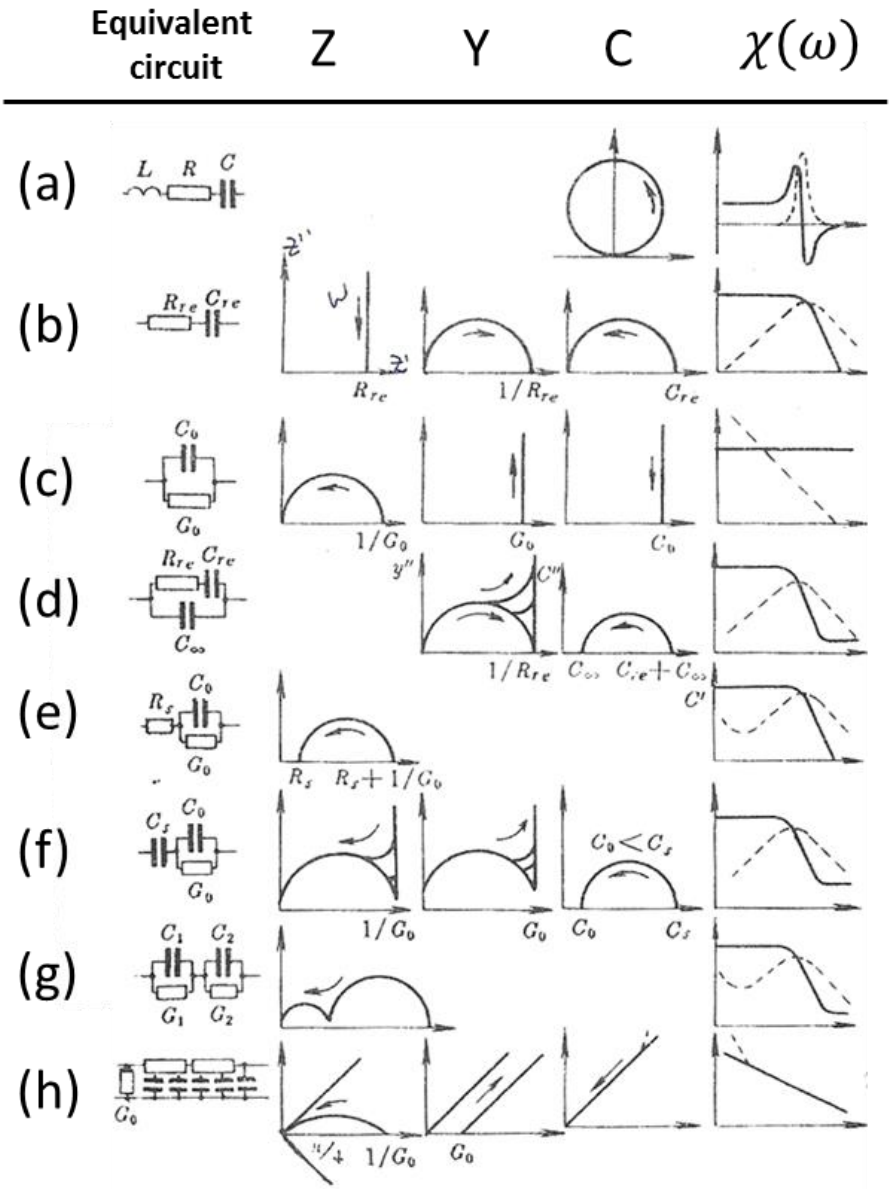

Figure 2-12. Some important equivalent circuit models. Z is the impedance. Y is admittance, C is capacitance, $\chi = \kappa - 1$ is the susceptibility. In Z, Y and C columns, all graphs use the real part as the x-axis while use the imaginary part as the y-axis. The arrows in each plot means the increase of angular frequency. In $\chi(\omega)$ column, x-axis is the angular frequency while the y-axis is the amplitude of either the real (solid line) or the imaginary part (dashed line) of susceptibility. Taken from the literature[43].

2.2.3 Testing Technologies for Characterising Dielectric Properties of Solids:

As shown in Figure 2-13 (a) & Figure 2-13 (b), the full range of dielectric testing covers more than 18 orders of magnitude in test frequency if a range of different testing techniques are adopted. Figure 2-13 (c) shows the sample cell for different testing frequencies. This thesis mainly focuses on the impedance method, which uses the AC-bridge technique. A frequency-response analysis was also used to test the materials at low frequencies ($f < 10Hz$) as well as the network analysis and the quasi-optical spectroscopy for the very high frequency ranges.

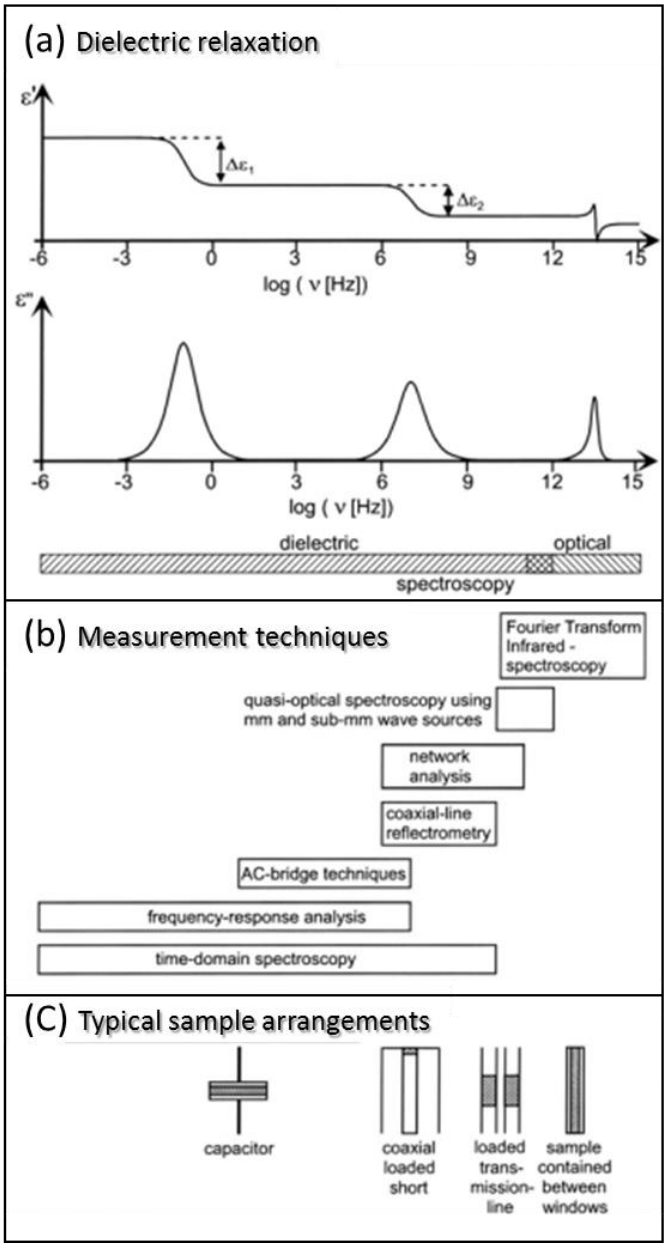

Figure 2-13. (a) A dielectric relaxation sketch; (b) different dielectric techniques and their working frequency range; (c) the sample arrangements for different techniques.[39]

Impedance Test

The impedance characterisation is the most common way to measure dielectric properties such as permittivity at frequencies below 100 MHz. The impedance technique cannot only characterise the dielectric properties of a dielectric material but it can also measure the conductivity behaviour of conductive or semi-conductive materials (with a high loss). It is very important to emphasise that although the dielectric parameters such as permittivity and dielectric modulus can be worked out from the measured complex impedance for all the different classes of materials, the physical meaning behind those dielectric parameters is lost when dealing with the semi-conductive materials that exhibit a high loss. There are several very good reviews, for example, by Runt[2], Kremer[39] and MacDonald[48] that introduce these techniques and in what follows a general introduction of this technique is presented.

In an impedance test, a disk plane capacitor cell is normally used where the material under test (MUT) is sandwiched by two electrodes as shown in Figure 2-13 (c). To ensure a good contact, the MUT can be coated by gold, silver or other conductive materials. But one should be careful about the type of electrode-material interphase[38, 49] that may cause a strong interfacial polarisation which can even dominate the measured behaviour. As shown in Figure 2-14, a sinusoidal voltage signal $U(t)$ is generated and applied to this testing cell:

$$U(t) = U_0 \sin(\omega t) \qquad \text{Equation 2-31}$$

where U_0 is the amplitude of applied voltage, ω is the phase angle and *t* is time. At the same time, the current signal received is also sinusoidal but is slightly out of phase with a phase angle φ:

$$I(t) = I_0 \sin(\omega t - \varphi) \qquad \text{Equation 2-32}$$

where I_0 is the amplitude of the current. Similar to the mechanical test behaviour characterised for example by using a DMA, the voltage and the current can be rewritten in a complex format as:

$$U^* = U_0 \exp(i\omega t) \qquad \text{Equation 2-33}$$

$$I^* = I_0 \exp\left[i\left(\omega t - \varphi\right)\right] \qquad \text{Equation 2-34}$$

Therefore, the complex impedance can be derived as:

$$Z^* = \frac{U^*}{I^*} = R + iX = \frac{U_0}{I_0}\cos\left(\varphi\right) + i\frac{U_0}{I_0}\sin\left(\varphi\right) \qquad \text{Equation 2-35}$$

where R and X are the real part and imaginary part of impedance respectively. They are also known as the resistance and reactance. The dielectric loss is defined as:

$$D = \frac{R}{X} = \frac{\kappa''}{\kappa'} \qquad \text{Equation 2-36}$$

For an ideal resistor, the phase angle $\varphi = 0$ and $Z^* = R$. But for an ideal capacitor or inductor, $\varphi = -90^\circ$ or 90° and $Z^* = -iX$ or iX respectively. When the MUT is a dielectric material which behaves like a capacitor, the imaginary part of the impedance becomes a negative value. In this case, the absolute value of X should be used in Equation 2-36.

The next step is to calculate the capacitance from the measured complex impedance. No MUT is a perfect dielectric material. Therefore, an equivalent circuit model is required to obtain the capacitance. One should be aware, that although the results based on different models may be different from each other, all the models are correct and there is not a best model. Moreover, the differences between the results obtained by different models is highly dependent upon D. The simplest and most widely used circuits for this analysis are RC series and parallel circuits. The relationship between RC series capacitance C_S and RC parallel capacitance C_P is:

$$C_S = C_P\left(1 + D^2\right) \qquad \text{Equation 2-37}$$

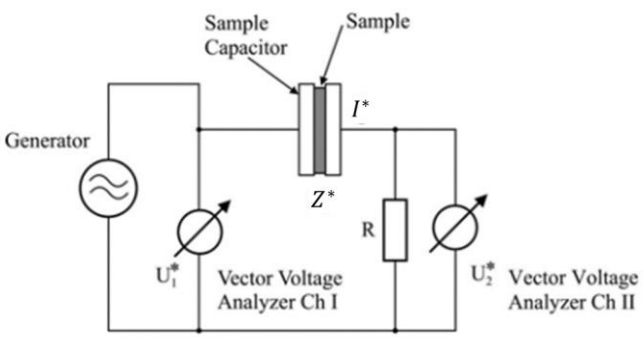

Figure 2-14. A general schematic of the impedance test.

Figure 2-15 shows an example of the differences between C_S and C_P for two different materials with either a large or a small D value. It demonstrates that a consistent result for both values can be obtained when $D < 0.1$ and it is the nominal suggested threshold value for measuring an accurate dielectric value. When D increases above this threshold, only the general trend of the dielectric parameters (such as permittivity) as a function of, for example, temperature, frequency or strain are measured rather than an absolute value. Although this is a fundamental aspect of measuring the impedance of dielectric materials, it has been ignored by many different research groups, who have claimed in the past huge permittivity values for high loss materials. For example, materials with very high permittivity have been reported by Panda[50], He[51], Dang[52] and Yuan[53] which suggested potential materials for use in electronic devices. However, such permittivity is meaningless as the loss value of their materials is also very high.

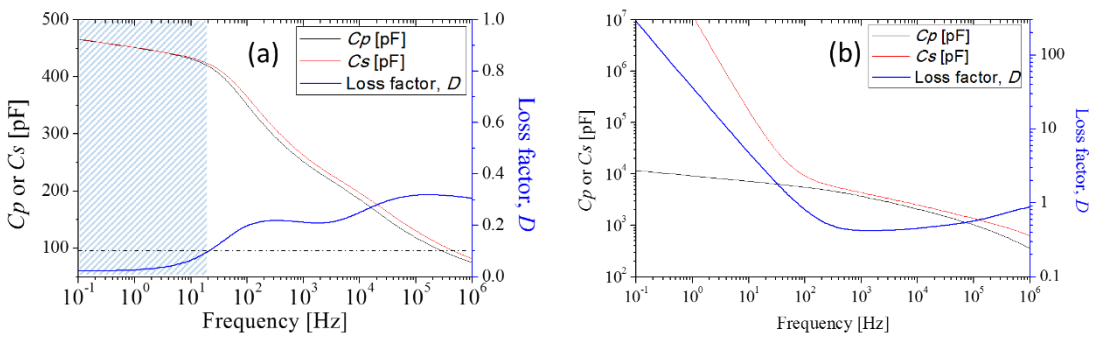

Figure 2-15. The frequency dependence of RC series capacitance C_S, RC parallel capacitance C_P and dielectric loss D of: (a) natural rubber filled by 15 phr carbon black N330; (b) natural rubber filled by 20 phr carbon black N330.

To maintain consistency, all the calculations derived in this thesis are based on the RC series model except the ones that are highlighted as being different. Therefore, the capacitance can be expressed as:

$$C = -\frac{1}{2\pi fX} \qquad \text{Equation 2-38}$$

where f is the electrical frequency. Therefore, the real part of permittivity can be obtained by:

$$C = \kappa_{vac}\kappa' \frac{Area}{Thickness} \qquad \text{Equation 2-39}$$

where κ_{vac} is the permittivity of the free space which is equal to 8.85419 pF/m and the imaginary part of the permittivity can be obtained using Equation 2-36. Dielectric properties can also be represented using alternative parameters including the electrical modulus M^* or the ac conductivity σ^*:

$$M^* = M' + iM'' = \frac{1}{\kappa^*} \qquad \text{Equation 2-40}$$

$$\sigma^*_{\text{ac}} = \sigma'_{\text{ac}} - i\sigma''_{\text{ac}} = i2\pi\kappa_0\left(\kappa^* - 1\right) \qquad \text{Equation 2-41}$$

Microwave Test

Microwave refers to the electromagnetic radiation with a wavelength between 1 mm to 1 metre which coincides with a frequency range from 300 MHz to 300 GHz. There are a lot of important electronic applications in this range from the home internet routers to the radar absorption skin of a Lockheed F-117 Nighthawk. However, determination of the electromagnetic parameters (permittivity and permeability) in this range is very complex and difficult, even though the electromagnetic theory was devised more than 100 years ago by Maxwell[54]. The microwave property testing technique is still being advanced and developed. There are several methods[55] that can be used to measure the electromagnetic parameters such as cavity resonators, free space, open-ended coaxial probe and transmission-line with the latter three techniques adopting a transmission /

reflection (TR) method. The transmission-line approach has been the most widely used because of its accuracy and simplicity.

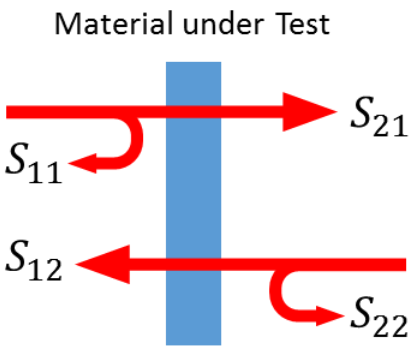

Figure 2-16. The transmission/reflection coefficients in a transmission/reflection test.

TR methods measure the transmission/reflection coefficients (S_{ij}) from which the complex permittivity κ^* and complex permeability μ^* can be determined. It is normally made up of a section of a coaxial lines or uses a rectangular wave guide[55, 56] where the sample is located. Note that, because specific wave guides have different cut-off frequencies, one has to use different waveguides to measure over a broad frequency domain. Figure 2-16 gives an idea of the transmission/reflection method as well as the definition of each transmission/reflection coefficient which can be obtained by a vector network analyser (VNA). Nicolson, Ross and Weir[57] proposed their famous (NRW) method to derive the electromagnetic parameters from the measured S_{ij} in 1970s. However, there are some problems when adopting their equations:

1. When the thickness of the sample is an integer multiplied by half of the wavelength, then the calculation becomes unstable and this phenomenon is known as the thickness resonance.

2. Multiple solutions may exist. Therefore, one may have to do multi tests using different specimens that have different thicknesses or use one specimen but repeat the test at different frequencies.

3. A small error in measuring the thickness may result in large errors in the final results. Therefore, the error becomes significant for ultra-thin samples.

To overcome these uncertainties, Tang[58] proposed a new calculation method based on the transmission-line technique. He used three different equations to independently calculate the electromagnetic parameters. He then optimised the solution from these three different results which has been proven to be more accurate[58].

The free space method[55, 59] is another important transmission/reflection technique to measure the electromagnetic parameters over the millimetre and submillimetre wave range up to 1 THz. It is a simple but accurate technique. Moreover, this setup is quite flexible in use because the material under test (MUT) is held in a free space where there are no other electrodes or waveguides applied. For example, the material can be placed in an oven so that high temperature testing[60] can be undertaken. Figure 2-17 show the latest free space quasi-optical testing system[59, 61] from Keysight Technology. Just like other transmission/reflection tests, S_{ij} will initially be worked out using a vector network analyser from which other electromagnetic parameters can be calculated.

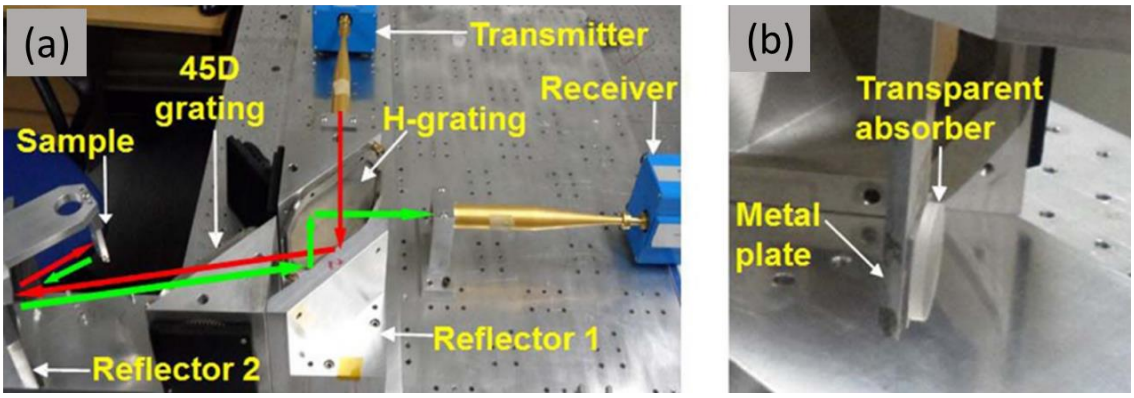

Figure 2-17. (a) Free space reflection test. Red line: incident wave. Green line: reflected wave. (b) Sample holder of the reflection test. Taken from the literature[61].

2.3 Nanodielectric Elastomers

2.3.1 Twenty Years of Nanodielectrics: Opportunities and Challenges

Nanodielectrics

The importance of the concept of nanodielectric (or nanometric dielectric) was proposed by Lewis[1] in 1994. He predicted that nanometric composites will be a

significant challenge in dielectric materials research and that the greatest challenge arises at the interface between the fillers and the matrix. Ten years later in 2004, he made an even stronger statement that '*interface and nanodielectric are synonymous*'[62, 63]. Around the same period, the experimental works on the interface of nanodielectrics were started. For example, Nelson[64] studied the charge storage and transportation of property of TiO_2 /epoxy interface. It was found that the nano-sized TiO_2 brings substantial changes to the dielectric property of the composites compared to micro-sized TiO_2 . Roy[65] characterised the dielectric properties of silica/polyethylene composites and found that when the particle size decreased to nanometric range, the dielectric breakdown strength and voltage of the composites were dramatically changed compared to the micro-composites. Another important development was the different layered models developed built by Lewis[62], Tsagaropoulos[66] and Tanaka[67]. Although they are only an approximate treatment of the electronic structures, it has been widely adopted and therefore, the important role of the interface has gradually been accepted (This is discussed in detail in Section 2.3.4). In recent years, researchers have realised the importance of a good filler dispersion to ensure effective dielectric properties. The dielectric method has become established as a technique to ensure consistency in the extent of a controlled dispersion of the filler throughout the system. Although researchers have changed the resulting dielectric properties of a nanometric composite by modifying the interface[68], the actual mechanism that gives rise to the specific electrical behaviour is still not clear. Also, this topic has become an interdisciplinary subject as materials scientists have been drawn into a field historically occupied only by electrical engineers. Many different nanodielectric applications such as sensors and actuators have now been proposed. At the outset of the third decade of dielectric research of polymer materials, the development of new testing technologies has enabled a clearer view of the electrical structures as well as the polymer dynamics of the interfaces to be developed. Examples of such tests include local impedance testing on the nanoscale coupled with AFM[69] (measuring the dielectric properties of materials focusing at a dimension of a few nanometres), the strained impedance test[70] (measuring the dielectric properties of materials under a mechanical strain) or THz range dielectric characterisations[71] (to achieve a very broadband frequency range).

Nanodielectric Elastomers

Most polymers are good dielectrics except the family of pi-conjugated conducting polymers[72]. Therefore, the elastomers mentioned in Section 2.1.1 such as NR and PDMS are all good examples of dielectric elastomers. When they incorporate features at the nanometric scale, for example by being filled by nano-particles or if they contain nano-sized crystal domains, then the resulting composites are known as nanodielectric elastomers. However, for some cases, the nano-particles can transform the material from being a dielectric to being a conductive material as a consequence of a conductive filler network being created as is suggested by the percolation theory[73] (This behaviour will be explained in more detail in Section 2.3.4). In such cases, the elastomers are known as nanometric conductive elastomers instead.

Their flexibility and coupled mechanical and dielectric properties, makes dielectric elastomers useful in a wide range of applications, for example being used as: transducers (artificial muscles or actuators[74]); energy switching or storage devices (solar cells and batteries[75]), deformable electrodes[76] and other electronic devices such as force sensors using in touchscreen panels[77] or health monitoring devices[76]. Compared to alternative traditional dielectric materials such as those made using functional ceramics, dielectric elastomers also have a high dielectric breakdown field strength[78] and low dielectric loss values. Like ceramics, some can even be used at high temperatures of up to 250 $^{\circ}C$ [79]. And more importantly, their mechanical flexibility makes them easy to be fabricated or assembled. However, electronic applications typically also require a high permittivity which limits the dielectric elastomers that can be adopted in real applications. The permittivity of a pure polymer material is relatively low (normally smaller than 10) which is orders of magnitude smaller than that of ceramic materials. An effective method that can be used to increase the permittivity is to incorporate fillers, which is a similar approach to that adopted to improve the mechanical behaviour. By considering the filler size, these fillers can be either micro or nanometric fillers. However, it is well established that the nano-fillers are more efficient [1, 75] at modifying the dielectric behaviour of composites due to a higher interface surface area per unit volume.

Conductive Filler Systems

When considering the conductivity of filler particles, nanodielectrics can also be classified into two types. The first are conductive fillers such as carbon based fillers (including carbon black[80], carbon nanotubes[81] and graphene[82]), metallic fillers (such as nickel[83, 84] and silver[85]) or even some conducting polymers[86] . The other filler type are non-conductive fillers such as mineral particles (such as montmorillonite[87]), metal oxides (such as TiO_2 [88]) or other poorly conductive polymer materials. Multi-filler systems[89] have also been used to try and develop synergistic effects in their behaviour but they are much more complex and are not discussed in detail here. Compared to non-conductive filler systems, conductive filler composite systems can build high permittivity composites at low filler volume fractions as shown in Figure 2-18. This can be explained using percolation theory which is discussed in Section 2.3.4. Although the permittivity is enhanced by incorporating conductive fillers, there are still some issues or challenges when using this type of nanodielectric elastomers:

1. Interface structure between filler-polymer, including the charge distribution, the energy band structure and the dynamics of confined polymer in that region are all still not fully understood.
2. Fillers introduce defects into the system that may lower the breakdown strength.
3. A known and ideally a uniform dispersion of the fillers is the best, but it is very hard to achieve experimentally.
4. There is a sharp change in the electrical properties around the percolation threshold. Therefore it is very difficult to get reproducible behaviour around this region as even modest changes in composition, processing or test environment can have unpredictable and large changes in the measured behaviour.
5. Conductive fillers not only bring a high permittivity but also increase the dielectric losses due to an introduction of a greater leakage current and interface effect.
6. Finally, the strain dependence of the dielectric properties has only rarely been investigated or even discussed.

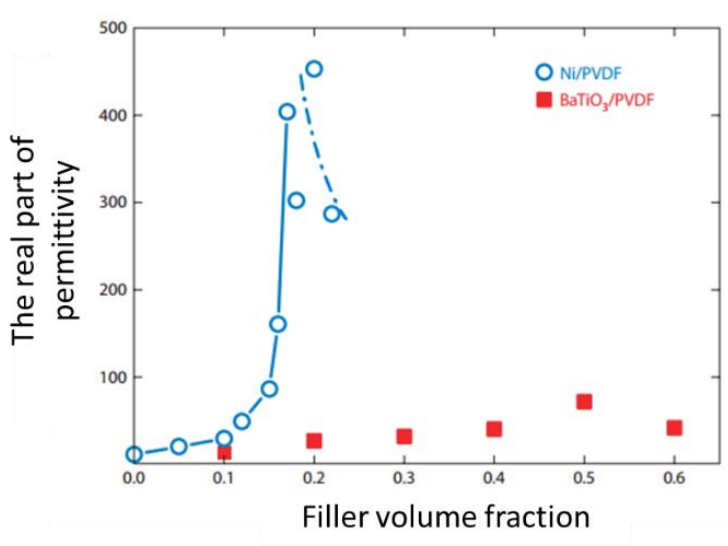

Figure 2-18. Enhancing the dielectric permittivity of PVDF using different fillers. Data taken from literatures [84, 90].

The first issue is currently the most important consideration in nanodielectric research. However, this complex behaviour requires a more detailed understanding. Take for example the confined polymer dynamics at the interface[91], where there is as yet still no consensus in the literature. Other issues that lack agreement include the electrification and polarisation[92, 93] of the materials. The second issue is particularly important for developing industrial applications as the breakdown strength relates to the safety, the working condition as well as the working life of the products. The problem is that, the testing of breakdown strength is relatively difficult for elastomers as they are electroactive[94] under a high electrical potential. Namely, the specimen is squashed by the electric force known as the Maxwell Force, when the electrical potential is applied. Therefore, the currently reported data on this topic typically ignores this geometric change under test and so a robust design of the breakdown test is required. The third and the fourth issues are the problem for all polymer nanocomposites (filled by conductive fillers). Although it can be better controlled by filler surface modification, using coupling agents or in-situ polymerisation[95], compounding is still a challenge. Zhang[96] proposed a solution that it is easier to increase and broaden the percolation region than to control the dispersion itself. Therefore, the error or the uncertainties of the dispersion can be reduced and hopefully even ignored for such systems. A potential

way to resolve the large loss problem when using a conductive filler-polymer composite system might be to adopt a core-shell structure. That is, to coat each filler particles with a layer of electrically insulating material[97]. As shown in Figure 2-19, all the conductive particles are then separated by these shell layers. This not only decreases the electrical contact between fillers but it can also increase the dispersion level. One of the problems with this core-shell structure is that it introduces extra interfaces and makes the interface structure even more complex. Thus making it even more difficult to control and reliably produce a specific dielectric behaviour.

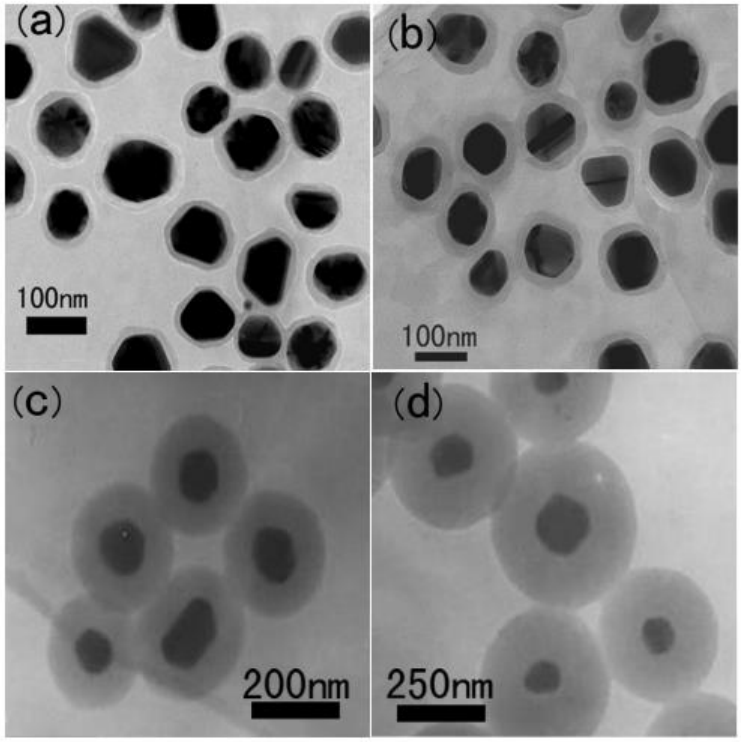

Figure 2-19. TEM pictures of different core-shell particles made by Ag (core) and a carbonaceous (shell). Taken from the literature[97].

The sixth issue, relates to the dynamic behaviour of nanodielectric elastomer devices under strain. Although the strain dependent dc electrical properties have been well studied[98] and this approach has even been adopted in sensor applications[99], the strain dependent dielectric behaviour has only been examined occasionally. The reason may result from actual testing difficulties (which are discussed in greater detail in Chapter 5) and the complexity encountered when analysing the data. Curiously, the strained

dielectric spectrum was used to study the molecular dynamics at the start of polymer material research back to 1950s[100, 101]. However, this technique of measuring the strained dielectric spectrum had not been significantly improved over the second half of the last century until more recent investigations this century where it has been adopted again. This time though for a different purpose, for example, to study the filler networks[102, 103], to build new type of strain sensors or actuators[104] or to monitor the strain induced crystallisation[70, 105]. Although researchers have noticed that this technique might be a powerful tool, there has not been up to now a reliable way to obtain the simultaneously dielectric spectrum of the strained materials. Moreover, it seems that the literature does not pay enough attention to the strain dependent dielectric behaviour of nanodielectric elastomers. As even today, the dielectric properties of those materials are still considered as strain independent for most cases. Therefore, based on this review, there has not yet been a systematic study of the strain dependent behaviour of real nanodielectric elastomers filled with conductive fillers. In this context, 'real' means that the filler volume fraction is low enough so that the material is still non-conductive. Further details about these types of investigations (including those already mentioned above) into this topic are reviewed in Section 2.3.7.

2.3.2 Dielectric Relaxation of Cis-polyisoprene (PI)

As discussed in Section 2.2, there are a range of types of dipoles inside of the materials. It becomes more complex for polymer materials because of their long chain structures. Stockmayer[106] classified dipoles in polymers by their vibration orientations. That is, some of the dipoles have the same direction (parallel) as the polymer chain while some others are perpendicular to the chain direction. A-type dipoles are parallel and B-type dipoles are perpendicular as illustrated in Figure 2-20. Dipoles that are located in the pendant groups are called C-type dipoles. As shown in the Figure 2-20(a), A-type dipoles refer to the global movement of the whole chain therefore, they relate to relatively long time scales. Their dielectric relaxation behaviour fits the normal mode of Rouse-Zimm theory[107, 108] (the bead-spring model) when it is in a dilute solvent while it can be described using the tube theory[109] in the condensed solvent. Therefore, it is usually

known as the normal mode relaxation or β relaxation. The dipole moment vector of an A-type chain $\boldsymbol{P}_A$ is proportional to the end-to-end vector $\boldsymbol{r}$ [107] which can be written as:

$$\boldsymbol{P}_A = \mu \boldsymbol{r} \qquad \text{Equation 2-42}$$

where μ is the dipole moment per unit contour length which can be treated as a constant. It means that the polarisation can provide a direct measurement of the end-to-end vector. Therefore, the dielectric test can be used to help determine the viscoelastic relaxation behaviour. There are some highly appreciate books and papers concerning both mechanical and dielectric relaxations such as McCrum (1967)[110], Adachi (1990)[111], Pakula (1996)[112], Jonscher (1996)[113], Runt (1997)[2], Santangelo (1998)[114] and Steeman[115] (2003). Steeman in particular gave a detailed comparison between dielectric and mechanical spectroscopy. Conversely the B-type dipole moment vector $\boldsymbol{P}_B$, does not correlate with $\boldsymbol{r}$ for polymers with a high molecular weight. That is $\langle \boldsymbol{P}_B \cdot \boldsymbol{r} \rangle = 0$ where the angular bracket stands for a statistical average value[2]. Instead it refers to the movements of local segments which are linked to the glass transition behaviour of the material. This behaviour is known as the segmental relaxation or α relaxation. It has a much shorter length scale when compared to the β relaxation. Finally, the C-type dipole moment vector $\boldsymbol{P}_C$ only reflects the dynamics of the side group.

Norman[116] undertook pioneering studies into the dielectric properties of cis-polyisoprene (PI) in 1953. However, PI was not at that time considered to be an ideal type-A polymer (one that has both type A and B dipoles) until more than 30 years later[117]. Since then, the relaxation processes in PI have been extensively studied using dielectric techniques. Pioneering works have been done by Adachi (in both the solvent state[118] and the solid state[111]), Schönhals[119] and Boese[120]. These investigations mainly focused on the frequency and temperature domain spectrum of materials with a wide range of molecular weights or in polymers in different kinds of solution. More recently, the dielectric relaxation of PI in a confined state attracts more and more attentions[121], whereby the relaxation process can be controlled by confining[122] the materials in a limited dimension (more details are given in Section 2.3.4). At the same time, computational modelling works[123] have also been proposed.

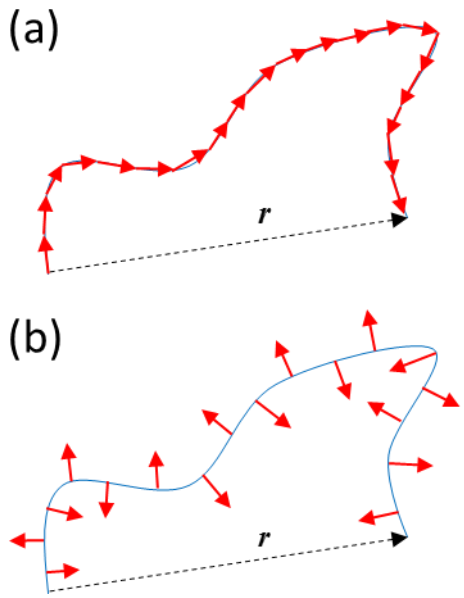

Figure 2-20. Illustrations of (a) Type-A chain and (b) Type-B chain. The red arrows stands for the dipole moments of each unit of the polymer chain. The black dashed arrow stands for the end-to-end chain vector.

General Frequency and Temperature Dependent Behaviour

The real part of permittivity of natural rubber is essentially constant over a wide frequency range with a typical value around 2.45 (at 1000 Hz). Its value depends on the detailed processing of the NR as shown in Table 2-4. As a good electrical insulator material, its dielectric loss value is also very small. Figure 2-21 shows the frequency and temperature dependence of the imaginary part of permittivity of non-crosslinked cis-polyisoprene with a molecular weight of 11700 $g \cdot mol^{-1}$ [120]. Both α and β mode relaxations can be identified in this graph. As the α mode is of a shorter length scale compared to the β mode, it can only be observed at low temperature or at high frequencies. For some filled materials, the peak of these α modes can be broadened or shifted and this in part provides evidence for a small change of glass transition temperature[95, 124]. Moreover, if the frequency is decreased, an extra term, the conductivity mode can be observed (Figure 2-22)[125]. Each of the relaxation peaks can be decomposed in a frequency plot as shown in Figure 2-22. Chapter 3 will give a detailed description of using this method to analyse the dielectric data.

Table 2-4. The dielectric properties of different rubber products treated by different methods. Taken from the literature[101].

SAMPLE	COMPOSITION OR TREATMENT	κ' @1 KHZ	DIELECTRIC LOSS@1 KHZ
Pale crepe	Unvulcanised	2.43	0.0016
Smoked sheet	Washed and dried	2.35	0.0029
Rubber from latex	Proteins and resins removed	2.37	0.0015
Smoked sheet	Sulphurless cure (0 phr)	2.52	0.0022
Smoked sheet	Low sulphur cure (0.75 phr)	2.51	0.0023
Smoked sheet	Normal sulphur cure (3 phr)	3.01	0.043

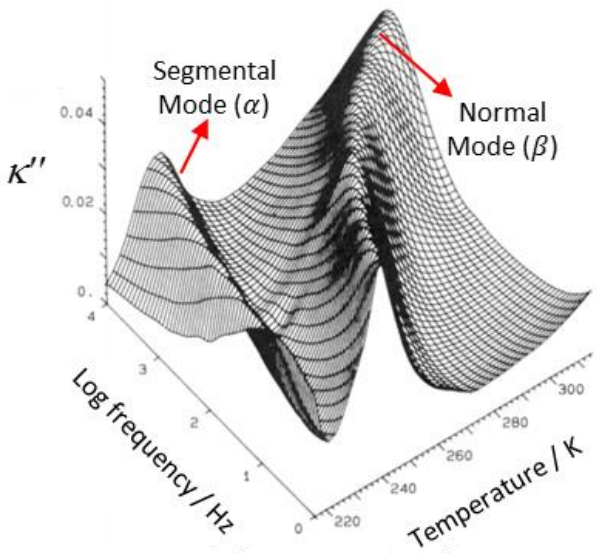

Figure 2-21. The 3D plot of the frequency and temperature dependence of the imaginary part of permittivity of cis-polyisoprene with a molecular weight of 11700 $g \cdot mol^{-1}$, taken from Schönhals[120].

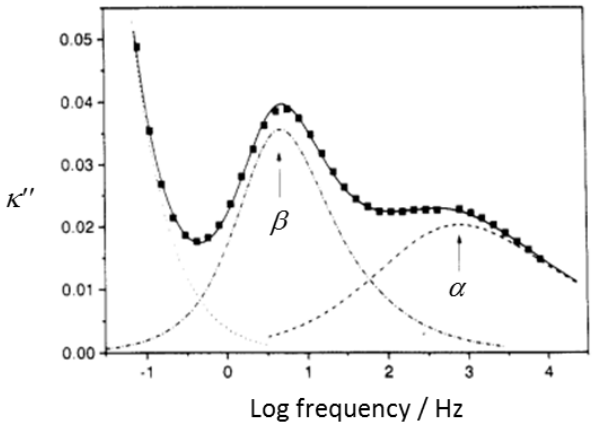

Figure 2-22. Decomposition of the imaginary part of permittivity of cis-polyisoprene at 216 K. Molecular weight is 1400 $g \cdot mol^{-1}$. Taken from the literature[125].

Figure 2-23 shows a comparison between the dielectric and mechanical spectrum of cis-polyisoprene[126]. Both the normal mode and the segmental mode in the dielectric spectrum can find equivalent features in the mechanical spectrum. However, the dielectric features are much clearer to see than the mechanical results.

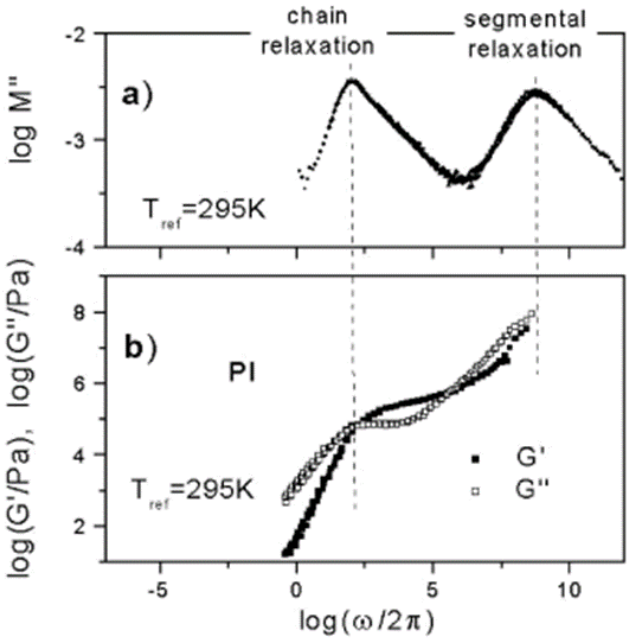

Figure 2-23. The dielectric (a) and mechanical (b) spectrum of linear polyisoprene melt with a molecular weight of 50,000 $g \cdot mol^{-1}$ at a temperature of 295 K. The mechanical spectrum is built by the time-temperature superposition technique using a DMA. Taken from the literature[126].

Molecular Weight

A higher molecular weight M_w brings longer relaxation time of the β process that can now only be observed at very high temperatures or at the lowest frequencies. Figure 2-22 shows a very strong β peak that results from the low M_w of the material under test. This β peak becomes too small to be observed under similar conditions for a sample with a higher M_w (for example using NR) above Tg. Fragiadakis[95] showed a very broad β relaxation peak of NR at around 10 Hz and below 213 K. This may be because NR has a broad molecular weight distribution ($10^4 - 10^7$). Floudas[39] summarised the molecular weight dependent behaviour of the normal mode process as shown in Figure 2-24. There is a particular value of the molecular weight $M_c \approx 10,000\ g \cdot mol^{-1}$ below which the relaxation time τ can be fitted by the Rouse model: $\tau \sim M^2$. Therefore the cis-polyisoprene chains can be treated as either untangled or entangled chains below or above M_c respectively. Compared to the β process, the segmental process is normally unaltered by the molecular weight as it is mainly affected by low range local vibrations[107].

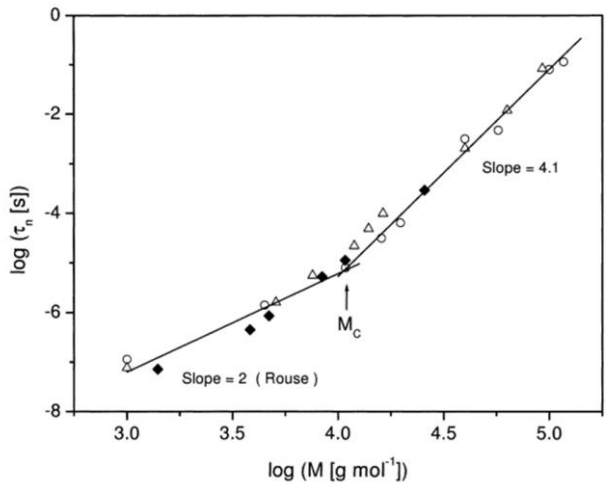

Figure 2-24. The relaxation time of the normal mode process for cis-polyisoprene measured at a temperature of 320 K as a function of the molecular weight. Taken from the literature[39].

Curing Additives

As shown in Section 2.1.2, curing additives can chemically change the chain structure. Moreover, the remaining unutilised additives or by-products left over after vulcanisation can be treated as fillers which can introduce additional contributions to the measured dielectric properties. Hernández[127] studied the role of the sulphur curing additives on the chain dynamics of unvulcanised NR using the dielectric spectrum. She found slower segmental dynamics of the composites with the presence of curing additives. This can be explained by considering the additional interfacial interactions between the curing additives and the polymer chains. Later in 2015, her group studied NR vulcanised by both sulphur and peroxide system using BDS and NMR[128]. A restriction of the segmental dynamics was found in both curing systems. But this effect was much weaker in the peroxide cure. Therefore, using a fully-cured peroxide system may reduce the effect from the introduction of these additives. Desamges[129] also found that the amplitude of κ' increased while κ'' decreased during the cure process of carbon black filled compounds. It can be linked to the increased number of crosslink sites. Therefore, the dielectric technique gives a potential approach that might help characterise the crosslink density of filled compounds.

2.3.3 Dielectric Properties of Carbon Black

As a carbon-based material, carbon black is itself highly conductive along the planes of the aromatic carbon structure. Although the dielectric constant is normally used for dielectric matters, good conductors such as metals and carbon black still have a permittivity that is dominated by the polarisation of electron clouds and the atoms (Section 2.2.1). However, the impedance technique can only be used to study the conductivity rather than the dielectric behaviour of conductive matters. Thus, most of the dielectric studies of carbon blacks are characterised in the microwave range (0.3 GHz-300 GHz) using a vector network analyser (Section 2.2.3). Moreover, in this frequency range, graphitised carbon blacks show a very high dielectric loss value. As a consequence, they have been used in heating applications which has attracted a lot of scientific research[130-132]. Atwater[131] studied the dielectric relaxation of graphitised carbon black with a wide range of surface areas ranging from 10 to 240 $m^2 \cdot g^{-1}$ at a

frequency range between 0.2 and 26 GHz and over a temperature ranging from 296 K to 464 K. The real part of permittivity was found to decrease from around 200 to 20 when the frequency increased from 0.2 to 26 GHz. Whereas, the imaginary part of the permittivity showed a peak at around 2 GHz. Higher temperatures increase the permittivity value (both the real and the imaginary components). However, the temperature dependence of the permittivity is only obvious at lower frequencies and becomes very weak above 10 GHz. The relaxation time was found to be around $5\times10^{-11}s$. Masahiro[130] studied the dielectric relaxation of graphite, carbon black and coal powders in a frequency range between 1 and 10 GHz. The complex permittivity was found to be related to the relative density, the ash content, the crystal size and the specific surface area in his investigation. As shown in Figure 2-25, both the real and imaginary parts exhibit a dependence that is related to the surface area. This was explained to be a consequence of the air-carbon interface polarisation. However, their tests were based on the carbon materials in different format as well as being of a limited purity. This may have caused unexpected uncertainties and therefore to draw definite conclusions a simpler material system might be worth investigating.

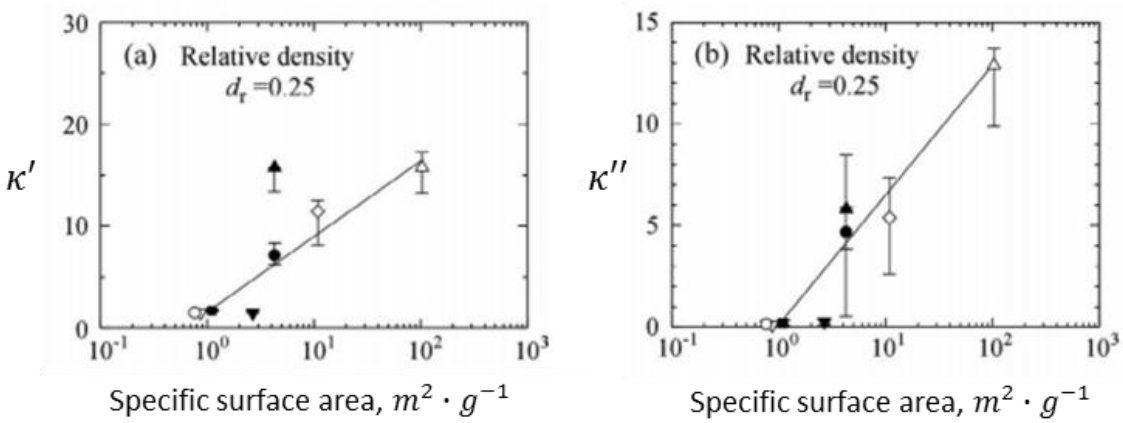

Figure 2-25. The (a) real and (b) imaginary part of the permittivity against the specific surface area. The filled circle and the triangle are graphite. The unfilled diamonds show pure carbon and the unfilled triangle is carbon black. Other symbols are different coal powders. Taken from the literature[130].

2.3.4 The Interface of Nanodielectrics

The Electrical Structure at the Metal-Polymer Interface

The knowledge of the electrical structure of solid interfaces has developed rapidly in recent years due to the importance of organic electroluminescent devices such as organic light-emitting diodes (OLED) and organic photovoltaics (OPV). The exact details of the various mechanisms involved are still not fully understood and investigations about the charge distribution, energy band bending, formation of the surface dipoles and other issues surrounding the use of an organic material are still in their infancy when compared to traditional inorganic materials. Ishii[93] gave a basic but comprehensive introduction of the interface between organic and organic materials as well as those between organic and metal materials in 1999. Since then, a lot of experimental and modelling work has also been proposed[133, 134]. However, most of the works were focused on the interface between metal and pi-conjugated organic materials (conductor and semiconductor) because of the system's efficiency when used in organic electroluminescent applications. The situation for carbon-saturated polymers (conductor and dielectric) has rarely been discussed.

Here the carbon materials have been treated as a conductive "metallic" material. The free electrons on the inner surface of a metal are moveable. They can shift to the outer surface making the vacuum negatively charged whilst the inner surface becomes positively charged. Therefore, this system automatically forms surface dipoles. Figure 2-26(a)[93] shows the electrical structure at the interface between a metal and organic material. When the two phases are in contact with each other, the potential level of both surfaces will merge into a single one which is presented as VL level (the potential well at a specific value for the vacuum) in Figure 2-26. One should be careful that the VL is normally defined as the vacuum level of the infinite distance which is lower than the vacuum level near the metal surface. Here they are not separated except to simplify the model. Moreover, an additional dipole layer will also be formed as a result of the charge transfer across the surface, redistribution of the electron cloud and chemical reactions at the interface[93]. This extra dipole layer creates a shift of VL by Δ magnitude to the right interface as shown in Figure 2-26(a). This process is known as the energy level

alignment. For most cases, the Fermi level is different between metals and organics. Therefore, the state shown in Figure 2-26(a) is electrically unstable as electrons prefer to stay in the phase with a higher work function (the metal phase in this case). Here the work function can be regarded as the energy between the Fermi level and the VL. It is the minimum energy for an electron to escape from the solid to the vacuum. To achieve an equilibrium state, charges will redistribute very quickly and bend the energy band in the organic phase near the interface until the Fermi level of both phases are aligned as shown in Figure 2-26(b). The bending area is known as the diffusion zone which depends on the permittivity of both phases. However, resulting from a lack of experimental data, the exact thickness of this structure for an insulating polymer-metal interface is still unknown. But it has been crudely treated as being of the order of tens of nanometres[67] in the literature. The effects mentioned above are summarised in Figure 2-27. Examples and details can be found in the review work by Ishii[93].

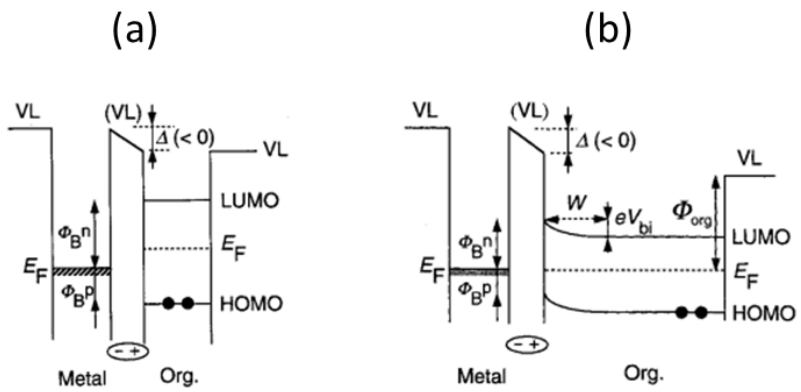

Figure 2-26. The electrical structure of the metal-organic interface. Taken from the literature[93]. (a) Interfacial energy diagram with a shift of vacuum level (VL) of Δ at the interface due to dipole layer formation. E_F is the Fermi level. LUMO is the lowest unoccupied molecular orbital while HOMO is the highest occupied molecular orbital. Φ_B^n and Φ_B^p are the injection barriers for electron and hole respectively. (b) Compared to (a), it shows an interfacial energy diagram with band bending. The energy levels are bent by the charge redistribution in the organic layer to achieve the electrical equilibrium with the alignment of the Fermi levels of the two sides. This leads to the formation of built-in potential V_{bi} within a diffusion layer of thickness W.

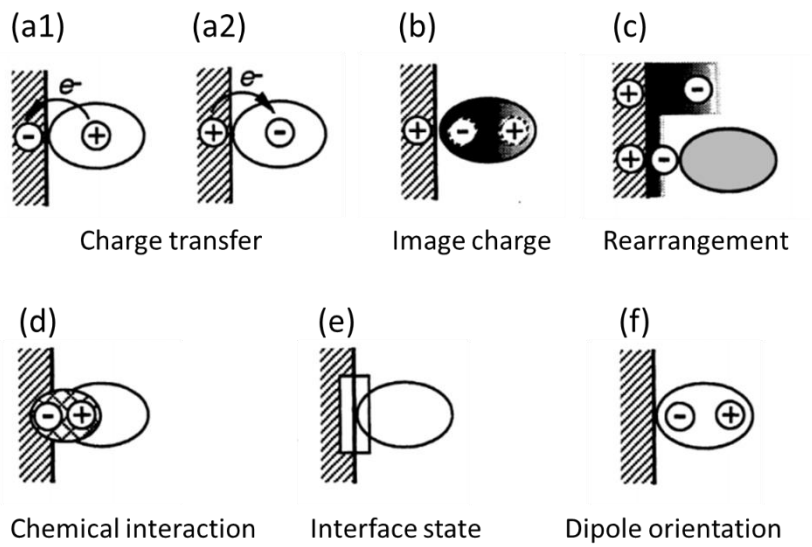

Figure 2-27. The possible factors that form and affect the dipoles around the interface, summarised by Ishii[93]. (a1) & (a2) Charge transfer of the metal surface. (b) The surface charge formed by the process of (a1) or (a2) induces the image charge in the vacuum phase. (c) Rearrangement of the electron cloud on the metal surface. (d) Chemical reactions rearrange the existing bond or form new bonds. (e) The interface may serve as a charge buffer. (f) The orientation effect of permanent dipoles in the organic phase surface.

The work function of different types of carbon blacks (CB) was carefully studied by Fabish[15] in 1984. It was found to be 0-0.46 eV larger than the work function of gold for most carbon blacks. Surface dipoles were also found on the outer surface of carbon blacks just as is the case with normal metals. As NR or polyisoprene is a non-saturated but highly non-conductive polymer, the carbon black-NR interface was classified as a weak type of interaction with an absence of charge transformation by Slawomir[133]. This is based on the studies of the interface between the smallest molecules and the metal[135]. However, the charge transfer in contact electrification was clearly observed with this type of contact[92, 136]. Therefore, in this thesis, the charge transfer effect of such CB/NR interface is considered even though it is much weaker than that in the conductor/ semiconductor type of contact.

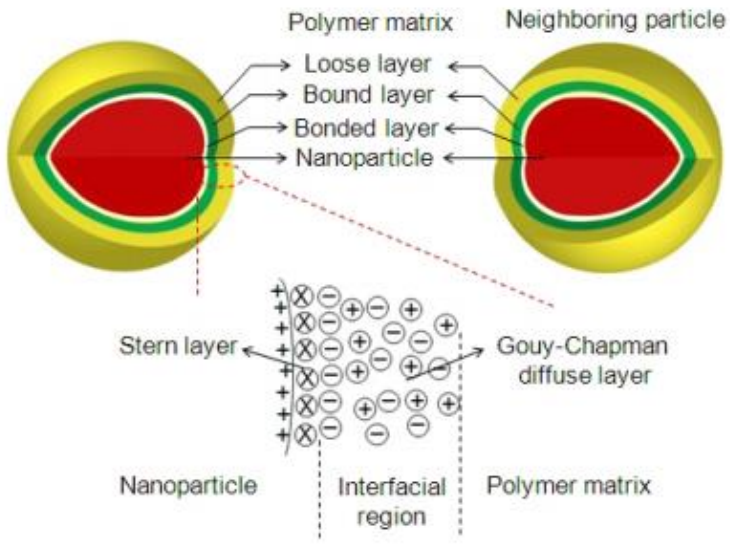

Figure 2-28. The multi-core model of the nanodielectrics and the interface electrical double layer[67, 137].

In electrochemistry, there is a similar interface structure formed between the electrolytes and electrodes where an electrical double layer (Gouy-Chapman layer) is found. A lot of material scientists used this concept to describe the nanocomposite interface (solid-solid interface) such as Lewis[1], Tanaka[67], Dang[137] and Nelson[138]. A typical electrical double layer of a solid-solid system is shown in the lower portion of Figure 2-28. The particle in this model also has surface dipoles that are formed by the shift of the electrons from the inside to the outside of the particle surface. Material that directly attaches to the particle surface is known as the Stern layer while the transition area next to it is known as the Gouy-Chapman layer (band bending area). Therefore, this model actually matches the band theory described above for the case of a solid-solid interface. Further details of this model of an electrical double layer can be found in Chapter 13 of the electrochemical method book by Bard[139] or in Chapter 7 of the supercapacitor book by Conway[140].

Multi-core Model

Based on the electrical structure mentioned in the previous section (page 49), Tanaka[67] proposed his multi-core model for nanodielectrics as shown in Figure 2-28. The polymer

layer that is tightly bonded to the filler surface (by both physical and chemical bonds) forms the bonded layer where it is electrically covered by the Stern layer. It is a transition layer with a very thin thickness of around a nanometre. The second layer is known as the bound layer which is strongly attached to the first layer with a thickness of around several nanometres. The chain movement in this layer is highly restricted (confined). A third layer, known as the loose layer, corresponds to a thicker layer of tens of nanometres which is also loosely connected to the bound layer. Moreover, the electrical Gouy-Chapman layer covers both bound and loose layer.

Polymer Dynamics around the Filler Surface

As predicted by the multi-core model mentioned above, the presence of rigid fillers produces slower dynamics of the polymer chains around the filler surface (the first and the second layer of the multi-core model) which is known as the confinement effect. This confined polymer is often described in the literature as the glassy layer[141]. It is important in understanding the nonlinear viscoelasticity and the filler reinforcement mechanism of the rubber components. Therefore, this topic attracts a lot of attention. Some researchers have produced evidence for this layer by observing a shift or broadening of the bulk Tg using different techniques such as differential scanning calorimetry[95], dynamic mechanical analysis[142], broadband dielectric spectroscopy[95], neutron scattering and Nuclear Magnetic Resonance[141], while the confinement effect has also been widely studied in very thin polymer films which are restricted by rigid substrates, container walls or surroundings[122]. There is even an equivalence between the confinement effects in nanocomposites and the polymer thin films[143]. However, it is still an open debate concerning the existence of such a glassy layer in nanocomposites as various researchers have reported contradictory results whereby the confined dynamics of the polymer at the interface in filled materials cannot be observed. For example, Robertson and Roland have reviewed these disagreements with a wealth of experimental evidence[91] in 2008. More recently Huang et al.[124] addressed this problem specifically with a focus on rubber and silica or carbon black reinforced systems. They suggested that the contradictory evidence reported in the literature may in fact arise from differences in the dispersion state of the nanocomposites. Therefore, the real

confinement effect may be too weak to be observed in relatively poorly dispersed systems (most of the commercial compounds).

Charge Accumulation at the Interface

Maxwell[54] first found that charges will accumulate at the dielectric interface. This pioneering work has been further developed by Wagner[144] for the spherical filler systems and by Sillars[145] for fillers with different shapes. Their theories predict a polarisation process which is known as the interfacial polarisation or the Maxwell-Wagner-Sillars (MWS) polarisation. As most of the literature does not describe the accumulation process in detail, here a brief introduction of this process is given.

Consider a capacitor made from two dielectric materials connected in series as shown in Figure 2-29. When a step potential U is applied to the capacitor, it starts to charge. Because of the consistency of the electrical displacement in each phase:

$$\kappa_1' \cdot E_1 = \kappa_2' \cdot E_2 \qquad \text{Equation 2-43}$$

where E_1 and E_2 are the local field in each phase. κ_1' and κ_2' are the real part of permittivity in each phase. When the capacitor is fully charged and reaches an equilibrium state, the current density $j_{current}$ in each phase is the same:

$$j_{current} = \sigma_1 \cdot E_1 = \sigma_2 \cdot E_2 \qquad \text{Equation 2-44}$$

where σ_1 and σ_2 are the conductivity of each phase. Comparison between Equation 2-43 and Equation 2-44 shows that unless $\frac{\sigma_1}{\sigma_2} = \frac{\kappa_1}{\kappa_2}$ (which is not often the case), then the electric field in each phase is rearranged before the equilibrium state. This creates a time dependence of the current density in both phases where $j_{current1}(t) \neq j_{current2}(t)$. Therefore, the charges accumulate during this process. Thus, the charge density of the interface at the equilibrium state can be written as[43]:

$$\int_0^\infty \left(j_{current1} - j_{current2} \right) dt = \frac{\kappa_0 \left(\sigma_1 \kappa'_2 - \sigma_2 \kappa'_1 \right)}{d_2 \sigma_1 - d_1 \sigma_2} U \qquad \text{Equation 2-45}$$

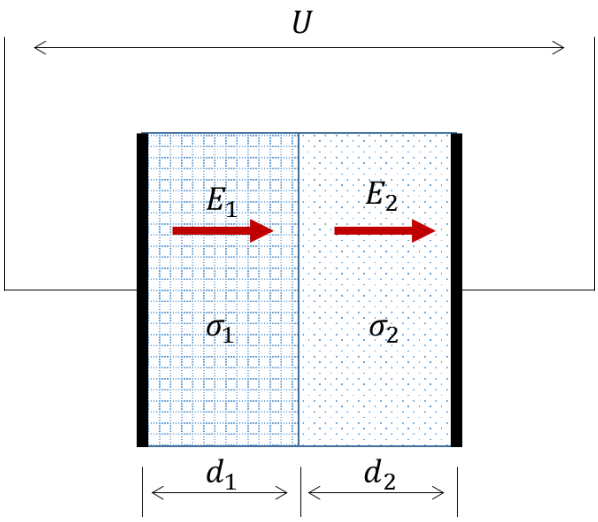

Figure 2-29. The capacitor model of the charge accumulation on the interface. Figure is redrawn from the literature[43].

2.3.5 The Mixing Laws of Inhomogeneous Systems

One of the most important questions for dielectric composites is how to accurately evaluate the effective permittivity of the composite from the permittivity of each phase κ'_q ($q =$ 1 or 2 for composites consisting of two phases). Generally, the simplest mixing law to describe the dielectric properties can be written as[146]:

$$(\kappa')^n = \sum_q \phi_q (\kappa'_q)^n \qquad \text{Equation 2-46}$$

where $-1 \le n \le 1$ and q stands for the qth phase of the composite. ϕ_q is the volume fraction of the qth phase. Note that, this equation can be used to describe other physical properties as well (as an example κ' and κ'_q can be replaced by σ_{dc} and σ_{dcq} for the dc conductivity mixing law). Specific relations can be obtained when $n = \pm 1$. Under such circumstances Equation 2-46 becomes the model for either the series or parallel case and gives the limits of κ' [147]:

$$\frac{1}{\sum_q \varphi_q (\kappa'_q)^{-1}} \le \kappa' \le \sum_q \varphi_q \kappa'_q \qquad \text{Equation 2-47}$$

However, Equation 2-46 can only give a rough indication of the real behaviour and a number of other equations have been proposed in the literature[146-148] where many are based on the effective medium theory. There are many comprehensive reviews on this topic. For example, Beek[148] did a thorough review including many models published before 1967. In 1993, Nan[146] gave a more general and detailed discussion of the relationship between the microstructure and the physical properties. Steeman summarised some of the basic equations with experimental illustrations as a chapter in Kremer's impedance book[39]. More recently, Zhang[147] reviewed some of the most important models. Achour[149] did a comparative study to fit their experimental data based upon carbon black mixed with epoxy resin using various different equations. As the results changed from case to case, it is hard to find a universal law to characterise all the materials.

2.3.6 Percolation Theory

Percolation theory is another effective tool that can help unravel the complex permittivity of nanodielectrics or multiphase components. Originally, it was applied to describe dc conductivity but it has now also been used to examine the dielectric properties.

Percolation Theory in the dc Test

As has been discussed previously, nanodielectrics filled by conductive fillers can transform to nano-conductors when the filler volume fraction is above a certain value which is known as the percolation threshold. This process can be well described using percolation theory[73, 150]. Although the percolation theory is normally used to describe the dc conductivity of composites[151], it is also applicable to describe other properties[73] of the composites, such as the dielectric constant, optical nonlinearity, the glass transition and viscosity, where those properties dramatically change around the percolation threshold.

For dc conductivity, the percolation theory describes a system wherein all the particles or aggregates are filled into the material randomly. And they are assumed to be

unaffected by the position of their neighbouring particles or aggregates. Therefore, a completely random filler network is formed and its conductivity follows the scale law.

$$\sigma_{dc} \propto \sigma_0 \left| \phi - \phi_c^{dc} \right|^{\pm t_{dc}} \qquad \text{Equation 2-48}$$

where σ_{dc} is the dc conductivity, σ_0 is a constant which relates to the conductivity of the filler and polymer. ϕ is the volume fraction of fillers while ϕ_c^{dc} is the dc percolation threshold. t_{dc} is a constant. When $\phi < \phi_c^{dc}$, t_{dc} becomes a negative value, σ_{dc} increases very slowly with an increase of ϕ. This is because there a complete conductive pathway is lacking for the electrons to be transported throughout the material, although the average distance between the particles is getting smaller and smaller. When $\phi \sim \phi_c^{dc}$, σ_{dc} dramatically increases by many orders of magnitude because of the formation of fully connected networks. Note that, although the direct connection paths are ideal for dc conducting, the electrons can also tunnel[152] between neighbouring particles when the separation distance is less than a few nanometres. Simmons[153] gave a relationship between the current density and the tunnel distance. This behaviour has been experimentally observed by Toker[152] using conductance atomic force microscopy. When $\phi > \phi_c^{dc}$ the conductivity is dominated by the conductivity of the filler particle network. The change of σ_{dc} with filler content again becomes quite modest.

An ideal percolating 3D network should have a constant value of $\phi_c \approx 0.28$[154]. However, in reality, this value is normally reduced because the filler networks are made up in practice using fillers with a high structure. In those case, the filler networks are much more complex and the possibility of forming a percolated network is very high. This is also useful when a lower percolation threshold is desired for conductive applications. The percolation behaviour relies on the morphology, distribution and concentration of the fillers as well as the viscosity and molecular weight of the polymer. Medalia[80] and recently Zhang[155] wrote comprehensive reviews of these effects based on carbon black filled composites. Finer particles with high aspect ratios can bring a lower percolation threshold. This is because smaller particles bring a greater surface area (higher surface energy) which means they have more chances to connect to each other and to form a

more complex structure. This process is driven by flocculation[17] during the curing process. This is also the main reason why carbon nanotubes[156, 157] or graphene[158] become promising candidates to produce conductive composites with very low percolation thresholds. An effective dispersion is the key factor required to obtain a low percolation threshold[159]. Therefore, direct electrical measurements are sometimes now used as an alternative method to evaluate the dispersion state of a compound during compounding[157]. For example, it is much easier than examining the Payne effect on the subsequently cured compound.

Percolation in the ac Electrical Test

The percolation theory has also been used to describe the dielectric constant and the ac conductivity of nanodielectrics. Bergman[160] studied both the effective dielectric constant and dc conductivity of the inhomogeneous system which is made up of nonconductive matrix with conductive fillers randomly dispersed inside. He found that the permittivity had a different percolation value when compared to the dc conductivity. Stroud[161] studied a similar system later at a very low frequency and derived the percolation mixing law of permittivity which has similarities with Equation 2-48:

$$\kappa' \propto \kappa'_m \left|\phi - \phi_c^{ac}\right|^{-s} \qquad \text{Equation 2-49}$$

where κ'_m is the dielectric constant and *s* is a fitting parameter[147]. The value of *s* typically varies from 0.7 to 2.0 for different systems[162]. Based on Stroud's work, Equation 2-49 is only valid when the angular frequency is very low (say as $\omega \to 0$ and therefore accordingly $\kappa' \to \kappa_s$). This equation may also work at higher frequencies, but there is insufficient evidence to support this at present. In reality, the percolation threshold of $\phi \sim \kappa'$ plot changes dramatically at different frequencies. For example, Zhang[96] studied Ni/P(VDF-TrFE) composites at different frequencies. He found that the percolation threshold of the composites increased from around 0.55 to 0.65 when the frequency increased from 1 kHz to 1 MHz. Bergman[160] described a frequency dependent κ' when $\phi \to \phi_c^{ac}$:

$$\kappa' \propto \omega^{s'-1} \qquad \text{Equation 2-50}$$

where s' is another fitting parameter with a value of around 0.73 ± 0.05[160]. This relationship may be used to explain the frequency dependent ϕ_c^{ac} . Pötschke[162] considered the frequency carefully in their fitting work and suggested that a frequency below 0.1mHz is ideal. However, in reality such a low frequency test takes a very long time, therefore a frequency normally below 1 Hz can be used instead. Interestingly, Nuzhnyy[163] studied the dc and ac conductivity (see Equation 2-41 in Section 2.2.3) of polycarbonate and multi wall carbon nanotube (MWCNT) composites over a broad frequency range. He found that below 1 Hz, the dc and ac conductivity almost overlapped each other and shared the same percolation threshold while large differences exist between them at the higher frequencies (Figure 2-30).

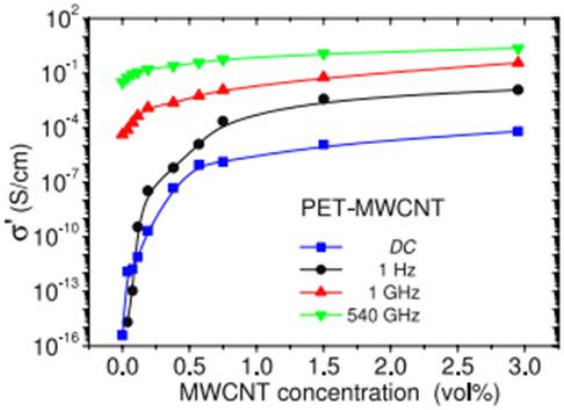

Figure 2-30. The percolation behaviour of dc conductivity as well as ac conductivity measured at different frequencies of PET filled by MWCNT with different volume fractions. Taken from the literature[163].

This is because ac conductivity consists of both a dc term and an ac term:

$$\sigma_{\mathrm{ac}} = \sigma_{\mathrm{dc}} + A\omega^r \qquad \text{Equation 2-51}$$

where σ_{ac} and σ_{dc} are the ac and dc conductivity respectively. *A* and *r* are the fitting parameters while $A\omega^r$ is known as the ac term. From this equation, the ac term becomes very small at low frequencies. As a consequence $\sigma_{ac} \approx \sigma_{dc}$. Moreover, $\omega \sim \sigma_{ac}$ plots normally show plateau areas at low frequencies which refer to the dc conductance σ_{dc} being frequency independent as shown in Figure 2-31(b)[164]. If the material is a

good insulator, the plateau cannot be observed unless the frequency is sufficiently low. At the same time, κ' behaves with a weak frequency dependent behaviour over the same frequency range as shown in Figure 2-31(a). Furthermore, the transition point where the plateau disappears will shift to higher frequencies when the material becomes more conductive. Accordingly, κ' shows a decrease with an increase of frequency. It has been described as a dielectric relaxation process, namely, the Debye type relaxation[165]. However, this process is quite problematical as the dc conductance makes the material a poor dielectric. Therefore, such "relaxation" processes may not be dominated only by the dipole relaxation. It means that the Debye's theory may not be suitable in this situation any more. Unfortunately, there are insufficient experimental results to discuss this problem. Nevertheless, one can still make a rough judgment of the conductivity of the material from the transition point of ac conductivity as shown in Figure 2-31(b).

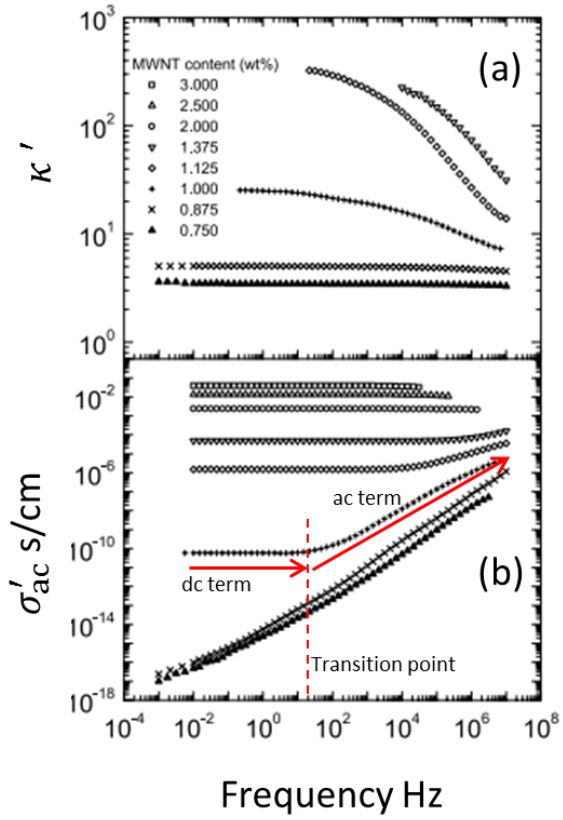

Figure 2-31. The frequency dependent behaviour of (a) the real and imaginary part of permittivity and (b) the real part of the ac conductivity of polycarbonate filled by multiwall carbon nanotubes with different volume fractions. Taken from the literature[164].

The percolation process described by Equation 2-49 has also been widely explained by a random RC (resistor/conductor) network[166] that mentioned in Section 2.2.2. That is, each conductive filler works as a micro-conductor while the polymer matrix between two particles can be treated as a micro-capacitor. The capacitance of the micro-capacitors will increase when the average distance between fillers are decreased by using more fillers. Therefore, the measured permittivity is significantly enhanced near the percolation threshold. The local field applied to the micro capacitors becomes very large and stronger polarisation processes are expected. This mechanism can also be used to explain the reduction of the dielectric breakdown strength as the local fields are normally larger than the externally applied electrical field. It is quite similar to the local strain amplification effect in mechanical testing[167]. The random network has been modelled by Almond[45] in 2-D and Galvao[46] in 3-D. It seems that this model can explain the frequency dependant dielectric behaviour very well.

Finally, although Equation 2-49 and Equation 2-50 can work well to fit the experimental behaviour, there are still some issues when using percolation theory to describe the dielectric behaviour. Firstly, the permittivity of a composite is mainly contributed to by the dipoles around the interface which are completely different when compared to the dc conductivity. Therefore, the percolation theory can hardly explain the dependence on frequency and temperature of the observed behaviour. Secondly, the permittivity obtained from the impedance test is affected by the conductivity of materials. That is, the conductivity can also contribute to the dielectric losses and the permittivity (Section 2.2.3). Around the percolation threshold, the material itself transforms from dielectric to either a semiconductor or even a conductor[73, 162-164]. In this situation there is a high conductivity and an equivalent high loss, therefore permittivity loses its original physical meaning (as it is no longer primarily related to the amount of polarisation). Hence the percolation behaviour of permittivity is merely a kind of “dc percolation”. This complexity can of course be ignored for the non-conductive fillers such as SiO_2 or the core-shell fillers that where mentioned in Section 2.3.1 as they have limited loss values (conductivity). The complexity can also be ignored during microwave testing as it is not based on the impedance theory at all.

2.3.7 The Strain Dependent Dielectric Behaviour of Elastomers.

As mentioned in Section 2.3.1, the dielectric spectrum of deformed elastomers is a powerful tool but it has rarely been systematically studied. Back to 1950s, F.H. Müller and K. Huff[100] studied the strain dependent dielectric loss spectrum of vulcanised natural rubber. They carried out this study because they realised that the mechanical strain can orientate the polymer chains, which may bring a different dielectric response. Moreover, researchers at that time had already realised that dielectric spectrum had parallel properties to the mechanical spectrum (Figure 2-23). Therefore, understanding the strained dielectric spectrum can help clear the non-linear mechanical properties of elastomers. As shown in Figure 2-32, both the position and the shape of the dielectric loss peaks are modified by applying mechanical strain. Müller and Huff attributed it to the strain induced orientation effect. However, they did not realise that this could also be explained by the strain induced crystallisation effect. Moreover, they could not explain their data in greater detail because of the dielectric research of polymer materials was not well developed at that time.

Later on, it has been gradually understood that mechanical strains can not only force the polymer chains to align, ultimately in some stereo regular systems this might allow crystal structures to be formed more easily and this in turn gives more structured and densely packed regions. This so-called strain induced crystallisation is very important for some elastomers such as natural rubber as it can dramatically increase their mechanical strength. Therefore, it has been widely studied in details, normally, using on-line X-ray technology[168]. However, this technique is complex to perform and the data measured is not easy to interpret. Moreover, powerful sources such as those found a synchrotron sites are only available at a limited number of laboratories around the world. Compared to this technique, the dielectric spectrum has been shown to be sensitive enough to detect strain induced crystallisation. This is because the dipoles in the crystal region are confined by their neighbours. Thus, the dielectric segmental relaxation mode is slowed down in the crystalline regions.

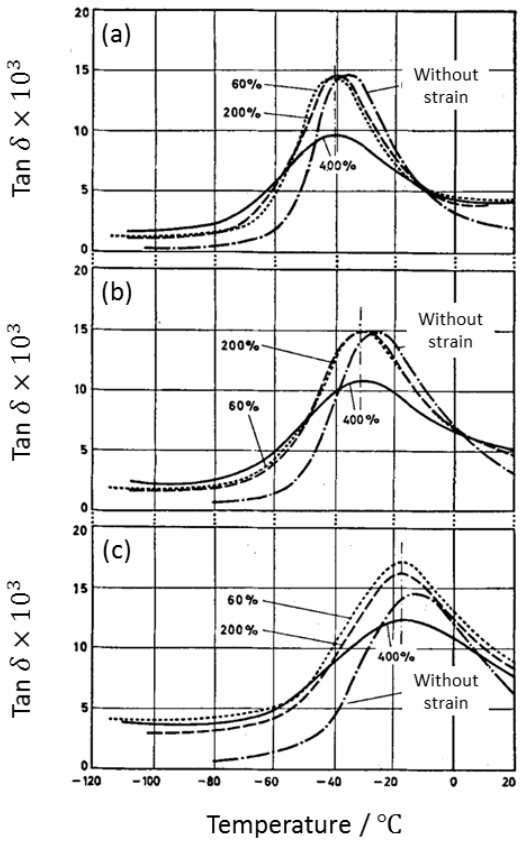

Figure 2-32. The strain dependent of dielectric loss of vulcanised unfilled natural rubber at different mechanical strain. (a), (b) and (c) were measured at 1 kHz, 10 kHz and 100 kHz respectively. Taken from the literature[100].

In 2011 and 2013, M. Hernández et al.[70, 169] characterised the dielectric loss spectrum of both unfilled and filled natural rubber to study the strain induced crystallisation behaviour of those materials. They decomposed the imaginary part of permittivity verses frequency graphs to obtain the positions of the segmental relaxation peaks (the relaxation time). It is very interesting that, for unfilled natural rubber, there is not a systematic decrease of the relaxation time with an increase in strain as predicted whilst it appears for filled natural rubber as shown in Figure 2-33. Moreover, they detected an increase of the dielectric strength before the strain induced crystallisation process whilst it only decreased a little during the crystallisation[169]. As shown in Figure 2-34, their dielectric results also coincided with the X-ray data collected in situ. Similarly, T. Choi et al.[170] used similar technique to study elastic polyurea and they also found slower broadened segmental dynamics once the material was strained. This kind of slowdown

of the segmental dynamics can be observed for not only stretched, but also rubber materials under high pressure. For example, P. Ortiz-Serna et al.[171] found a systematically decrease of the segmental dynamics of natural rubber with an increase of pressure from 0.1 MPa up to more than 200 MPa.

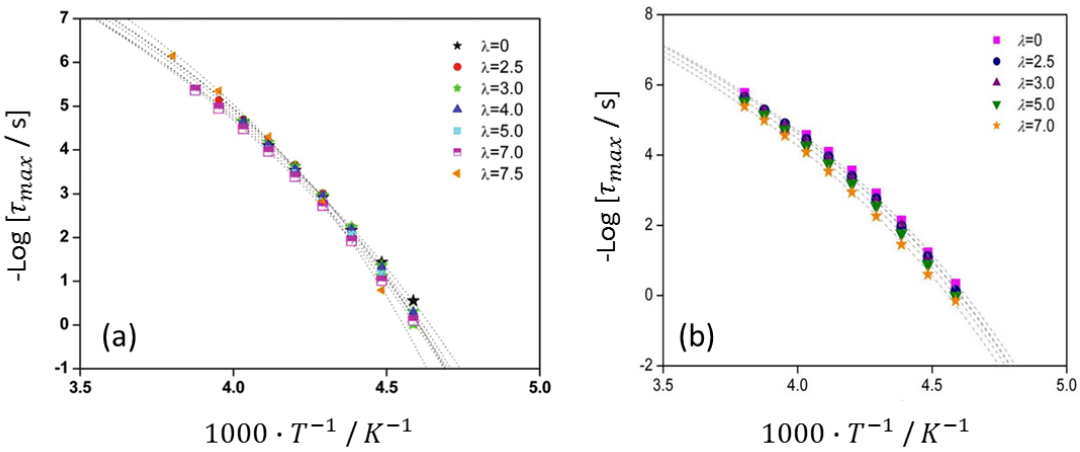

Figure 2-33. The segmental relaxation times of (a) unfilled natural rubber and (b) layered silicate filled natural rubber that measured at different temperature and at different strain. Taken from the literatures[70, 169].

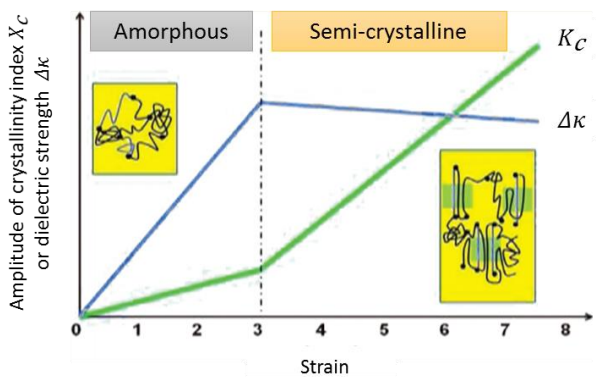

Figure 2-34. The strain induced crystallisation of natural rubber characterised by both X-ray and dielectric technologies. X_c is the crystallinity index and $\Delta\varepsilon$ is the dielectric strength. Taken from the literature[169].

However, for the investigations mentioned above, their dielectric data was not simultaneously measured under strain. It means that the materials were initially stretched to a certain strain and then their dielectric properties were measured. A

typical set-up of this kind of test is shown in Figure 2-35 (a). In these cases, the relaxation of the polymer chains has not been considered. In addition, the real part of permittivity has not been presented either, which made their results look incomplete. C. Brosseau and P. Talbot designed their experiments as shown in Figure 2-35 (b). Although they claimed it to be an in-situ dielectric/mechanical measurement, the dielectric property was still not simultaneously measured during tension. Moreover, their technique is based on microwave measurement, which covers a test frequency range from 0.1 GHz to 1GHz. With this technique, they reported a reduction of both the real and imaginary permittivity of carbon black filled rubber (SBR) with strain. This was attributed to the change of the filler networks under strain. This phenomenon is also stronger in lower frequency range, which suggests the interface polarisation may play an important role[103].

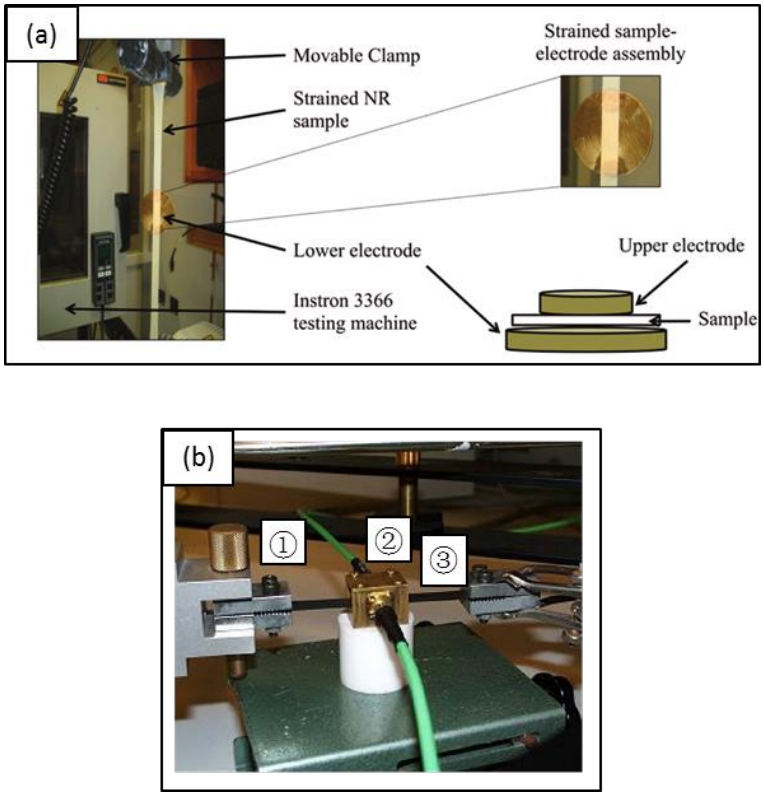

Figure 2-35. (a) The experimental set-ups to measure the dielectric properties of rubber materials under strain that designed by M. Hernández et al.[169] and C. Brosseau et al.[172]

Beside elastomers, other polymers or composites can also exhibit strain dependent behaviour. For example, Bowler[173] found that higher crystallinity brings a lower

permittivity of strained PTFE at fixed frequencies. Z. Dang [103] also reported the decrease in the permittivity of carbon nanotube/PVDF composites after straining and subsequent relaxation. However, their material becomes conductive with an increase of the filler volume fraction, which makes them not real nanodielectrics but more typically conductors or semiconductors.

Although those composites mentioned above exhibit strain dependent dielectric behaviour, it has to be clear that, for unfilled elastomers (or other type of polymers such as PTFE), the change of complex permittivity should be very small when a small strain lower than the threshold for strain induced crystallisation or any strong orientation effects is applied. For example, G. Kofod et al[174] only observed around 1% decrease of the real part of permittivity (0.1 Hz-100 Hz) for a commercial polyacrylate elastomer VHB4910 (made by 3M) when 100% bi-axial strain was applied. Moreover, the impedance based dielectric measurement is highly dependent upon the quality of electrode and the accuracy of the thickness measurement. Therefore, those small changes may also be caused by the measurement error. On another point, Figure 2-32 shows a shift of dielectric loss peak at just 60% strain which is too low a strain to produce any strain induced crystallisation of the NR. It is thought likely that the shift of the amplitude of dielectric loss factor may come from the sample preparation as well as errors in the measurement.

2.4 Summary

This review gives a basic understanding of the mechanical and dielectric behaviour of a special type of nanodielectrics: rubber composites (also known as nanodielectric elastomers). The mechanical properties are important for the vast majority of rubber products. However, it is impossible to fully understand their behaviour particularly under strain by considering the mechanical spectrum alone. That is why people have started to consider dielectric spectroscopy for its broad range, sensitivity and for its ability to probe the detailed nature of the various different relaxation processes of these materials.

Although there are several different theories available to explain the microstructure-dielectric relationship of elastomer composites, most considered only the effect of the frequency and the temperature. This is unsurprising as time and temperature are the key issues when considering the relaxation time not only for the mechanical but also dielectric behaviour. However, the nonlinearity of the mechanical properties under the application of strain suggests that the existing dielectric theories (although they are not yet fully understood) should be examined in some detail for strained materials. Can strain be used as the third variable to study the microstructure-dielectric relationship in dielectric spectroscopy? This is very difficult for traditional dielectrics as most of them (ceramics) are rigid, but it is very convenient and important for nanodielectric elastomers as they serve in a deformed condition for most applications. To explore the dielectric properties in a strained condition, several questions need to be studied: 1. How can the filler reinforcement of the dielectric properties be explained? 2. What is the structure of the filler interface, from the electrical point of view? 3. What can the strained dielectric spectrum tell us about the changes to the microstructure of these composites under the application of a strain?

This review has attempted to examine what is already known about the first two questions. However, there are virtually little references relating to the third question and therefore there are only similar phenomena have been highlighted in the literature. It is clear that there is an urgent need to develop methods that can allow the simultaneous observation of the dielectric and mechanical specimens and this is the major topic that is tackled in the remainder of this thesis.

3 Chapter Three: Broadband Dielectric Spectroscopy of Natural Rubber and Carbon Black Composites

3.1 Introduction

The dielectric method can be utilised over a wide frequency domain that can extend over more than 15 orders of magnitude from mHz to THz ($10^{-3} \sim 10^{12}$ Hz). However, for nanodielectrics containing conductive fillers, most of the previous studies have adopted the dielectric/impedance technique to study the 'dielectric' percolation behaviour of the nanodielectrics below 1 MHz. Here quotation marks are used to imply that the test has typically been used to measure materials that behave more like a conductor than a dielectric as the filler volume fraction is increased as is discussed in detail in the previous chapter. This is because it is convenient to use the impedance method below 1 MHz in combination with simultaneously modifying other variables such as the temperature. In order to cover the whole broadband spectrum (of say 15 orders magnitude of frequency), it is necessary to adopt a range of different testing techniques (Section 2.2.3). Some of the techniques such as quasi-optics that can operate in the THz range are still in their infancy and the facilities are still quite expensive to acquire. Therefore, only a few limited investigations have been undertaken using the entire broadband spectrum. Based on the author's knowledge, no reports have examined the broadband spectrum of natural rubber and carbon black (NR/CB) composite systems.

To obtain a broadband dielectric spectrum for NR/carbon black nanodielectrics is therefore a pressing requirement in the field. Firstly, the spectrum can be used to investigate a wide range of different relaxation processes of the material in comparison to a single frequency impedance test that can only give a limited subset of this information. Secondly, there are a number of applications used in microwave technologies such as wave absorption and electromagnetic shielding[175] where the dielectric behaviour would be important over a wide range of frequencies. Thirdly, the existing approaches that are adopted to fit the experimental behaviour normally ignore the effect of changing the frequency of the test. For practical purposes it is important to

show how to fit the experimental data and how to use it to understand the microstructural properties of the composite system.

The main aim of this chapter is to measure the broadband frequency domain dielectric spectrum of NR/CB nanodielectric elastomers and use existing Havriliak-Negami (HN) functions (page 27) and percolation theory approaches to evaluate the results. The impedance and RF tests were done by the author at Xi'an Jiaotong University in collaboration with Dr. Jian Zhuang and Prof. Wei Ren. The microwave tests were again carried out by the author at Xidian University with the help of Dr. Gang Zhao and Prof. Jiaming Tang.

3.2 Experiments

3.2.1 Materials

The NR/CB masterbatch was provided by Cabot Corporation, MA, USA. The compounds were milled using a two roll mill prior to moulding to blend the carbon black-containing master batch into unfilled natural rubber, SMR CV(60) (TARRC, UK) to create a range of filler volume fractions. Then the cure ingredients of 2 phr (per hundred grams of rubber) dicumyl peroxide (Sigma Aldrich, UK) were also introduced using the mill. Two types of carbon black filled masterbatch were supplied one containing N134 the other N330.The nitrogen specific surface areas of N134 and N330 are 134 and 77 m^2/g respectively[17]. All of the materials were mixed by a two-roll mill for around 20 minutes and, post milling they were cured at 433 K for 1 hour. This optimum curing condition was determined using an Alpha 2000 rheometer. Fifteen different samples were used in this study as identified in Table 3-1.

Table 3-1. List of the different materials samples used in this chapter. (phr: per hundred grams of rubber)

Sample Code	Filler Type	Filler Concentration [phr]	Filler Volume Fraction
NR/0	/	0	0
N134/0.025	N134	5	0.025
N134/0.049		10	0.049
N134/0.071		15	0.071
N134/0.093		20	0.093
N134/0.13		30	0.133
N134/0.17		40	0.170
N134/0.20		50	0.204
N330/0.025	N330	5	0.025
N330/0.049		10	0.049
N330/0.071		15	0.071
N330/0.093		20	0.093
N330/0.13		30	0.133
N330/0.170		40	0.170
N330/0.20		50	0.204

3.2.2 Impedance test: 0.1 Hz - 1 MHz

Impedance tests were carried out from 0.1 Hz to 1 MHz using a Novocontrol Concept 40 Dielectric Spectrometer at room temperature. Specimen dimensions were 25 mm x 25 mm x 0.7 mm and the surface of each sample was coated by gold using vacuum deposition in order to ensure a good contact with the fixed electrodes (the thickness of gold was around 100 nm). The diameter of the overlapping gold layers was 22 mm allowing the impedance of the specimen sandwiched between the electrodes to be measured.

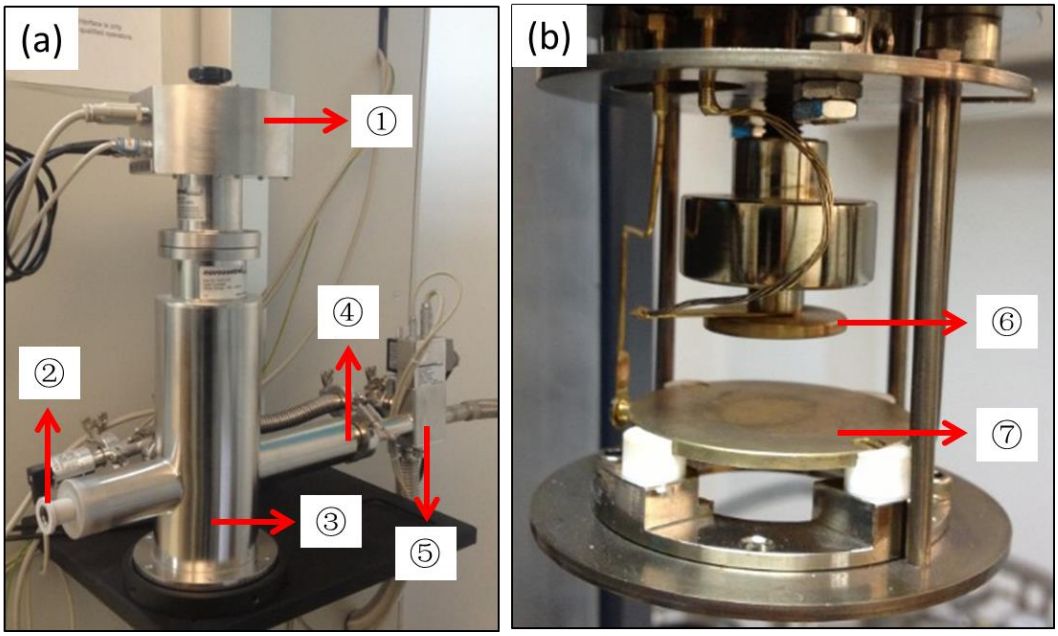

Figure 3-1. (a) The temperature controlling system and (b) the sample stage of Novocontrol Concept 40 Dielectric Spectrometer. The symbols refer to: 1. The sample stage; 2. Nitrogen out; 3. The temperature controller chamber; 4. Nitrogen in; 5. Temperature controller; 6. Upper electrode; 7. Bottom electrode.

3.2.3 RF Impedance test: 100 MHz-1 GHz

An Agilent 4291B RF Impedance Analyser was used to measure the complex permittivity between 100 MHz and 1 GHz at room temperature of all the samples. The test specimens all had dimensions of around 30 mm x 20 mm x 0.7 mm. The equipment was calibrated using a standard PTFE block. All the samples were directly clamped using a standard Agilent 16453A test fixture where a minimum constant clamping force was used.

3.2.4 Microwave test: 7-40 GHz

Microwave characterisation was used to measure the complex permittivity of all the samples at six frequencies: 7, 9, 11, 25, 30 and 40 GHz at room temperature. The transmission/reflection parameters were obtained using a Wiltron 37269A Network Analyser. For this technique, the sample size varied depending upon the size of the wave guide used. For 7, 9 and 11 GHz the sample dimensions were 22.86 mm × 10.16 mm ×

0.7 mm and 7.11 mm × 3.56 mm × 0.7 mm was used for the remaining frequencies. The theoretical background for analysing the measured data can be found from the literature[176].

3.3 Theory

3.3.1 Dielectric Relaxation Process

Dielectric relaxations come from the lag of the dipoles on different length scales. Dielectric relaxations can be fitted by the HN equation which is shown in Table 2-3 in Chapter 2. It considers the relaxation as a Debye-type relaxation with a single relaxation time but with two shape parameters. For the material containing multiple relaxation processes (say n in total), the permittivity can be expressed as the linear combination of different HN functions:

$$\kappa^* = \sum_{j=1}^{n} \left\{ \kappa_{\infty j} + \frac{\Delta\kappa_j}{\left[1+\left(i\omega\tau_j\right)^{\alpha_j}\right]^{\beta_j}} \right\} \qquad \text{Equation 3-1}$$

where j stands for the jth relaxation process. α and β are the shape parameters which have a value between 0 and 1. Note that they are only empirically introduced for a better fitting. The physical meaning behind of these parameters is yet not clearly understood. τ is the relaxation time and $\Delta\kappa = \kappa_s - \kappa_\infty$ is the dielectric strength. Equation 3-1 can be separated into real and imaginary parts:

$$\kappa' = \sum_{j=1}^{n} \left[\kappa_{\infty j} + \Delta\kappa_j \cdot A_j^{-\beta_j/2} \cdot \cos\left(\beta_j B_j\right) \right] \qquad \text{Equation 3-2}$$

$$\kappa'' = \sum_{j=1}^{n} \left[\Delta\kappa_j \cdot A_j^{-\beta_j/2} \cdot \sin\left(\beta_j B_j\right) \right] \qquad \text{Equation 3-3}$$

where

$$A_j = 1 + \left(\omega\tau_j\right)^{2\alpha_j} + 2\left(\omega\tau_j\right)^{\alpha_j} \cdot \cos\left(\frac{\pi\alpha_j}{2}\right) \qquad \text{Equation 3-4}$$

$$B_j = \arctan\left[\frac{(\omega\tau_j)^{\alpha_j}\cdot\sin\left(\frac{\pi\alpha_j}{2}\right)}{1+(\omega\tau_j)^{\alpha_j}\cdot\cos\left(\frac{\pi\alpha_j}{2}\right)}\right] \qquad \text{Equation 3-5}$$

Especially for materials which have considerable conductivity an additional conducting term is needed for the imaginary part of the permittivity. Therefore, Equation 3-3 can be rewritten as:

$$\kappa'' = \sum_{j=1}^{n}\left[\Delta\kappa_j\cdot A_j^{-\beta_j/2}\cdot\sin\left(\beta_j B_j\right)\right] + \frac{\sigma_{dc}}{\kappa_{vac}\omega^t} \qquad \text{Equation 3-6}$$

Where *t* is the fitting parameter and it is equal to 1 for Ohm-type conductivity. For some cases, an extra THz oscillator term can be added into Equation 3-1[163] when considering a situation at the frequency of THz. However, as the frequency limit here is 40 GHz, it was not considered on this occasion.

3.3.2 Classifying the Dipoles of Nanodielectrics

The bulk dielectric constant of any material is composed of contributions from a range of different dipoles of varying length and time scales. As shown in Section 3.3.1, those different dipoles can be separated by their length scales. However, for nanodielectrics, it is more convenient to group different dipoles apart according to their locations and origins (similar to the multi-core model shown in Section 2.3.4). Here all kinds of dipoles of nanodielectrics are classified into five types. Firstly, polarisation of polymer chains results in dipoles which can be classified by the dipole orientation[106]. For example, A-type dipoles, which are aligned parallel to the main chain, reveal the global motion of the whole chain. At smaller length and shorter time scales, dipoles aligned perpendicular to the main chain reflect the chain segmental motions underpinning the polymer glass transition, and are called B-type. Secondly, it has been proposed that the polymer in close proximity to the filler surface may exhibit a gradient of slower dynamics compared with that of the bulk, unfilled polymer[143]. Such interphase material has been reported to have raised glass transition temperature (T_g) to such an extent that 'glassy layers' of several nanometres thick surrounding filler particles have been claimed to dominate the

bulk mechanical and dielectric properties of filled rubbers[95, 177, 178]. Therefore, the dipoles in such interphase polymer may behave differently in comparison to the bulk matrix. However, there is an active debate as to the existence of 'glassy layers' and their applicability to commercial materials. Such interphase polymer is found to be highly dependent on the filler size and dispersion which clearly varies from case to case[91, 95, 124]. Thirdly, charge transfer between filler-polymer interfaces can generate surface dipoles and form an electrical double layer[1, 93, 139]. This charge transfer or charge distribution may arise from the differences in the degree of alignment of Fermi levels of the components and is highly dependent upon the type of contact[93]. Moreover this behaviour becomes rather complex as recently it has been shown to also depend on mechanical strain[92]. Fourthly, charges (space charges) will gather on the interface when the current density varies from one phase to another phase. This is known as interfacial polarisation or Maxwell-Wagner-Sillars (MWS) polarisation[54, 144, 145]. It is dominant at low electrical frequencies (f) and becomes weaker with increasing f. Finally, dipoles located inside the fillers themselves can contribute to the measured dielectric constant. For clarity, each of the dipoles mentioned above is assigned using the following names: BULK-dipole, GLASSY-dipole, CHARGE-dipole, MWS-dipole, and FILLER-dipole respectively.

3.3.3 Percolation Theory

Equation 2-49 in Chapter 2 shows a general percolation fitting function of permittivity. Consider the case when $\phi = 0$, a standardised equation can be written as:

$$\kappa' = \kappa'_m \left| \frac{\phi_c^{ac}}{\phi_c^{ac} - \phi} \right|^s \qquad \text{Equation 3-7}$$

This equation predicts an increase of κ' before the percolation threshold and a decrease above the percolation threshold. As dielectric measurements above the percolation are affected by the conductivity of NR/CB systems, the data when $\phi < \phi_c^{ac}$ will be used for fitting. In this case, the absolute symbol in Equation 3-7 can be ignored. For a reasonable fitting of the results, κ'_m should be fixed at the value of unfilled NR

and *s* can also be fixed between 0 and 5 which covers the value quoted most regularly from the literature[162].

3.4 Results and Discussion

3.4.1 The Broadband Dielectric Spectrum

Figure 3-2 shows the frequency-dependent dielectric behaviour of natural rubber filled by carbon black N134 or N330. Although these graphs are built from a combination of different testing techniques, they appear to show a good level of continuity between the various test frequency regimes. In Figure 3-2(a), κ' increases with an increase in the filler volume fraction ϕ except for the highest filler volume fractions for N134/0.17 and N134/0.20. This can be explained by Equation 3-7 where κ' decreases with an increase of ϕ when above the percolation threshold. At higher frequencies when $f > 1$ MHz, they follow an increasing trend again together with other samples. The random drop of κ' for N134/0.13, N134/0.17 and N134/0.20 arose from the limit of the testing equipment as the dielectric loss, $D = \kappa'' / \kappa'$, in these cases is very high. Just as has been the case previously in the literature[163] these data points can be ignored due to this error. Here the value of κ' is fixed in this region as a constant of the plateau value at low frequencies. The enhancement of κ' by carbon blacks can be referred to as dielectric reinforcement. This reinforcement is very strong at low frequencies such as $f < 1$ MHz while it becomes weaker and weaker with an increase in the frequency. It is primarily a response to the MWS-dipoles induced by MWS interface polarisation which is strongest at the lower frequencies.

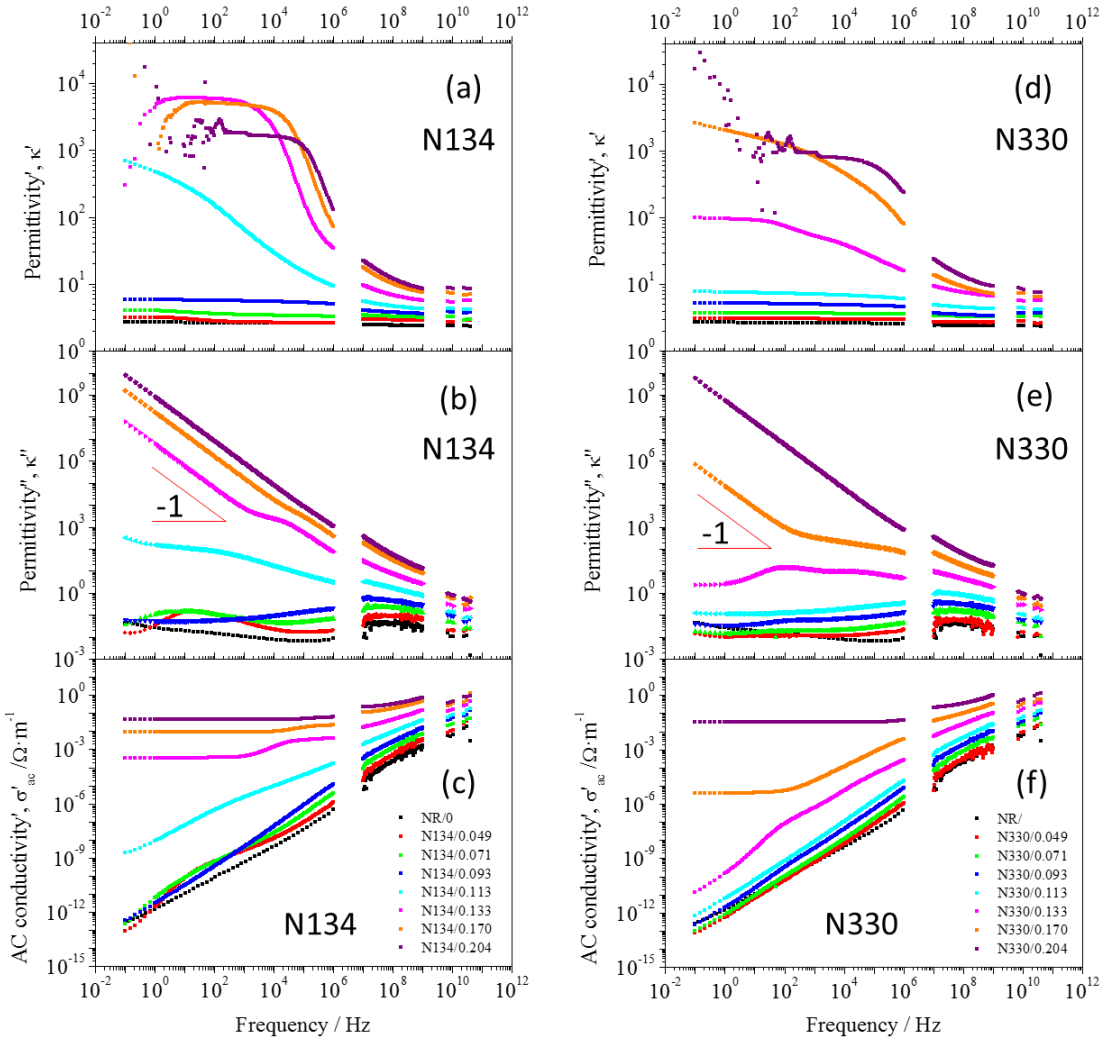

Figure 3-2. The frequency dependent dielectric behaviour of carbon black N134 (a, b & c) and N330 (d, e & f) filled natural rubber presented by the real and imaginary part of permittivity as well as the real part of the ac conductivity. Symbols shown in (c) and (f) are the same for the rest of the graphs.

As shown in Figure 3-2(b), the imaginary part of the permittivity, κ'', is also increased with an increase in the filler concentration over most of the frequencies. The κ'' increased nearly nine orders of magnitude as the filler volume fraction, ϕ was increased. In these cases, the dielectric loss D was very high, which suggests that materials in this condition behave more like semi-conductors or even conductors. Moreover, the increase of κ'' follows a slope of -1 which confirms a dc-type of conductance[39]. This meets the prediction from Equation 3-6 (exactly in the case that t=1). For some cases, the MWS-dipoles are separated as they are caused by the accumulated charges rather

than the dipoles introduced in Section 2.2.1 which follow the Debye type relaxation. Therefore, Equation 3-6 can actually be expressed as:

$$\kappa'' = \kappa''_{MWS} + \kappa''_{rest-dipoles} + \kappa''_{\mathrm{dc}} \qquad \text{Equation 3-8}$$

where κ''_{MWS}, $\kappa''_{rest-dipoles}$ and κ''_{dc} stands for the contribution from MWS-dipoles, the other four kinds of dipoles and the dc conductance respectively. This can be further confirmed from Figure 3-2(c) where the dc plateau is larger for the more highly filled samples. Therefore κ'' is dominated by κ''_{dc} for highly filled samples (below 1 GHz). For other samples with lower filler volume fractions (ϕ), κ'' mainly arises from κ''_{MWS} and $\kappa''_{rest-dipoles}$.

For highly filled samples, κ' also has a step decrease (Figure 3-2 a) which is similar to that described by the Debye equation although is lacking a corresponding peak in κ''. By considering the frequency domain process in Figure 3-2(a) and Figure 3-2(b) as a Debye-type relaxation, the data can be fitted using Equation 3-2 and Equation 3-6. However, although single fitting of κ' is possible as shown in Figure 3-3, it is hard to simultaneously satisfy both functions. It suggests that the Debye type fitting may not work for this system. This may result from a difficulty in making these measurements. On the other hand, the absolute value of κ' is very high which is partially due to the increase of dielectric lose. That is, such colossal κ' values and concurrent frequency dependent behaviour can no longer be explained only by the Debye relaxation process of the dipoles. However, this misunderstanding of such 'dielectric' phenomena existed since 1980s. In 1982, Kawamoto[179] observed a dramatically decrease of permittivity' around 100 Hz of his carbon black (CB) filled rubbers which he treated as a relaxation. He explained this relaxation as RC resonance where the gaps between fillers can be treated as a resistor in parallel with a capacitor. Followed this idea, Ouyang[180] and Geberth[181] used Equation 3-1 to fit $\kappa' \sim f$ graph and obtained a so called relation time. Moreover, they applied tunnel conducting mechanism into Kawamoto's RC model and obtained an average distance between filler particles. More recently, Nuzhnyy[163] simultaneously fitted both κ' and κ'' of MWCNT/PC composites. Although κ' fitted their results very well, κ'' was less well fitted. They had to adopt multiple relaxation

processes to balance their fitting (even with 3 Cole-Cole functions and 14 different fitting parameters). Moreover, they did not give a physical explanation as to why so many Cole-Cole functions were needed or what kind of dipoles were behind those Cole-Cole functions. Note that, although single κ' fitting is not reliable, the single fitting of κ'' has been widely accepted[39] as it shows different peaks related to different relaxation processes.

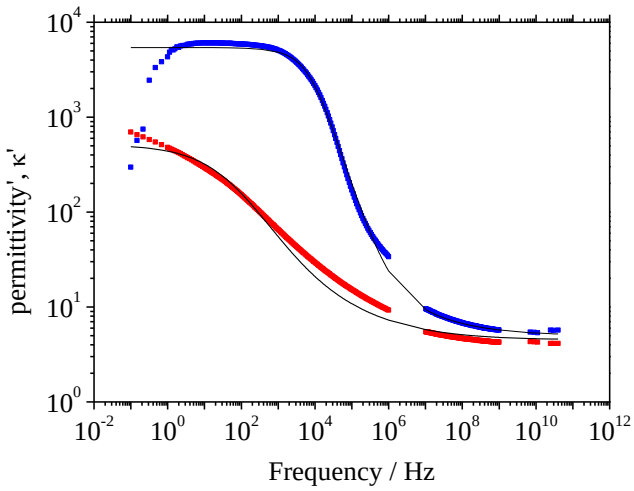

Figure 3-3. Fitting the real part of the permittivity of N134/0.13 (red dots) and N134/0.17 (blue dots) using Equation 3-2 where $j = 1$ (adopting a single relaxation process).

Figure 3-2(d) shows the $f \sim \kappa'$ graph of N330 filled NR. It behaved very similarly to NR/N134 but the dielectric reinforcement of N330 appeared weaker than that for N134. This may because N330 has a lower surface area when compared to N134. Therefore the MWS polarisation of NR/N330 compound was weaker. As κ' is dominated by the frequency dependent MWS interface polarisation, the difference of κ' between NR/N134 and NR/N330 should be smaller at lower filler volume fractions and at higher frequencies. As shown in Figure 3-4, there was almost no difference between that data measured at 40 GHz, which means the MWS polarisation donates little to the measured κ' at this frequency. Moreover, the dc percolation threshold for the N330 filled composites was higher than that for N134[17]. In other words, NR/N330 was less conductive than NR/N134 at equivalent values of ϕ. Therefore, NR/N330 should

normally have a lower κ'' and σ'_{ac} value when compared to NR/N134 at equivalent values of ϕ as shown in Figure 3-2(e) and Figure 3-2(f).

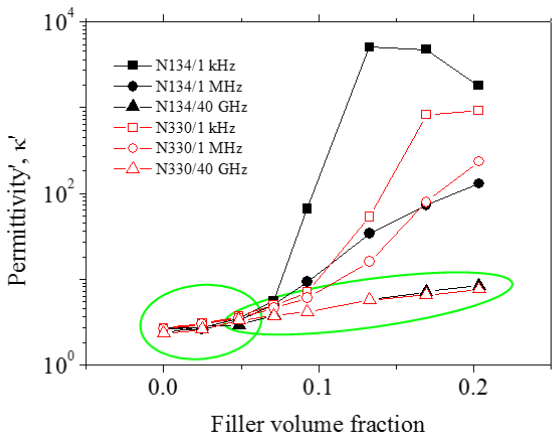

Figure 3-4. Comparison of the real part of permittivity between NR/N134 and NR/N330 at three different frequencies.

3.4.2 Explanation of the Dielectric Behaviour using the Percolation Theory

Figure 3-5(a) shows the $\phi \sim \kappa'$ graph for NR/N134 measured at different frequencies. Only the data measured below 100 kHz had a typical percolation behaviour (Equation 3-7). When ϕ was smaller than around 0.08, κ' was almost frequency independent and data measured at different frequencies almost overlap each other. It means that, in this region, the increase in κ' with filler volume fraction is caused by the introduction of an increased number of dipoles that is not sensitive to this frequency range. When ϕ was above 0.08, κ' therefore showed a very strong frequency dependence. This is because the reinforcement at this region is mainly caused by the MWS interface polarisation. Therefore, the percolation behaviour of κ' can be treated as an interface percolation process. That is why Equation 3-7 was suggested to only be used at low frequencies (Section 2.3.6). Further the percolation threshold of κ' refers to a certain point where the MWS polarisation exhibits a dramatic increase which is different to the dc percolation behaviour. This can be further explained by the electrical structure of the interface. When the filler volume fraction is low, the average particle distance is large, so the electron diffusion zones around each interface are separated from each other. The accumulated charges can only vibrate to a limited distance under an ac electrical

field which creates only a limited amount of polarisation. However, with the increase of ϕ, these diffusion zones can start to overlap one another, which enables the charges to move over a greater distance[63]. Therefore a much stronger polarisation is formed. Following this proposition, the ac percolation threshold ϕ_c^{ac} can be regarded as being the filler volume fraction at which the diffusion zones start to connect to each other. If the thickness of the diffusion zones were larger than the electron tunnelling distances, then the ac percolation threshold would be lower than the dc percolation threshold: $\phi_c^{ac} < \phi_c^{dc}$. However, when it is smaller than the electron tunnelling distance, the ac percolation process is not observed as it is covered by the dc percolation process first (as the electrons can tunnel through the barriers rather than vibrate across them in the diffusion zone).

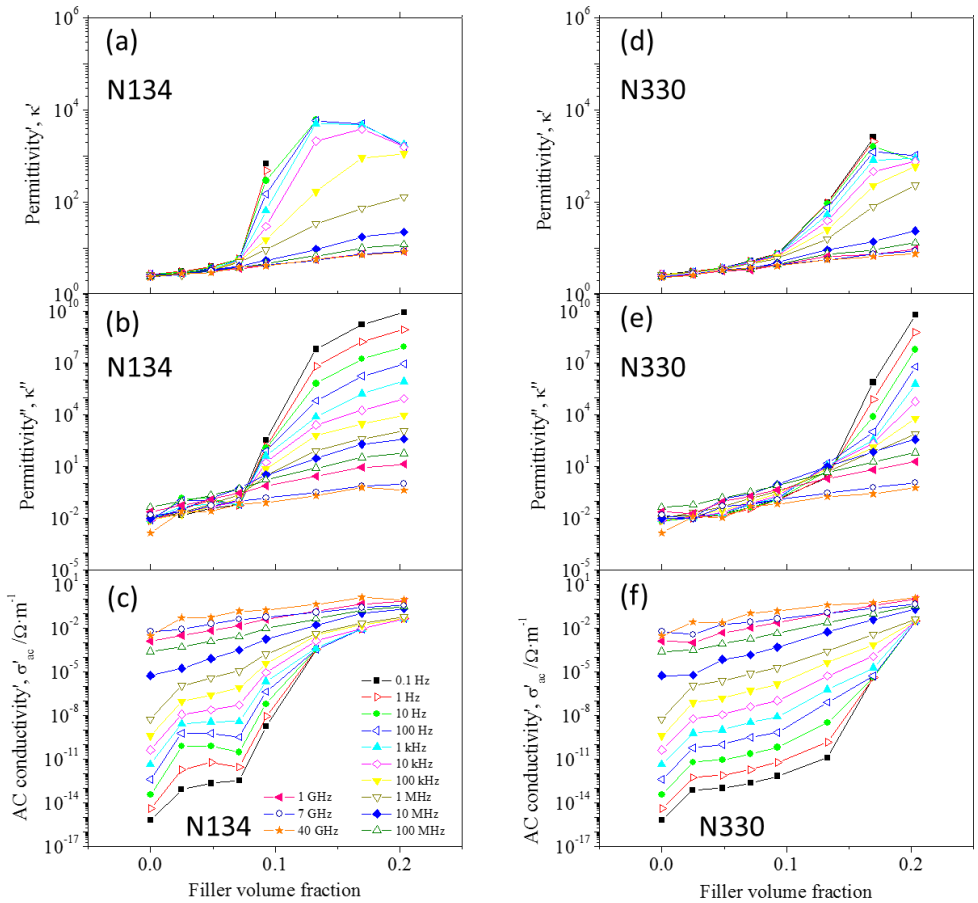

Figure 3-5. The filler concentration dependent dielectric behaviour of carbon black N134 (a, b & c) and N330 (d, e & f) filled natural rubber presented by the real and imaginary part of permittivity as well as the real part of the ac conductivity. Symbols shown in (c) and (f) are the same for the rest of the figures.

Figure 3-5(b) shows the percolation behaviour of κ'' which is very similar when compared to κ'. However, the dc conductance contributes more significantly to κ'' for these highly filled materials. Therefore, the percolation behaviour observed using κ'' actually represents the situation of both ac and dc. This is again similar for the ac conductivity presented in Figure 3-5(c). Unlike κ', the ac term of σ'_{ac} is limited at low frequencies while most of the σ'_{ac} comes from the dc term. In this case, the ac and dc percolation is the same (here ϕ_c^{ac} is represented by σ'_{ac}). From this discussion, the percolation behaviour of the various ac parameters should be treated differently.

Figure 3-5(d) to Figure 3-5(f) are the percolation graphs of NR/N330. They show a very similar behaviour when compared to the plots for NR/N134. The main difference between them is the location of ϕ_c^{ac}. To quantitatively compare the difference, ϕ_c^{ac} was fitted based on κ' using Equation 3-7. As shown in Figure 3-6 (a) and (b), the percolation threshold of NR/N134 and NR/N330 samples were 0.0927 and 0.1354 respectively (at 10 Hz). The inset graphs in both images show a linear relationship between $\log\left(\phi_c^{ac} - \phi\right)$ and $\log\left(\kappa'\right)$ which confirms the quality of the fitting. This difference again arises from the extent of the interface area being larger for the NR/N134 compounds while the average inter-particle filler separation distance is smaller when compared to NR/N330. The fitting parameter for NR/N134 was 0.543 while it was 0.886 for NR/N330. They correspond reasonably well to the reported values in the literature[182]. However they are both smaller than the standard value of 1 which means the speed of building the network of diffusion zones is slower than that predicted by the percolation theory. It also suggests that the formation of such networks in NR/N134 samples was easier than that in NR/N330. When fitting data measured at higher frequency such as at 10 kHz, different results were obtained. The value for the percolation threshold varied when different amounts of data points were used as shown in Figure 3-6 (c) and (d). From this consideration, only the κ' measured at low frequencies should be used to represent the actual ac percolation behaviour.

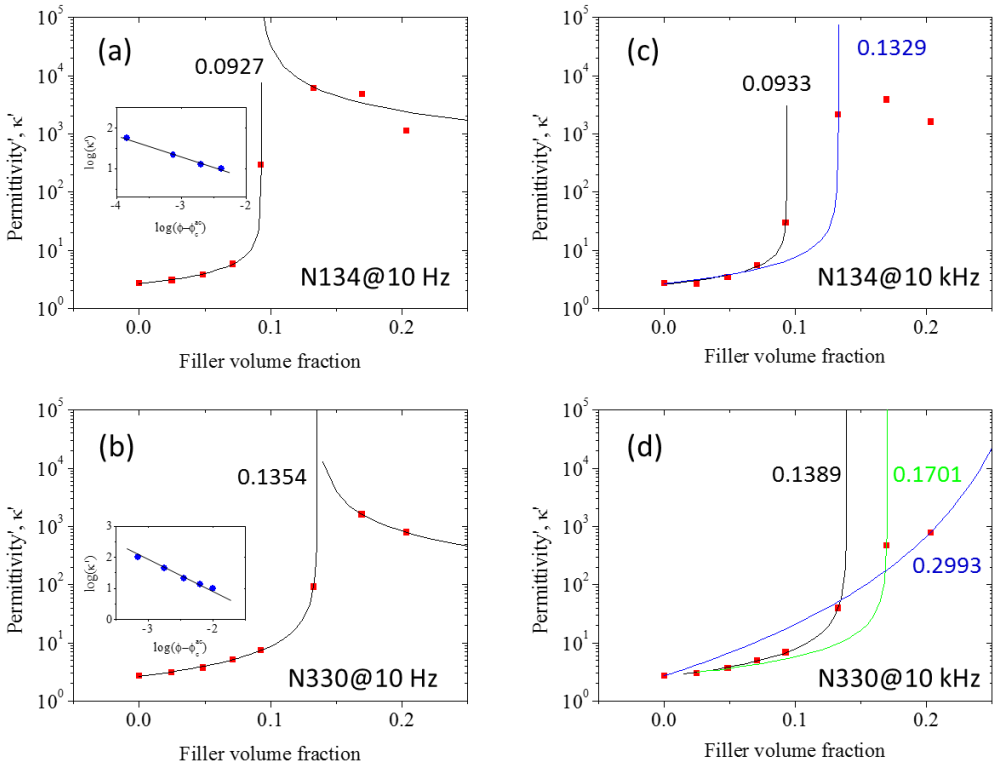

Figure 3-6. The percolation fitting of carbon black N134 and N330 filled natural rubber at different frequencies. (a) & (c) are at 1 Hz while (b) & (d) are at 10 kHz. All the solid and dashed lines are from data fitting of the results. There may be several fitting approaches shown in the same graph where the numbers show the value of the percolation threshold from the fitting. The inset graphs in (a) & (c) are shown to highlight the fit quality.

3.5 Summary

A very broad band dielectric spectrum of natural rubber/carbon black system has been built. The κ' value decreases with an increase in the test frequency. This is mainly caused by the MWS-dipoles. These MWS-dipoles also brings an exceptionally high value of κ' at low frequencies; however this effect gradually disappears as the frequency approaches the GHz range. Moreover in this frequency region, κ' is almost independent of the filler size which means the MWS-dipoles are less active. Nevertheless this behaviour cannot be readily fitted using the Debye type relaxation.

The dielectric parameters κ', κ'' and σ'_{ac} can all be fitted by percolation theory at low frequencies. The percolation behaviour of κ' is dominated by the increase of the MWS

polarisation. The percolation threshold arises when the electrical diffusion zones outside the filler surfaces start to connect to each other. However, the percolation behaviour of κ'' and σ'_{ac} are affected by both the dc conductance as well as the MWS polarisation. Therefore, it is recommended to undertake the ac percolation fitting using κ' measured at low frequencies.

4 Chapter Four: Segmental Dynamics at the Filler-Rubber Interface

4.1 Introduction

The percolation behaviour of conductive fillers such as carbon black has already been discussed in this thesis. It is clear that the MWS polarisation makes a significant contribution to the dielectric properties. Besides the MWS polarisation, the intrinsic dielectric relaxation behaviour of the polymer network is also important - although it is very difficult to observe in carbon black filled compounds. From a scientific viewpoint, the importance of this coupling between the dielectric behaviour and the mechanical behaviour (as demonstrated in Equation 2-42) needs to be investigated. Expressed another way, can the dielectric relaxation be used to directly evaluate the segmental dynamics of the polymers around the filler surface? If it can, then this approach will help one of the key outstanding issues concerning the filler reinforcement mechanisms to be understood and it will also allow a much clearer understanding of the nonlinear viscoelastic behaviour of filled compounds. From a consideration of the dielectric behaviour, the mobility of dipoles inside of the polymers near the filler interface may be slowed down which may result in weaker charge transportation behaviour. Therefore, it is very important to understand the dielectric reinforcement behaviour.

In this chapter, the segmental dynamics of both precipitated silica and carbon black filled natural rubber is studied, using both impedance spectroscopy (IS) and dynamic mechanical analysis (DMA). The reason for using silica is because it is a good dielectric material and the interface polarisation is much weaker compared with carbon black. Therefore, the segmental relaxation (the α relaxation) can be reliably characterised. The key point of this chapter is to investigate if the segmental dynamics are slowed down by the incorporation of a filler.

*Part of this chapter has been published in *'European Polymer Journal'* as a paper entitled *'The glass transition, segmental relaxations and viscoelastic behaviour of particulate-reinforced natural rubber'.*

4.2 Experiments

4.2.1 Materials

Two kinds of precipitated silica were used in this work: conventional silica (CVS) and highly dispersible silica (HDS). To modify the dispersion and the silica-NR interface, tri-ethoxyvinyl silane (TEVS) was also added to some of the samples. TEVS modified CVS (CVS_TEVS) was supplied premixed by the manufacturer whilst the TEVS modified HDS (HDS_TEVS) was added in-situ and reacted during the rubber compounding. The resulting four different silica compounds all contained the same volume fraction ($\varphi = 0.2$) of silica. The rubber compounding process was the same as that described in Chapter 3. The carbon black compounds were each diluted from a master batch as also described in Chapter 3. All the filled compounds and one of the unfilled compounds used two phr DCP. A set of unfilled test samples was also prepared using different DCP contents. The curing time for each samples was fixed at either 40 or 60 minutes at 160 degrees depending upon the individual compound cure trace. All the sample code names, processing conditions and compound details are summarised in Table 4-1.

Table 4-1. Samples used in this study and their curing conditions.

Sample Code	Filler Type	Filler Volume Fraction	DCP Concentration [phr]	Curing Time [min]
NR/0.5DCP	/	/	0.5	40
NR/1DCP			1	40
NR/2DCP			2	40
NR/3DCP			3	40
NR/0			2	60
N330/0.025	N330	0.025		
N330/0.049		0.049		
N330/0.093		0.093		
CVS/0.2	CVS	0.203		
CVS_TEVS/0.2	CVS+TEVS			
HDS/0.2	HDS			
HDS_TEVS/0.2	HDS+TEVS			

4.2.2 Impedance spectroscopy

The technique described in Section 3.2.2 was used for all the tests in this chapter. In addition, all the samples were placed into a vacuum oven at 373.15 K for 24 hours prior to testing. This was to remove, as far as was practical, all the residual moisture from the samples prior to testing. Temperature sweeps were performed from 173.2 K to 323.2 K with steps of 1 K. The accuracy of the temperature control system was set at ± 0.1 K. At each temperature there was an initial dwell of 10 minutes to ensure thermal equilibrium and then the frequency domain dielectric spectrum was evaluated from 0.1 Hz to 1 MHz.

4.2.3 Dynamical Mechanical Analysis

A Perkin Elmer 800 DMA was used in a tensile deformation mode to obtain the dynamic mechanical properties of the samples. Samples were initially cooled down below their glass transition temperature and then they were clamped and fixed into the DMA tensile fixture. This process minimised any potential initial pre-strains. The DMA tests started from 197 K up to 237 K with incremental temperature steps of 2 K. The dynamic mechanical properties were measured at each temperature step after a dwell time of 10 mins to ensure thermal equilibrium had been established which was consistent with the dielectric test. The dynamic strain was 0.1% at a frequency of 1 Hz and a preload force of 0.1 N was applied.

4.3 Results and Discussion

4.3.1 The Dielectric Relaxation Presented by 3D Dielectric Plots

The broad-band dielectric results shown in the previous chapter (Figure 3-1), showed a very broad peak for unfilled NR in the MHz range at room temperature. This is further confirmed here when examining the behaviour at lower temperatures, the peak in the permittivity is at lower frequencies. This is the behaviour that one would have expected from the time temperature superposition principle. Figure 4-1 (a) shows the 3D plot of both frequency and temperature domain dielectric spectrum of the real part of the permittivity κ' for unfilled NR/0, while Figure 4-1 (b) shows the corresponding imaginary part of the permittivity κ''. In Figure 4-1 (a), κ' decreases with increasing

frequency which is caused by some of the dipoles not being able to respond to the field frequency in time. This frequency dependent behaviour of κ' is negligible at very low temperatures but becomes considerably larger at higher temperatures. This is because most of the dipoles are inactive or 'frozen' when the temperature is below about 210 K. Correspondingly, κ'' is almost flat in this temperature region as a result of this 'frozen dipole' effect. However, above 210 K, the segmental dipoles start to 'unfreeze'. Consequently, there arises a loss peak in the κ'' graph shown in Figure 4-1 (b). This peak moves continuously to a higher frequency region as the temperature increases. Also a modest decrease with increasing frequency is also visible in Figure 4-1 (a). There is also an increase in κ' as the test temperature increases above the glass transition temperature of NR. The scale of the change reduces and the position of the change moves to a higher temperature as the frequency is increased. This is because at low frequencies and at higher temperatures (above Tg) most of the dipoles can follow the externally applied electrical field. But below Tg, the segmental dipoles can no longer follow the electrical field resulting in a decrease of κ' . In this case, the $T \sim \kappa'$ relationship measured at low frequency can be used as a method to directly evaluate the glass transition.

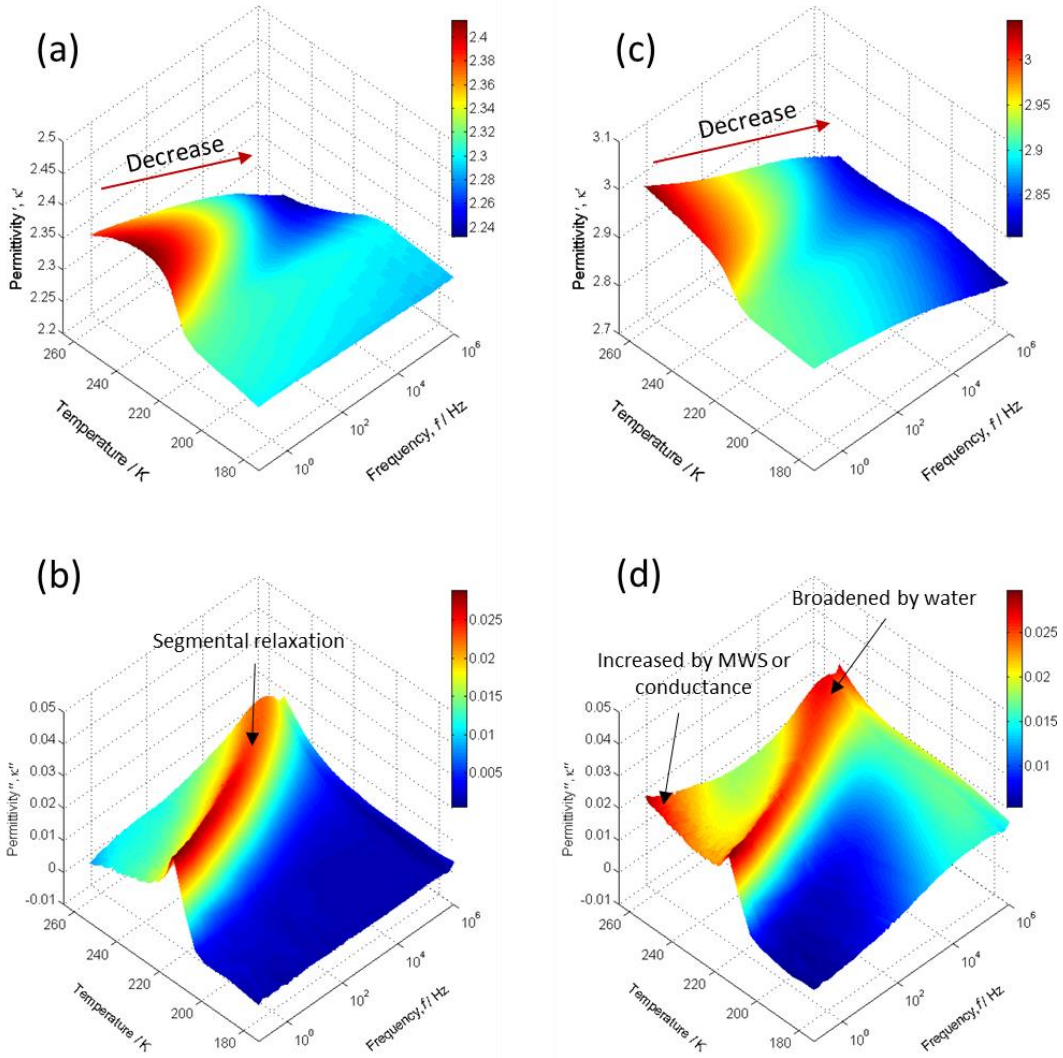

Figure 4-1. The frequency and temperature dependence of the complex permittivity of (a) & (b) unfilled natural rubber NR/0 and (c) & (d) HD filled natural rubber ($\varphi = 0.2$). (a) & (c) both show the data for the real part of the permittivity while (b) & (d) are the imaginary parts of the permittivity.

Figure 4-1 (c) and Figure 4-1 (d) show the dielectric relaxation data of silica-filled NR, HDS/0.2. Firstly, κ' of HDS/0.2 has clearly been reinforced by the presence of the silica. Secondly, κ' shows a stronger frequency dependence for HDS/0.2 compared to NR/0 because of the MWS type interface dielectric relaxation process. Thirdly, κ'' of HDS/0.2 behaves differently at both very low and very high frequencies when compared to NR/0. At high frequencies of around 1MHz, κ'' increases significantly and is also significantly

broadened. This may be a consequence of the absorbed water creating hydroxyl groups on the silica surface. The remaining water has a high conductivity therefore, there are charges accumulated between the interface of water and NR which results in a relaxation time of around 10^{-6} s corresponding to a frequency of around 1 MHz[38]. The increase of κ'' in the low frequency range may be caused by another type of MWS process occurring at the filler NR interface. As the conductivity of the silica is very low compared to water, the relaxation time of this MWS process would be much longer than is the case of the water/NR MWS process. Otegui[183] also studied the low frequency relaxation of silica filled SBR in detail and he also concluded that this low frequency contribution arose from the moisture present at the surface. However, compared to their results, the amplitude of κ'' in Figure 4-4 (b) is much smaller than the value that Otegui reported. Therefore, the MWS should be the main contribution to κ'' in this region. One should note that, in most of the cases the leakage current may also donate to κ'' as there is no such thing as a perfect insulator.

The relaxation shown in Figure 4-1 can be well described by a Debye type of relaxation (a decrease in the real part corresponding to the appearance of a loss peak). However, the data are not fitted by the standard Debye function because the loss peaks in Figure 4-1 (b) and Figure 4-1 (d) are not symmetrical along the frequency axis. Therefore, Equation 3-1 can be used to fit the $f \sim \kappa''$ plot over different temperatures and to identify the peak relaxation frequency f_{max} at each temperature. It is possible either to use the imaginary data to make the fitting or to use both the real and the imaginary data simultaneously. Fitting using the real data alone, however, would not be very reliable (Section 3.4.1). Figure 4-2 shows the α relaxation of unfilled NR/0 at selected temperatures. The temperature at which the α relaxation is first observed is close to the glass transition temperature of NR. The fitting results can be plotted as $T \sim f_{max}$ which can be further fitted using a Vogel-Fulcher-Tamman (VFT) relation or an Arrhenius-type of relationship. The α relaxation has widely been shown to follow a VFT function[120]:

$$\log f_{max} = \log f_0 - \frac{A_0}{T - T_0} \qquad \text{Equation 4-1}$$

where f_0 and A_0 are the fitting parameters. T_0 is also a fitting parameter known as the Vogel temperature or ideal glass transition temperature. Using this approach the glass transition temperature can be defined as the temperature when the segmental relaxation time is 100 seconds[184].

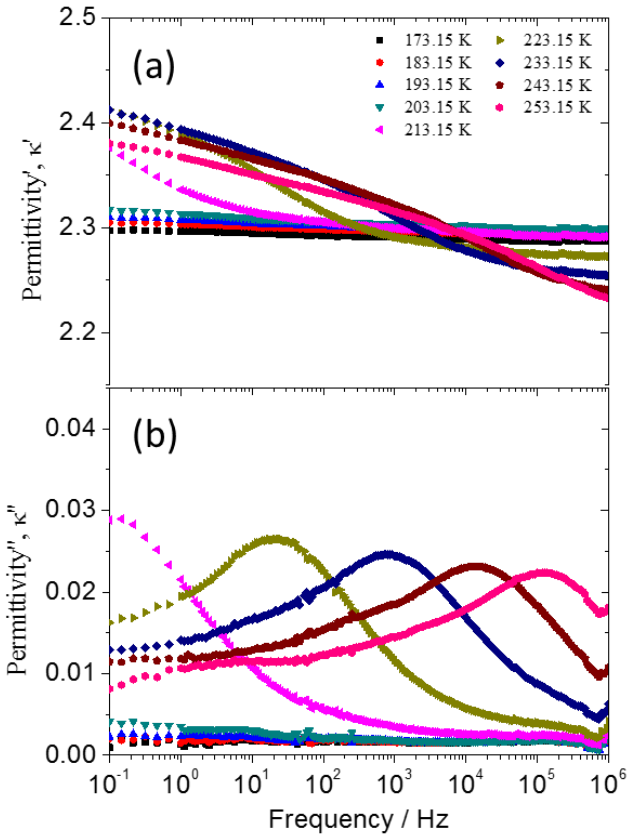

Figure 4-2. Frequency domain dielectric relaxation of unfilled NR/0 at specific temperatures.

4.3.2 The Segmental Relaxation of Unfilled NR

Figure 4-3(a) shows the $T \sim f_{max}$ plot of NR/0 where each of the points was identified from the $f \sim \kappa''$ plot for each specific temperature. There are also two extra curves of NR materials digitized from literature data[95, 185]. The difference between the curves might arise from the different curing processes used by different researchers as well as the variations of the molecular weight of the base polymer. To further study these effects, NR cured using different amount of DCP and different curing times has been tested. The fitting results are shown in Figure 4-3(b). Firstly, NR/0 has a shorter relaxation time compared to NR/2DCP, where the only difference between them is the

cure time which was 60 min and 40 min for NR/0 and NR/2DCP respectively. The shorter cure time for NR/2DCP meant that there was more residual unreacted DCP remaining in the samples and a lower crosslink density when compared to NR/0. These effects might be thought to slow down the segmental dynamics[128]. By comparing the differences between NR/0.5DCP, NR/1DCP, NR/2DCP and NR/3DCP, the increase of the concentration of DCP can be seen to systematically increase the relaxation time or slow down the dynamics. That is why for most of this thesis a cure time of 60 minutes was chosen by which time most of the residual curatives are consumed. Also shown in the figure are the glass transition temperatures which have been obtained from the VFT fitting. Samples with faster segmental relaxations have a higher Tg.

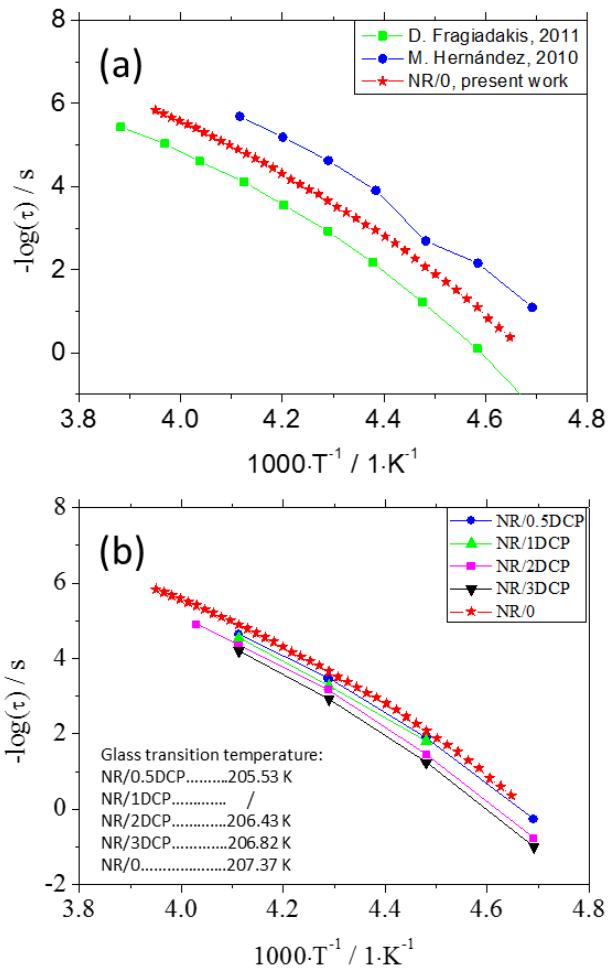

Figure 4-3. (a) The α relaxation fitting results of unfilled NR/0 with a comparison with data digitized from the works by D. Fragiadakis[95] and M. Hernández[185]. (b) The α relaxation fitting results of NR/0 that are cured for different times and with various different concentrations of the curatives (DCP). The Tg was obtained from the VFT fitting of the temperature dependence of the α relaxation.

4.3.3 The Segmental Relaxation of Filled NR

As shown in Figure 4-1 (c) and Figure 4-1 (d), silica filled NR show a comparable segmental relaxation process to the unfilled NR. Figure 4-4 (a) and Figure 4-4 (b) present this process for a range of different temperatures. As previously discussed there are two extra terms at both the lower and the higher frequencies. It is very interesting that Figure 4-4 (b) shows an extra term at around 100 kHz when the temperature is below Tg that does not exist with NR/0 in Figure 4-2(b). It corresponds to a relatively fast response rate that is not present in the NR phase. This peak cannot result from atomic or electronic relaxations, as these two relaxations are way beyond the scope of the current testing facilities. It may arise from the dipole relaxation in the silica phase or even more likely as a consequence of dielectric relaxation of the silanol groups and hydration shells at the silica surface as has been proposed previously by other researchers[95].

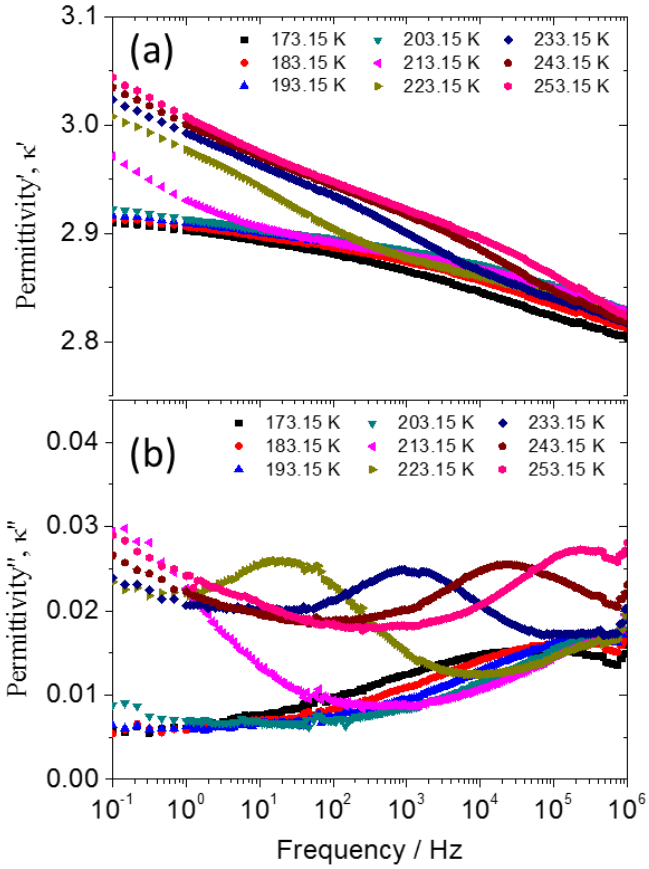

Figure 4-4. Frequency domain dielectric relaxation of HDS/0.2 measured at different temperatures.

To determine if the α relaxation is shifted by the presence of the filler, several different samples were plotted together at a fixed temperature of 223.15 K in Figure 4-5. Most obviously from Figure 4-5(a) the conductive filler is much more effective in reinforcing κ'. However, the precise position of the segmental relaxation peak looks consistent between different samples as shown in Figure 4-5(b). The decrease of κ' with frequency is very modest as shown in Figure 4-5(a). The carbon black filled NR also shows a high frequency term which is comparable to that of the silica filled NR. One possible reason is that the carbon black, being conductive, can have an even stronger MWS interfacial polarisation than the hydroxy coated silica surfaces. Also as the NR/CB specimens used here were far below their percolation threshold, a low frequency dc term was not expected to make any contribution - especially at temperatures as low as 223.15 K. For a better comparison, κ'' was normalised by dividing each value by the corresponding peak value for each curve as shown in Figure 4-6. It can be deduced that the α relaxation is not significantly different between the various filled samples. The significant differences are primarily from the extra terms in both the low and high frequency range. Therefore, the HN fitting functions were only applied to the medium temperature range of filled samples to avoid any complications that might arise from the appearance of these additional terms. Although one can increase the number of fitting parameters and functions to perform a full de-convolution of the BDS spectrum, this increases the computational complexity and introduces additional uncertainties and multiple solutions to the error minimisation process. In practice, an additional dc term can be used to de-convolute the data as shown in Figure 4-7. The result is very similar though when compared to the result fitted by a single HN function. Unlike silica filled samples, the sample with a high concentration of carbon black becomes increasingly conductive. This creates a very strong high frequency term which superposes with, and appears to shift, the original segmental peak as shown in Figure 4-8. As a consequence it is not sensible to try to fit the function to the highly filled carbon black test sample data.

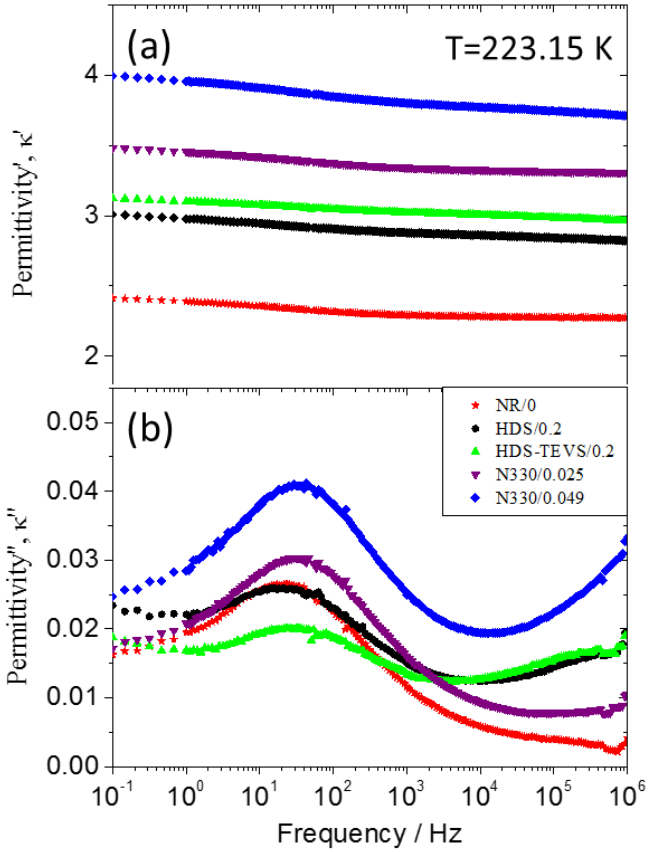

Figure 4-5. Comparison of the α relaxation peak for unfilled NR/0 and those filled using different fillers at 223.15 K.

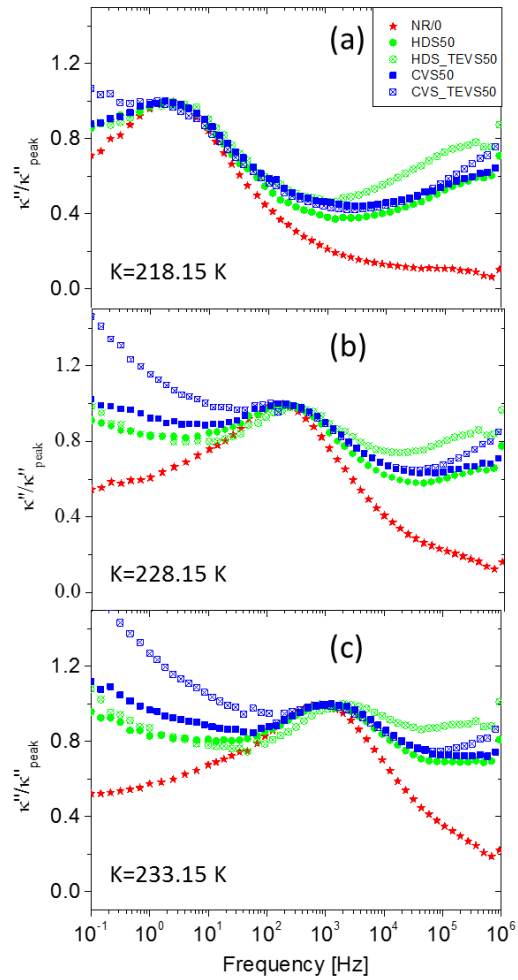

Figure 4-6. The normalised α relaxation peaks of natural rubber, unfilled or filled with different silicas.

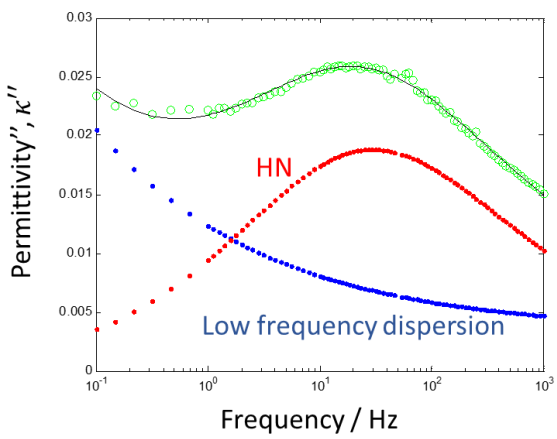

Figure 4-7. Example of the de-convolution of the low frequency relaxation process of the polymer using an HN function and a conductivity contribution. The green dots are the original data while the blue and the red dots are fitted by the dc conductivity term and the HN term respectively. The black solid line is the overall fitting.

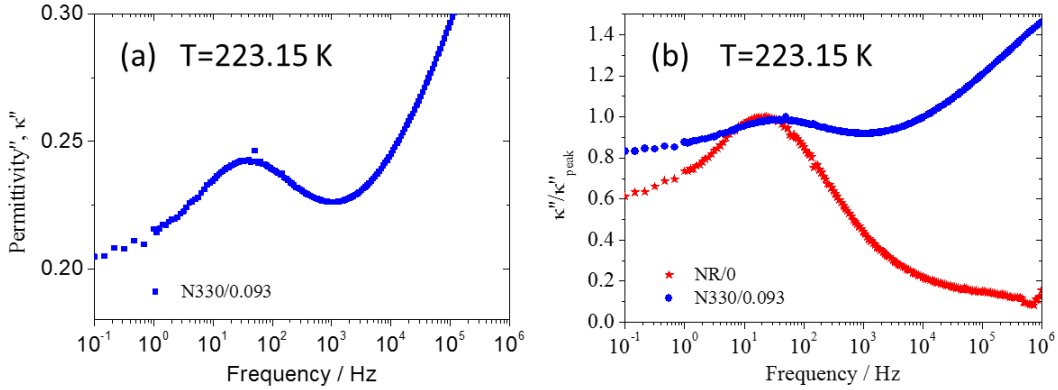

Figure 4-8. (a) The α relaxation peak of CB/0.093 at 223.15 K. (b) The normalised α relaxation peak of NR/0 (red dots) and N330/0.093 (blue dots).

Figure 4-9 shows the HN fitting result for all the unfilled and silica filled samples. There are only very limited differences between the filled and unfilled samples which means that only a consistent segmental relaxation process exists. However, the α relaxation peak has been broadened for silica filled samples, especially for TEVS treated silica as shown in Figure 4-5(b). This indicates that the distribution of the relaxation processes may be broadened while the overall behaviour remains the same. This broadening phenomenon of filled materials may also be caused by the extra terms in both low and high frequency region. Therefore, here only the location rather than the shape of the α peak is emphasised. More evidence can be found in the mechanical characterisation using DMA, whose results are shown in Figure 4-10. Although there is around a 1K difference between the locations of the peaks of the loss modulus and an even smaller difference in the tan delta peaks (which is not shown here), these differences are within the experimental accuracy of the DMA test. This result is perhaps not too surprising as on one side the rigid filler does inhibit the movement of the polymer chain[143] whilst conversely this effect is relatively weak due to the tiny volume of polymer that is involved and also as the actual surface area available to effect this constraint is also reduced by the formation of complex filler networks during the flocculation process that arises during curing[178]. Similar behaviour has been observed by Fragiadakis et al.[95] who proved the importance of the filler dispersion on the interfacial dynamics. From the work reported here, there is no direct evidence for a substantial glassy layer being present around the filler particles. It is proposed as an alternative, that a difference of

the dispersion states is a more likely explanation of the contradictory data in the literature that has been invoked in the past and which has resulted in the development of theories that require substantial glassy or immobilised polymer layers around the filler surface.

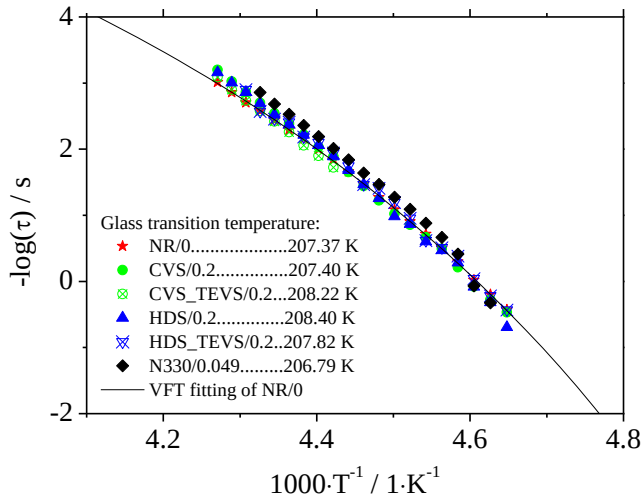

Figure 4-9. The temperature dependence of the relaxation time for different samples.

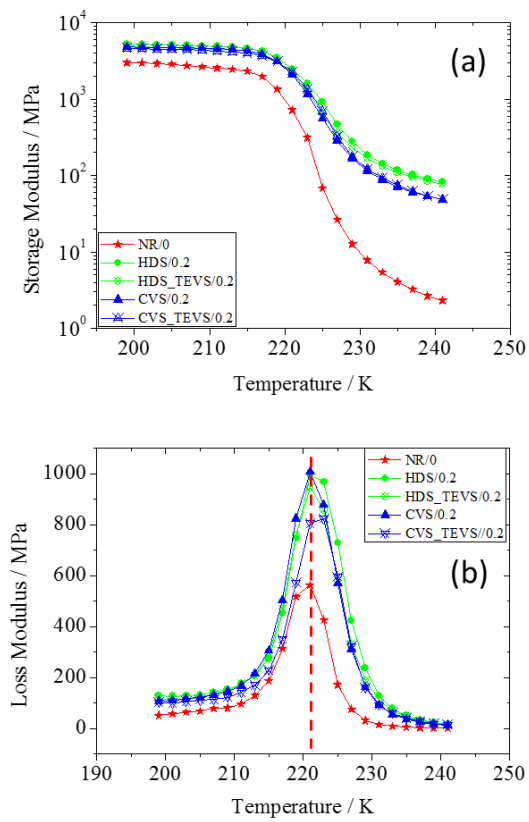

Figure 4-10. Storage and loss modulus of unfilled and filled natural rubber.

4.4 Summary

Although the confinement effect around the filler surfaces may slow down the segmental process in the dielectric spectrum, this effect is limited in the commercial compounds that were used in this study due to imperfect filler dispersion. The results from the DMA test could also barely identify the shift of Tg as the change was too small to be accurately defined. Moreover, in carbon black filled rubbers, the effect of confinement could essentially be ignored as it would be much weaker than the strong interfacial polarisation. Therefore, the GLASSY-dipoles could be roughly treated as a part of BULK-dipoles of the natural rubber/carbon black or natural rubber/silica composites used in this study.

The segmental relaxation was also affected by the curing process as well as the quantity of the curatives. Increases in both slowed down the segmental dynamics and brought about a slightly higher glass transition temperature.

5 Chapter Five: Measuring Dielectric Properties under Strain using Stretchable Electrodes

5.1 Introduction

Impedance spectroscopy is widely used to characterise the dielectric properties of materials at frequencies under 100 MHz. It is also known as dielectric spectroscopy in this testing range. One of the most important considerations for impedance testing is the behaviour of the electrodes during the test as well as the contact between the electrodes and the materials under test (MUT). Any defects at the interfacial contact area may result in large and unexpected errors in the measured data. That is why in most applications, the MUT is carefully coated by metal, such as gold or silver, in order to secure good contacts before being clamped into the rigid testing fixtures as shown in Figure 5-1(a).

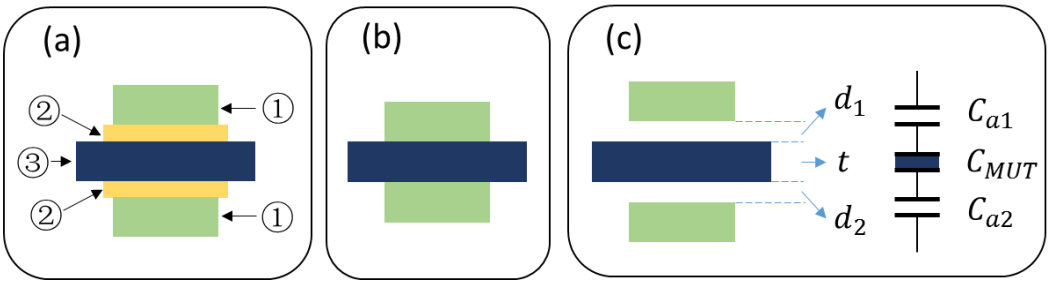

Figure 5-1. The side view of the impedance test with different types of contact: (a) Materials under test (MUT) is coated by a thin layer of conductive materials such as gold or silver and then clamped using rigid electrodes. Numbers are defined as follows: 1. Rigid electrode; 2. Coating layer; 3. MUT. (b) MUT is directly clamped by two rigid electrodes. (c) A schematic to show a capacitance gap of a finite size between the electrode and the sample. d_1 and d_2 are the distances between each electrode and the sample. t is the thickness of the sample. The air layer between the electrode and the sample can be treated as capacitors which are marked as C_{a1} and C_{a2}. The specimen itself is also a capacitor: C_{MUT} .

There is an essential difficulty in measuring the dielectric properties of a material under strain, as it becomes difficult to maintain a good electrical contact between the electrodes and the MUT due to their significantly different mechanical properties.

Traditional evaporation coating or magnetron sputtering methods break and crack easily even under a few percent of strain[186]. In this case, the coating layer has to be abandoned as shown in Figure 5-1(b). Therefore the contact is relatively poor which significantly reduces the accuracy of any measurements. A non-contact method has been proposed by Keysight Technologies (previously called Agilent) where the rigid electrodes do not have to make direct contact with the MUT as shown in Figure 5-3(c)[187]. However, whilst this approach appears simple, in practice the air-MUT interface may introduce large deviations and bring huge uncertainties into the data during testing of carbon black filled rubbers.

Another approach that facilitates the simultaneous measurement of the dielectric behaviour whilst under a mechanical strain requires the use of stretchable electrodes which have been directly pasted on the surface of the MUT. A typical setup is shown in Figure 5-2. Stretchable electrodes can be made by percolated metallic nanowires as well as carbon nanotubes, graphene or carbon grease. The MUT is sandwiched by two stretchable electrodes whose shape is deformable under strain. This allows them to retain a high conductivity and a good contact with the MUT. Although this testing setup, shown in Figure 5-2, has been widely used for capacitance strain sensors, it has never been applied to measure the dielectric properties, such as permittivity, of soft materials such as elastomers under strain.

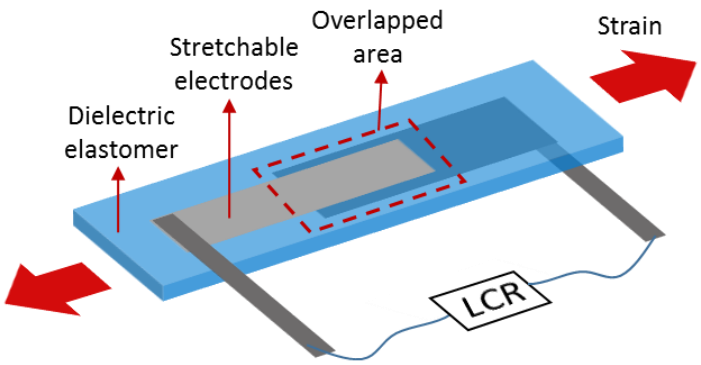

Figure 5-2. Typical setup to measure the impedance of the materials using stretchable electrodes.

This chapter will focus on characterising the dielectric properties of strained natural rubber (NR) using stretchable electrodes as shown in Figure 5-2. The dielectric properties are presented as the complex dielectric constant $\kappa^{*}=\kappa'-j\kappa''$ where the real part κ' is assigned as the permittivity and $D=\kappa''/\kappa'$ is known as the dielectric loss. Two different stretchable electrodes were used: silver nanowire (AgNW) and carbon grease (CG). An accurate formula (in page 114) was derived to describe the relationship between the capacitance and the strain. This analytical method also successfully derived κ' and D as well, allowing the accurate measurement of the dielectric properties under strain to be made. In addition, the traditional method using rigid copper electrodes was also undertaken.

*Part of this work has been published in '*Constitutive Models for Rubber Viii*' as a paper entitled '*The application of a carbon black filled elastomer to create a smart strain sensor*'
**Part of this work is going to be submitted to '*Sensors and Actuators A: Physical*' as a paper entitled *'An Insight Study of the Capacitance-Strain relationship of Capacitance Strain Sensors'*

5.2 Experiments

5.2.1 Materials

The samples used in this study were natural rubber (SMR CV60). They were initially mixed with dicumyl peroxide (Sigma Aldrich) curative at a w/w ratio of 50:1 using a two roll mill. The compound was then cured at 160 ^{o}C under a pressure of around 60 bars for 1 hour. The thickness of the sample sheets were all approximately 0.7 mm.

5.2.2 Standard Impedance Test (under no Strain)

A Novocontrol Concept 40 Impedance Spectrometer (Figure 3-1) was used to characterise the unstrained dielectric properties of all the samples from 0.1 Hz to 1 MHz at room temperature according to ASTM D 150-11[188]. The dimensions of the test specimens were 25 mm x 25 mm x 0.7 mm. The surfaces of each sample were coated

with gold using vacuum deposition in order to ensure a good contact with the fixed electrodes. The diameter of the overlapping gold layers was 22 mm.

5.2.3 Impedance Test under Strain: AgNW as Stretchable Electrodes

By adopting AgNW for the stretchable electrodes, the sample could be made very thin and sufficiently small enough to fit into a dynamic mechanical analyser (DMA). The impedance and the mechanical signal were recorded simultaneously during the test. Therefore, this test is called Simultaneous Dielectric Mechanical Spectroscopy (SDMS) test.

Preparation of the Silver Nanowire Electrodes

Silver Nanowire (AgNW) SLV-NW-40 isopropanol suspension was synthesized by Blue Nano Inc. The average nanowire diameter was 40 nm and the average length was 10-30 micrometre. The concentration of the AgNW suspension purchased was 10mg/ml. It was diluted to 0.003 mg/ml which was subsequently filtered to produce the electrodes. Figure 5-3(a) shows the morphology of the silver nanowires from dried solvent. Figure 5-3(b) shows the AgNW dispersed on the filter membrane at the first beginning of filtering while Figure 5-3(c) shows the case when the filtering was finished. In Figure 5-3(c), an area of entangled AgNW is marked out. This kind of entanglement exists randomly in the finished AgNW film.

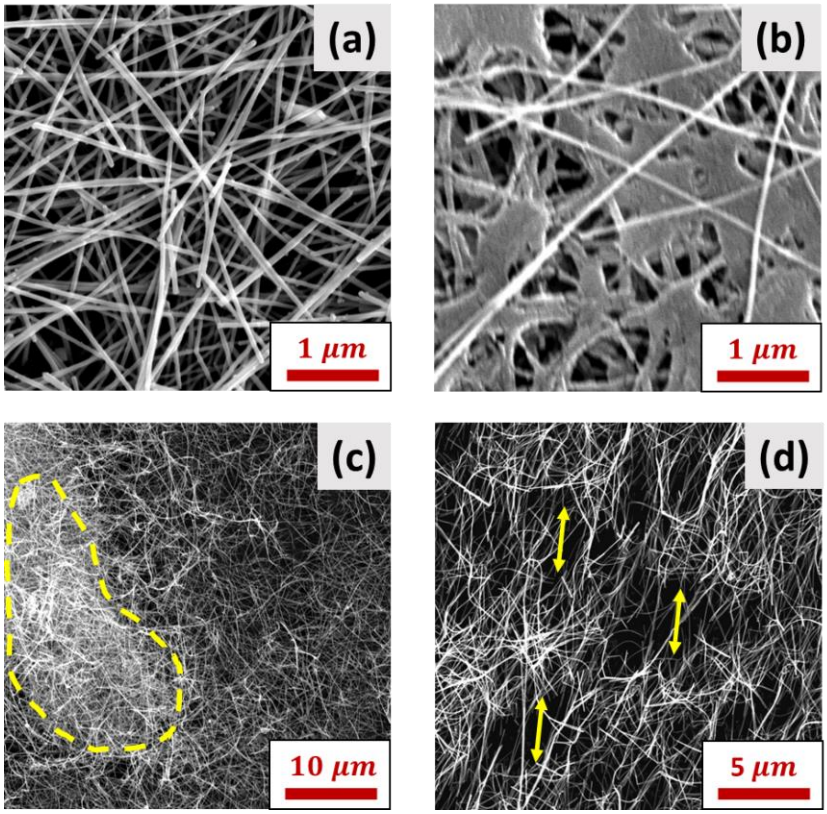

Figure 5-3. (a) AgNW electrodes before removing from a PTFE filter membrane. (b) Several Silver AgNW on top of a PTFE filter membrane. (c) AgNW electrodes, the highlighted area is showing the entangled AgNWs. (d) AgNW electrodes bonded to the top of a NR sample at approximately 50% strain. The arrows indicate the cracks generated by strain.

The filtration set up is shown in Figure 5-4(a). In this process 200 ml of 0.003mg/ml solvent were filtered through sintered discs. The filter membrane used was a JVWP04700 Hydrophilic PTFE membrane made by Millipore (diameter: 47 mm & pore size: 100 nm). As the fritted base of the filter assembly was not perfectly flat, another thick PVDF membrane with a pore size of 0.1 μm was used in between the actual PTFE membrane and the filter base. Therefore, the final PTFE/AgNW sheet could be very flat and uniform as shown in Figure 5-4 (c). After the solvent was fully evaporated from the filter surface, the filter was cut to obtain a AgNW/ PTFE sheet of the required shape. This silver nanowire coated surface was then pasted onto the surface of the rubber test sample (32 mm*9 mm*0.7 mm) and a uniform pressure was applied for about 10 seconds. The PTFE membrane was then peeled off leaving a layer of AgNW on the specimen surface as shown in Figure 5-4 (d). Repeating this approach on the other

surface of the sample allowed two AgNW electrodes to be pasted on both sides of each specimen which gave an overlapped area in the middle of the sample with a size of around 6 mm*6 mm. The surface density of the final AgNW electrode was around 490 mg/m^2. The sheet resistance, tested using a four-probe method, was found to be around 15.9 $\Omega/\square$. The whole resistance of two AgNW electrodes in series as shown in Figure 5-4 (d) was around 20 ohms and it increased to around 200 ohms at around 50% strain. The electrodes were not broken for at least several hundred strain cycles (when 50% maximum strain was applied for each cycle). Figure 5-3(d) shows the situation when a AgNW film (on top of a NR sample) was strained to around 50%.

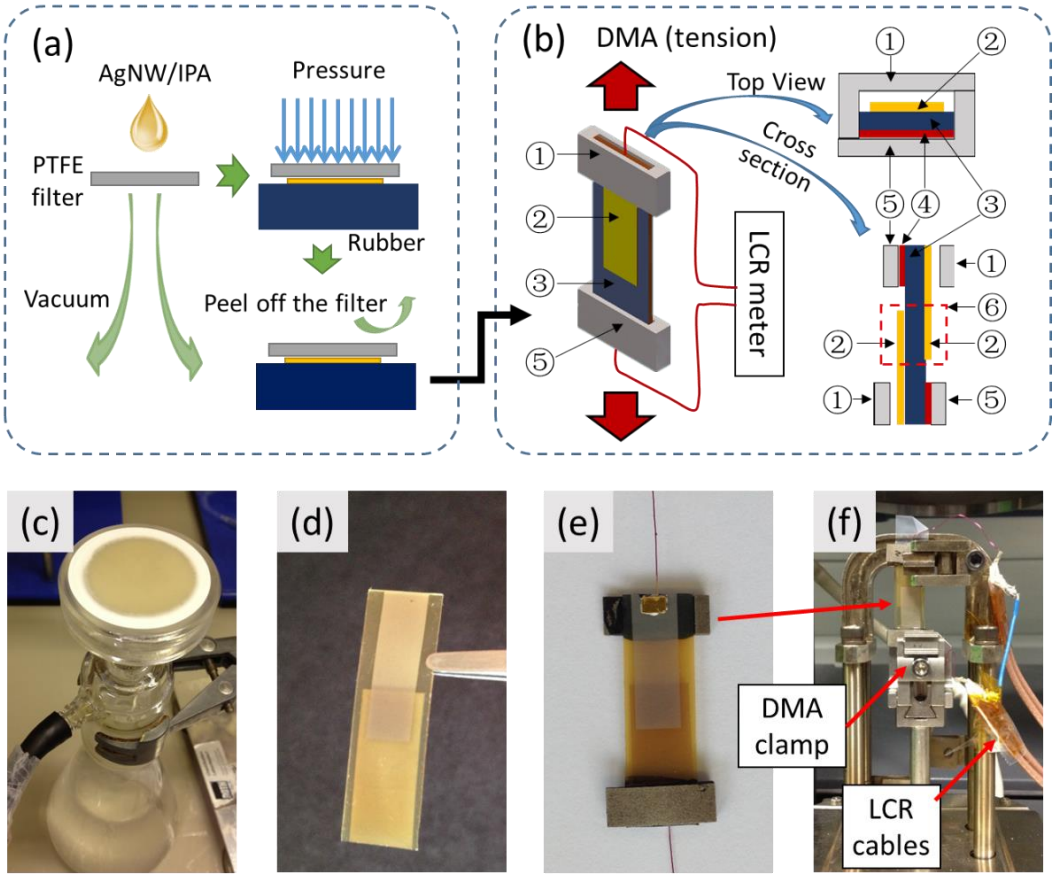

Figure 5-4. (a) Manufacturing processes of silver nanowire electrodes and the transfer method to locate them onto a rubber sample (side view). (b) Connections that link the test sample to the LCR meter. A top view and a cross sectional view of the sample gives details of each. Each number is defined as: 1. Top fixture; 2. AgNW electrode; 3. Rubber sample; 4. Adhesive; 5. Bottom fixture (only this type is glued to the sample). (c) Filtering set up. (d) Sample coated by two layers of AgNW one each on either side. (e) Sample fixed to the bottom fixture (top fixture has still to be glued). (f) Sample positioned using the DMA tension clamp.

Preparing the Specimen for SDMS Testing

Figure 5-4(b) shows a sketch of the finished sample under the SDMS test. The sample area that is covered by AgNW electrodes cannot be directly clamped for a DMA tension test as the AgNW electrodes would be broken. Moreover, the DMA clamp also compresses the sample. This strongly affects the result especially at small strains. To avoid these problems the specimen was firstly glued onto a stainless steel fixture (top fixture) which could then be clamped onto the DMA as shown in Figure 5-4(e). In this figure one can also see the electrical connection inside the fixture. The ends of the AgNW electrodes were glued to very thin varnished wires (around 30 mm long) using a conductive epoxy adhesive (RS Components) for further connection to the LCR terminals. This small region formed the electrical connection and was not deformed during the test. It did however permit a very conductive connection to be maintained under strain. Finally, another stainless steel fixture (bottom fixture) was positioned above the top fixture. This cover piece was hanging over the AgNW so that there was no electrical connection between them as shown in the top view of Figure 5-4(b). The finished sample was then fixed to the DMA tension clamp as shown in Figure 5-4(f).

SDMS Experiment Setup

The MUT was connected to an LCR meter to permit the impedance measurement. For any impedance test, it is important to properly connect the electrodes to the LCR terminals. This is because the connecting cable will also cause extra fringing and parasitic capacitance (This is because each cable can be regarded as a long electrode, which brings an additional capacitance contribution between them). As shown in Figure 5-5, the four-terminal pair configuration (4TP) was used to connect the sample and the testing terminals of the LCR meter (Keysight E4980A) according to the manufacturer's manual[189]. The typical impedance measurement range using this connection is from 1 mΩ to 10 MΩ. Before connecting the sample to the system, OPEN and SHORT compensations were carried out. The LCR meter was connected to a laptop and an in-house developed LabVIEW program was used to continuously record the data at four electrical frequencies: 1 kHz, 10 kHz, 100 kHz and 1 MHz. The details of the program can be found in Appendix of the thesis.

Figure 5-5. The four-terminal pair configuration (4TP) for the LCR meter[189].

5.2.4 Impedance Test under Strain: Carbon Grease (CG) as Electrodes

CG has a low viscosity and therefore even light handling can cause it to smear or be wiped off, hence an extra protective layer of PDMS was used to maintain its shape. This layer by layer construction created specimens that were too large to be fitted into the DMA. Therefore the sample was stretched using a rigid manual tensile testing frame. The impedance data was recorded during hold phases at each specific strain. Therefore, as the electrical properties of the sample were only tested during the rest period it can be considered to be a discrete dielectric mechanical spectroscopy (DDMS) test.

Preparation of the Elastomer Specimen for DDMS

Conductive carbon grease 846, a carbon black filled silicone oil, (volume resistivity = 117 Ωcm , MG Chemicals) was used as stretchable electrodes as the CG electrodes needed extra protection to prevent smearing on the sample surface. Figure 5-6 shows the procedure for the careful preparation of the test specimens. PDMS (Blue Star) channel layers were applied to both sides of the MUT. The MUT was firstly placed in between the moulds as shown in Figure 5-6 (a) to Figure 5-6 (c). The uncured PDMS was then poured into the moulds and the moulds were closed, Figure 5-6 (d) and Figure 5-6 (e). The whole part was placed into an oven at 150 ^{o}C for around 15 minutes so that the PDMS channel layer would be fully cured. After carefully removing the samples from the

moulds CG was smeared into the PDMS channel (Figure 5-6 (f)). The overlapped area of the CG was around 5mm*10mm. The whole CG and the channel layer were sealed with an extra PDMS sealing layer which was then cured in the oven at 150 ^{o}C for a further 15 minutes. Figure 5-6 (g) shows a sample with one finished CG electrode where a thin aluminium plate was used to make further electrical connection.

DDMS Experiment set up.

The sample was clamped on a manual tensile frame. At each strain point, the image of the specimen was captured using a camera. The images were then further analysed using a MATLAB program developed by the author to define the actual strains. The MUT was firstly stretched or released to a certain strain and held for around 20 seconds while its impedance was measured by a Keysight 4294A precision LCR meter. Afterwards it was moved to the next strain step. The maximum strain using this set up was around 50%.

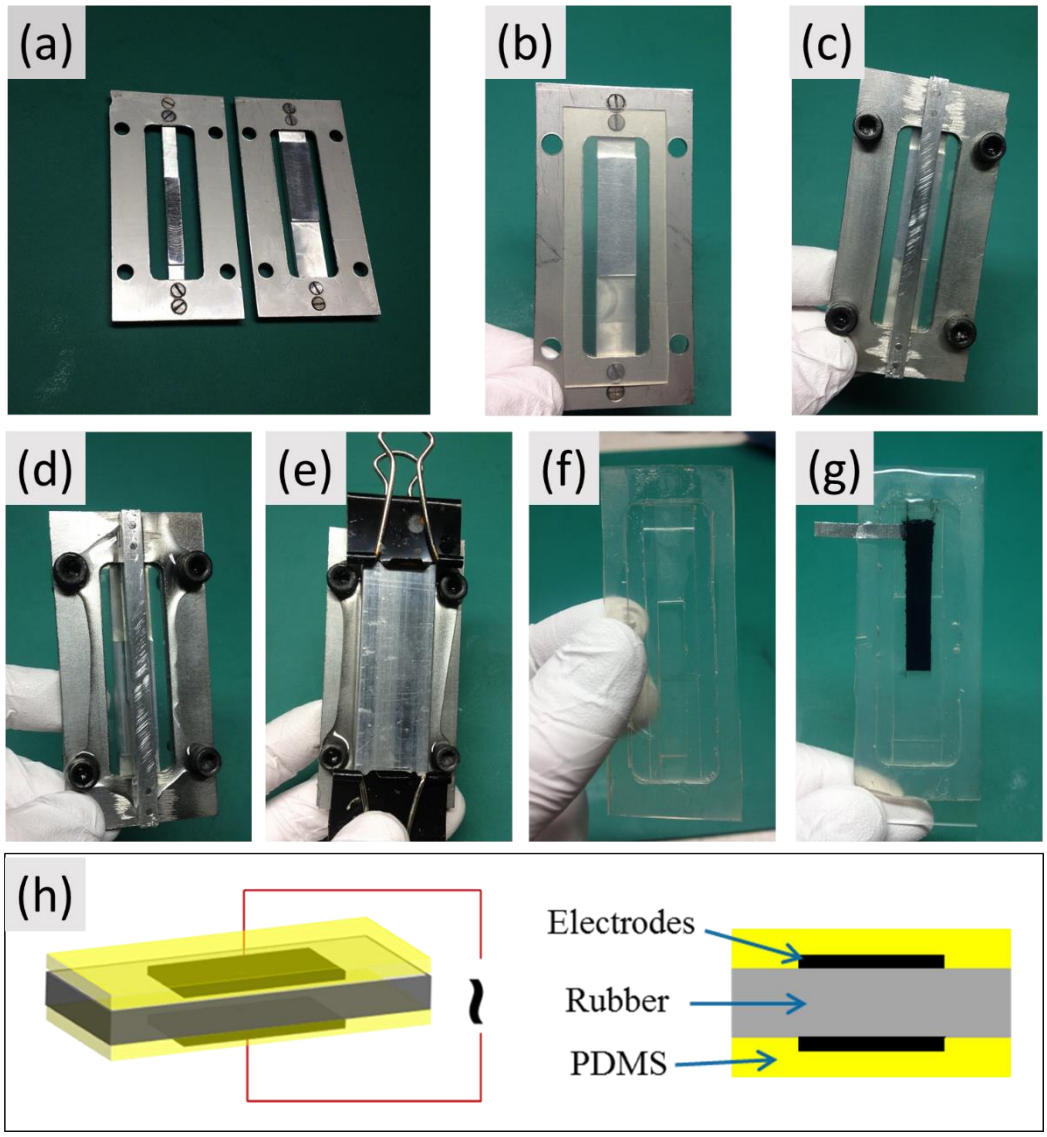

Figure 5-6. Preparation of the specimen for dielectric test under strain using carbon grease as stretchable electrodes. (a) Mould. (b) Place a specimen on the mould. (c) Close the mould with sample trapped inside. (d) Pour PDMS into the moulds. (e) Close the cover. (f) Sample with the moulded PDMS layers on both sides. (f) Cover the carbon grease onto the PDMS layer on one side and then coat the carbon grease with another layer of PDMS as protection. A thin aluminium plate was used to create an effective electrical connection. (h) A finished sample and its side view.

5.2.5 Impedance Test under Strain: Rigid Copper as Electrodes

As shown in Figure 5-7, The MUT has a dimension of 15 mm $\times$ 70 mm $\times$ 0.7 mm and was clamped on the manual tensile frame. The bottom electrode had a diameter of 18 mm

which was fixed on the stage. The upper electrode was movable and was connected to a drop gauge allowing the thickness of the MUT to be measured during loading. The inner circle of the upper electrode, with a diameter of 8 mm, was the test electrode. The outer circle of the upper electrode with a diameter of 18 mm was the protection electrode. The gap between the inner and outer circle was 1 mm. This design follows the recommendation of ASTM D 150-11[188].

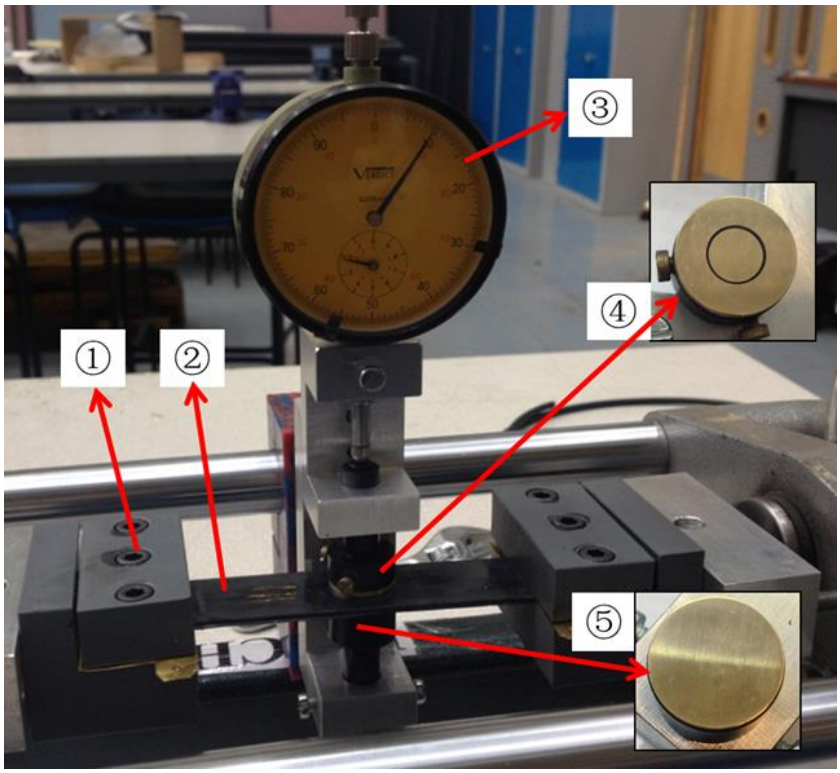

Figure 5-7. Experiment set up for measuring the dielectric property under strain using rigid metal electrodes. Each number is defined as: 1. Sample holder; 2. Materials under test (MUT); 3. Drop gauge for measuring the thickness of MUT; 4. Upper electrode: The inner ring is the testing electrode while the outer ring is for shielding. 5. Bottom electrode.

Before stretching or relaxing the MUT, the upper electrode was lifted out of contact with the rubber surface. When the required strain level had been attained, the top electrode was brought into contact with the sample which was now sandwiched between the two electrodes. The thickness from the drop gauge was recorded simultaneously with the impedance data using the Keysight E4980 LCR meter. These steps were repeated in order to measure the impedance behaviour over a wide range of strains during both a

loading and an unloading sequence. The sample was tested from 0% strain up to 50% strain. It took around 20 seconds for each measurement.

5.3 Results and Discussion

5.3.1 Dielectric Property of NR under No Strain: via Standard Impedance Test

Figure 5-8 shows the permittivity and dielectric loss of an unfilled NR which was tested according to ASTM D 150-11[188] without strain. κ' decreased with increase of strain which was caused by the deactivation of some dipoles with an increase of the testing frequency. It is typical behaviour for most solids in this frequency range as different dipoles inside the materials have different molecular dynamics and therefore they have different time scales in which they are activated. As a consequence specific types of dipoles can be filtered using the test frequency. The dielectric loss increased with the frequency, hence it obeyed Debye type behaviour as there is greater energy loss when dipoles cannot follow the frequency. This behaviour is quite similar when applied to the frequency response during dynamic mechanical testing. The absolute value of κ' shown in Figure 5-8 was higher than that shown in Figure 4-1(a). This is because the NR samples used in Chapter 4 were all dried before measurements.

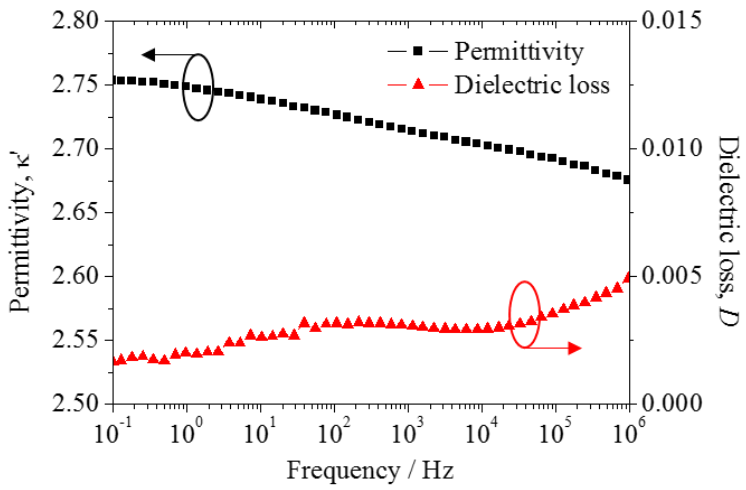

Figure 5-8. The permittivity and dielectric loss of unfilled NR under no strain at room temperature. Data was obtained using a Novocontrol Concept 40 Impedance Spectrometer.

5.3.2 Capacitance-Strain Relationship in SMDS & DDMS

A Standard Derivation

Although SDMS and DDMS use different electrodes, they are based on the same testing structure as shown in Figure 5-2. Therefore the complex impedance of the MUT (overlapped by the stretchable electrodes) can be obtained and the permittivity of the material can be derived according to Equation 2-39:

$$C = \kappa_{vac}\kappa' \frac{wl}{d} \qquad \text{Equation 5-1}$$

where κ_{vac} is the permittivity of the free space which is equal to 8.85419 pF/m. *w*, *l* and *d* are the width, length and thickness of the overlapped area of MUT respectively. As the stretchable electrodes are flexible and attached to the MUT, their shapes change in relation to that of the MUT region during mechanical testing. In a mechanical testing environment the specimen width and the distance between the electrodes are both reduced by an amount that is determined for an elastomer using a Poisson's ratio of approximately 0.5. Therefore, the change of dimensions follows the incompressibility constraint:

$$\Delta w / w_0 = \Delta d / d_0 = \nu_p \times \Delta l / l_0 \qquad \text{Equation 5-2}$$

where Δ stands for the dimension change, subscript 0 stands for the initial size and ν_p is Poisson's ratio. Therefore, when the sample is stretched, its dimensions will become:

$$l_i = (1 + \Delta l / l_0) l_0 \qquad \text{Equation 5-3}$$

$$w_i = (1 - \Delta w / w_0) w_0 \qquad \text{Equation 5-4}$$

$$d_i = (1 - \Delta d / d_0) d_0 \qquad \text{Equation 5-5}$$

where subscript *i* stands for the dimension at a specified tensile strain. By substituting Equation 5-3 to Equation 5-5 into Equation 5-1, the capacitance under strain can be derived as:

$$C_i = \kappa_{vac}\kappa'_i \frac{l_0 w_0}{d_0} \lambda \qquad \text{Equation 5-6}$$

where the extension ratio $\lambda = e + 1 = (l_i - l_0)/l_0 + 1$ and e is the uniaxial tensile strain. From this equation, the initial capacitance without any applied deformation ($\lambda = 1$) can be determined as

$$C_0 = \kappa_{vac}\kappa'_0 \frac{l_0 w_0}{d_0} \qquad \text{Equation 5-7}$$

As the permittivity of an unfilled elastomer can be treated as being approximately constant under strain (that is: $\kappa' = \kappa'_0 = \kappa'_i$)[190], Equation 5-6 can be further simplified as

$$C_{\mathrm{i}} = C_0 \lambda \qquad \text{Equation 5-8}$$

or

$$\frac{\Delta \mathrm{C}}{C_0} = \left(\mathrm{C}_i - C_0\right)/C_0 = e \qquad \text{Equation 5-9}$$

However, although the slope of $\left(\Delta \mathrm{C}/C_0\right)/e$ is predicted to be one according to this equation, in reality, it was found from the literature to be smaller than one (Table 5-1). To balance Equation 5-9, another parameter, which is called the gauge factor η has been added by some researchers:

$$\frac{\Delta C}{C_0} = \eta \times e \qquad \text{Equation 5-10}$$

This equation is commonly applied to the case of capacitance strain sensors. Table 1 summarises recent findings from the literature which show that η can be any value between 0 to 1. Although this equation can be used to fit the testing results well, the origin of such a gauge factor appears to be confused in the literature. Therefore this equation cannot be used to accurately calculate the permittivity of the materials. This appears to be one of the reasons why none of the researchers from the papers included in Table 1 went on to calculate the permittivity during testing. It seems they only simply used Equation 5-10 to help design sensors.

Table 5-1. Summary of the capacitance strain sensor reported in recent literatures.*

Name	Year	Electrode	Elastomer	Dimension [mm]	Gauge Factor	Sensitivity [pF]	Frequency [Hz]
M. Kollosche[191]	2010	Carbon Grease	PANI grafted co-polymer	25*10*0.04	~ 1	190.3 to 7560.8	100
D. Lipomi[192]	2011	CNT/PDMS	PDMS	2*2*0.3	0.41	/	/
F. Xu[193]	2012	AgNW/PDMS	PDMS	/	~ 1	1.75	/
D. Cohen[190]	2012	CNT/PDMS	PDMS	17*7.5*0.275	0.99	~ 16	10 k
M. Huang[194]	2013	Carbon Grease/PDMS	PI	15*5*0.6	0.85	-349.1	10k
W. Hu[195]	2013	AgNW/PU	Acrylic elastomer	15*8*0.25	0.5	5.83	1 k
C. Le[196]	2013	CNT/PDMS	PDMS	10*2*0.5	0.97	/	5 k
U. Shin[197]	2014	Aligned CNT/Ecoflex	Ecoflex	10*10	~ 1	/	/

*Some of data were digitized from the graphs of the related literature and were then further recalculated for finding the comparable parameters. This will probably lead to a loss of accuracy.

A More Accurate Expression

Figure 5-9(a) shows the data obtained by SMDS tests of unfilled NR (three repeat specimens are presented). The capacitance of the sample is linear against the extension ratio. Although this linear fitting has very good quality ($R^2 > 0.9997$), it does not follow the theory described by Equation 5-6 as the intercept is not zero. As was mentioned previously, this situation also existed in the literature[192, 195, 196]. Cohen[190] and Le[196] mentioned that this mismatch may arise from the fringing and parasitic capacitance which is caused by the non-uniform electric field around the edge of the electrodes. Therefore, the measured capacitance should always be larger than the predicted value. This might help explain such non-zero-intercept of the fitting line in Figure 5-9(a). In other words, the predicted capacitance was just linear shifted to a higher value. To verify this assumption, all the fringing and parasitic capacitance can be defined as a single parameter C_{corr}. Therefore, Equation 5-6 and Equation 5-7 can be rewritten as:

$$C_i = \kappa_{vac}\kappa'_i \frac{l_0 w_0}{d_0}\lambda + C_{corr} \qquad \text{Equation 5-11}$$

and

$$C_0 = \kappa_{vac}\kappa'_0 \left(\frac{w_0 l_0}{d_0}\right) + C_{corr} \qquad \text{Equation 5-12}$$

As κ'_i is strain independent for unfilled NR ($\kappa' = \kappa'_0 = \kappa'_i$), C_{corr} has to be strain independent as well. In this case, Equation 5-11 can be a linear equation to fit the data in Figure 5-9(a). Although a C_{corr} that is linear against λ can also linearize Equation 5-11, it is very complex and is not necessary. Fitting the results in Figure 5-9(a) can give the value of C_{corr} from the intercept. By knowing the value of C_{corr}, κ'_i of the MUT under strain can be calculated from Equation 5-11. Figure 5-9(b) shows that κ'_i is strain independent just as predicted. The difference between each test is mainly due to the errors in dimension measurements and the additional pre-strain that arises when the sample is loaded onto the DMA. An average value of κ'_i from three SDMS tests is 2.750 while κ'_i for the same material tested by the standard impedance test at the same frequency is 2.715. The difference between the two is only 1.3% which demonstrates

that Equation 5-11 is reliable. As shown in Figure 5-9(b), a similar result of κ'_i =2.723 has been determined for the DDMS test using the same method under the same conditions of NR. Note that Equation 5-11 is only in a linear format for the MUT whose κ'_i value is independent of the strain.

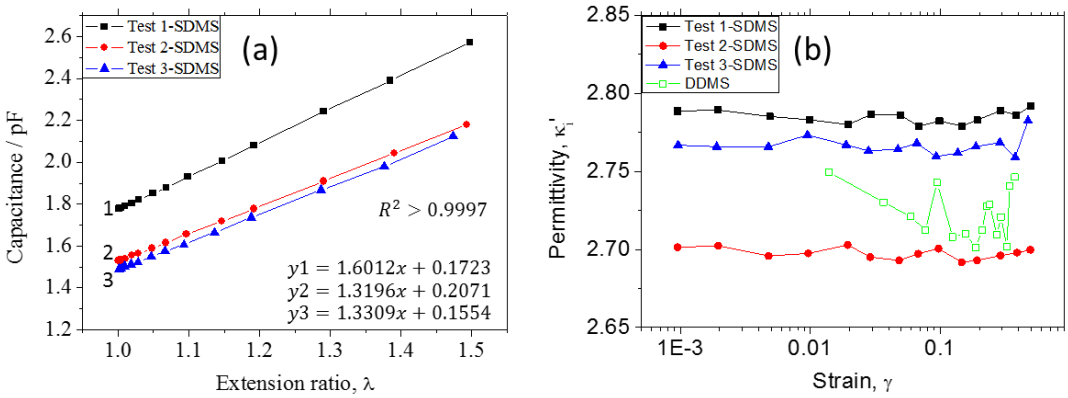

Figure 5-9. (a) The capacitance of unfilled NR tested by SDMS at an electrical frequency of 1 kHz. Tests 1 to 3 refer to three repeat tests for three different specimens. (b) The permittivity of NR calculated from SDMS tests and DDMS tests.

Explanation of the Gauge Factor

As shown in Table 5-1, most of the MUTs used in the literature have a strain independent permittivity, as the bulk of the work reported is based upon unfilled elastomers. Therefore, their results fitted the linear case of Equation 5-11. Considering $\kappa' = \kappa'_0 = \kappa'_i$, and then subtracting Equation 5-11 from Equation 5-12 gives:

$$\Delta C = \left(\kappa_{vac} \frac{l_0 w_0}{d_0} \right) \kappa' e \qquad \text{Equation 5-13}$$

Substituting Equation 5-12 into Equation 5-13 gives:

$$\frac{\Delta C}{C_0} = \left(1 - \frac{C_{corr}}{C_0} \right) e \qquad \text{Equation 5-14}$$

By comparing Equation 5-14 and Equation 5-10, an expression for the gauge factor can be obtained:

$$\eta = 1 - \frac{C_{corr}}{C_0} \qquad \text{Equation 5-15}$$

This equation suggests that η is governed by the ratio between C_{corr} and C_0. Generally speaking, a capacitor with a larger area to thickness ratio will have less fringing and parasitic capacitance (as C_{corr} decreases and C_0 increases). That is why ASTM D 150-11[188] suggests a large area to thickness ratio when making impedance measurements. Therefore, η should become larger with an increase of the area to thickness ratio. Figure 5-10 shows the relationship between the area to thickness ratio and η for the different capacitance strain sensors reported in the recent literature (including the current SDMS work). It shows that a large area to thickness ratio brings the value of η closer to the theoretical maximum value of 1. This is except for the work done by W. Hu whose anomalous result may come from poor test fixture calibration). As C_{corr} always exists, most of the literature data is presented with $\eta < 1$. Although these tests were carried out at different frequencies by different approaches, the results from the current SDMS measurement shows that the gauge factor is almost a constant value under different frequencies (0.888, 0.889, 0.884, 0.893 for 1 kHz, 10 kHz, 100 kHz and 1 MHz respectively).

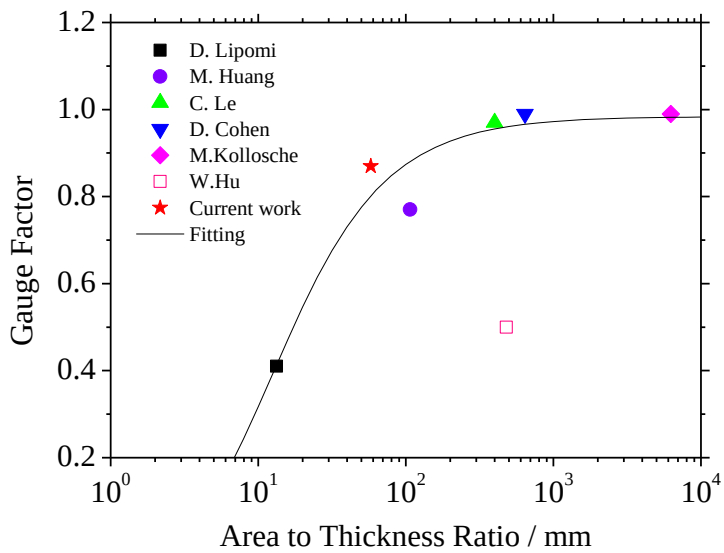

Figure 5-10. The relationship between the gauge factor and the shape factor of capacitance strain sensors reported in the literature.

5.3.3 Error Analysis of the SDMS and DDMS test

The fringing and parasitic capacitance

As discussed in the previous section, the fringing and parasitic capacitance only adds an extra term C_{corr} to the standard equation. It will not affect the calculated κ'_i value if it can be obtained from the linear fitting of an unfilled sample of the equivalent same size. So for the SDMS and DDMS test, a calibration test is needed using an MUT with a strain independent value of κ'_i (unfilled elastomers).

The Electrodes

Another issue of this test arises from the stretchable electrodes themselves. It is widely accepted that an ideal electrode should be able to maintain its high conductivity value at a large strain. Although there are reported[198] electrodes with good conductivity, it is still very difficult to make an electrode of acceptable high quality. However, as shown in Figure 5-9(b), the κ'_i obtained by the SDMS and the DDMS test matches to each other very well although the resistance of carbon grease ($\sim 10k\Omega$) is approximately an order of magnitude larger than that of AgNW (around a few hundred ohms) under strain. It seems that the conductivity is not as important for these types of test.

This is because the κ'_i value comes from the capacitance which is calculated using the imaginary part of the impedance X. During impedance testing, the electrodes can be treated as two resistors that are in series with the MUT (capacitor). Therefore, the resistance will only contribute to the real part of the impedance R and κ'_i and should always be accurate using any electrodes unless the electrodes become capacitive or the electrodes introduce huge interface effects. However, the resistance of the electrodes affects the dielectric loss value according to Equation 2-36. This effect will be increasingly obvious when the value of R becomes comparable to the resistance of the electrodes.

As is shown in Figure 5-11 (a), R decreased with an increase of the test frequency (by SDMS). When the frequency was below 100 kHz, R was almost strain independent. This is because the value of R was much higher than the resistance of the electrodes. However, when the frequency increased to 1 MHz, R increased with an increase of the strain. This increase came from the increase of the resistance of AgNW electrodes under strain as it dominated the value of R when at 1 MHz. As is shown in Figure 5-11 (b), X decreased with an increase of the test frequency which came from the geometric change of the MUT (by the SDMS). Figure 5-11 (c) shows the dielectric loss obtained by SDMS test as well. The dielectric loss was strain independent for all the frequencies except at 1 MHz and only at large strain. All the dielectric loss data (except of 1 MHz) obtained by SDMS matched the results from tests using a standard impedance test. The error of 1 MHz data may have been caused by the AgNW electrodes. Compared to the SDMS test, although DDMS tests gave reliable κ'_i values, as shown in Figure 5-9 (b), their dielectric loss data was very large. As shown in Figure 5-11 (b), only the dielectric loss measured at 1 kHz at low strain met the standard required of a loss of less than 0.01 during the DDMS test. That is because the resistance of CG was higher than AgNW.

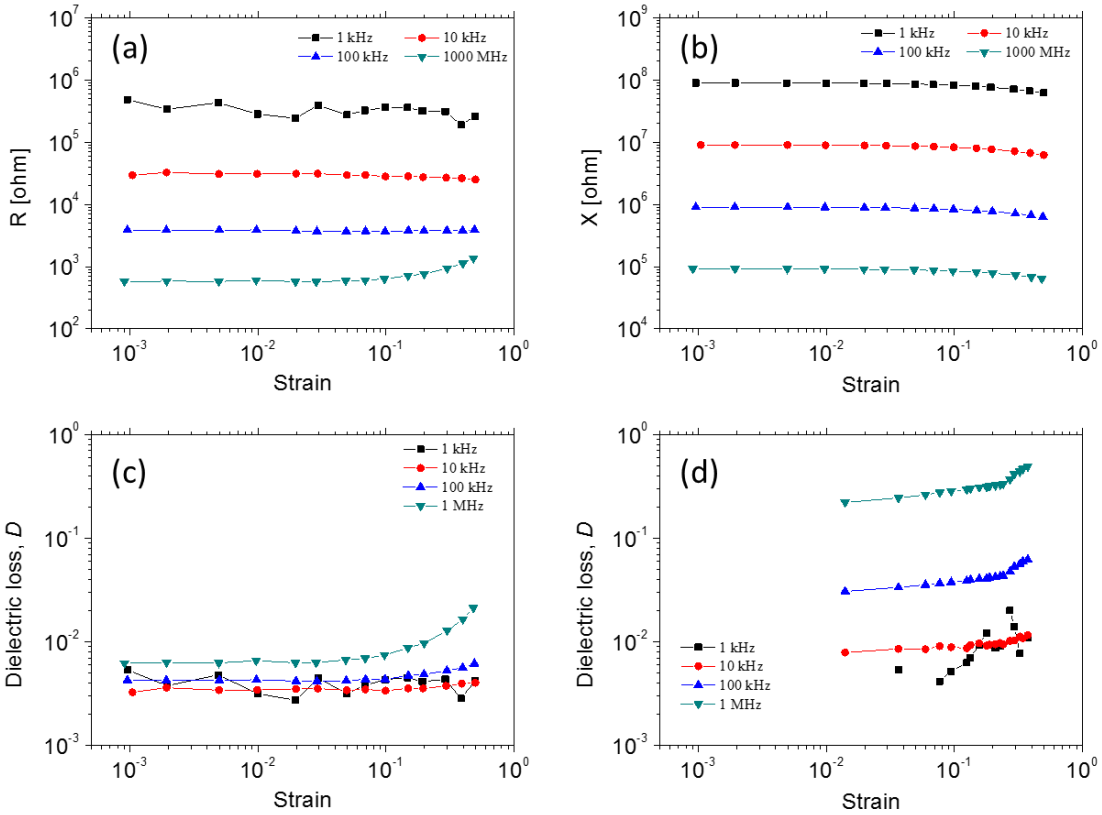

Figure 5-11. (a)-(c) the real (*R*) and imaginary (*X*) part of impedance as well as the dielectric loss (*D*) of unfilled NR tested at different strains and different frequencies using the SDMS test. (d) The dielectric loss data obtained by DDMS test of unfilled NR at different frequencies.

The Testing Equipment

When considering an accurate measurement of the dielectric loss, it is therefore only sensible to focus on the SDMS test. In this test, the strain was applied using a DMA which gives a displacement resolution of 0.5 nm while the resolution of the LCR meter is 0.001 pF at 1 kHz. However, the resolution of the LCR meter should be worse than the suggested value in the SDMS as nonstandard fixtures were adopted. The resolution of the SDMS system can be obtained from Figure 5-12 which shows the results of an unfilled NR sample tested at an electrical frequency of 1 kHz. It shows that the LCR meter can resolve changes in capacitance of approximately 0.005pF at 1 kHz. This sensitivity is enhanced dramatically at higher frequencies as the noise/signal ratio decreases. This means the resolution of the SDMS testing system is high enough to obtain reliable data

even at 0.5% strains for unfilled NR at 1 kHz. But this resolution can be dramatically enhanced when measuring materials with much higher permittivity values and at higher test frequencies. For example, the resolution is sufficient to be able to measure changes at 0.05% strains in NR at 10 kHz.

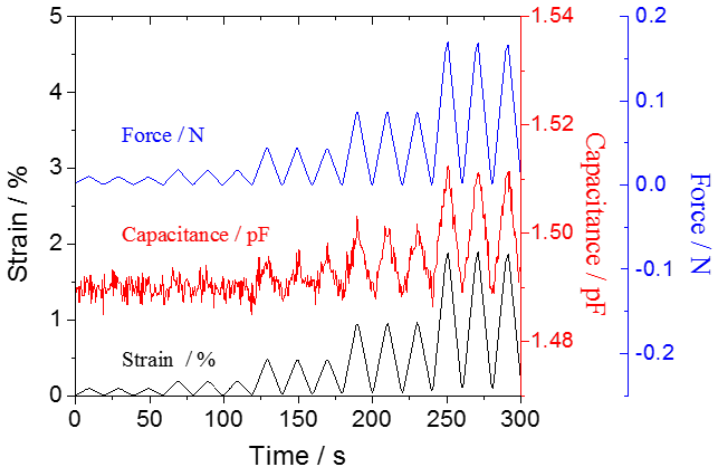

Figure 5-12. Typical data obtained from SDMS test of NR. The impedance data was measured at 1 kHz. Data was based one SDMS test without been averaged.

5.3.4 Disadvantages of Rigid Copper as Electrodes

Figure 5-13 shows the strained impedance data obtained by the rigid copper electrodes. The black squares are the data calculated via Equation 5-1. The absolute value of permittivity seems too high compared to that of the standard impedance test. Clearly the fringing and parasitic capacitance values need to be considered. However, it is hard to do accurate calibrations for 'home-built' fixtures. Recalculating the data using Equation 5-11 whilst considering a rough value of 2.85 pF experienced as the contribution from fringing and parasitic capacitance, the data after calibration looks reasonable. However, the permittivity increases from 2.63 to 2.85 when the strain increases from 0% to 50%. It might be caused by the quality of the calibration or because of a poor contact. Therefore, it is difficult to accurately obtain the dielectric properties of MUT under strain using this method. Testing in compression was shown to be preferable as the electrodes were always fixed on top of the sample during each test.

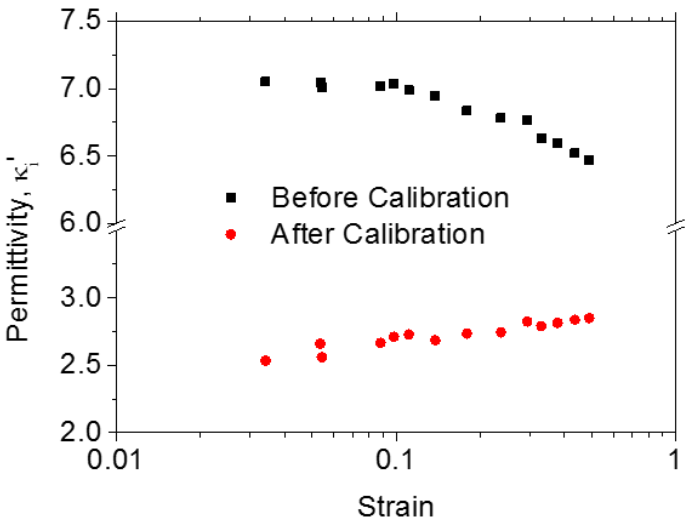

Figure 5-13. The permittivity of NR under strain tested with the rigid copper electrodes. Black squares are the data before calibration and red diamonds are the data after calibration.

5.4 Conclusion

In this chapter, a reliable equation has been proposed to calculate the dielectric properties from the measured impedance under strain using stretchable electrodes. The reliability has been established for different types of stretchable electrodes. This equation also explained the gauge factor in details and proved that this gauge factor is mainly affected by the shape of the MUT. Moreover, the capacitance or the permittivity is not affected by the quality of the electrodes whilst the dielectric loss can be dominated by the conductance of the electrodes when its resistance is comparable to the real part of the impedance. Therefore, for the following chapters, all of the strained dielectric measurements use the most versatile testing adopting the SMDS method.

6 Chapter Six: The Dielectric Behaviour of Strained Nanodielectric Elastomers

6.1 Introduction

As has been stated previously in this thesis, nano-structured particulate fillers such as carbon black and precipitated silica are widely used as the primary reinforcing materials in the tyre and rubber industries. Such fillers are often used to provide modifications to the static and dynamic moduli, fracture and abrasion resistance and more generally, as a means to modify the strain (e) dependent viscoelastic spectrum of rubber materials. However, although such technology has been in use for well over a century, the precise physical mechanisms behind the reinforcement phenomena are still not clearly understood or agreed upon.

Over the past century a wide range of predominantly mechanical-based experimental techniques have been used to investigate the mechanisms of reinforcement[36, 199]. Only relatively recently has significant, focussed attention been paid to the characterisation and interpretation of the dielectric properties of reinforced rubbers. Dielectric investigations present new opportunities for furthering the understanding of reinforcement based upon the sensitivity of the technique for observing changes in the morphology of flocculated or jammed filler particle networks as well as the interactions between filler particles and the polymer matrix. Thus, another possible novel approach to understanding the mechanical behaviour of filled rubbers under mechanical deformation is to simultaneously evaluate their mechanical and dielectric properties.

In rubber science and technology, the mechanical properties of filler-reinforced rubbers[1] are intimately linked to the filler particle size and morphology, the strain dependence of the flocculated/jammed filler network and the filler-polymer interaction(s). Key phenomenology associated with filler reinforcement is the onset of a non-linear strain dependence of the viscoelastic properties with increasing filler volume fraction, ϕ (called the Payne effect[34]). Additionally, particle reinforced rubbers can also exhibit significant strain history effects at finite deformations (Mullins effect)[200] and

cyclic stress softening phenomena. A range of microstructural mechanisms have been proposed to account for this behaviour including rupturing of the filler network[34, 201], polymer-filler interfacial de-bonding[202], the strain dependence of interphase polymer[203] and the unjamming of the filler network through the application of mechanical and/or thermal energy[204]. However, none of these mechanisms currently provide a unified microstructural description of the reinforcement phenomenon.

Over the past few decades, dielectric spectroscopy has been used to study filler particle flocculation[162] and distribution[165], filler network structure[103], strain induced crystallization[169] and compound degradation[205]. These investigations have demonstrated that the dielectric method is highly sensitive to the filler structure. However, only a few of these investigations[103, 105, 169, 172, 206] have applied the dielectric method to deformed rubber materials. This is very important because only by performing the test on materials under strained conditions, can the unsolved questions described previously be investigated. Furthermore, none of these studies[103, 105, 169, 172] have reported simultaneous in-situ measurements. In this way, their results are strongly affected by the time dependent viscoelastic nature of the polymer matrix. This may be due, in part, to the fact that traditional dielectric spectroscopy uses fixed, rigid electrodes to ensure a good connection between the electrode and the sample.

Fortunately, a reliable technique to simultaneously characterise the dielectric spectrum of rubbery materials under deformation is presented in Chapter 5. Therefore, in this chapter the simultaneous mechanical dielectric spectroscopy (SMDS) technique is used to study natural rubber compounds filled with different kinds of fillers. The aim being to answer the following two questions:

1. Will the dielectric properties change during deformation of the nanodielectric elastomers?
2. Can the dielectric spectrum be lined with the structure of filler networks and how might these networks change under strain?

* Part of this chapter has been published in *'Macromolecules'* as a paper entitled *'Strain Dependent Dielectric Behaviour of Carbon Black Reinforced Natural Rubber'*.

6.2 Experiments

6.2.1 Materials

The materials used in this chapter are listed in Table 6-1. Natural rubber (SMR CV60) / carbon black (HAF N330 or N220) masterbatch (ϕ=0.204) and natural rubber / carbon black (MT N990) compounds was prepared by compounding in a Banbury-type internal mixer for 5 minutes at around 149 $^{\circ}C$ with a rotor speed of 80 rpm (performed at Cabot Corporation, Boston, USA). To obtain a range of volume fractions (summarised in Table 6-1), the masterbatch was diluted by compounding with unfilled NR on a two-roll mill. At the same time, dicumyl peroxide (Sigma Aldrich) curative was compounded in to the masterbatch at a NR:DCP w/w ratio of 50:1. Samples were then cured at a pressure of around 60 bars for 1 hour at 160 $^{\circ}C$. Each sample had a thickness of around 0.7 mm.

Table 6-1. Samples codes and corresponding volume fractions used in this study

Sample Code	Filler Type	Filler Volume Fraction
NR/0	/	/
N330/0.025	N330	0.025
N330/0.049		0.049
N330/0.071		0.071
N330/0.093		0.093
N330/0.11		0.113
N330/0.13		0.133
N330/0.15		0.152
N330/0.19		0187
N220/0.049	N220	0.049
N220/0.071		0.071
N220/0.093		0.093
N990/0.20	N990	0.204
N990/0.34		0.338
HDS/0.20	Silica (HDS)	0.204

6.2.2 Tensile Mechanical Tests:

Samples were cut into dumbbell shapes for tensile tests according to ASTM D 412-06A(2013)[207]. Tests were all performed on an Instron 5566 tensile machine with a 1 kN

load cell and a video extensometer. The strain rate was around 1000 %/min. Three specimens of each sample were tested. The averaged data is shown in the following part.

6.2.3 Electrical Test (dc)

Keithley 6517A electrometer was used to measure the dc conductivity of all the samples via unshielded connection method. The dimension of each sample was approximately 20 mm x 20 mm x 0.7 mm. A pair of copper disc electrodes with a diameter of 14 mm were used with the sample was sandwiched in between. A voltage potential was applied across the thickness of the sample and the current was measured from which the resistance was calculated using Ohm's law. Each data point was averaged from three readings of the same sample. Finally, the conductivity was obtained based on the sample geometry.

6.2.4 Dielectric Test without Strain

Different dielectric testing methods were applied depending on the applied electrical frequency when there is no strain applied to the specimens. Experimental details were previously described in Section 3.2. Results based on single measurement but a good reproducibility has been checked and confirmed.

6.2.5 Simultaneous Dielectric-Mechanical Spectroscopy (SDMS) test

The SDMS method (using silver nanowires as electrodes) was previously described in Section 5.2.3. A uniaxial, multi-hysteresis strain profile was applied to the sample by a commercial DMA while collecting impedance data at electrical frequencies of 1, 10, 100, 1000 kHz using an LCR meter. The multi-hysteresis profile consisted of a linear ramp to 0.1 % strain followed by a linear ramp down to 0 % strain as shown in Figure 6-1. This cycle was repeated 3 times before loading to higher strains and cycling up to a maximum of 50% strain. The strain cycle frequency was 0.05 Hz. Only data measured at the maximum applied strain for each initial cycle is presented in this chapter except where it is otherwise stated. All the data is based on at least three repeats except where indicated.

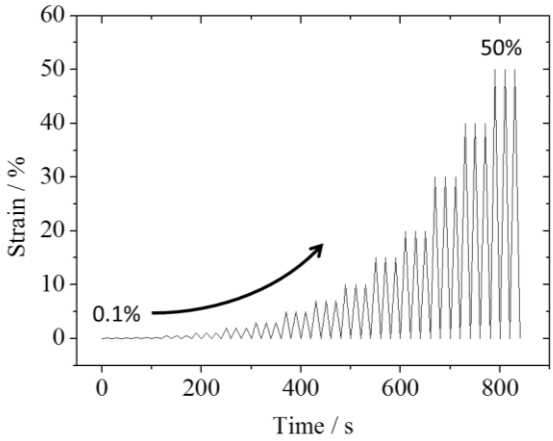

Figure 6-1. Schematic of the multi-hysteresis loading cycle use in the SDMS technique.

6.2.6 Dielectric Compression Tests

The dielectric properties have also been tested under mechanical compression using the setup shown in Section 5.2.5. Specimens were directly clamped by the copper electrodes without a metallic coating. The material was pressed to a certain strain and held in position by locking the electrodes. The dielectric measurement was then carried out via a Keysight E4980 LCR meter. Each data point was averaged from three readings of the same sample.

6.3 Result and Discussion

6.3.1 Carbon Black Networks in NR

Table 6-1 summarises the sample codes and corresponding volume fractions used in this study. The nitrogen-specific surface area of carbon black N220, N330 and N990 is 114, 77 and 8 $m^2.g^{-1}$ respectively. In rubber compounds, CB typically forms different levels of network structure depending primarily on the CB volume fraction, ϕ. The dc electrical conductivity, of filled compounds under static mechanical conditions has been widely used to investigate such CB structures[17, 73, 98]. Figure 6-2 shows a typical ϕ-σ_{dc} trend for CB N330 filled materials that used in this study. For low values of ϕ, the material is non-conductive and filler aggregates form only non-percolated, discontinuous filler networks (sub-clusters) during the curing process. For example, the inset SEM picture in

Figure 6-2 shows a cryogenic fracture surface image of N330/0.071 as an illustration of the filler dispersion in the rubber compound where only isolated CB aggregates and sub-clusters can be observed. However, when ϕ approaches the dc percolation threshold, ϕ_c^{dc}, the dc conductivity is found to increase by several orders of magnitude (its absolute value is still low). This corresponds to the formation of a percolating network of filler particles throughout the material, which established conductive pathways. Only when $\phi > \phi_c^{dc}$, does the dc conductivity become large (the material is essentially conductive) and it continues to increase somewhat with increasing ϕ due to further jamming of the filler network.

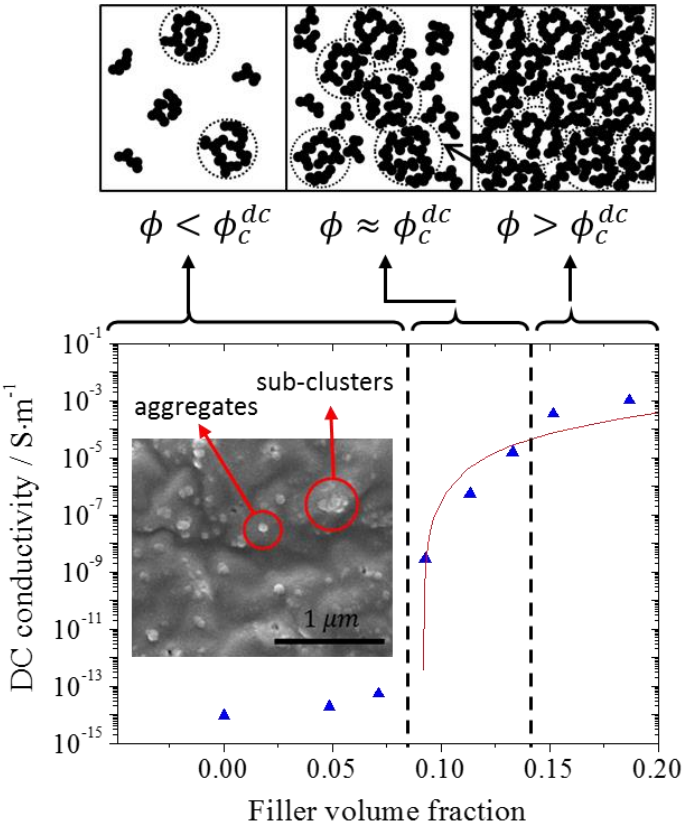

Figure 6-2. DC percolation trend for carbon black N330 filled NR. The inset graph is a SEM cryo-fracture surface image of the state of aggregate distribution throughout the NR matrix for sample N330/0.071.

The non-percolated filler networks exhibit a relatively low dielectric loss in a typical frequency range between 1 kHz and 1 MHz used in this study. Such low D values are very important for obtaining accurate values of κ^* via the impedance method as

previously discussed in page 30. This is because the κ^* derived from impedance methods always have multiple-solutions which depend on the magnitude of D. The difference between those solutions, can be ignored when D is small ($D < 0.1$). But huge differences in κ^* exist when D is large (for example the difference $> 100\%$ in κ^* when $D > 1$). For such cases, one can only focus on the general trend of κ^* as a function of, for example, temperature, frequency or strain rather than the absolute value. Therefore, for the dielectric measurement in this chapter, the samples with relatively low dc conductivity and low dielectric loss are the main focus (for example: $\phi < 0.13$ for carbon black N330 filled materials).

6.3.2 Effects of Filler Dispersion Quality on Dielectric Properties of Unstrained NR/CB

The dielectric behaviour of filled NR is highly dependent on the state of filler dispersion[73]. Figure 6-3(a) shows the permittivity and dielectric loss as a function of electrical frequency (f) for N330/0.13 with varying levels of carbon black dispersion. In this case the dispersion state was controlled by increasing the mixing time on a 2-roll mill (50, 100 and 300 passes through the rollers set at a gap distance of around 0.2 mm). As the dispersion state improved with the increased mixing energy, a greater number of interfacial MWS-dipoles and CHARGE-dipoles were achieved corresponding to increased polymer-filler interaction areas. Consequently both κ' and D values increased with increasing dispersion quality. These effects were reduced with increasing frequency. As shown in Figure 6-3(a), both the κ' and D values of different samples coalesced at higher frequencies. In the filled compounds the carbon black particles are highly conductive and the NR matrix surrounding the particles is insulating. This structure is somewhat analogous to colossal dielectric constant ceramic materials, where grains are much more conductive than grain boundaries. Lunkenheimer et al.[42] concluded that such high κ' is mainly caused by a strong MWS effect at the interface rather than the intrinsic dielectric properties of the component materials.

Figure 6-3(b) shows the tensile stress-strain behaviour of these materials. In the strain range below 150%, the mechanical behaviour of the materials with varying filler dispersion states was essentially identical. However, at strains above 150 % significant

differences are observed - with the better dispersed material showing a reduced incremental modulus. Probable explanations for this may be related to the shear modification of polymer chain lengths during mixing which may affect the crosslinked rubber network structure and therefore the ability of the material to strain crystallise. Additionally the improved dispersion of the filler aggregates may alter the magnitude of local strain amplification effects which may again affect the strain crystallisation process. The data presented in Figure 6-3 demonstrates that the dielectric method is far more sensitive to dispersed filler structures when compared with more traditional mechanical measurements. For all the samples discussed in this chapter, the mixing processes were controlled on a 2-roll mill at 100 roller passes.

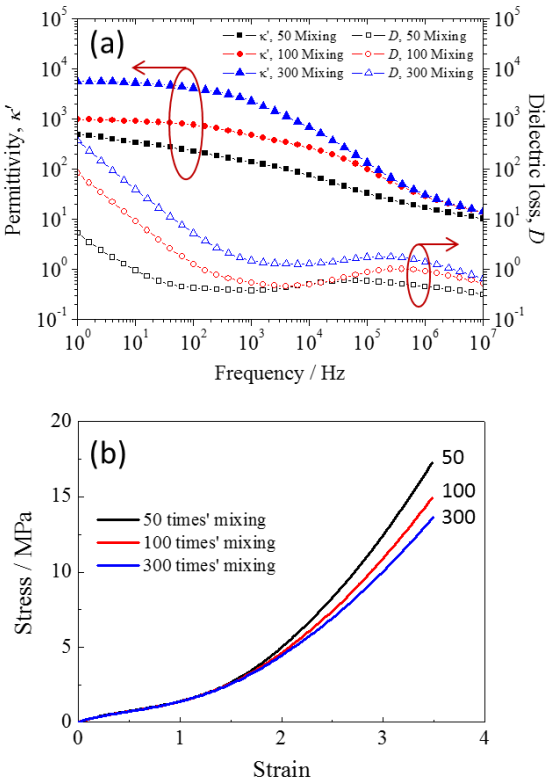

Figure 6-3. (a) Influence of mixing time on the measured dielectric properties. Samples were N330/0.13 mixed 50 times/100 times/300 times by two roll mill, named as 50 mix, 100 mix and 300 mix respectively. (b) Uniaxial stress-strain behaviour of the same samples.

6.3.3 SDMS of Unfilled NR

CV60 grade NR typically consists of around 95% cis-polyisoprene (PI) polymer and a few percent of other constituents such as proteins and fatty acids[208]. In dielectric terms PI

possesses both A-type and B-type dipoles. They are responsible for the 'slow' chain relaxation (β) and 'fast' segmental relaxation (α) respectively[120]. Figure 6-4 shows (a) κ' and (b) D that were both measured as a function of strain for NR/0 from 1 kHz up to 1 MHz. The data measured at small (0.1%) strain by the SDMS technique tends towards that measured at 0% strain by the standard impedance method when compared to the results shown in Figure 5-8. Results also show a strain independent κ' and κ'' for all the testing frequencies in each repeat test. The very small discrepancy between the values is within the error associated with either the calibration of the equipment or the accuracy of the measurements of the sample geometry. As has already been discussed in Chapter 5 (page 117), the increase of κ'' shown in Figure 6-4(b) is caused by the electrodes. However, it only affects a very limited region of the tests as shown in the top view of Figure 6-4(c). This effect is significantly smaller for the filled materials.

Due to the multi-component composition of NR, it possessed a broad distribution of dipole timescales. The dielectric properties of unfilled NR were highly dependent on electrical frequency. In the frequency domain κ' decreased with increased frequency as shown in Figure 6-4(a). Conversely, the dielectric properties of unfilled NR were essentially independent of applied strain at a fixed frequency (Figure 6-4(a)). Lee et al.[38] reported that the dielectric segmental relaxation was independent of strain for cured synthetic polyisoprene. But Hernández et al.[34] found an increase of the dielectric strength with strain for cured NR in conflict with Lee's results. They explained this increase was a consequence of increased dipole moments of the polymer under strain. For the rubber materials used here, although the rubber chains were aligned and confined in the direction of tension, there was very little change in the overall dielectric response. This may because the strains in the test were too small to develop any additional dielectric response. This suggests that the BULK-diploes (defined in Section 3.3.2) were independent of strain over the range tested here.

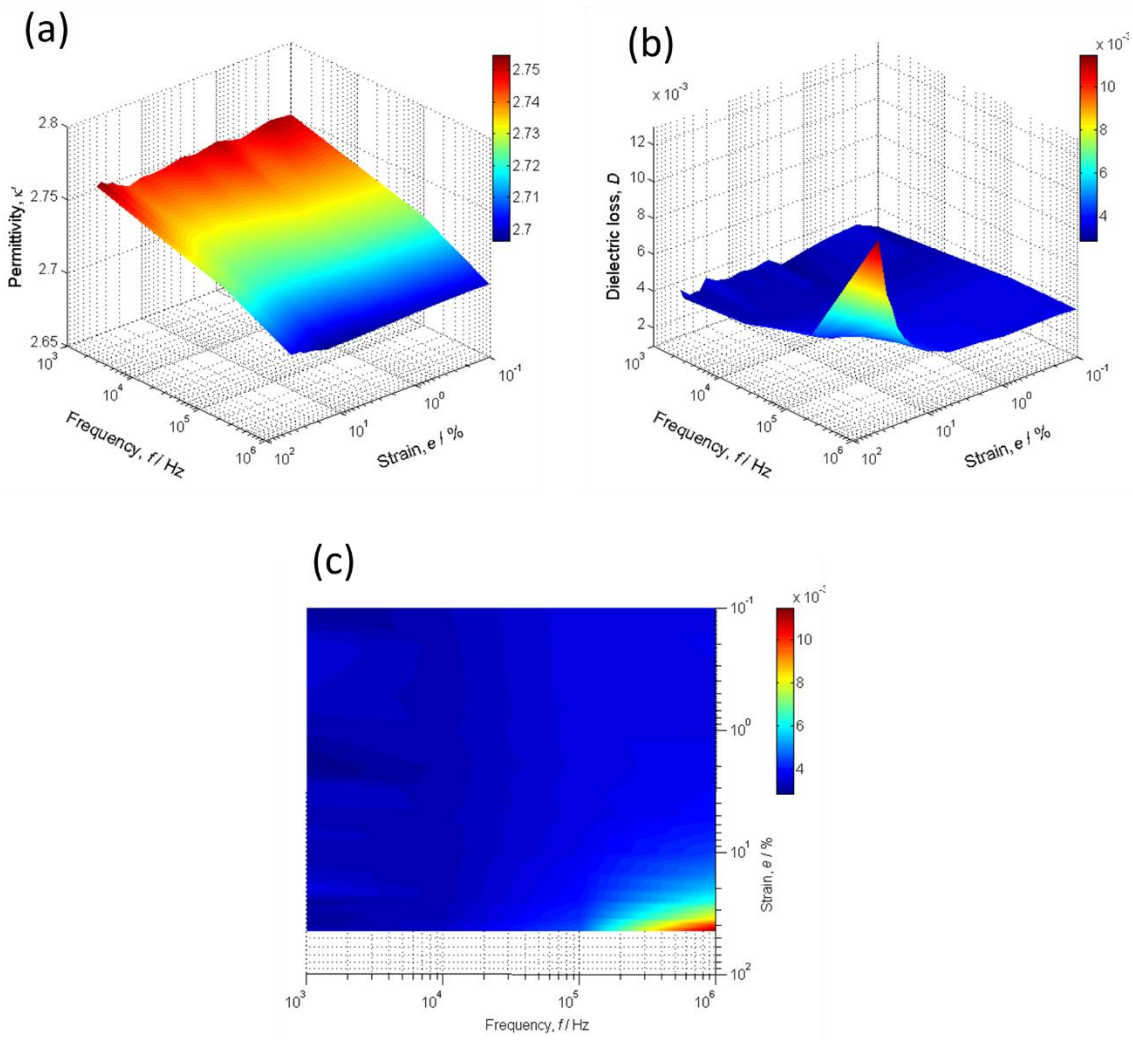

Figure 6-4. The (a) real part and (b) imaginary part of permittivity of unfilled NR as a function of strain and frequency. (c) is the top view of (b).

6.3.4 SDMS of Carbon Black Reinforced NR

The dielectric behaviour of NR becomes significantly more complex when carbon black particles are introduced. As summarized in section 3.3.2, at least five types of dipole may contribute to the observed permittivity under any given electrical frequency or deformation condition. As these different dipoles operate over differing length and time scales, it is possible to use the electrical frequency and/or the mechanical deformation as 'dipole filters' in order to discriminate between the different dipole relaxation timescales as a function of filler volume fraction.

As was discussed in Chapter 5, for unfilled NR, κ' was independent of the applied strain throughout the testing range. In such cases, the measured capacitance should be linearly proportional to the extension ratio as shown in the inset picture in Figure 6-5. It also shows the breakdown of this linear relationship as the filler volume fraction was increased. It therefore demonstrates that κ' of these filled materials was not constant under the application of strain.

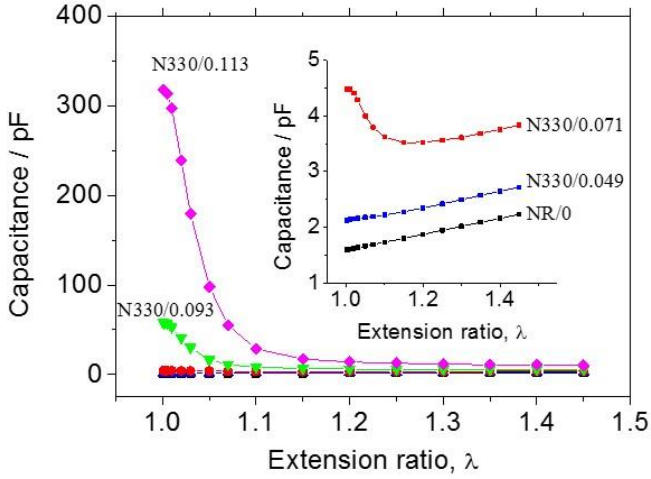

Figure 6-5. (a) Sensitivity limits of the SDMS method. The data is based on a single SDMS test of unfilled NR. All the dielectric data was measured at 1 kHz electrical frequency. (b) Measured capacitance under strain for different samples. The inset graph shows a magnification of data for NR/0, N330/0.049 and N330/0.071.

Figure 6-6(a) details the permittivity of natural rubber as a function of carbon black volume fraction under various electrical frequency and deformation conditions. The data collected for the samples at 1 kHz under 0.1%, 10% and 45 % strain are indicated by black squares, green inverse triangles and red circles respectively. Finally the permittivity measured under the no-strain condition at 40 GHz are indicated by the blue triangles. It is clear from Figure 6-6(a) that the measured permittivity of carbon black-reinforced NR depends upon the filler volume fraction, the electrical frequency and the applied strain. Figure 6-6(a) can be broken down into linear combinations of certain types of dipoles:

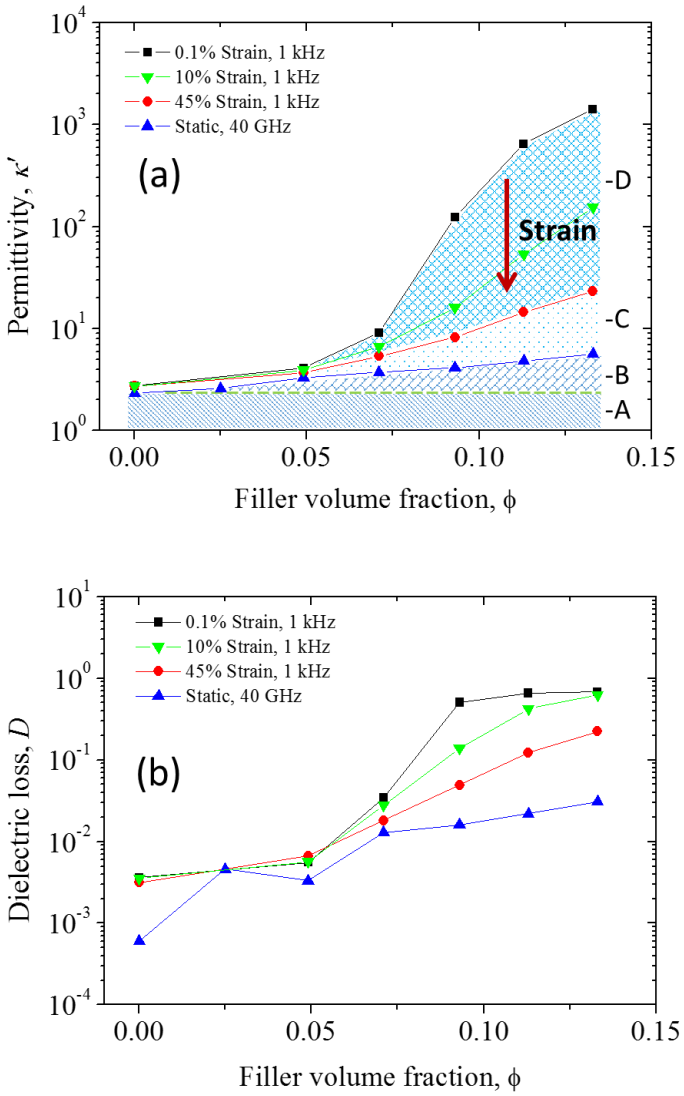

Figure 6-6. (a) The relationship between permittivity κ' and filler volume fraction, ϕ under different frequencies and strain conditions. (b) Dielectric loss against ϕ under different conditions. The filler is carbon black N330.

Zone A: This region refers to the bulk polarisation of the NR matrix at an electrical frequency of 40 GHz. In fact, all samples (filled and unfilled) showed very limited frequency dependent dielectric behaviour when the electrical frequency is above 7 GHz. Further to this it was found that at such high frequencies there was no systematic dependence of permittivity on the filler surface area which contrasted with other data from the literature performed at much lower electrical frequencies[209] (See Figure 3-3). This means that dielectric contributions from MWS-dipoles and CHARGE-dipoles, which

are highly dependent on the quantity of polymer-filler interfacial area, were filtered out at higher frequencies and could be ignored in the high frequency range.

Zone B: the permittivity collected at 40 GHz under no-strain conditions displayed an increasing logarithmic relationship between κ' and the filler volume fraction. Zone B could therefore only consist of contributions from GLASSY-dipoles and FILLER-dipoles since the electrical frequency is too high to observe any contribution from MWS-dipoles and CHARGE-dipoles. However, in previous work on similar materials (Chapter 4), no evidence for the existence of glassy/immobilised polymer domains was found[124]. This could be due to the volumes of glassy/immobilised material being too small to be observed by existing testing technologies. Assuming that there is no evidence for the glassy layer, then the GLASSY-dipoles are also considered to make an insignificant contribution to the total dielectric behaviour. This can be further confirmed from the strain independent dielectric behaviour of silica/0.2 shown in Figure 6-7.

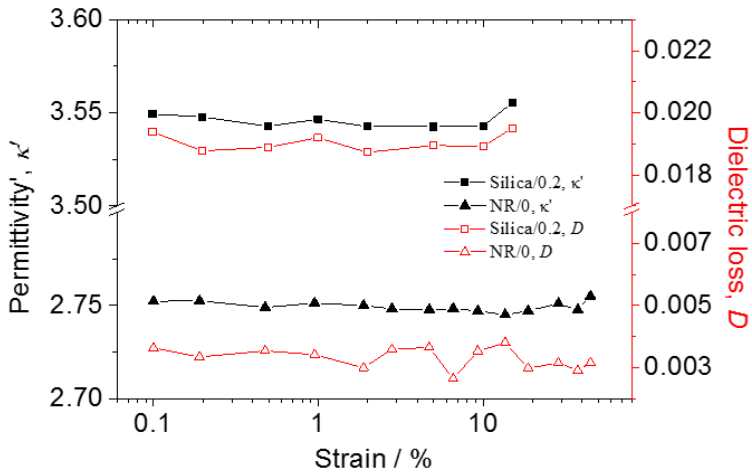

Figure 6-7. The strain dependent dielectric behaviour of Silica/0.2 and NR/0 measured at 1 kHz.

Zones C and D: for filled materials highlight that the contributions from interfacial MWS dipoles and CHARGE dipoles were substantial. For data collected at low frequency (1 kHz) with no applied strain, the contributions from the dipoles were at a maximum (the summation of Zone C and Zone D). However, when the mechanical strain was increased, the contributions from these dipoles (1 kHz) decreased dramatically (indicated by the transition from Zone D to Zone C in Figure 6-6(a)). Sow el al.[92] demonstrated that

mechanical strain can change the magnitude or even the direction of charge transfer between surfaces. Additionally, the MWS polarisation was highly dependent on the morphology of the filler network[39] which was also modified by the application of strain[98]. In this sense the application of mechanical strain is analogous to an increase in electrical frequency.

Due to limitations with the testing set up, the maximum strain which could be applied was limited to around 50%. It is presumed that Zone C would systematically reduce in magnitude if even larger strains were applied. Therefore a depleted Zone C refers to strain-independent dipoles such as extra FILLER-dipoles and some of the CHARGE-dipoles and MWS-dipoles. Figure 6-6(b) shows the dielectric loss for all the data presented in Figure 6-6(a). The maximum loss was around 0.68 which was relatively high but still allows one to discuss the relationship between κ' and strain using dielectric physics.

Figure 6-8(a) and Figure 6-8(b) show the whole SDMS spectra for the N330/0.071 sample. Thus the strain ($e: 0.1\% - 45\%$) and frequency ($f: 1\text{kHz} - 1\text{MHz}$) dependent dielectric behaviour of the material was constructed. Figure 6-8(c) and Figure 6-8(d) present projections of the data from Figure 6-8(a) and Figure 6-8(b) onto different planes. In the $\kappa' - e$ plane in Figure 6-8(c), the total strain dependence of κ' (that is $\kappa'_{e\to 45\%} - \kappa'_{e\to 0.1\%}$) was significantly larger at lower electrical frequencies. At the same time the total strain dependence of D (that is $D_{e\to 45\%} - D_{e\to 0.1\%}$) became more significant at higher frequencies as shown in the $D - e$ plane in Figure 6-8(d). This behaviour is due to the different timescales of the various dipoles and, as stated previously, there was a certain analogy between the role of strain and electrical frequency in suppressing dipolar contributions. Similarly, in the $f - e$ plane in Figure 6-8(c), the total frequency dependence of κ' (that is $\kappa'_{f\to 1\text{kHz}} - \kappa'_{f\to 1\text{MHz}}$) became much smaller at higher strain. In the $f - e$ plane in Figure 6-8(d) the total strain frequency dependence of D (that is $D_{e\to 1\text{k}} - D_{e\to 1\text{M}}$) was less significant at higher strains. This may be because most of the frequency-sensitive dipoles had already been filtered out by the application of strain. Figure 6-8 therefore shows that it is possible to 'filter' the contributions of dipoles to the

strain-dependent dielectric properties of the material by simply tuning the frequency of the applied electrical field. Unlike the limited range of strain rate accessible to DMA tests, electrical frequency in SDMS technology can be varied by orders of magnitude. This enables a very broad frequency filter for dipolar activity during the straining process.

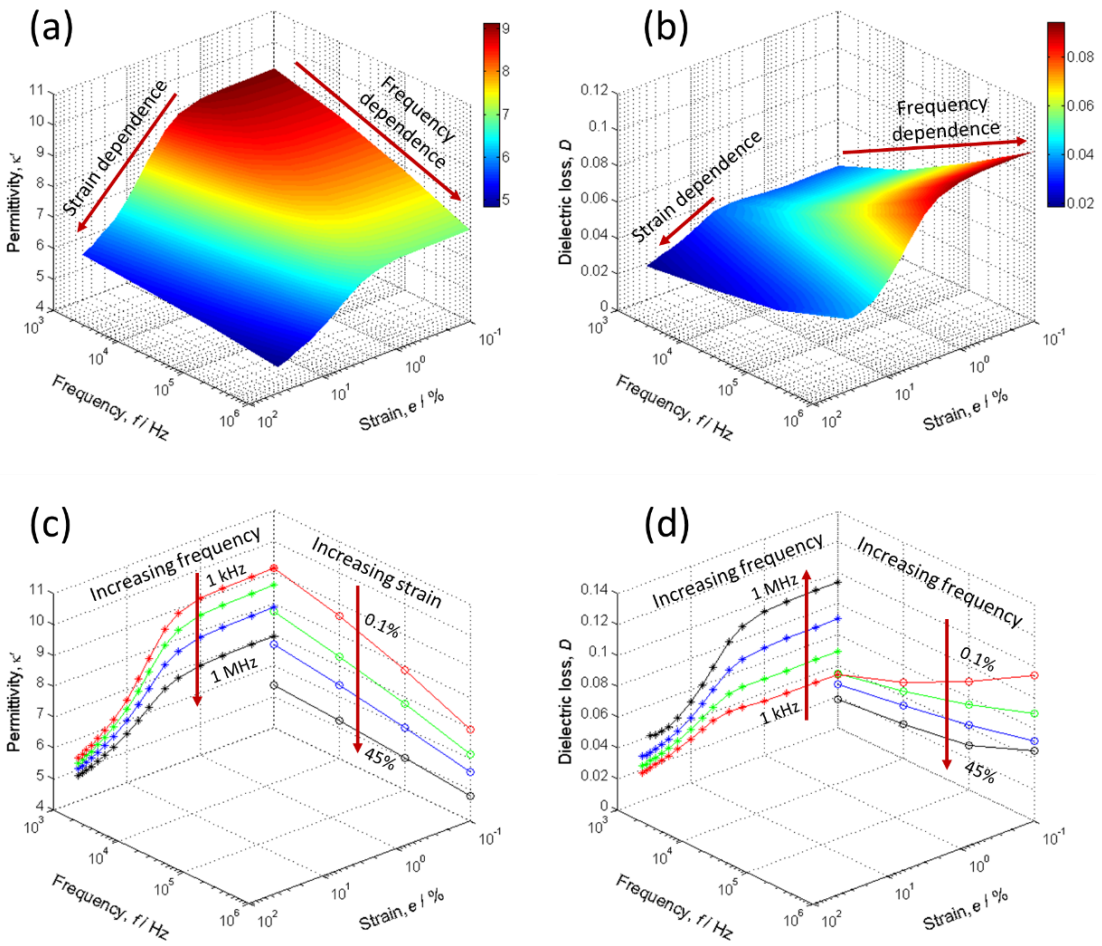

Figure 6-8. (a) & (b) Strain (e) and electrical frequency (f) dependent behaviour of the permittivity and the dielectric loss of N330/0.071. (c) & (d) Projections of data from (a) and (b) respectively with selected data. Solid lines connect the data measured at the same strain (Frequency-Permittivity plane) or frequency (Strain-Permittivity plane) as guides for the eye.

6.3.5 Dielectric vs Mechanical Spectroscopy

Figure 6-9(a) shows the dielectric and the mechanical behaviour of N330/0.071 subjected to a series of cyclic strain cycles, whereby each strain loop was repeated three times before the strain was increased incrementally to a slightly higher value. These

multi-hysteresis cyclic strain sweeps were all performed at a fixed electrical frequency of 1 kHz and at a relatively slow fixed strain cycle frequency of 0.05 Hz. Figure 6-9(b) and (c) were sub-data from Figure 6-9(a) of the cyclical softening sections of the multi-hysteresis strain sweep showing the three cycles undertaken between zero strain and a peak strain of 5%. The dielectric loss of N330/0.071 was smaller than 0.1 for all the strains which confirms the physical meaning of the derived permittivity.

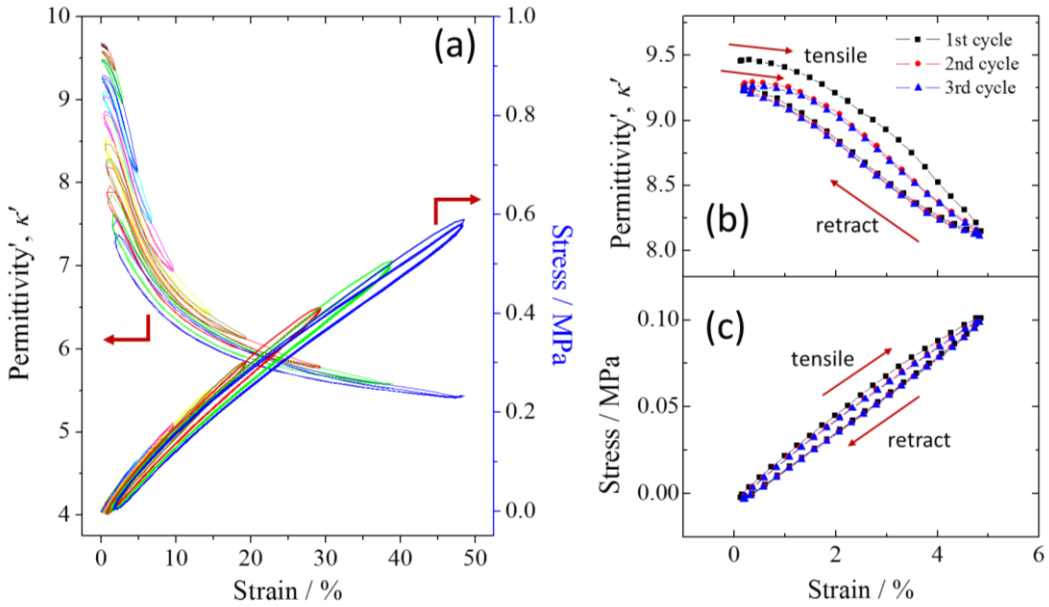

Figure 6-9. κ' and stress vs strain for N330/0.071. (a) Multi-hysteresis data from 0 to 50% strain. (b) & (c) Sub-data taken from the multi-hysteresis sweeps showing the 0-5 % cycle data more clearly. All SDMS data was measured at an electrical frequency of 1 kHz. Data was collected from one test and all data collected during the test is presented.

As discussed in Section 6.3.4, κ' decreased with an increase in strain amplitude. The primary reason for this is the strain dependence of MWS-dipoles and CHARGE-dipoles. However there are several other possible contributing and competing factors. For example, the filler aggregates can re-orientate with the direction of strain[98]. Recent work by Wang et al.[210] has shown that such re-orientation effects can be correlated with a decrease in κ'. Other factors may even compete to increase the measured κ' under applied strain. For example, the strain-induced rupturing of the filler cluster-cluster agglomerates actually increases the filler-rubber interface area (and therefore the extent of the interfacial polarisation) with increasing strain. Furthermore, there is a

strain dependence on the level of occluded rubber in the filled materials. Occluded rubber is defined as the rubber polymer trapped between agglomerated filler clusters and thereby mechanically 'shielded' from the globally applied strain field and electromagnetically 'shielded' from the global alternating electrical field[80]. As the agglomerated filler clusters break down under strain, this occluded rubber is progressively exposed to the global mechanical and electrical fields. Therefore, the strain induced dielectric behaviour was a result of competition of all these possible mechanisms. Examining the phenomenology of the dielectric response of the material under strain, following observations can be made:

1. The magnitude of the strain-induced decrease in κ' depended on the largest strain applied to the sample.
2. When strain was removed, κ' could only partially recover its initial small strain magnitude and did not fully recover its original magnitude (at least within the experimental timescale).
3. The cyclic strain dependence of κ' became increasingly reversible after the initial cycle at a specific value of maximum strain (Figure 6-9(b)). A dielectric hysteresis was apparent between loading and unloading cycles.

This behaviour is analogous to the simultaneously measured mechanical behaviour shown in Figure 6-9, Figure 6-10(a) and Figure 6-9(c) which exhibits the typical 'Mullins' effect and cyclic stress softening responses to multi-loop hysteresis testing. This similarity arose from the structural dynamics of the filler network and the filler-polymer interaction. However, the dielectric behaviour was dominated by dielectric phenomena at the polymer-filler interface rather than the bulk polymer. The full potential of the interfacial information extracted from such new experiments is still to be fully exploited.

Figure 6-10 shows both mechanical and dielectric data measured simultaneously for the various volume fractions of carbon black. Figure 6-10(a) shows the classical 'Payne' effect for these materials with the characteristic strain-dependence of the tensile modulus becoming more apparent with increasing carbon black volume fraction. Similarly, Figure 6-10(b) and Figure 6-10(c) show a corresponding systematic strain-

dependent decrease in both κ' and *D*. Clearly this can be seen as a dielectric analogy of the mechanical 'Payne' effect. Note that the strain dependence of the dielectric properties spans several order of magnitude from small to high strains. This again indicates that the SDMS method is significantly more sensitive to microstructural dynamics in filled rubber than traditional mechanical testing. This was more obvious in the normalised plot shown in Figure 6-11. The normalised mechanical modulus and permittivity (the real part) is defined as $|E_t - E_{t0}| / E_{t0}$ and $|\kappa' - \kappa'_0| / \kappa'_0$ respectively where E_t is the modulus, E_{t0} is the modulus without strain and κ'_0 is the real part of permittivity without strain. In Figure 6-10(c), although the dielectric loss data of these samples were increased by carbon black, it is still very useful to exploit this strain sensitivity of both κ' and D to study the morphology of filler structures or to build strain sensors.

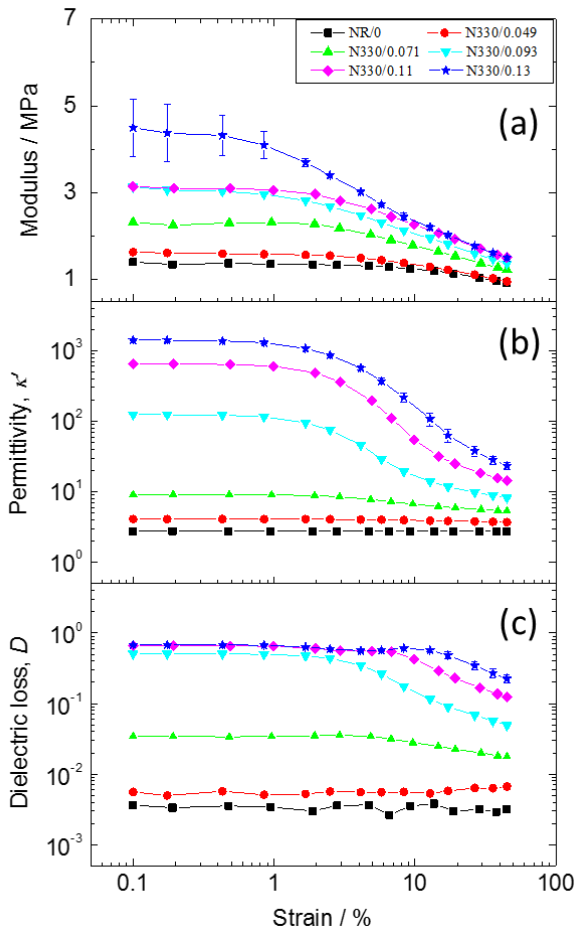

Figure 6-10. (a) Static modulus (stress/strain) vs strain collected simultaneously with the dielectric data. (b) & (c) Strain-dependence of permittivity and loss factor of all samples (measured at 1 kHz electrical frequency).

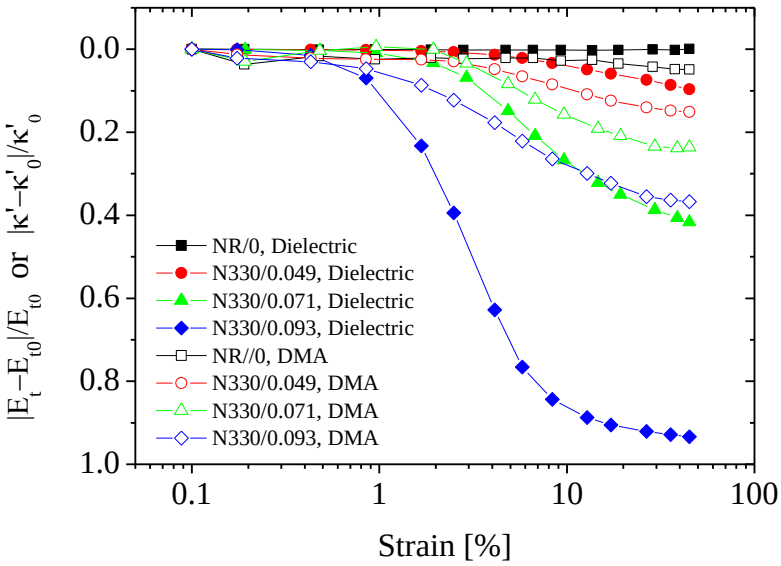

Figure 6-11. The strain dependent behaviour of standardised modulus and the permittivity of unfilled and filled (N330) materials.

6.3.6 SDMS at Different Strain Rates

Two strain rates were used here. As shown in Figure 6-12(a), the N330/0.071 sample was strained to 50% using a high strain rate of 300%/min with a return to 0% strain using the same rate and then repeated for 3 times. After that, a slow strain (24%/min) and a fast strain (300%/min) was used in turn for four strain cycles in total. Figure 6-12(b) is the simultaneously measured κ' of N330/0.071. Figure 6-13 shows the same data as Figure 6-12(b) but presented against strain. Moreover, Figure 6-13(a) only shows the initial 3 cycles (black line) as well as the subsequent slow strain cycle (red chain line). Figure 6-13(b) adds one more cycle (fast rate, blue chain line) and Figure 6-13(c) presents the rest of the cycles.

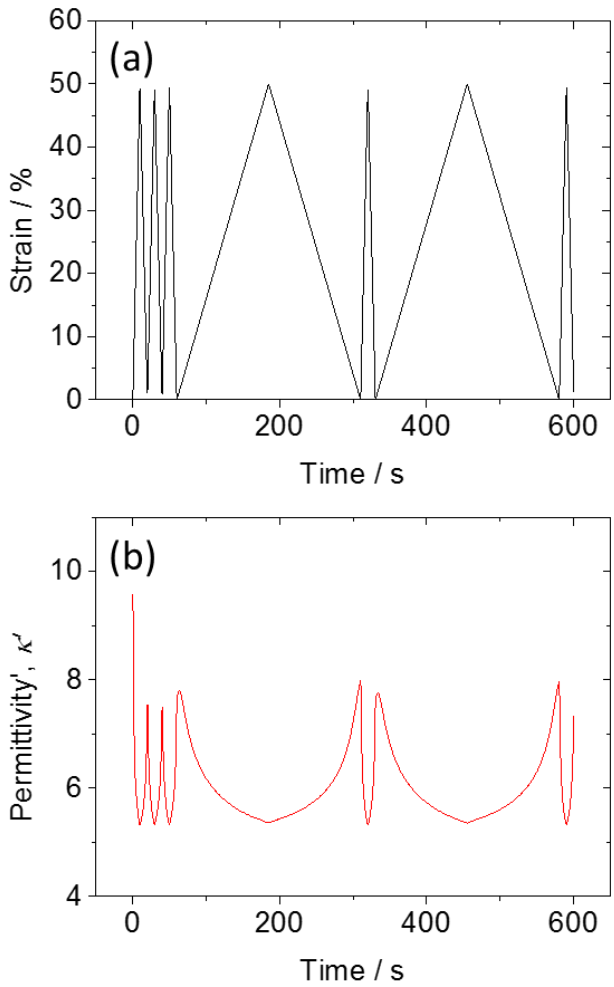

Figure 6-12. (a) Strain steps and the (b) corresponding dielectric data (measured at 1 kHz) of a various strain rate test. The sample under test is N330/0.071.

As shown in Figure 6-13(a), κ' measured during slow rate cycle was always higher than that measured during high rate (including the high strain region although the difference is too small to be seen in this graph). A smaller hysteresis was observed in the slow rate cycle. Interestingly, at small strain, κ' measured during retraction could be even larger than that of tension at the same strain. It means that although the tension force breaks the filler structure and brings about a decrease of κ' (MWS), this kind of break, from the dielectric point of view, is also only partly reversible (as κ' cannot go to its original value). Figure 6-13(b) adds the subsequent cycle with high strain rate (blue chain line). In the tension step, κ' was larger compared to the previous tension step. However, the retraction step overlapped with the previous high rate cycles which means this part of

break-rebuild process was more reversible. Similar behaviour was also observed in the in-situ dc electrical-mechanical test showing that there both reversible and irreversible breakdown of the filler networks existed[98].

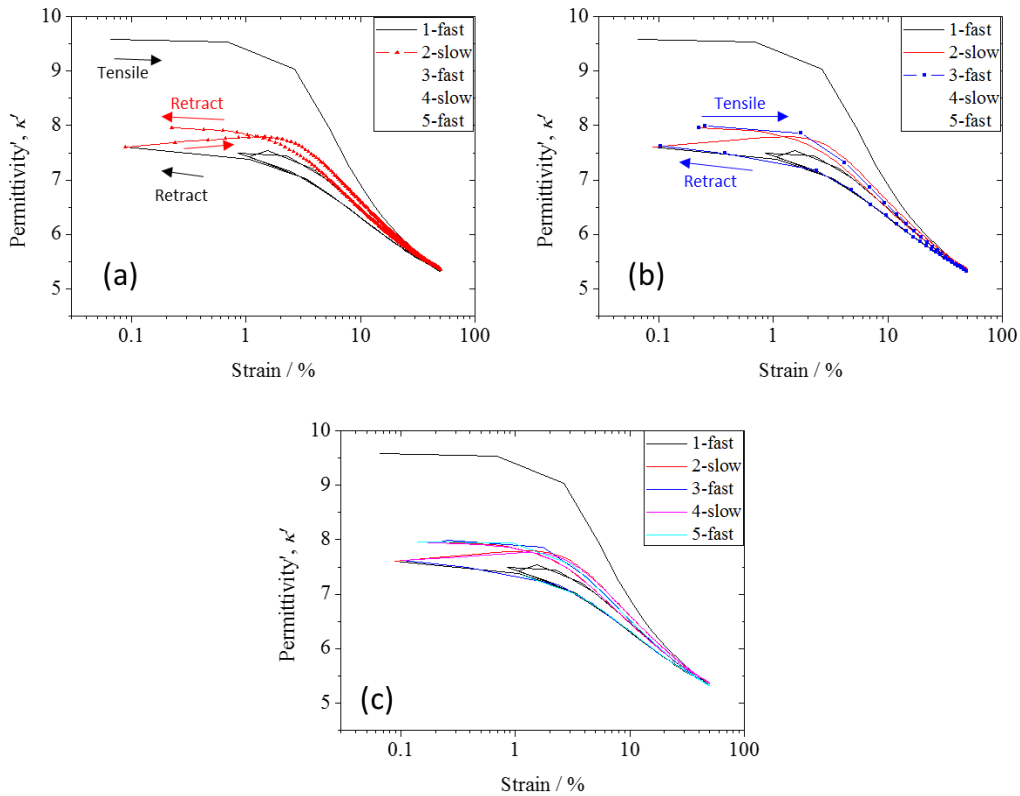

Figure 6-13. The strain dependent behaviour of the real part permittivity of N330/0.093 that measured at 1 kHz under different strain rate. (c) is the overall data represented from Figure 6-12 while (a) & (b) are shown step by step. Arrows indicate the tension or retraction steps.

6.3.7 The Dielectric Behaviour of NR/CB Composites under Compression

Figure 6-14 shows the dielectric behaviour of N330/0.071 under compression. Firstly, the absolute value in this graph may be shifted by a few percents compared to the real value because the in-house made fixtures were difficult to accurately compensate for the background. Compared to the tension test, κ' shows a similar trend in compression which is not surprising as the electrodes were placed in the same direction for both tests. However, the decreasing trend of κ' was much weaker in Figure 6-14(a) than that in Figure 6-9(a). This may be because the strain perpendicular to the electrodes in the

tension test is larger than that in the compression test. Therefore, the direction of the electrical field may affect the strain dependent dielectric properties.

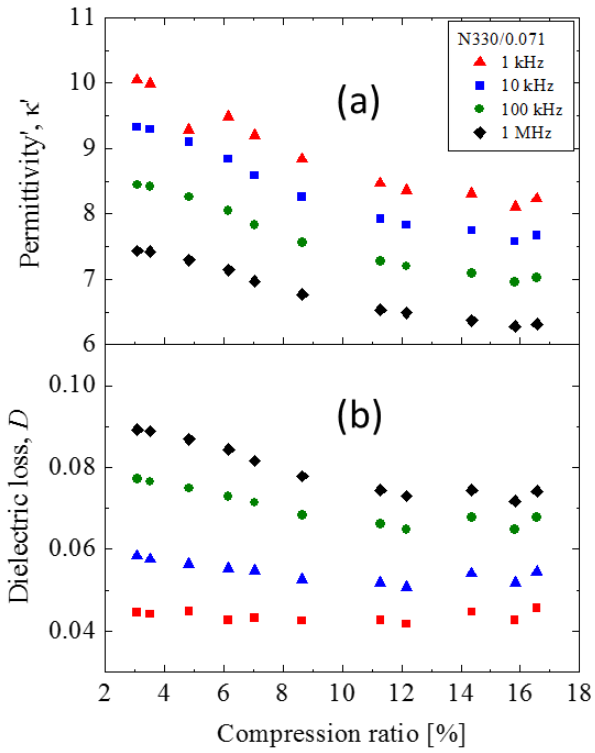

Figure 6-14. The dielectric behaviour of N330/0.071 under compression.

6.3.8 SDMS of NR filled by Carbon Black with Different Morphologies.

Carbon black N220 had the smallest particulate size. Therefore, it had the highest structure compared to carbon black N330 and N990. Moreover, the primary particle size of N990 was relatively large and consequently it had only a very limited structure[17]. Figure 6-15(a) shows the strain dependent behaviour of NR filled by N220, N330 and N990. The filler volume fraction ϕ of N220 and N330 were the same (0.093). However, NR/N990 composite was used with a much higher volume fraction ($\phi = 0.20$). This is because N990 shows almost no strain dependence when the filler volume fraction is below 0.2 (low structure). Fillers with a smaller particle size had a stronger strain dependence which has also been observed by the storage modulus in the mechanical test[34]. It is more obvious in the normalized data in Figure 6-15(b). As has already been shown, the decrease of κ' arises from the decrease of the intensity of MWS and CHARGE-dipoles. Therefore, the MWS and charge polarisation should be proportional

to the level of the filler structure of the NR/CB system. Once again, this effect is much stronger compared to the mechanical test as the decrease of κ' can be an order of magnitude larger for samples with even a very low filler volume fraction.

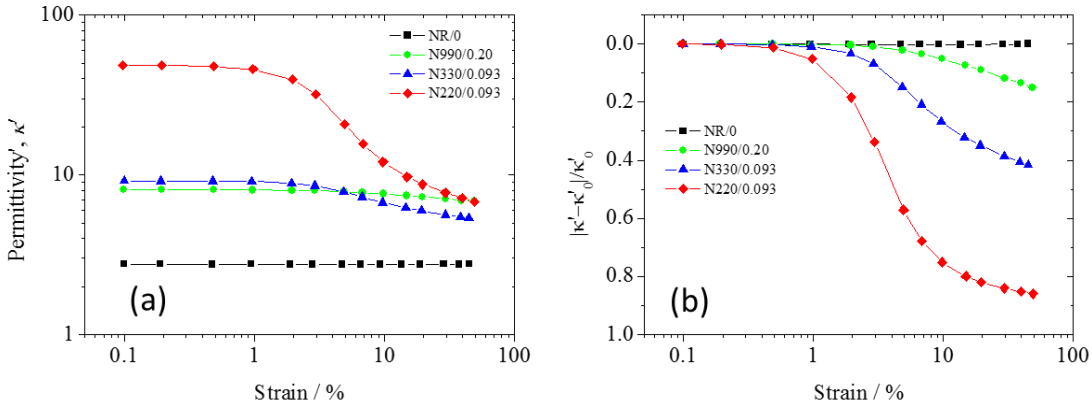

Figure 6-15. Comparison of the strain dependent dielectric behaviour of samples filled by different kinds of carbon blacks.

6.4 Conclusion

This chapter clearly demonstrates that, not only the mechanical modulus but also the permittivity displayed a nonlinear dependence on mechanical strain. Therefore the permittivity of nanocomposites (even with a very low filler concentration) was not a fixed 'constant' (although it is also known as dielectric constant) but varied dramatically under even a few percent applied strain. This effect is highly dependent upon the filler morphology and the strain rate. The underlying reason for this is the strain dependence of MWS polarisation and strain dependent charge transfer effects at the interface. Secondly, dipoles around the interface region could be suppressed or 'filtered' by applying mechanical strain. Additionally, at each strain level the contributing dipoles could be further 'filtered' by modulating the electrical frequency. This technique provides an effective way to study the electrical structure of the interface region. Finally, in comparison with traditional mechanical testing, the dielectric spectrum has a far more sensitive dependence on the structural dynamics of the compounds. This may be useful as a powerful tool in the tyre and rubber industries for characterising, understanding and monitoring of rubber products.

7 Chapter Seven: Conclusion, Ongoing Work and Future Work

7.1 Conclusion

This thesis has examined the filler polymer interface as well as the dynamic behaviour of filler-filler networks within filled rubber composites under strain, using the newly developed SDMS (simultaneously dielectric mechanical spectroscopy) technique. This development has initiated a new technique for the study of the microstructure-property relationship as well as the filler reinforcement mechanism of nanodielectric elastomers. It has been demonstrated that the dielectric properties can not only reveal information of the different relaxation processes in the composite but also details of the filler network. Now this technique has been developed, it should be possible to use the technique to extensively study the strained dielectric spectrum. This thesis has focussed on natural rubber/carbon black systems and the key findings are summarised in the following chapters as:

In chapter 3:

- Based on existing knowledge [1, 67, 93], a new way to classify different types of dipoles in nanodielectrics was proposed. The classifications refer to: dipoles that belong in the bulk polymer phase; dipoles in the confined polymer phase; dipoles caused by the charge transfer between two phases; the dipoles caused by the MWS effect and dipoles that are inside the fillers. They are named as BULK-dipoles, GLASSY-dipoles, CHARGE-dipoles, MWS-dipoles and FILLER-dipoles respectively. This concept groups the dipoles by their location and their origin rather than their length scales or relaxation times. This approach helps simplify the analysis and can be used to explain the measured results comprehensively.
- Conductive fillers such as carbon black can reinforce the dielectric properties of the composites mainly due to the MWS-dipoles although the other four types of dipoles also make a contribution. Therefore, the percolation behaviour of κ' is only observed at low frequencies. It is caused by the increased interface as well as the interconnection of the diffusion electrical layers. However, the percolation

behaviour of the other dielectric parameters, such as κ'', D and σ_{ac}, mainly arise from a dc percolation type theory and they possibly even share the same percolation threshold as the dc percolation.

- The dielectric reinforcement is almost independent of the filler size in the GHz range because of the minimised MWS polarisation.

In chapter 4:

- The segmental relaxation of natural rubber was not shifted but it was slightly broadened by the presence of silica and carbon black. This may be due to the highly structured filler network. The interface regions appeared to be considerably smaller than has been suggested in the past. This indicates that the GLASSY-dipoles can be roughly treated as a kinds of BULK-dipoles in the materials throughout the rest of this thesis.
- The segmental relaxation of natural rubber was also affected by the quantity of curatives and the crosslink density. Increases in both slowed down the segmental dynamics and brought about a slightly higher glass transition temperature.

In chapter 5:

- Stretchable electrodes such as carbon grease and silver nanowire were used to accurately measure κ' of rubbery materials using the relationship given in Equation 5-11. However, the accuracy of the measured D depended on the testing frequency and the conductivity of the electrodes under strain. Generally speaking, the measured D was more accurate at lower frequencies and with the most highly conductive stretchable electrodes such as silver nanowires.

In chapter 6:

- The dielectric parameters, both κ' and D both decreased dramatically with strain even for the non-percolated carbon black filled natural rubber. This is because the conditions of the interface were changed under strain. However those dielectric parameters were almost independent of strain for silica filled natural rubber because the MWS interface polarisation in these materials was much weaker.

- The dielectric properties also exhibited a nonlinear strain dependent behaviour as well as a cyclical softening behaviour under various types of strains. These changes to the behaviour related to strain rate and the filler morphology.
- It is apparent that the strain depend dielectric properties and the mechanical properties are both a reflection of broadly similar mechanisms in the composite system: the nature of filler structures and filler-polymer interactions. However, the dielectric signal is a much more sensitive indicator and it has a great potential for use as a probe to investigate changes to the filler structure or the polymer mobility at the interface.

7.2 Ongoing Investigations

7.2.1 Smart Strain Sensors Using SDMS Technology

As discussed in chapter 5, the current capacitance strain sensors are normally made using unfilled elastomers. The sensitivity is limited from the theory (the gauge factor is always smaller than 1). Although it is possible to detect very small strains, it requires a high resolution of an advanced LCR meter. However, such equipment is expensive and cannot be applied to simple devices on a massive scale. Fortunately, by using nanodielectric elastomers, the sensitivity of these sensors can be easily increased by orders of magnitude. Figure 7-1 shows the sensing behaviour of a capacitor strain sensor made by Polyisoprene (IR) filled by N220 with a filler volume fraction of 0.093. Its sensitivity between 0 and 10% strain was around 24.8 pF. If this sensor is made by unfilled IR with the same dimensions, then the sensitivity, defined as the change of capacitance under a percent of strain, can be no more than 0.03 pF (assuming κ' of IR is 3 at 1k Hz) as predicted by Equation 5-15. Moreover, the sensor showed very good reversibility after the first strain cycle as demonstrated in Figure 7-1. Based on this idea, the present work is to use other conductive fillers such as carbon nanotubes or graphene, to further enhance the sensitivity and at the same time to maintain this reversibility.

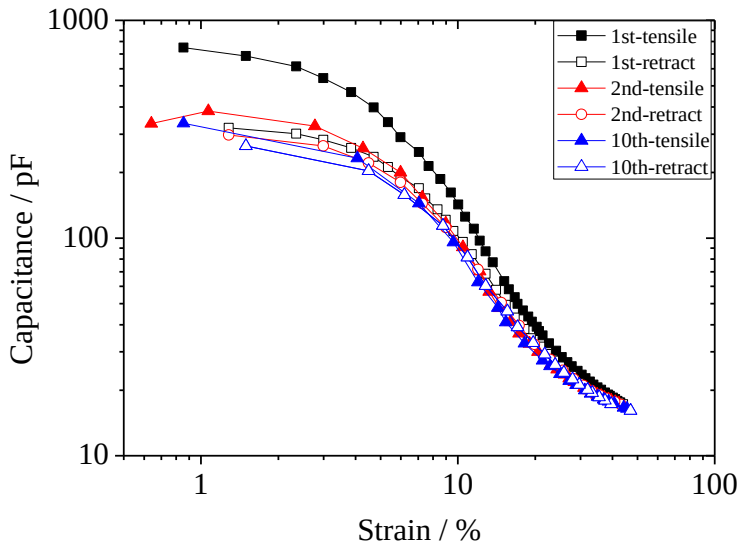

Figure 7-1. The sensing behaviour of IR filled by carbon black N220 with a volume fraction of 0.093. Data measured at 1 kHz. Carbon grease is used as the electrode.

7.2.2 Quasi-optical Test of Nanodielectric Elastomers under Strain

Although an SDMS test can produce very reliable results, it requires the very careful preparation of the electrodes. Section 2.2.3 introduced the newly developed quasi-optical system that can test the dielectric property of the material in a free space. It means the material can be tested without using any contacts. As shown in Figure 7-2(a), the testing signal transports from the transmitter to receiver via four reflectors while the material is held between Reflector 2 and Reflector 3. Figure 7-2(b) shows an enlarged view of the area where the sample is held. The transmission/reflection parameters were obtained by a VNA (vector network analyser) and the complex permittivity can then be worked out by the transmission function discussed in Section 2.2.3.

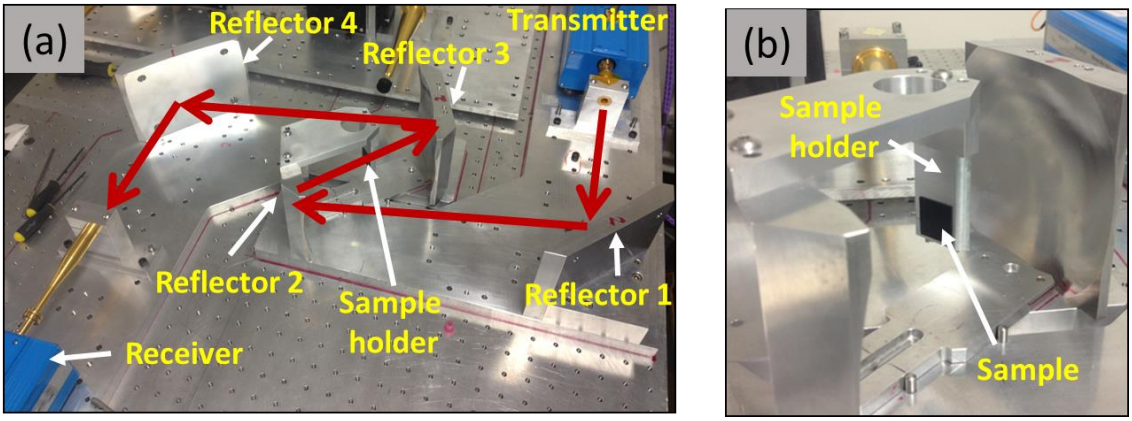

Figure 7-2. (a) The setup of a quasi-optical dielectric testing system (transmission). (b) A close up of the sample holder shown in (a).

The results of initial studies using this system to test natural rubber cured by different concentration of DCP (0.5 phr, 2 phr and 3 phr) are shown in Figure 7-3(a). It can be clearly seen that, even in the THz range, the permittivity is systematically decreased with an increase of the curing additives. Therefore, it may be used to evaluate the crosslink density of rubber components in the future as a powerful non-contact and non-destructive technique. A further experiment on N330/0.049 (NR filled by N330 at a volume fraction of 0.049) has been tested prior to the application of a strain, immediately after being strained to around 200% and released and again after being relaxed for 3 hours as shown in Figure 7-3(b). After being strained and released, κ' of the materials decreased by around 2 percent but the values fully recovered after 3 hours. In fact the relaxed results even showed a slightly higher κ' than the original value although the modest increase was of the order of the accuracy of making the measurements of the sample's dimensions. Clearly the frequency used here was far too high for the MWS polarisation to be observed, therefore this change may arise from the CHARGE-dipoles. That is, the electrical diffusion layer was modified under strain due to the break and rebuilt process of the filler structures which recovered with time. From this demonstration, it can be found that this quasi-optical system has great potential to study both unfilled and filled elastomers. One aspect of the ongoing work of this thesis is to design a new sample holder which can simultaneously apply a strain to the materials allowing the SDMS approach to be broadened to THz range.

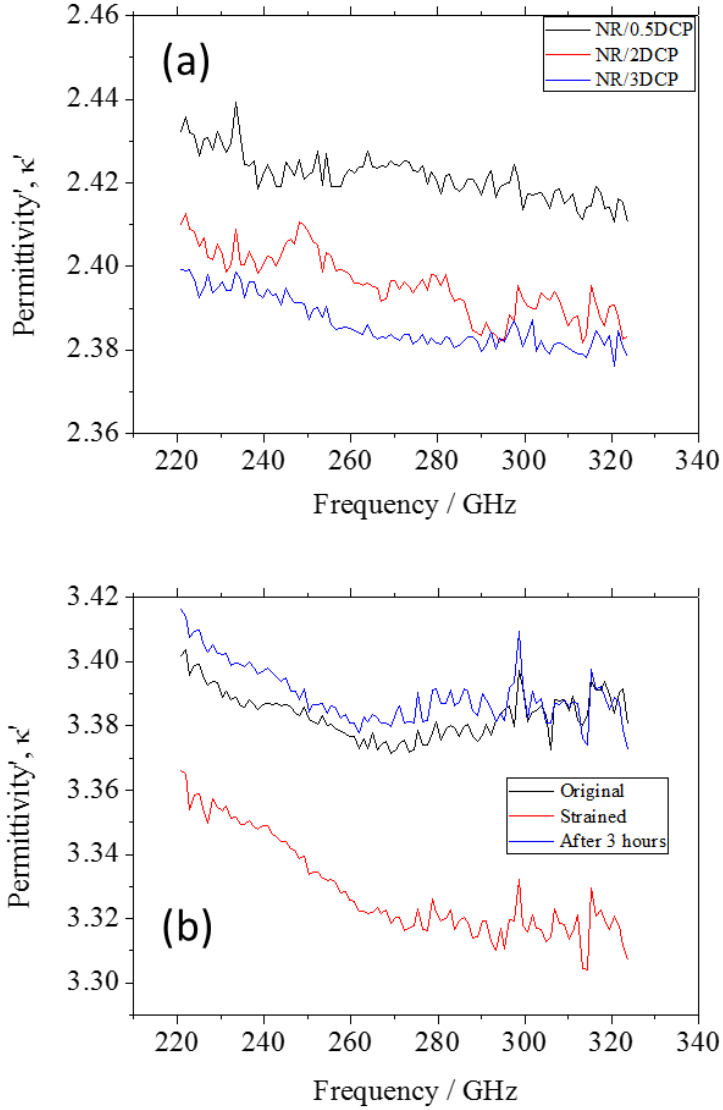

Figure 7-3. The THz range dielectric properties of (a) unfilled NR cured by different amount of DCP (b) NR filled by carbon black N330 with a volume fraction of 0.049. The

7.3 Future work

It is believed that, this thesis reports for the first time a systematic study using the simultaneous dielectric and mechanical property tests on nanodielectric elastomers. Although interesting behaviours was investigated using this SDMS technique, a deeper understanding or a precise explanation of the phenomena is now needed. This can be achieved by applying this SDMS technique to different nanocomposite systems. For example, the filler surface can be modified using silane or other suitable thermal treatments to provide different surface activities. Also it is possible to use fillers

manufactured using different methods that then adopt a different morphology. By controlling the surface activity and the shape of the primary particles different filler structures can be designed. Analysing SMDS results of these materials, it may be able to precisely locate the origin of the dielectric reinforcement. This will clearly allow a deeper understanding of the relationship between the dielectric properties and the microstructure of materials to be known.

In addition, as has been shown in Chapter 6, the dielectric properties such as κ' show a recovery of their behaviour with time. Therefore, studying the recovery behaviour of κ' at different temperatures might help identify the activation energy of the recovery. As the mechanical data can be obtained simultaneously via the SDMS technique, the recovery energy can actually be obtained from the mechanical data as well. By comparing the differences in these two rates of recovery, even stronger evidence for the relationship between the dielectric spectrum and the mechanical spectrum can be obtained.

References

[1] T. J. Lewis, *Nanometric Dielectrics*, IEEE Transactions on Dielectrics and Electrical Insulation 1994, 1, 812.
[2] J. P. Runt, J. J. Fitzgerald, *Dielectric Spectroscopy of Polymeric Materials: Fundamentals and Applications*, American Chemical Society, 1997.
[3] ASTM, Astm D1566-14 Standard Terminology Relating to Rubber, ASTM International, West Conshohocken, PA 2014.
[4] J. Priestley, *A Familiar Introduction to the Theory and Practice of Perspective*, Printed for J. Johnson and J. Payne, 1770.
[5] M. Sethuraj, N. T. Mathew, *Natural Rubber: Biology, Cultivation and Technology*, Vol. 23, Elsevier, 1992.
[6] C. M. Blow, *Rubber Technology and Manufacture*, Butterworths London, England 1971.
[7] R. N. Datta, *Rubber Curing Systems*, Vol. 12, iSmithers Rapra Publishing, 2002.
[8] P. R. Dluzneski, *Peroxide Vulcanization of Elastomers*, Rubber Chemistry and Technology 2001, 74, 451.
[9] D. Zhao, *Synthetical Technologies of Polymers*, Chemical Industry Press, 2008.
[10] R. L. Anthony, R. H. Caston, E. Guth, *Equations of State for Natural and Synthetic Rubber-Like Materials. I. Unaccelerated Natural Soft Rubber*, The Journal of Physical Chemistry 1942, 46, 826.
[11] L. R. G. Treloar, *The Physics of Rubber Elasticity*, Oxford university press, 1975.
[12] J. D. Ferry, *Viscoelastic Properties of Polymers*, John Wiley & Sons, 1980.
[13] J.-B. Donnet, *Carbon Black: Science and Technology*, CRC Press, 1993.
[14] A. C. C. LTD, Production Reactor in the Oil Furnace Method, 2010.
[15] T. Fabish, D. Schleifer, *Surface Chemistry and the Carbon Black Work Function*, Carbon 1984, 22, 19.
[16] D. Rivin, *Surface Properties of Carbon*, Rubber Chemistry and Technology 1971, 44, 307.
[17] L. B. Tunnicliffe, J. Kadlcak, M. D. Morris, Y. Shi, A. G. Thomas, J. J. Busfield, *Flocculation and Viscoelastic Behaviour in Carbon Black-Filled Natural Rubber*, Macromolecular Materials and Engineering 2014, 299, 1474.
[18] S. Brunauer, P. H. Emmett, E. Teller, *Adsorption of Gases in Multimolecular Layers*, Journal of the American Chemical Society 1938, 60, 309.
[19] ASTM, Astm D6556-14 Standard Test Method for Carbon Black-Total and External Surface Area by Nitrogen Adsorption, ASTM International, West Conshohocken, PA 2014.
[20] ASTM, Astm D1510-13 Standard Test Method for Carbon Black--Iodine Adsorption Number, ASTM International, West Conshohocken, PA 2013.
[21] ASTM, Astm-D3765-03-Standard Test Method for Carbon Black—Ctab (Cetyltrimethylammonium Bromide) Surface Area, ASTM International, West Conshohocken, PA 2003.
[22] ASTM, Astm D2414-14 Standard Test Method for Carbon Black-Oil Absorption Number (Oan), ASTM International, West Conshohocken, PA 2014.
[23] ASTM, Astm D3493-14 Standard Test Method for Carbon Black-Oil Absorption Number of Compressed Sample (Coan), ASTM International, West Conshohocken, PA 2014.

[24] ASTM, Astm D1765-14 Standard Classification System for Carbon Blacks Used in Rubber Products, ASTM International, West Conshohocken, PA 2014.
[25] D. Twiss, *The Theory of Vulcanisation*, J Soc Chem Ind 1925, 44, 106.
[26] C. Blow, *Polymer/Particulate Filler Interaction—the Bound Rubber Phenomena*, Polymer 1973, 14, 309; J. L. Leblanc, *Rubber–Filler Interactions and Rheological Properties in Filled Compounds*, Progress in Polymer Science 2002, 27, 627.
[27] E. Dannenberg, *Bound Rubber and Carbon Black Reinforcement*, Rubber Chemistry and Technology 1986, 59, 512.
[28] L. Ban, W. Hess, L. Papazian, *New Studies of Carbon-Rubber Gel*, Rubber Chemistry and Technology 1974, 47, 858.
[29] N. K. Dutta, N. Roy Choudhury, B. Haidar, A. Vidal, J. Donnet, L. Delmotte, J. Chezeau, *High-Resolution Solid State Nmr Investigation of the Filler-Rubber Interaction: Part Iii. Investigation on the Structure and Formation Mechanism of Carbon Gel in the Carbon Black-Filled Styrene-Butadiene Rubber*, Rubber Chemistry and Technology 2001, 74, 260.
[30] S. Wolff, *Chemical Aspects of Rubber Reinforcement by Fillers*, Rubber Chemistry and Technology 1996, 69, 325; J. O'Brien, E. Cashell, G. Wardell, V. McBrierty, *An Nmr Investigation of the Interaction between Carbon Black and Cis-Polybutadiene*, Rubber Chemistry and Technology 1977, 50, 747.
[31] J. Leblanc, P. Hardy, *Evolution of Bound Rubber During the Storage of Uncured Compounds*, Kautschuk und Gummi, Kunststoffe 1991, 44, 1119.
[32] A. Kato, M. Nishioka, Y. Sato, E. Nagano, R. Yamashita, N. Kimura, T. Taguchi, *Studies on Bound Rubber of Cb before/after Vulcanization of Isoprene Rubber*, Rubber Chemistry and Technology 2014, 87, 471.
[33] W. Fletcher, A. Gent, *Nonlinearity in the Dynamic Properties of Vulcanized Rubber Compounds*, Rubber Chemistry and Technology 1954, 27, 209.
[34] A. R. Payne, *The Dynamic Properties of Carbon Black ‐ Loaded Natural Rubber Vulcanizates. Part I*, Journal of Applied Polymer Science 1962, 6, 57.
[35] A. R. Payne, *The Dynamic Properties of Carbon Black Loaded Natural Rubber Vulcanizates. Part Ii*, Journal of Applied Polymer Science 1962, 6, 368.
[36] M.-J. Wang, *Effect of Polymer-Filler and Filler-Filler Interactions on Dynamic Properties of Filled Vulcanizates*, Rubber Chemistry and Technology 1998, 71, 520.
[37] W. Luo, X. Hu, C. Wang, Q. Li, *Frequency-and Strain-Amplitude-Dependent Dynamical Mechanical Properties and Hysteresis Loss of Cb-Filled Vulcanized Natural Rubber*, International Journal of Mechanical Sciences 2010, 52, 168.
[38] A. R. Blythe, D. Bloor, *Electrical Properties of Polymers*, Cambridge University Press, United Kingdom 2005.
[39] F. Kremer, A. Schönhals, *Broadband Dielectric Spectroscopy*, Springer, Berlin 2003.
[40] K. S. Cole, R. H. Cole, *Dispersion and Absorption in Dielectrics I. Alternating Current Characteristics*, The Journal of Chemical Physics 1941, 9, 341.
[41] S. Havriliak, S. Negami, *A Complex Plane Representation of Dielectric and Mechanical Relaxation Processes in Some Polymers*, Polymer 1967, 8, 161.
[42] P. Lunkenheimer, V. Bobnar, A. Pronin, A. Ritus, A. Volkov, A. Loidl, *Origin of Apparent Colossal Dielectric Constants*, Physical Review B 2002, 66, 052105.
[43] L. Zhang, X. Yao, *Physics of Dielectrics*, Xi'an Jiaotong University, Xi'an 2008.

[44] D. Almond, B. Vainas, *The Dielectric Properties of Random R-C Networks as an Explanation of Theuniversal'power Law Dielectric Response of Solids*, Journal of Physics: Condensed Matter 1999, 11, 9081.

[45] D. Almond, C. Budd, M. Freitag, G. Hunt, N. McCullen, N. Smith, *The Origin of Power-Law Emergent Scaling in Large Binary Networks*, Physica A: Statistical Mechanics and its Applications 2012.

[46] R. K. H. Galvao, S. Hadjiloucas, K. H. Kienitz, H. M. Paiva, R. J. M. Afonso, *Fractional Order Modeling of Large Three-Dimensional Rc Networks*, IEEE Transactions on Circuits and Systems I-Regular Papers 2013, 60, 624.

[47] A. K. Jonscher, *Dielectric Relaxation in Solids*, Journal of Physics D: Applied Physics 1999, 32, R57.

[48] J. R. Macdonald, E. Barsoukov, *Impedance Spectroscopy: Theory, Experiment, and Applications*, 2005.

[49] A. Serghei, M. Tress, J. Sangoro, F. Kremer, *Electrode Polarization and Charge Transport at Solid Interfaces*, Physical Review B 2009, 80, 184301.

[50] M. Panda, V. Srinivas, A. Thakur, *On the Question of Percolation Threshold in Polyvinylidene Fluoride/Nanocrystalline Nickel Composites*, Applied Physics Letters 2008, 92, 132905.

[51] F. He, S. Lau, H. L. Chan, J. Fan, *High Dielectric Permittivity and Low Percolation Threshold in Nanocomposites Based on Poly (Vinylidene Fluoride) and Exfoliated Graphite Nanoplates*, Advanced Materials 2009, 21, 710.

[52] Z.-M. Dang, L. Wang, Y. Yin, Q. Zhang, Q.-Q. Lei, *Giant Dielectric Permittivities in Functionalized Carbon‐Nanotube/Electroactive‐Polymer Nanocomposites*, Advanced Materials 2007, 19, 852.

[53] J.-K. Yuan, S.-H. Yao, Z.-M. Dang, A. Sylvestre, M. Genestoux, J. Bai, *Giant Dielectric Permittivity Nanocomposites: Realizing True Potential of Pristine Carbon Nanotubes in Polyvinylidene Fluoride Matrix through an Enhanced Interfacial Interaction*, The Journal of Physical Chemistry C 2011, 115, 5515.

[54] J. C. Maxwell, *A Treatise on Electricity and Magnetism*, Vol. 1, Clarendon press, 1881.

[55] L. F. Chen, C. Ong, C. Neo, V. V. Varadan, V. K. Varadan, *Microwave Electronics: Measurement and Materials Characterization*, John Wiley & Sons Ltd, United Kingdom 2004.

[56] A.-H. Boughriet, C. Legrand, A. Chapoton, *Noniterative Stable Transmission/Reflection Method for Low-Loss Material Complex Permittivity Determination*, IEEE Transactions on Microwave Theory and Techniques 1997, 45, 52.

[57] A. Nicolson, G. Ross, *Measurement of the Intrinsic Properties of Materials by Time-Domain Techniques*, IEEE Transactions on Instrumentation and Measurement 1970, 19, 377; W. B. Weir, *Automatic Measurement of Complex Dielectric Constant and Permeability at Microwave Frequencies*, Proceedings of the IEEE 1974, 62, 33.

[58] B. Tian, *New Advances in Automatic Analysis Technique of Microwave Newwork and Its Applications*, National Key Laboratory of Antennas and Microwave Technology, Xidian University, Xi'an, China, 2002, Doctor of Philosophy, 134.

[59] R. S. Donnan, D. H. Martin, R. J. Wylde, B. Yang, "Assessment of Magnetic Materials for Use in Quasi-Optical Non-Reciprocal Devices Operating at Frequencies above 90 Ghz", presented at *Infrared and Millimeter Waves, 2007 and the 2007 15th*

International Conference on Terahertz Electronics. IRMMW-THz. Joint 32nd International Conference on, 2007.

[60] V. V. Varadan, R. D. Hollinger, D. K. Ghodgaonkar, V. K. Varadan, *Free-Space, Broadband Measurements of High-Temperature, Complex Dielectric Properties at Microwave Frequencies*, IEEE Transactions on Instrumentation and Measurement 1991, 40, 842.

[61] B. Wu, H. M. Tuncer, M. Naeem, B. Yang, M. T. Cole, W. I. Milne, Y. Hao, *Experimental Demonstration of a Transparent Graphene Millimetre Wave Absorber with 28% Fractional Bandwidth at 140 Ghz*, Scientific Reports 2014, 4.

[62] T. Lewis, "Interfaces and Nanodielectrics Are Synonymous", presented at *Solid Dielectrics, 2004. ICSD 2004. Proceedings of the 2004 IEEE International Conference on*, 2004.

[63] T. J. Lewis, *Interfaces Are the Dominant Feature of Dielectrics at the Nanometric Level*, IEEE Transactions on Dielectrics and Electrical Insulation 2004, 11, 739.

[64] J. K. Nelson, J. C. Fothergill, L. A. Dissado, W. Peasgood, "Towards an Understanding of Nanometric Dielectrics", presented at *Electrical Insulation and Dielectric Phenomena, 2002 Annual Report Conference on*, Cancun, Quintana Roo, Mexico, 2002.

[65] M. Roy, J. K. Nelson, C. W. Reed, R. K. MacCrone, R. J. Keefe, W. Zenger, L. S. Schadler, *Polymer Nanocomposite Dielectrics - the Role of the Interface*, IEEE Transactions on Dielectrics and Electrical Insulation 2005, 12, 1273.

[66] G. Tsagaropoulos, A. Eisenberg, *Dynamic Mechanical Study of the Factors Affecting the Two Glass Transition Behavior of Filled Polymers. Similarities and Differences with Random Ionomers*, Macromolecules 1995, 28, 6067.

[67] T. Tanaka, M. Kozako, N. Fuse, Y. Ohki, *Proposal of a Multi-Core Model for Polymer Nanocomposite Dielectrics*, IEEE Transactions on Dielectrics and Electrical Insulation 2005, 12, 669.

[68] L. S. Schadler, S. K. Kumar, B. C. Benicewicz, S. L. Lewis, S. E. Harton, *Designed Interfaces in Polymer Nanocomposites: A Fundamental Viewpoint*, MRS Bulletin 2007, 32, 335.

[69] M. M. Kummali, L. A. Miccio, G. A. Schwartz, A. Alegría, J. Colmenero, J. Otegui, A. Petzold, S. Westermann, *Local Mechanical and Dielectric Behavior of the Interacting Polymer Layer in Silica Nano-Particles Filled Sbr by Means of Afm-Based Methods*, Polymer 2013, 54, 4980.

[70] M. Hernández, A. Sanz, A. Nogales, T. A. Ezquerra, M. A. López-Manchado, *Structure and Segmental Dynamics Relationship in Natural Rubber/Layered Silicate Nanocomposites During Uniaxial Deformation*, Macromolecules 2013, 46, 3176.

[71] A. I. McIntosh, B. Yang, S. M. Goldup, M. Watkinson, R. S. Donnan, *Terahertz Spectroscopy: A Powerful New Tool for the Chemical Sciences?*, Chemical Society Reviews 2012, 41, 2072.

[72] T. A. Skotheim, R. L. Elsenbaumer, R. J. R, *Handbook of Conducting Polymers*, Marcel Dekker, INC, USA 1997.

[73] C.-W. Nan, Y. Shen, J. Ma, *Physical Properties of Composites near Percolation*, Annual Review of Materials Research 2010, 40, 131.

[74] F. Carpi, D. De Rossi, R. Kornbluh, R. E. Pelrine, P. Sommer-Larsen, *Dielectric Elastomers as Electromechanical Transducers: Fundamentals, Materials, Devices,*

Models and Applications of an Emerging Electroactive Polymer Technology, Elsevier Ltd, Hungary 2011.

[75] Z. M. Dang, J. K. Yuan, S. H. Yao, R. J. Liao, *Flexible Nanodielectric Materials with High Permittivity for Power Energy Storage*, Advanced Materials 2013, 25, 6334.

[76] M. L. Hammock, A. Chortos, B. C. K. Tee, J. B. H. Tok, Z. Bao, *25th Anniversary Article: The Evolution of Electronic Skin (E‐Skin): A Brief History, Design Considerations, and Recent Progress*, Advanced Materials 2013, 25, 5997.

[77] R. Rahimi, M. Ochoa, W. Yu, B. Ziaie, *Highly Stretchable and Sensitive Unidirectional Strain Sensor Via Laser Carbonization*, ACS Applied Materials & Interfaces 2015, 7, 4463.

[78] L. A. Dissado, J. C. Fothergill, *Electrical Degradation and Breakdown in Polymers*, Peter Peregrinus Ltd, London 1992.

[79] Q. Li, L. Chen, M. R. Gadinski, S. Zhang, G. Zhang, H. Li, A. Haque, L.-Q. Chen, T. Jackson, Q. Wang, *Flexible High-Temperature Dielectric Materials from Polymer Nanocomposites*, Nature 2015, 523, 576.

[80] A. I. Medalia, *Electrical Conduction in Carbon Black Composites*, Rubber Chemistry and Technology 1986, 59, 432.

[81] A. S. Abu-Surrah, S. A. Jawad, E. Al-Ramahi, A. B. Hallak, Z. Khattari, *Effect of Multi-Walled Carbon Nanotubes Aspect Ratio and Temperature on the Dielectric Behavior of Alternating Alkene-Carbon Monoxide Polyketone Nanocomposites*, Physica B: Condensed Matter 2015, 463, 76.

[82] M. Hernández, M. del Mar Bernal, R. Verdejo, T. A. Ezquerra, M. A. López-Manchado, *Overall Performance of Natural Rubber/Graphene Nanocomposites*, Composites Science and Technology 2012, 73, 40.

[83] L. Zhang, W. Wang, X. Wang, P. Bass, Z.-Y. Cheng, *Metal-Polymer Nanocomposites with High Percolation Threshold and High Dielectric Constant*, Applied Physics Letters 2013, 103, 232903.

[84] Z. M. Dang, Y. H. Lin, C. W. Nan, *Novel Ferroelectric Polymer Composites with High Dielectric Constants*, Advanced Materials 2003, 15, 1625.

[85] L. Qi, B. I. Lee, S. Chen, W. D. Samuels, G. J. Exarhos, *High‐Dielectric‐Constant Silver–Epoxy Composites as Embedded Dielectrics*, Advanced Materials 2005, 17, 1777.

[86] M. Molberg, D. Crespy, P. Rupper, F. Nüesch, J. A. E. Månson, C. Löwe, D. M. Opris, *High Breakdown Field Dielectric Elastomer Actuators Using Encapsulated Polyaniline as High Dielectric Constant Filler*, Advanced Functional Materials 2010, 20, 3280.

[87] M. Pluta, J. Jeszka, G. Boiteux, *Polylactide/Montmorillonite Nanocomposites: Structure, Dielectric, Viscoelastic and Thermal Properties*, European Polymer Journal 2007, 43, 2819.

[88] J. Li, S. I. Seok, B. Chu, F. Dogan, Q. Zhang, Q. Wang, *Nanocomposites of Ferroelectric Polymers with Tio2 Nanoparticles Exhibiting Significantly Enhanced Electrical Energy Density*, Advanced Materials 2009, 21, 217.

[89] J. Lu, K.-S. Moon, J. Xu, C. Wong, *Synthesis and Dielectric Properties of Novel High-K Polymer Composites Containing in-Situ Formed Silver Nanoparticles for Embedded Capacitor Applications*, Journal of Materials Chemistry 2006, 16, 1543.

[90] Z.-M. Dang, Y. Shen, C.-W. Nan, *Dielectric Behavior of Three-Phase Percolative Ni–Batio3/Polyvinylidene Fluoride Composites*, Applied Physics Letters 2002, 81, 4814.

[91] C. Robertson, C. Roland, *Glass Transition and Interfacial Segmental Dynamics in Polymer-Particle Composites*, Rubber Chemistry and Technology 2008, 81, 506.
[92] M. Sow, R. Widenor, A. Kumar, S. W. Lee, D. J. Lacks, R. M. Sankaran, *Strain‐Induced Reversal of Charge Transfer in Contact Electrification*, Angewandte Chemie 2012, 124, 2749.
[93] H. Ishii, K. Sugiyama, E. Ito, K. Seki, *Energy Level Alignment and Interfacial Electronic Structures at Organic/Metal and Organic/Organic Interfaces*, Advanced Materials 1999, 11, 605.
[94] Z. G. Suo, *Theory of Dielectric Elastomers*, Acta Mechanica Solida Sinica 2010, 23, 549.
[95] D. Fragiadakis, L. Bokobza, P. Pissis, *Dynamics near the Filler Surface in Natural Rubber-Silica Nanocomposites*, Polymer 2011, 52, 3175.
[96] L. Zhang, P. Bass, Z.-Y. Cheng, *Revisiting the Percolation Phenomena in Dielectric Composites with Conducting Fillers*, Applied Physics Letters 2014, 105, 042905.
[97] Y. Shen, Y. Lin, C. W. Nan, *Interfacial Effect on Dielectric Properties of Polymer Nanocomposites Filled with Core/Shell‐Structured Particles*, Advanced Functional Materials 2007, 17, 2405.
[98] K. Yamaguchi, J. Busfield, A. Thomas, *Electrical and Mechanical Behavior of Filled Elastomers. I. The Effect of Strain*, Journal of Polymer Science Part B: Polymer Physics 2003, 41, 2079.
[99] T. Yamada, Y. Hayamizu, Y. Yamamoto, Y. Yomogida, A. Izadi-Najafabadi, D. N. Futaba, K. Hata, *A Stretchable Carbon Nanotube Strain Sensor for Human-Motion Detection*, Nature Nanotechnology 2011, 6, 296.
[100] F. Müller, K. Huff, *Dependence of Dielectric Relaxation Spectrum of Rubber on Stretching*, Rubber Chemistry and Technology 1959, 32, 1027.
[101] A. T. McPherson, *Electrical Properties of Elastomers and Related Polymers*, Rubber Chemistry and Technology 1963, 36, 1230.
[102] I. Alig, T. Skipa, D. Lellinger, P. Pötschke, *Destruction and Formation of a Carbon Nanotube Network in Polymer Melts: Rheology and Conductivity Spectroscopy*, Polymer 2008, 49, 3524; C. Brosseau, W. Ndong, A. Mdarhri, *Influence of Uniaxial Tension on the Microwave Absorption Properties of Filled Polymers*, Journal of Applied Physics 2008, 104, 074907.
[103] Z.-M. Dang, S.-H. Yao, H.-P. Xu, *Effect of Tensile Strain on Morphology and Dielectric Property in Nanotube/Polymer Nanocomposites*, Applied Physics Letters 2007, 90, 012907.
[104] L. Jiang, A. Betts, D. Kennedy, S. Jerrams, *Investigation into the Electromechanical Properties of Dielectric Elastomers Subjected to Pre-Stressing*, Materials Science and Engineering: C 2015, 49, 754.
[105] H. Lee, D. Fragiadakis, D. Martin, A. Milne, J. Milne, J. Runt, *Dynamics of Uniaxially Oriented Elastomers Using Broadband Dielectric Spectroscopy*, Macromolecules 2010, 43, 3125.
[106] W. H. Stockmayer, *Dielectric Dispersion in Solutions of Flexible Polymers*, Pure and Applied Chemistry 1967, 15, 539.
[107] K. Adachi, T. Kotaka, *Dielectric Normal Mode Relaxation*, Progress in Polymer Science 1993, 18, 585.
[108] P. E. Rouse Jr, *A Theory of the Linear Viscoelastic Properties of Dilute Solutions of Coiling Polymers*, The Journal of Chemical Physics 1953, 21, 1272; B. H. Zimm, *Dynamics*

of Polymer Molecules in Dilute Solution: Viscoelasticity, Flow Birefringence and Dielectric Loss, The Journal of Chemical Physics 1956, 24, 269.
[109] T. McLeish, *Tube Theory of Entangled Polymer Dynamics*, Advances in Physics 2002, 51, 1379.
[110] N. G. McCrum, B. E. Read, G. Williams, *Anelastic and Dielectric Effects in Polymeric Solids*, Dover, New York 1967.
[111] K. Adachi, H. Yoshida, F. Fukui, T. Kotaka, *Comparison of Dielectric and Viscoelastic Relaxation Spectra of Polyisoprene*, Macromolecules 1990, 23, 3138.
[112] T. Pakula, S. Geyler, T. Edling, D. Boese, *Relaxation and Viscoelastic Properties of Complex Polymer Systems*, Rheologica Acta 1996, 35, 631.
[113] A. K. Jonscher, *Universal Relaxation Law: A Sequel to Dielectric Relaxation in Solids*, Chelsea Dielectrics Press, London 1996.
[114] P. Santangelo, C. Roland, *Temperature Dependence of Mechanical and Dielectric Relaxation in Cis-1, 4-Polyisoprene*, Macromolecules 1998, 31, 3715.
[115] P. Steeman, J. Van Turnhout, in *Broadband Dielectric Spectroscopy*, (Eds: F. Kremer, A. Schönhals), Springer, Berlin 2003, 495.
[116] R. Norman, *The Dielectric Properties of Rubber*, Proceedings of the IEE-Part IIA: Insulating Materials 1953, 100, 41.
[117] K. Adachi, T. Kotaka, *Influence of Entanglement on the Dielectric Normal Mode Process of Cis-Polyisoprene*, Macromolecules 1984, 17, 120.
[118] K. Adachi, T. Kotaka, *Dielectric Normal Mode Process in Dilute Solutions of Cis-Polyisoprene*, Macromolecules 1987, 20, 2018; K. Adachi, T. Kotaka, *Dielectric Normal Mode Process in Undiluted Cis-Polyisoprene*, Macromolecules 1985, 18, 466.
[119] A. Schönhals, *Relation between Main and Normal Mode Relaxations for Polyisoprene Studied by Dielectric Spectroscopy*, Macromolecules 1993, 26, 1309.
[120] D. Boese, F. Kremer, *Molecular Dynamics in Bulk Cis-Polyisoprene as Studied by Dielectric Spectroscopy*, Macromolecules 1990, 23, 829.
[121] A. Serghei, F. Kremer, *Confinement-Induced Relaxation Process in Thin Films of Cis-Polyisoprene*, Physical Review Letters 2003, 91, 165702.
[122] G. McKenna, *Ten (or More) Years of Dynamics in Confinement: Perspectives for 2010*, The European Physical Journal Special Topics 2010, 189, 285.
[123] M. Doxastakis, D. Theodorou, G. Fytas, F. Kremer, R. Faller, F. Müller-Plathe, N. Hadjichristidis, *Chain and Local Dynamics of Polyisoprene as Probed by Experiments and Computer Simulations*, The Journal of Chemical Physics 2003, 119, 6883.
[124] M. Huang, L. B. Tunnicliffe, A. G. Thomas, J. J. C. Busfield, *The Glass Transition, Segmental Relaxations and Viscoelastic Behaviour of Particulate-Reinforced Natural Rubber*, European Polymer Journal 2015, 67, 232.
[125] A. Schönhals, E. Schlosser, *Relationship between Segmental and Chain Dynamics in Polymer Melts as Studied by Dielectric Spectroscopy*, Physica Scripta 1993, 1993, 233.
[126] K. Gohr, T. Pakula, K. Tsutsumi, W. Schärtl, *Dynamics of Copolymer Micelles in an Entangled Homopolymer Matrix*, Macromolecules 1999, 32, 7156.
[127] M. Hernández, T. A. Ezquerra, R. Verdejo, M. A. López-Manchado, *Role of Vulcanizing Additives on the Segmental Dynamics of Natural Rubber*, Macromolecules 2012, 45, 1070.
[128] M. Hernández, J. L. Valentín, M. A. López-Manchado, T. A. Ezquerra, *Influence of the Vulcanization System on the Dynamics and Structure of Natural Rubber: Comparative*

Study by Means of Broadband Dielectric Spectroscopy and Solid-State Nmr Spectroscopy, European Polymer Journal 2015, 68, 90.
[129] H. Desanges, R. Chasset, P. Thirion, *Changes in the Electrical Properties of Natural Rubber/Carbon Black Compounds During Vulcanization*, Rubber Chemistry and Technology 1958, 31, 631.
[130] M. Hotta, M. Hayashi, M. T. Lanagan, D. K. Agrawal, K. Nagata, *Complex Permittivity of Graphite, Carbon Black and Coal Powders in the Ranges of X-Band Frequencies (8.2 to 12.4 Ghz) and between 1 and 10 Ghz*, ISIJ International 2011, 51, 1766.
[131] J. E. Atwater, R. R. Wheeler, *Complex Permittivities and Dielectric Relaxation of Granular Activated Carbons at Microwave Frequencies between 0.2 and 26 Ghz*, Carbon 2003, 41, 1801.
[132] J. Atwater, R. Wheeler Jr, *Microwave Permittivity and Dielectric Relaxation of a High Surface Area Activated Carbon*, Applied Physics A 2004, 79, 125.
[133] S. Braun, W. R. Salaneck, M. Fahlman, *Energy-Level Alignment at Organic/Metal and Organic/Organic Interfaces*, Advanced Materials 2009, 21, 1450.
[134] X. Crispin, V. Geskin, A. Crispin, J. Cornil, R. Lazzaroni, W. R. Salaneck, J.-L. Bredas, *Characterization of the Interface Dipole at Organic/Metal Interfaces*, Journal of the American Chemical Society 2002, 124, 8131.
[135] N. Lang, *Interaction between Closed-Shell Systems and Metal Surfaces*, Physical Review Letters 1981, 46, 842.
[136] M. Sow, D. J. Lacks, R. M. Sankaran, *Effects of Material Strain on Triboelectric Charging: Influence of Material Properties*, Journal of Electrostatics 2013, 71, 396.
[137] Z.-M. Dang, J.-K. Yuan, J.-W. Zha, P.-H. Hu, D.-R. Wang, Z.-Y. Cheng, *High-Permittivity Polymer Nanocomposites: Influence of Interface on Dielectric Properties*, Journal of Advanced Dielectrics 2013, 3.
[138] J. K. Nelson, "Nanodielectrics-the First Decade and Beyond", presented at *Electrical Insulating Materials (ISEIM), Proceedings of 2014 International Symposium on*, 2014.
[139] A. J. Bard, L. R. Faulkner, in *Electrochemical Methods: Fundamentals and Applications, Second Edition*, Wiley, New York 2001.
[140] B. E. Conway, *Electrochemical Supercapacitors: Scientific Fundamentals and Technological Applications*, Springer Science & Business Media, New York 1999.
[141] A. Papon, H. Montes, M. Hanafi, F. Lequeux, L. Guy, K. Saalwächter, *Glass-Transition Temperature Gradient in Nanocomposites: Evidence from Nuclear Magnetic Resonance and Differential Scanning Calorimetry*, Physical Review Letters 2012, 108, 065702.
[142] J. G. Meier, M. Klüppel, *Carbon Black Networking in Elastomers Monitored by Dynamic Mechanical and Dielectric Spectroscopy*, Macromolecular Materials and Engineering 2008, 293, 12.
[143] A. Bansal, H. Yang, C. Li, K. Cho, B. C. Benicewicz, S. K. Kumar, L. S. Schadler, *Quantitative Equivalence between Polymer Nanocomposites and Thin Polymer Films*, Nature Materials 2005, 4, 693.
[144] K. W. Wagner, *Erklärung Der Dielektrischen Nachwirkungsvorgänge Auf Grund Maxwellscher Vorstellungen*, Arkiv für Electrotechnik 1914, 2, 371.

[145] R. Sillars, *The Properties of a Dielectric Containing Semiconducting Particles of Various Shapes*, Institution of Electrical Engineers - Proceedings of the Wireless Section 1937, 12, 139.
[146] C.-W. Nan, *Physics of Inhomogeneous Inorganic Materials*, Progress in Materials Science 1993, 37, 1.
[147] L. ZHANG, Z.-Y. Cheng, *Development of Polymer-Based 0–3 Composites with High Dielectric Constant*, Journal of Advanced Dielectrics 2011, 1, 389.
[148] L. K. H. Van Beek, in *Progress in Dielectrics*, Vol. 7, Heywood Books, London 1967, 69.
[149] M. Achour, M. E. Malhi, J. Miane, F. Carmona, F. Lahjomri, *Microwave Properties of Carbon Black–Epoxy Resin Composites and Their Simulation by Means of Mixture Laws*, Journal of Applied Polymer Science 1999, 73, 969.
[150] D. Stauffer, A. Aharony, *Introduction to Percolation Theory*, Taylor & Francis, London 1994.
[151] K. Yong, P. Foot, H. Morgan, S. Cook, A. Tinker, *Conductive Poly (Butadiene-Co-Acrylonitrile)-Polyaniline Dodecylbenzenesulfonate [Nbr-Pani. Dbsa] Blends Prepared in Solution*, European Polymer Journal 2006, 42, 1716.
[152] D. Toker, D. Azulay, N. Shimoni, I. Balberg, O. Millo, *Tunneling and Percolation in Metal-Insulator Composite Materials*, Physical Review B 2003, 68, 041403.
[153] J. G. Simmons, *Generalized Formula for the Electric Tunnel Effect between Similar Electrodes Separated by a Thin Insulating Film*, Journal of Applied Physics 1963, 34, 1793.
[154] M. Rintoul, S. Torquato, *Precise Determination of the Critical Threshold and Exponents in a Three-Dimensional Continuum Percolation Model*, Journal of Physics A: Mathematical and General 1997, 30, L585.
[155] W. Zhang, A. A. Dehghani-Sanij, R. S. Blackburn, *Carbon Based Conductive Polymer Composites*, Journal of Materials Science 2007, 42, 3408.
[156] L. Bokobza, *Multiwall Carbon Nanotube Elastomeric Composites: A Review*, Polymer 2007, 48, 4907.
[157] W. Bauhofer, J. Z. Kovacs, *A Review and Analysis of Electrical Percolation in Carbon Nanotube Polymer Composites*, Composites Science and Technology 2009, 69, 1486.
[158] D. G. Papageorgiou, I. A. Kinloch, R. J. Young, *Graphene/Elastomer Nanocomposites*, Carbon 2015.
[159] M. Sumita, K. Sakata, S. Asai, K. Miyasaka, H. Nakagawa, *Dispersion of Fillers and the Electrical Conductivity of Polymer Blends Filled with Carbon Black*, Polymer Bulletin 1991, 25, 265.
[160] D. J. Bergman, Y. Imry, *Critical Behavior of the Complex Dielectric Constant near the Percolation Threshold of a Heterogeneous Material*, Physical Review Letters 1977, 39, 1222.
[161] D. Stroud, D. J. Bergman, *Frequency Dependence of the Polarization Catastrophe at a Metal-Insulator Transition and Related Problems*, Physical Review B 1982, 25, 2061.
[162] P. Pötschke, S. M. Dudkin, I. Alig, *Dielectric Spectroscopy on Melt Processed Polycarbonate—Multiwalled Carbon Nanotube Composites*, Polymer 2003, 44, 5023.
[163] D. Nuzhnyy, M. Savinov, V. Bovtun, M. Kempa, J. Petzelt, B. Mayoral, T. McNally, *Broad-Band Conductivity and Dielectric Spectroscopy of Composites of Multiwalled Carbon Nanotubes and Poly (Ethylene Terephthalate) around Their Low Percolation Threshold*, Nanotechnology 2013, 24, 055707.

[164] P. Pötschke, M. Abdel-Goad, I. Alig, S. Dudkin, D. Lellinger, *Rheological and Dielectrical Characterization of Melt Mixed Polycarbonate-Multiwalled Carbon Nanotube Composites*, Polymer 2004, 45, 8863.
[165] E. Geberth, M. Klüppel, *Effect of Carbon Black Deactivation on the Mechanical and Electrical Properties of Elastomers*, Macromolecular Materials and Engineering 2012, 297, 914.
[166] C. Pecharromán, J. S. Moya, *Experimental Evidence of a Giant Capacitance in Insulator–Conductor Composites at the Percolation Threshold*, Advanced Materials 2000, 12, 294.
[167] K. Akutagawa, K. Yamaguchi, A. Yamamoto, H. Heguri, H. Jinnai, Y. Shinbori, *Mesoscopic Mechanical Analysis of Filled Elastomer with 3d-Finite Element Analysis and Transmission Electron Microtomography*, Rubber Chemistry and Technology 2008, 81, 182.
[168] S. Toki, I. Sics, S. Ran, L. Liu, B. S. Hsiao, S. Murakami, K. Senoo, S. Kohjiya, *New Insights into Structural Development in Natural Rubber During Uniaxial Deformation by in Situ Synchrotron X-Ray Diffraction*, Macromolecules 2002, 35, 6578.
[169] M. Hernández, M. A. López-Manchado, A. Sanz, A. Nogales, T. A. Ezquerra, *Effects of Strain-Induced Crystallization on the Segmental Dynamics of Vulcanized Natural Rubber*, Macromolecules 2011, 44, 6574.
[170] T. Choi, D. Fragiadakis, C. M. Roland, J. Runt, *Microstructure and Segmental Dynamics of Polyurea under Uniaxial Deformation*, Macromolecules 2012, 45, 3581.
[171] P. Ortiz-Serna, R. Diaz-Calleja, M. Sanchis, G. Floudas, R. Nunes, A. Martins, L. Visconte, *Dynamics of Natural Rubber as a Function of Frequency, Temperature, and Pressure. A Dielectric Spectroscopy Investigation*, Macromolecules 2010, 43, 5094.
[172] C. Brosseau, P. Talbot, *Instrumentation for Microwave Frequency-Domain Spectroscopy of Filled Polymers under Uniaxial Tension*, Measurement Science and Technology 2005, 16, 1823.
[173] N. Bowler, M. R. Kessler, L. Li, P. R. Hondred, T. Chen, in *Iowa State University, Ames, IA, NASA/CR-2012-217330*, Electromagnetic Nondestructive Evaluation of Wire Insulation and Models of Insulation Material Properties, 2012.
[174] G. Kofod, P. Sommer-Larsen, R. Kornbluh, R. Pelrine, *Actuation Response of Polyacrylate Dielectric Elastomers*, Journal of Intelligent Material Systems and Structures 2003, 14, 787.
[175] M. H. Al-Saleh, W. H. Saadeh, U. Sundararaj, *Emi Shielding Effectiveness of Carbon Based Nanostructured Polymeric Materials: A Comparative Study*, Carbon 2013, 60, 146.
[176] F. Zhao, C. T. Sha, G. Zhao, K. Wang, J. S. Kan, "A One-Port Waveguide Method and Its Application in Characterization of Radar Absorbing Materials", presented at *Applied Mechanics and Materials*, 2014.
[177] J. Berriot, H. Montes, F. Lequeux, D. Long, P. Sotta, *Evidence for the Shift of the Glass Transition near the Particles in Silica-Filled Elastomers*, Macromolecules 2002, 35, 9756.
[178] A. Mujtaba, M. Keller, S. Ilisch, H.-J. Radusch, M. Beiner, T. Thurn-Albrecht, K. Saalwächter, *Detection of Surface-Immobilized Components and Their Role in Viscoelastic Reinforcement of Rubber–Silica Nanocomposites*, ACS Macro Letters 2014, 3, 481.

[179] E. K. Sichel, *Carbon Black-Polymer Composites: The Physics of Electrically Conducting Composites*, Marcel Dekker, Inc, New York 1982.
[180] G. Ouyang, *On Immittance Spectroscopy for Carbon Black Network Characterization*, Kautschuk Gummi Kunststoffe 2002, 55, 104.
[181] E. Geberth, M. Klüppel, *Effect of Carbon Black Deactivation on the Mechanical and Electrical Properties of Elastomers*, Macromolecular materials and engineering 2012.
[182] Y.-J. Li, M. Xu, J.-Q. Feng, Z.-M. Dang, *Dielectric Behavior of a Metal-Polymer Composite with Low Percolation Threshold*, Applied Physics Letters 2006, 89, 072902.
[183] J. Otegui, G. Schwartz, S. Cerveny, J. Colmenero, J. Loichen, S. Westermann, *Influence of Water and Filler Content on the Dielectric Response of Silica-Filled Rubber Compounds*, Macromolecules 2013, 46, 2407.
[184] Y. Ding, S. Pawlus, A. P. Sokolov, J. F. Douglas, A. Karim, C. L. Soles, *Dielectric Spectroscopy Investigation of Relaxation in C60− Polyisoprene Nanocomposites*, Macromolecules 2009, 42, 3201.
[185] M. Hernández, J. Carretero-González, R. Verdejo, T. A. Ezquerra, M. A. López-Manchado, *Molecular Dynamics of Natural Rubber/Layered Silicate Nanocomposites as Studied by Dielectric Relaxation Spectroscopy*, Macromolecules 2010, 43, 643.
[186] D. Kang, P. V. Pikhitsa, Y. W. Choi, C. Lee, S. S. Shin, L. Piao, B. Park, K.-Y. Suh, T.-i. Kim, M. Choi, *Ultrasensitive Mechanical Crack-Based Sensor Inspired by the Spider Sensory System*, Nature 2014, 516, 222.
[187] Agilent, Solutions for Measuring Permittivity and Permeability with Lcr Meters and Impedance Analyzers, 2008.
[188] ASTM, Astm D150-11 Standard Test Methods for Ac Loss Characteristics and Permittivity (Dielectric Constant) of Solid Electrical Insulation, ASTM International, West Conshohocken, PA 2011.
[189] K. Okada, T. Sekino, *Impedance Measurement Handbook*, Agilent Technologies 2003, 128, 5950.
[190] D. J. Cohen, D. Mitra, K. Peterson, M. M. Maharbiz, *A Highly Elastic, Capacitive Strain Gauge Based on Percolating Nanotube Networks*, Nano Letters 2012, 12, 1821.
[191] M. Kollosche, H. Stoyanov, S. Laflamme, G. Kofod, *Strongly Enhanced Sensitivity in Elastic Capacitive Strain Sensors*, Journal of Materials Chemistry 2011, 21, 8292.
[192] D. J. Lipomi, M. Vosgueritchian, B. C. Tee, S. L. Hellstrom, J. A. Lee, C. H. Fox, Z. Bao, *Skin-Like Pressure and Strain Sensors Based on Transparent Elastic Films of Carbon Nanotubes*, Nature Nanotechnology 2011, 6, 788.
[193] F. Xu, Y. Zhu, *Highly Conductive and Stretchable Silver Nanowire Conductors*, Advanced Materials 2012, 24, 5117.
[194] M. Huang, A. G. Thomas, J. J. C. Busfield, *The Application of a Carbon Black Filled Elastomer to Create a Smart Strain Sensor*, CRC Press-Taylor & Francis Group, Boca Raton 2013.
[195] W. Hu, X. Niu, R. Zhao, Q. Pei, *Elastomeric Transparent Capacitive Sensors Based on an Interpenetrating Composite of Silver Nanowires and Polyurethane*, Applied Physics Letters 2013, 102, 083303.
[196] L. Cai, L. Song, P. Luan, Q. Zhang, N. Zhang, Q. Gao, D. Zhao, X. Zhang, M. Tu, F. Yang, *Super-Stretchable, Transparent Carbon Nanotube-Based Capacitive Strain Sensors for Human Motion Detection*, Scientific Reports 2013, 3.

[197] U.-H. Shin, D.-W. Jeong, S.-M. Park, S.-H. Kim, H. W. Lee, J.-M. Kim, *Highly Stretchable Conductors and Piezocapacitive Strain Gauges Based on Simple Contact-Transfer Patterning of Carbon Nanotube Forests*, Carbon 2014, 80, 396.
[198] T. Cheng, Y. Zhang, W. Y. Lai, W. Huang, *Stretchable Thin‐Film Electrodes for Flexible Electronics with High Deformability and Stretchability*, Advanced Materials 2015.
[199] G. Kraus, *Reinforcement of Elastomers by Carbon Black*, Rubber Chemistry and Technology 1978, 51, 297; T. A. Vilgis, G. Heinrich, M. Klüppel, *Reinforcement of Polymer Nano-Composites: Theory, Experiments and Applications*, Cambridge University Press, Cambridge 2009.
[200] L. Mullins, *Softening of Rubber by Deformation*, Rubber Chemistry and Technology 1969, 42, 339.
[201] G. Heinrich, M. Klüppel, in *Filled Elastomers Drug Delivery Systems*, Springer, 2002, 1.
[202] P. Maier, D. Göritz, *Molecular Interpretation of the Payne Effect*, Kautschuk Gummi Kunststoffe 1996, 49, 18.
[203] S. Merabia, P. Sotta, D. R. Long, *A Microscopic Model for the Reinforcement and the Nonlinear Behavior of Filled Elastomers and Thermoplastic Elastomers (Payne and Mullins Effects)*, Macromolecules 2008, 41, 8252.
[204] C. G. Robertson, X. Wang, *Isoenergetic Jamming Transition in Particle-Filled Systems*, Physical Review Letters 2005, 95, 075703; X. Wang, C. G. Robertson, *Strain-Induced Nonlinearity of Filled Rubbers*, Physical Review E 2005, 72, 031406.
[205] R. Raihan, J.-M. Adkins, J. Baker, F. Rabbi, K. Reifsnider, *Relationship of Dielectric Property Change to Composite Material State Degradation*, Composites Science and Technology 2014, 105, 160.
[206] M. Wissler, E. Mazza, *Electromechanical Coupling in Dielectric Elastomer Actuators*, Sensors and Actuators A: Physical 2007, 138, 384.
[207] ASTM, Astm D412-06a(2013) Standard Test Methods for Vulcanized Rubber and Thermoplastic Elastomers—Tension, ASTM International, West Conshohocken, PA 2013.
[208] L. Bateman, *Chemistry and Physics of Rubber-Like Substances*, Maclaren, London 1963.
[209] Z.-M. Dang, J.-K. Yuan, J.-W. Zha, T. Zhou, S.-T. Li, G.-H. Hu, *Fundamentals, Processes and Applications of High-Permittivity Polymer–Matrix Composites*, Progress in Materials Science 2012, 57, 660.
[210] Y. Wang, S. Kim, G. P. Li, L. Z. Sun, *Filler Orientation Effect on Relative Permittivity of Dielectric Elastomer Nanocomposites Filled with Carbon Nanotubes*, Computational Materials Science 2015, 104, 69.

Appendix 1： LabVIEW Remote Controlling Program

There is no controlling software for most of the LCR meters that are used for general purposes (frequency sweep), even for high spec meters (Keysight 4294a and E4980). In the SDMS test, data needs to be recorded with designed settings continuously over a long period. Therefore, an in-house designed software was developed by the author using LabVIEW which enabled fast data recording from a Keysight E4980 LCR meter via GPIB connection. The front control panel as well as the main loop of the LabVIEW program is presented in Figure A-1 and Figure A-2 respectively.

The general idea is: Firstly use the command '*:TRIG*' to trigger a single frequency sweep whilst at the same time record the time. Secondly, Read the data by using the command '*:FETC?*' when the testing sweep is finished. Thirdly, save the data in '*.lvm*' format. This process could be preformed for as many cycles as required.

As the raw data was obtained separately from the LCR meter and DMA, it means there were two time lines. As all the measured capacitance, R or X, have peak values at the maximum strain it could then be used to line them up. This process was done in MATLAB to enable consistent and accurate results. The MATLAB codes are listed in Appendix 2.

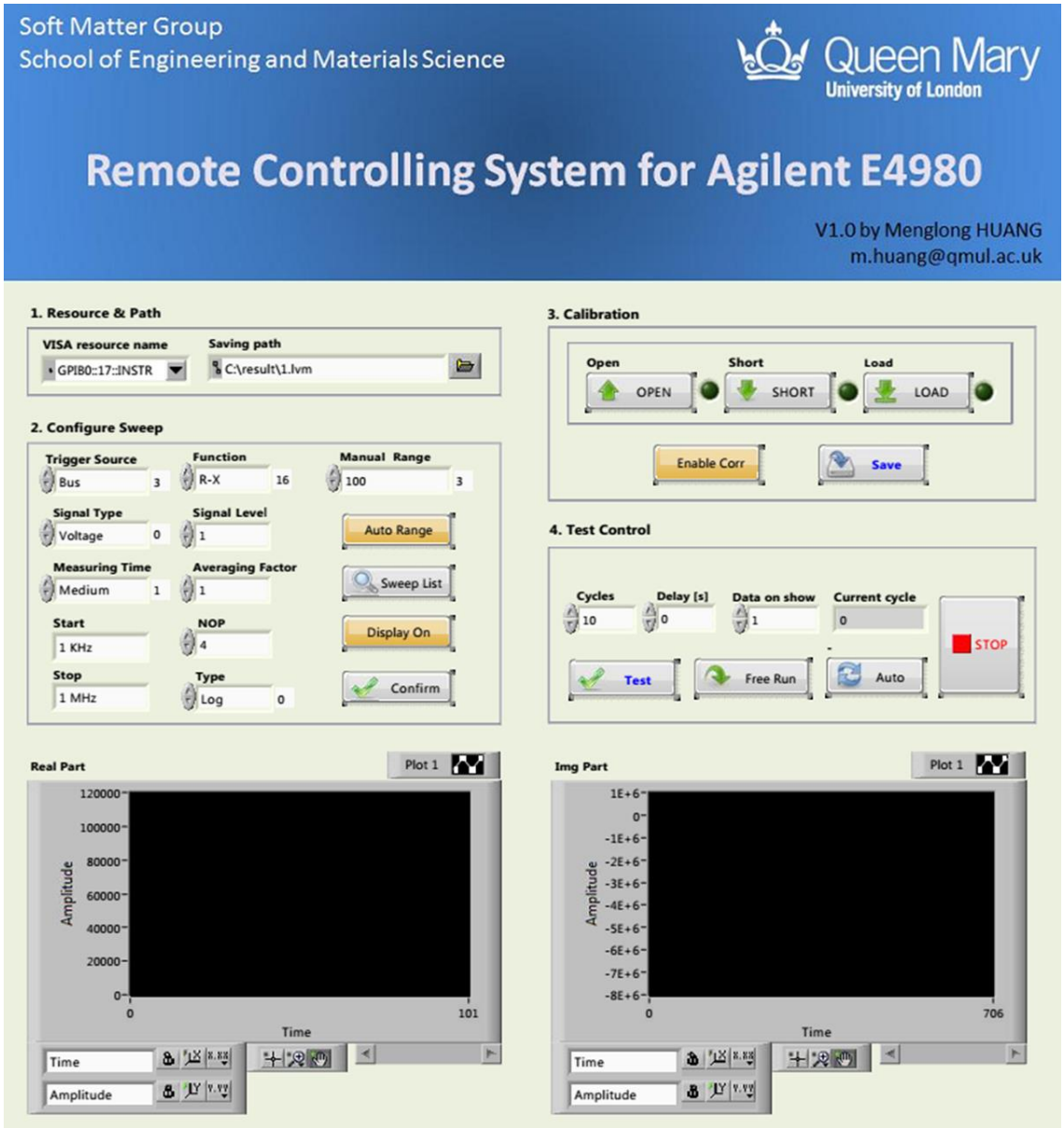

Figure A-1: The front panel of the remote controlling system of Keysight E4980.

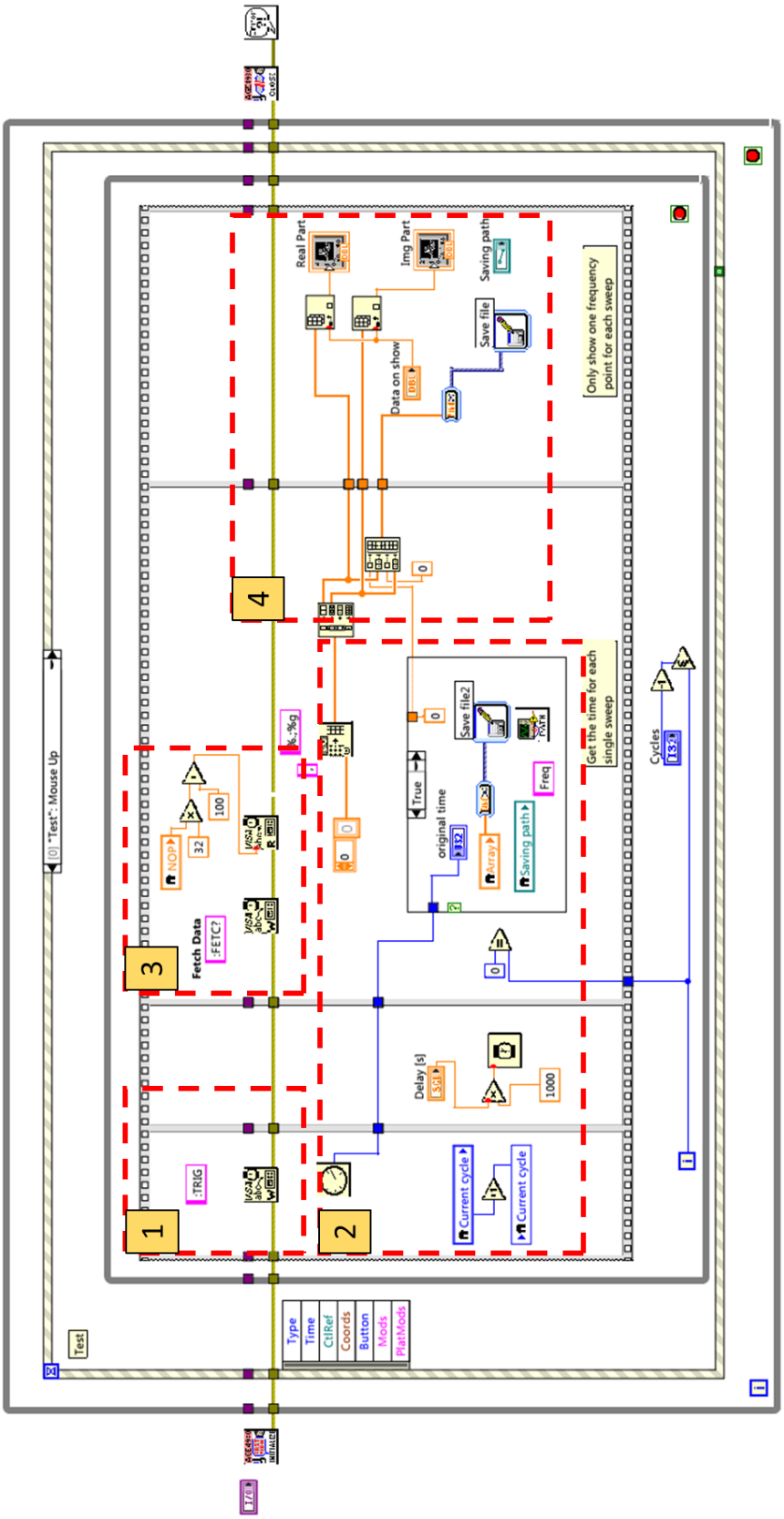

Figure A-2: The main loop of the LabVIEW program where 1 is for trigger a frequency sweep test, 2 is for recording the time; 3 is to receive the data from LCR meter; 4 is for saving the data.

Appendix 2： The MATLAB Code for Data Analysis

Part 1: The Main Program:

```
%1. Parameters
clear all
FileName='NR10N3_1_1';
Delta_T=[148.23,148.13,148.02,147.92];% Time difference between DMA
time line and LCR time line. Obtained from the alinement process. Here
only a rough value is needed. Iteration for several times of this
program to get the right value. Unit: second
Delta_Cp=[0.1656 0.1637 0.1642 0.1575 ]; % The fringing and parasitic
capacitance. Obtained from calibration. Unit: pF.
Delta_Strain=0;% Fixed at 0
NOP=1474;  % Number of data points
FrequencyList=[10^3,10^4,10^5,10^6];% frequency list. Unit: Hz
Thickness=0.648; % The thickness of sample
Width=6.20;      % The width of the overlapped area between electrodes
Length=5.94;     % The length of the overlapped area
Dimention=[Thickness Width Length]; Unit: mm
TestFreq=[1 4]; % The frequencies required for analysis
[Result,AC,DMA]=CalAC_DMA(FileName,Delta_T,Delta_Cp,NOP,FrequencyList,
Dimention,TestFreq); % More details of this function in next section

%2. Plot
doCalDelta=0; % Set it to 1 when ready to alignment. Make sure the
range (plx & ply) is in a proper value before setting doCalDelta==1.
doPlot=0;     % Set it to 1 to show the graph. It is better to be
turned off when do the alignments.(To speed up the calculation)
doOpt=0;      % Set it to 1 to find the right Delta_T. CAUTION: Be
careful as it takes time during this calculation. Make sure all of the
ranges are carefully set ready before turn it to 1.
plx=0;
ply=750;% When doPlot==1, program shows the graph. The range of the x-
axis is [plx, ply]. When do the alignment procedure, the whole
alignment calculation will only be based on the data between [plx,
ply](normally should include at least 10 cycles to secure the
accuracy). Two reasons: 1.to speed up the calculation; 2. choose the
clearest peaks to get more accurate alignment results.

Rang_1=[-1,50];    % Range of strain. eg: strain from -1% to 50%
Rang_2=[-0.01,0.01,2,3];   % Range of Delta Cp (-0.01pF to 0.01pF)& Cp
(2pF to 3pF)
Rang_3=[4,11];   % Range of permittivity

% The setting of ranges (plx, ply, Rang_1, Rang_2, Rang_3) is very
important as the data shown on the plot are decided by those value.
Moreover, only the data shown on the plot will be analysed.

Result_Fitting=Result(:,:,TestFreq(1)); % Choose the data measured at
one frequency to do the alignment analysis. At this stage, only 4
frequencies are used (1k, 10k, 100k, 1M Hz). When dealing with more
frequencies, a more efficient program is needed.
CalAlinement(Result_Fitting,plx,ply,Rang_1,Rang_2,Rang_3,doCalDelta,do
Plot,1);


%3. Alinement
```

```
if doOpt==1   % To do the alignment analysis or not.
    deltaTry=Delta_T(TestFreq(1));
    i=0;
    while Delta_T(TestFreq(1))<deltaTry+0.5
        Delta_T(TestFreq(1))=deltaTry-0.5+i*0.01; % The accuracy of
the Delta_T is set to 0.01 s.

Result=CalAC_DMA(FileName,Delta_T,Delta_Cp,NOP,FrequencyList,Dimention
,TestFreq); % Final results. CAUTION: Make sure that, Delta_T values
are correct before making use of this data. Which means: this program
should be executed for few times and manually iterate the latest
Delta_T.
        doCalDelta=1;
        doPlot=0;
        deltaMeanTry(i+1,1)=Delta_T(TestFreq(1));
        Result_Fitting=Result(:,:,TestFreq(1));
[timeStrain,timeCp]=CalAlinement(Result_Fitting,plx,ply,Rang_1,Rang_2,
Rang_3,doCalDelta,doPlot,1); % timeStrain and timeCp are the peaks of
the mechanical and dielectric graphs on shown.
        deltaMeanTry(i+1,2)=mean(timeStrain(:,1)-timeCp(:,1));
        i=i+1;
    end
    [minA, minB]=min(abs(deltaMeanTry(:,2)));
    deltaMeanTry(minB,:) % deltaMeanTry(1): The best Delta_T(i) that
found under the specified accuracy.
end
```

Part 2: The Function (CalAC_DMA) Used in The Main Program:

```
function
[AAA_Result,AC,DMA]=CalAC_DMA(FileName,Delta_T,Delta_Cp,NOP,FrequencyL
ist,Dimention,TestFreq)
% AAA_Result is the calculated result
%AC and DMA are the raw dielectric and mechanical data obtained from
the LCR meter and the dynamic mechanical analyser.

ACs=load([FileName,'_AC.mat']);
DMAs=load([FileName,'_DMA.mat']);
ACs=struct2cell(ACs);
DMAs=struct2cell(DMAs);
AC=ACs{1,1};
DMA=DMAs{1,1};
Thickness=Dimention(1);
Width=Dimention(2);
Length=Dimention(3);

DMA(:,1)=DMA(:,1)-DMA(2,1);% The first DMA should be deleted
DMA=DMA(2:end,:);% Use the second DMA data as the starting of the test
(time=0)
Time_DMA=DMA(:,1)*60;  % Change the unit into Second
Strain_DMA=DMA(:,8); % Unit [%]
Amp_DMA=DMA(:,3); % Unit: micro
Force_DMA=DMA(:,4);  % Force
Stress_DMA=DMA(:,7); % Stress
Modulus_DMA=Stress_DMA./Strain_DMA*100;
Time_AC=AC(:,1);
Epsilon_0= 8.854187817 *10^(-12);

for i=1:length(Time_AC)      % Work out the starting time of AC test
    if Time_AC(i)>Delta_T(2)
        startPoint=i;
        break
    end
end

if NOP>length(Time_AC)-startPoint+1
    NOP=length(Time_AC)-startPoint+1;
end
endPoint=startPoint+NOP-1;
NumOfFrequency=length(FrequencyList);
for iFreq=TestFreq(1):TestFreq(2)
    Frequency=FrequencyList(iFreq);
    R_AC=AC(:,1+iFreq);
    X_AC=AC(:,2+NumOfFrequency+iFreq);
    Cp_AC=abs(1/2/3.1415926./Frequency./X_AC)*10^12;
    D_AC=-R_AC./X_AC;

    % Result: Time/Strain/1+strain/Cp/D/Eps'/Eps''/Sig'/Sig''/M'/M''/
R / X /Displacement/Force/Stress/Modulus
    Result(:,1)=Time_AC(startPoint:endPoint)-Delta_T(iFreq);  % the
time that AC test really starts
    Result(:,2)=interp1(Time_DMA,Strain_DMA,Result(:,1),'spline'); %
Unit[%]
    Result(:,3)=Result(:,2)/100+1;
    Result(:,4)=Cp_AC(startPoint:endPoint);   % pF
    Result(:,5)=D_AC(startPoint:endPoint);
```

```
    Result(:,6)=(Result(:,4)-Delta_Cp(iFreq))*10^(-
12)/Epsilon_0*Thickness/Width/Length./Result(:,3)*1000; % Epsilon'
    Result(:,7)=Result(:,6).*Result(:,5);% Epsilon''

Result(:,8)=Epsilon_0*2*3.1415926*Frequency.*Result(:,6).*Result(:,5);
% Sigma'
    Result(:,9)=0-Epsilon_0*2*3.1415926*Frequency.*(Result(:,6)-
1);     % Sigma''

Result(:,10)=Result(:,6)./(Result(:,6).*Result(:,6)+Result(:,7).*Resul
t(:,7));  % M'

Result(:,11)=Result(:,7)./(Result(:,6).*Result(:,6)+Result(:,7).*Resul
t(:,7));  % M''
    Result(:,12)=R_AC(startPoint:endPoint); % R
    Result(:,13)=X_AC(startPoint:endPoint); % X
    Result(:,14)=interp1(Time_DMA,Amp_DMA,Result(:,1),'spline');  %
Displacement
    Result(:,15)=interp1(Time_DMA,Force_DMA,Result(:,1),'spline');  %
Force
    Result(:,16)=interp1(Time_DMA,Stress_DMA,Result(:,1),'spline');  %
Stress

Result(:,17)=interp1(Time_DMA,Modulus_DMA,Result(:,1),'spline');  %
Modulus
    AAA_Result(:,:,iFreq)=Result;
end
```

Part 3: The Function (CalAlinement) Used in The Main Program

```
function
[peakStrain,peakCp]=CalAlinement(Result,plx,ply,Rang_1,Rang_2,Rang_3,d
oCalDelta,doPlot,TypeValue)
% Result is in a 2D array belongs to a single electrical frequency.
Its format: Time/Strain/Ext Ratio/Cp/D…… More details in the previous
part.
% plx & plx is the working range (time)
% Range_1 is the range of strain
% Range_1 is the range delta Cp and Cp
% Range_3 is the range of permittivity
% doCalDelta: the delta_T calculation will only be performed when it
is set to 1
% doPlot: the program only gives plot when it is set to 1
% TypeValue: when it is set as 1, the program will use linear fitting
to get the peak positions or it will use mspeak function for fitting

peakStrain=[];
peakCp=[];
if doCalDelta==1
    time_index=knnsearch(Result(:,1),plx); % start time
    time_index2=knnsearch(Result(:,1),ply); % ending time

interTime=Result(time_index,1):0.1:(Result(time_index2,1)); %x=time
    interStrain=interp1(Result(:,1),Result(:,2),interTime,'spline');%
intercept y=Strain
    interCp=interp1(Result(:,1),Result(:,4),interTime,'spline');%
intercept y=Cp
    if TypeValue==1
        x0=Result(time_index:time_index2,1);
        y0=Result(time_index:time_index2,2);
        y1=Result(time_index:time_index2,4);
        [~,peakStrain]=ACDMA_fitting(x0,y0,1,1);
        [~,peakCp]=ACDMA_fitting(x0,y1,1,1);
    else
        peakStrain=mspeaks(interTime,interStrain); % peak strain
        peakCp=mspeaks(interTime,interCp); % peak Cp
    end
    peakStrain=peakStrain(find(peakStrain(:,2)>Rang_1(1) &
peakStrain(:,2)<Rang_1(2)),:);
    peakCp=peakCp(find(peakCp(:,2)>Rang_2(3) &
peakCp(:,2)<Rang_2(4)),:);
    filterCp=[];
    for j=1:length(peakCp(:,1))
        if abs(peakCp(j,1)-
peakStrain(knnsearch(peakStrain(:,1),peakCp(j,1)),1))<2
            filterCp=[filterCp,j];
        end
    end
    peakCp=peakCp(filterCp,:);
else
    DeltaMean=0;
end
if doPlot==1
    figure(2)
    subplot(2,1,1)
```

```
[AX,H1,H2]=plotyy(Result(:,1),Result(:,2),Result(:,1),[0;diff(Result(:
,4))]); % Strain/delta Cp
    set(AX(1),'ylim',[Rang_1(1),Rang_1(2)],'xlim',[plx,ply]);
    set(AX(2),'ylim',[Rang_2(1),Rang_2(2)],'xlim',[plx,ply]);
    set(get(AX(1),'Ylabel'),'String','Strain [%]','fontsize', 18)
    set(get(AX(2),'Ylabel'),'String','Delta Cp [pF]','fontsize', 18)
    xlabel('Time (s)','fontsize', 18)
    set(H1,'linestyle','-','marker','.','color','b');
    set(H2,'linestyle','-','marker','.','color','r');
    %legend ('Strain', 'Cp')
    subplot(2,1,2)

[AX,H1,H2]=plotyy(Result(:,1),Result(:,2),Result(:,1),Result(:,4)); %
Strain/Cp
    % plx=1100;
    % ply=1300;
    set(AX(1),'ylim',[Rang_1(1),Rang_1(2)],'xlim',[plx,ply]);
    set(AX(2),'ylim',[Rang_2(3),Rang_2(4)],'xlim',[plx,ply]);
    set(get(AX(1),'Ylabel'),'String','Strain [%]','fontsize', 18)
    set(get(AX(2),'Ylabel'),'String','Cp [pF]','fontsize', 18)
    xlabel('Time (s)','fontsize', 18)
    set(H1,'linestyle','-','marker','.','color','b');
    set(H2,'linestyle','-','marker','.','color','r');

    if doCalDelta==1 & doPlot==1
        %plot the peak strain
        hold on
        plot(AX(1),peakStrain(:,1),peakStrain(:,2),['g','*'])
        hold on
        for peaki=1:length(peakStrain)

text(peakStrain(peaki,1),peakStrain(peaki,2),num2str(peakStrain(peaki,
1)));
        end
        %plot the peak Cp
        hold(AX(2));
        plot(AX(2),peakCp(:,1),peakCp(:,2),['g','*'])
        for peaki=1:length(peakCp)

text(peakCp(peaki,1),peakStrain(peaki,2)./2,num2str(peakCp(peaki,1)));
        end
    end
end
hold off




function
[NeighIndex,CrossPoint]=ACDMA_fitting(x0,y0,thredStrain,NumOfDelet)
% This function is designed to find the peak position.
% y0=strain:from Result(:,2);
% x0=time: from Result(:,1);
% thredStrain=1;

diff_y=diff(smooth(y0));
j=1;
NeighIndex=[];
for i=7:size(diff_y)-5
```

```
    if diff_y(i).*diff_y(i+1)<0 & diff_y(i+1)<0 & y0(i)>thredStrain-
0.5

        ind1=(i+1)-1-5; % only use 5 points for fitting. Can use a
larger value when testing rate is slow.
        ind2=(i+1)-1-0;
        ind3=(i+1)+1;
        ind4=(i+1)+1+5;

[L1(j,:),L2(j,:),CrossPoint(j,:)]=TwoLineCross(x0(ind1:ind2),y0(ind1:i
nd2),x0(ind3:ind4),y0(ind3:ind4));

NeighIndex=[NeighIndex,knnsearch(x0,CrossPoint(j,1),'k',NumOfDelet)];
        j=j+1;
    end
end



function [L1,L2,CrossPoint]=TwoLineCross(x1,y1,x2,y2)
L1=polyfit(x1,y1,1);
L2=polyfit(x2,y2,1);
x=(L2(2)-L1(2))./(L1(1)-L2(1));
y=polyval(L1,x);
CrossPoint=[x,y];
end
```

Appendix 3 : Refereed Journal and Conference Papers Published by The Author as Part of This Thesis

Macromolecules

Article

pubs.acs.org/Macromolecules

Strain-Dependent Dielectric Behavior of Carbon Black Reinforced Natural Rubber

Menglong Huang,[†,‡] Lewis B. Tunnicliffe,[†,‡] Jian Zhuang,[§] Wei Ren,[§] Haixue Yan,[†,‡] and James J. C. Busfield*[,†,‡]

[†]School of Engineering and Materials Science and [‡]Materials Research Institute, Queen Mary University of London, Mile End Road, London E1 4NS, U.K.

[§]Electronic Materials Research Laboratory, Key Laboratory of the Ministry of Education & International Centre for Dielectric Research, Xi'an Jiaotong University, Xi'an 710049, China

Supporting Information

ABSTRACT: The nature of filler−polymer and filler−filler interactions in rubber composites under strain remains an open question in soft matter physics. These interactions are key to explaining the rich variety of complex behavior exhibited by particle-filled rubber products. In this paper we demonstrate a simultaneous dielectric/dynamic mechanical analysis technique (SDMS) which provides new insights into the structure−property relationships of filled rubbers. The complex permittivity of carbon black filled natural rubber has been characterized under a simultaneous tensile strain field (from 0.1% to 50%). The complex permittivity exhibits a dramatic nonlinear dependence on strain coupled with features which are analogous to mechanical strain softening and strain history, namely the "Payne" and "Mullins" effects. The sensitivity of the complex permittivity to such effects is several orders of magnitude greater than in corresponding, traditional mechanical tests. In addition, we demonstrate for the first time that it is possible to use both strain and electrical field frequency as "dipole filters" which can be used to selectively probe the dipoles present at the polymer−filler interface.

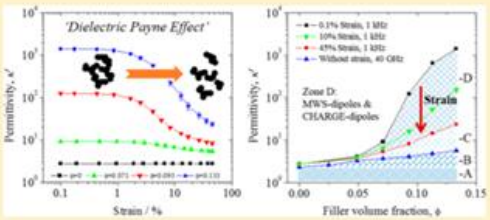

1. INTRODUCTION

Nanostructured particulate fillers such as carbon black and precipitated silica are widely used as the primary reinforcing materials in the tire and rubber industries. Such fillers are often used to provide modifications to the static and dynamic moduli, fracture, and abrasion resistance and, more generally, as a means to modify the strain-dependent viscoelastic spectrum of rubber materials. However, although such technology has been in use for well over a century, the precise physical mechanisms behind the reinforcement phenomenon are still not clearly understood or agreed upon.

Over the past century a wide range of predominantly mechanical-based experimental techniques have been used to investigate the mechanisms of reinforcement.[1−3] Only relatively recently has significant, focused attention been paid to the characterization and interpretation of the dielectric properties of reinforced rubbers. Dielectric investigations present new opportunities for furthering the understanding of reinforcement based upon the sensitivity of the technique to observing changes in the morphology of flocculated or jammed filler particle networks as well as the interactions between filler particles and the polymer matrix. Thus, another possible novel approach to understanding the mechanical behavior of filled rubbers under mechanical deformation is to simultaneously evaluate their mechanical and dielectric properties. Throughout this paper, the dielectric properties are presented as the complex permittivity (simplified as permittivity in the following parts): $\kappa^* = \kappa' - i\kappa''$, where κ' and κ'' are the real and imaginary part of permittivity, respectively. The dielectric loss is defined as $D = \kappa''/\kappa'$.

Elastomers filled with nanoparticles have also shown great potential in energy harvesting,[4] actuating,[5] and sensor devices[6] due to their relatively low moduli and optimized dielectric and mechanical properties. For such applications κ^* is a critical parameter. However, in the literature we find that in most of the cases κ^* is measured and discussed under static (nondeformed) conditions and is treated as a constant value during the devices' working life—despite the fact that such devices would normally operate in a dynamic mechanical environment. The dielectric performance of such materials in the dynamically deformed state is rarely discussed.

1.1. Mechanical Properties of Reinforced Rubbers. In rubber science and technology, the mechanical properties of filler-reinforced rubbers[3] are intimately linked to the filler particle size and morphology, the strain dependence of the flocculated/jammed filler network, and the filler−polymer

Received: October 26, 2015
Revised: January 26, 2016
Published: March 9, 2016

ACS Publications © 2016 American Chemical Society

DOI: 10.1021/acs.macromol.5b02332
Macromolecules 2016, 49, 2339−2347

European Polymer Journal 67 (2015) 232–241

Contents lists available at ScienceDirect

European Polymer Journal

journal homepage: www.elsevier.com/locate/europolj

The glass transition, segmental relaxations and viscoelastic behaviour of particulate-reinforced natural rubber

Menglong Huang [1], Lewis B. Tunnicliffe [1], Alan G. Thomas, James J.C. Busfield *

Materials Research Institute, Queen Mary University of London, Mile End Road, London E1 4NS, United Kingdom

ARTICLE INFO

Article history:
Received 1 September 2014
Received in revised form 14 March 2015
Accepted 17 March 2015
Available online 24 March 2015

Keywords:
Glass transition
Elastomer
Rubber
Reinforcement
Carbon black
Precipitated silica

ABSTRACT

The role of filler particles in defining local changes to the dynamics of elastomer polymers – specifically in relation to the reinforcement of commercial elastomer systems – is as yet incompletely resolved. This work examines the glass transition of filled, crosslinked natural rubber in relation to filler reinforcement mechanisms using a variety of complimentary experimental techniques. Carbon black and precipitated silica filler particles with a wide range of surface areas, structures and surface activities are used as the reinforcing phase. No effect of the filler particles on the calorimetric glass transition is observed in terms of shifting, broadening or transition strength. Dielectric spectroscopy measurements show that the polymer relaxation times of the filled rubbers in the glass-to-rubber transition zone remain essentially equivalent to that of the corresponding unfilled material. Dynamic mechanical analysis demonstrates that the storage moduli of the filled elastomers are significantly amplified on the rubbery side of the glass transition. Elastic stiffening mechanisms are discussed in the context of contributions from filler networking. The reason for a distinct lack of evidence for filler-induced polymer modification may be due to the nature of polymer confinement associated with the imperfect dispersion state of the fillers in the sample and the fact that the fillers themselves are formed from aggregated primary particles rather than being true nanoparticulates.

© 2015 Elsevier Ltd. All rights reserved.

1. Introduction

Crosslinked rubbers (elastomers) reinforced with carbon blacks and precipitated silicas are a widely used and well established type of high performance composite material. However the precise mechanisms of filler reinforcement of elastomers remain incompletely understood despite the large scale utilisation of filled elastomers for a wide range of safety–critical engineering applications. A particularly industrially important aspect of reinforcement is the modification of the strain-dependent viscoelastic spectrum of the elastomers imparted by the presence of the filler phase. For example, in passenger car tyres the performance factors such as wet grip and rolling resistance (contributing to total fuel efficiency) are intimately linked to the viscoelastic properties of the tyre tread material. Some of these modifications can be understood in terms of the structural dynamics of dissipative yielding and stress softening of fractal filler structures under increasing dynamic loadings; but even at small, linear viscoelastic strains where such yielding does not take place, the modification of the viscoelastic spectrum cannot be fully explained in an analytical sense by hydrodynamic, rigid volume reinforcement concepts alone [1–3].

To address this problem, a number of authors have proposed and/or demonstrated that the local segmental

* Corresponding author. Tel.: +44 (0)20 7882 8866.
E-mail addresses: m.huang@qmul.ac.uk (M. Huang), l.tunnicliffe@qmul.ac.uk (L.B. Tunnicliffe), a.g.thomas@qmul.ac.uk (A.G. Thomas), j.busfield@qmul.ac.uk (J.J.C. Busfield).

[1] These authors contributed equally to this work.

http://dx.doi.org/10.1016/j.eurpolymj.2015.03.024
0014-3057/© 2015 Elsevier Ltd. All rights reserved.

TIRE TECHNOLOGY INTERNATIONAL 2014

Carbon black behavior

Impedance characterization of carbon black network structures in elastomer composites

by Menglong Huang and James Busfield, Soft Matter Group, School of Engineering and Materials Science, Queen Mary University of London, UK

The reinforcement of rubber materials by filler particles such as silica or carbon black is a topic of ongoing debate in the rubber industry. There are many models that can explain specific aspects of the reinforcement, such as a constrained polymer layer around the filler or the polymer slippage around the filler surface. At this time there is no agreement into the exact mechanisms that are present to stiffen and toughen elastomer composites under strain. Although it is accepted that the mechanism is some manifestation of the filler structure, up to now there has been no direct method that can allow us to observe the real behavior at the nanoscale.

As carbon black is a conductive filler, the DC conductivity σ_{dc} of filled compounds mainly depends on the filler network structure of the carbon black network. Therefore, an in situ DC test can be used to monitor the formation during mixing and curing or the variation of these networks in cured compounds under strain.

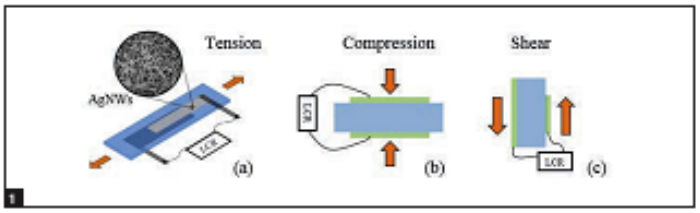

Figure 1: In situ AC test by different deformation mode: (a) Tension (b) Compression (c) Shear. (b) & (c) are side views where the electrodes (green lines) are made from copper. The material under test is marked by blue

Figure 2: R,X,D vs strain for carbon black N220 filled natural rubber

The material becomes conductive when the filler volume fraction is above a certain level, known as percolation threshold ϕ_c,[1] its value being decided by the nature of the CB. For example, finer, highly structured and well-dispersed fillers display a higher σ_{dc} and a lower ϕ_c,[2] while the filler network's break down under strain decreases σ_{dc}.[3]. However, there are several limitations when using this technique. Firstly, σ_{dc} is hard to measure accurately when the filler volume fraction is below ϕ_c. Secondly, contact resistance between the electrodes and the material always exists, limiting the repeatability and accuracy of the test.

AC electrical testing can help overcome these problems and provide more detail of the behavior of filler structures.[4] Impedance spectroscopy can be used to measure the AC electrical properties when dealing with matter with a wide range of resistivities at relatively low frequencies (normally less than 100MHz). The impedance test requires two electrodes to sandwich the material in between. It enables very accurate measurements over a wide frequency and temperature range.[5] The measured complex impedance is defined as

$$Z^*(f,T) = R + jX \quad [1]$$

where $R = |Z| \cdot \cos\theta$ and $X = |Z| \cdot \sin\theta$. The impedance loss factor can be calculated as

$$D = -R/X \quad [2]$$

Therefore, R, X and D are the data directly obtained from the impedance LCR meter and D is a geometrically independent parameter. By incorporating increasing amounts of carbon black fillers into the rubber, the composite changes from being a dielectric to a conductive material. Therefore $|Z|$ decreases while D grows with increasing carbon black volume fraction. By applying a simple serial or parallel model, the capacitance,

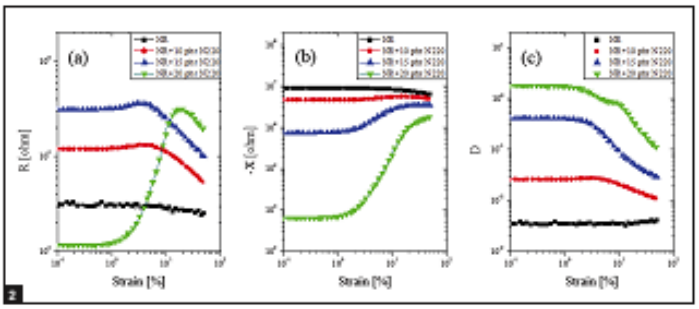

Constitutive Models for Rubber VIII – Gil-Negrete & Alonso (eds)
© 2013 Taylor & Francis Group, London, ISBN 978-1-138-00072-8

The application of a carbon black filled elastomer to create a smart strain sensor

M. Huang, A.G. Thomas & J.J.C. Busfield
Department of Materials, Queen Mary University of London, London, UK

ABSTRACT: Previous work has studied both DC and AC electrical behaviour of Carbon Black filled elastomer systems under cyclic mechanical loading. It has been demonstrated that the relationship between electrical and mechanical properties can be used as cheap and reliable strain sensor. In this work, the effect of tensile strain on the permittivity ε' of carbon black filled rubber has been explored for the first time. A hysteresis of ε' is observed in the first tensile cycle which becomes smaller or even disappears in subsequent cycles. An interesting electrical Payne effect has been observed which can be attributed to the morphology of filler structure and the interactions between filler and rubber. That is, the permittivity of carbon black filled rubber remains virtually constant at very low or very high tensile strains while it decreases over a certain intermediate range of strain. Transforms between filler micro-capacitors and micro-resistors are used to explain the dielectric behaviour under cyclic tensile test.

1 INTRODUCTION

The electrical properties of conductive filler reinforced rubber has attracted researchers' interest for many years not only using DC method (Kraus and Svetlik, 1956, Yamaguchi et al., 2003) but it has also become popular using AC method (Ouyang, 2002). AC technologies offer advantages of monitoring the network or filler-polymer interaction behaviour, especially, under deformation. It has been shown that a very fine and highly structured filler enables the composite to exhibit a reversible DC electrical property over a large range of strain up to thousands of cycles (Jha et al., 2010). AC Dielectric Spectroscopy (DS) techniques using a capacitor type strain sensors with an unfilled rubber as a dielectric materials has been reliably demonstrated (Hu et al., 2013) as shown in Figure 1(a).

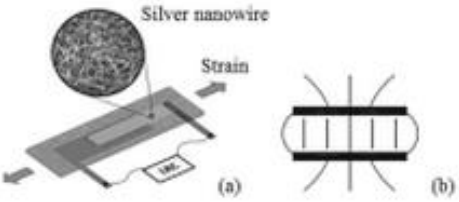

Figure 1. (a) A capacitor based rubber sensor using unfilled elastomer as the dielectric and silver nanowire as the stretchable electrode; (b) The parallel-plate capacitor model.

Therefore, it is proposed that rubber materials are capable of working as strain sensors.

In a polymer and conductive filler composite, an increase in the filler volume fraction to a certain point P_c, known as percolation threshold (Stauffer and Aharony, 1994), allows the filler particles to gather and form a series of continuous conductive paths which makes the material change from being an insulator to a conductor (Zhang et al., 2012). More interestingly, around P_c a slight change of the filler volume fraction can cause orders of magnitude shift in the conductivity, or permittivity. Actually, the filler particles do not need to have a directly contact with each other to be conductive if the distance between them is as small as a few nanometers, since the electrons can travel through thin polymer layers between the particles by tunneling or hopping mechanisms (Sheng, 1980, Trionfi et al., 2008). There are also theories based on Debye's relaxation which claim that the average distance between particles can be calculated by dielectric spectroscopy (Ouyang, 2002). Although it has agreed with the results from DC tests and mechanical tests for some composites (Geberth and Klüppel, 2012), more evidence from different filler-polymer systems are needed since the relaxation mechanism for a conductive filler-polymer system is still unclear. At least, it shows that the DS technologies can be a useful tool to study the filler structure.

The AC electrical properties normally refer to the permittivity and dielectric loss, generally tested by a parallel-plate capacitor model below 100 MHz.